TOWARDS MEDIUM-RESOLUTION SOIL MOISTURE RETRIEVAL FROM ACTIVE AND PASSIVE MICROWAVE OBSERVATIONS

Xiaoling Wu

Submitted in fulfilment of the requirements for the degree of

Doctor of Philosophy

October 2014

Department of Civil Engineering

MONASH University

Table of Contents

Synopsis

Surface soil moisture is essential to global water cycle monitoring, weather forecasting, prediction of drought and flood, and modelling of evaporation. The European Space Agency (ESA) launched the Soil Moisture and Ocean Salinity (SMOS) satellite in 2009, as the first-ever soil moisture dedicated satellite. It uses the passive microwave (radiometer) remote sensing technology due to the direct relationship with soil moisture, but due to technical limitations the spatial resolution is approximately 40 km. This places limitations on hydro-meteorological applications such as regional weather forecasting, flood prediction, and agricultural activities that have a resolution requirement of better than 10 km.

Active microwave (radar) remote sensing provides a much higher spatial resolution capability (better than 3 km), but it is less sensitive to changes in soil moisture due to the confounding effects of vegetation and surface roughness. Consequently, NASA has developed the Soil Moisture Active Passive (SMAP) mission, scheduled for launch in January 2015, which will merge passive and active observations to overcome their individual limitations, thus providing a soil moisture product with resolution better than 10 km at a target accuracy of 0.04 cm^3/cm^3. The rationale behind this mission is to use fine resolution (3 km) radar observations to disaggregate the coarse resolution (36 km) radiometer observations into a medium-resolution (9 km) product.

The downscaling algorithms for this purpose have so far undergone only limited testing with experimental data sets, and have therefore been tested mostly using synthetic data and a limited number of suitable experimental data sets mostly in the continental United States. Consequently, this thesis presents an extensive evaluation of soil moisture downscaling algorithms with an experimental data set collected from the Soil Moisture Active Passive Experiment (SMAPEx) field campaigns in south-eastern Australia. This research affords a unique opportunity to undertake a comprehensive assessment of the various downscaling approaches proposed, having applicability to the forthcoming SMAP mission. In particular, each approach is comprehensively assessed using a consistent data set collected over a diverse landscape exhibiting a range of conditions, and then inter-compared with the results from the others. A particular focus is placed on the SMAP baseline algorithm as this is currently the preferred algorithm and scheduled for implementation by NASA immediately upon launch.

A preliminary study on the SMAP baseline algorithm was conducted by using existing satellite data; results from which suggested that a better representation of the SMAP data stream characteristics was required. Consequently, a study was undertaken on how to prepare the simulated SMAP data stream from the airborne data set collected from the SMAPEx field campaigns in Australia. These data were processed in terms of spatial aggregation, incidence angle normalization and azimuth effect analysis so as to be in line with the characteristics of the SMAP observations. Results indicated that data from SMAPEx could be reliably processed to represent the characteristics of the SMAP observations.

The baseline algorithm was then tested using the simulated SMAP data set. Results showed that the baseline downscaling algorithm had the ability to fulfil the error requirement of medium resolution (9 km) brightness temperature product of SMAP over relatively homogenous area, but it had greater error than the requirement over the heterogeneous cropping area. Consequently, the baseline algorithm was assessed at higher resolutions in order to study the effect of land cover type and surface heterogeneity on the resulting downscaling accuracy. The medium resolution (9 km) brightness temperatures obtained from the baseline algorithm were then converted to a medium resolution soil moisture product, and results compared with other linear methods including the optional downscaling algorithm and a change detection method, and with a non-linear Bayesian merging method. The comparison of these different soil moisture downscaling algorithms suggested that the optional algorithm and the Bayesian merging method had a similar performance in retrieving medium resolution soil moisture products, with the lowest error and highest correlation between downscaled and reference soil moisture, amongst the downscaling algorithms tested. However, unless further improvements can be achieved with the Bayesian merging method the optional algorithm is recommended for application in

SMAP due to its simplicity of approach and low computational requirement, thus making it simpler to apply in an operational context.

Declaration

This thesis contains no material which has been accepted for the award of any other degree or diploma in any university or other institution and affirms that to the best of my knowledge, the thesis contains no material previously published or written by another person, except where due reference is made in the text of thesis.

Xiaoling Wu

Acknowledgements

I would like to express my gratitude to all those who helped me during my PhD study and the writing of this thesis.

My deepest gratitude goes first and foremost to Professor Jeff Walker, my main supervisor, for his constant encouragement and guidance. He has offered me valuable suggestions and has spent a lot of time helping me successfully accomplish each milestone during the entire period of my PhD. I do appreciate his time spent on reading my paper drafts and his very detailed comments/edits on those, which I have greatly benefited from. Without his patient instruction, insightful criticism and expert guidance, the completion of this thesis would not have been possible.

I would also like to express my heartfelt gratitude to my co-supervisors, Dr. Chris Rüdiger and Dr. Rocco Panciera, who have been the great support behind me and always provided me with inspiring advice during my study. I have learned a lot of knowledge and working skills from them. Without their valuable input on each stage of my PhD, I would not solve the problems I met and would not accomplish my thesis.

I am also greatly indebted to Ms. Jenny Manson, who has had everything organized for me and helped me a lot in the past three and half years. I feel so grateful for her kindness and patience and feel so happy to have her witnessed my "grow-up" in the department.

Special thanks to my dear friends/group-mates, Ying Gao, Ranmalee Bandara, and Mei Sun Yee, who have given me their helps and time in listening to me and helping me work out my problems during the difficult period of my PhD. I have to say, this "Gossip" group of four, really made me feel happy and relaxed especially when I encountered some problems from work or study.

My thanks would go to my beloved family for their loving considerations and great confidence in me all through these years. I would finally like to express my gratitude to my husband Ou Yang, who has always been helping me out of difficulties and supporting without a word of complaint. Thank you for comforting me whenever I felt sad and picking me up whenever I felt down, and thank you for always being around.

List of Symbols

Symbols	*Units*	*Definitions*
β_1	[K/dB]	Sensitivity of brightness temperature to backscatter
β_2	[(cm^3/cm^3)/dB]	Sensitivity of soil moisture to backscatter for optional algorithm
β_3	[(cm^3/cm^3)/dB]	Sensitivity of soil moisture to backscatter for change detection method
θ	[cm^3/cm^3]	Soil moisture
ω	-	Single scattering albedo
σ	[dB]	Backscatter coefficient
σ_{pp}	[dB]	Backscatter coefficient at co-polarization *pp*
σ_{pq}	[dB]	Backscatter coefficient at cross-polarization *pq*
τ	-	Opacity
Γ	[dB/dB]	Sensitivity of backscatter at *vv*-polarization to backscatter at *hv*-polarization
A	[°]	Azimuth viewing angle
b	-	Vegetation parameter relating to vegetation type
h	[cm]	Surface roughness parameter
h-	-	Horizontal polarization of brightness temperature
hh-	-	Horizontal co-polarization of backscatter
hv-	-	Cross-polarization of backscatter
$h[X^b]$	-	Brightness temperature and backscatter estimates from forward models at background soil moisture X^b
H	-	First derivative of $h[X^b]$
K	-	Kalman gain

Symbols	*Units*	*Definitions*
p	-	Polarization of brightness temperature
pp	-	Co-polarization of backscatter
pq	-	Cross-polarization of backscatter
P	[cm^3/cm^3]	Error covariance of background soil moisture and radar-retrieved soil moisture
R	-	Error variance of observations and predictions from models
R^2	-	Correlation coefficient
t	-	At time t
t_R	-	Revisit time of observations
Tb	[K]	Brightness temperature
Tb_p	[K]	Brightness temperature at polarization of p;
T_{surf}	[K]	Surface temperature
v-	-	Vertical polarization of brightness temperature
vv-	-	Vertical co-polarization of backscatter
x_c	[cm^3/cm^3]	Background soil moisture at 36 km resolution
x_f	[cm^3/cm^3]	Soil moisture at resolution of f
X^a	[cm^3/cm^3]	Soil moisture at fine resolution
X^b	[cm^3/cm^3]	Background soil moisture
Z	-	Radar and radiometer observations

List of Abbreviations

ALOS	Advanced Land Observing Satellite
AMSR-E	Advanced Microwave Scanning Radiometer for EOS
ASAR	Advanced Synthetic Aperture Radar
ASCAT	Advanced Scatterometer
ATBD	Algorithm Theoretical Basis Document
AVHRR	Advanced Very High Resolution Radiometer
C	Coarse resolution
CanEx-SM10	Canadian Experiment for Soil Moisture 2010
CDF	Cumulative Distribution Function
CLASIC	Cloud and Land Surface Interaction Campaign
COSMO-SkyMed	Constellation of small Satellites for the Mediterranean basin Observation Satellite
ENVISAT	ENVIronmental SATellite
ERS-1/2	The 1st/2nd European Remote Sensing Satellite
ESA	European Space Agency
F	Fine resolution
H	Horizontal polarization
HDAS	Hydraprobe Data Acquisition System
LAI	Leaf Area Index
M	Medium resolution
MetOp-A	Meteorological Operational Satellite
MODIS	MODerate resolution Imaging Spectroradiometer
NASA	National Aeronautics and Space Administration
NDVI	Normalized Difference Vegetation Index
NIR	Near Infrared
NOAA	National Oceanic and Atmospheric Administration
NRC	National Research Council
NSCAT	NASA Scatterometer

OSSE	Observation System Simulation Experiment
OzNet	Australian monitoring network for soil moisture and micrometeorology
PALS	Passive and Active L-band System
PALSAR	Phased-Array L-Band Synthetic Aperture Radar
PLIS	Polarimetric L-band Imaging Synthetic aperture radar
PLMR	Polarimetric L-band Multi-beam Radiometer
PRC	Passive Radar Calibrators
RADARSAT-1/2	The $1^{st}/2^{nd}$ RADARSAT satellite
RMS	Root Mean Square
RMSE	Root Mean Square Error
RMSD	Root Mean Square Deviation
RVI	Radar Vegetation Index
SAR	Synthetic Aperture Radar
SD	Standard Deviation
SGP99	Southern Great Plains experiments 1999
SJV10	San Joaquin Valley field campaign 2010
SMAP	Soil Moisture Active Passive
SMAPEx	Soil Moisture Active Passive Experiments
SMAPVEX2008	Soil Moisture Active Passive Validation Experiment 2008
SMAPVEX2012	Soil Moisture Active Passive Validation Experiment 2012
SMEX02	Soil Moisture Experiment 2002
SMOS	Soil Moisture Active Passive
SSM/I	Special Sensor Microwave Imager
SWC	Soil Water Content
SWIR	Short-Wave Infrared
TDR	Time-Domain Reflectometry
TerraSAR	TerraSAR satellite
TIR	Thermal Infrared
UAVSAR	Uninhabited Aerial Vehicle Synthetic Aperture Radar
USGS	U.S. Geological Survey

UTC	Coordinated Universal Time
V	Vertical polarization
VWC	Vegetation Water Content

List of Figures

List of Tables

1 Introduction

This thesis presents an extensive evaluation of soil moisture downscaling algorithms with applicability to NASA's new satellite mission - Soil Moisture Active Passive (SMAP). The principle of these downscaling algorithms is to retrieve an accurate soil moisture product at medium-resolution (around 10 km) through the combination of passive and active microwave observations. Data used for assessing the feasibility of different downscaling algorithms were primarily collected from the Soil Moisture Active Passive Experiment (SMAPEx) field campaigns in south-eastern Australia, which have the ability to simulate the SMAP data stream using an airborne simulator. A series of studies are shown in this thesis, including simulation of SMAP prototype data stream from the airborne observations and subsequent evaluation of different downscaling approaches with those simulated data, with contribution to the development of pre-launch algorithms for the forthcoming SMAP mission.

1.1 Statement of Problem

The global measurement of soil moisture is vital to understanding the global water, energy and carbon cycles, which play an important role in agriculture, hydrology and meteorology (Wagner et al., 2003). However, ascertaining the spatial and temporal variation in soil moisture is hampered by a general inability to model accurately and a lack of *in-situ* soil moisture observations globally. Even when available, *in-situ* soil moisture measurements are often spatially and temporally too sparse to be used in such studies (Hain et al., 2011). Therefore, the general infeasibility of sustaining large *in-situ* soil moisture monitoring network and limitation of numerical model prediction has led to retrieval of soil moisture from satellite-based remote sensing. With the development of remote sensing technology (Jackson et al., 2002), soil moisture mapping over large areas is becoming a practical alternative when compared with traditional monitoring by *in-situ* networks. Moreover, methods are being developed to make use of this emerging soil moisture information to constrain numerical model prediction of soil moisture (Shi et al., 2009), and hence improve the forecasting of weather, floods and agriculture-related applications.

Over the past decade, passive microwave remote sensing has become generally accepted as the most accurate of the soil moisture remote sensing methods, due to its stronger and more direct connection between the observed brightness temperature (*Tb*) and the surface soil moisture (~5 cm), than with active microwave sensing (radar backscatter) or thermal (skin temperature) data (Kerr, 2007). The best results were found at low frequency (~1.4 GHz) due to reduced interference by the atmosphere, surface roughness and vegetation, and an increased observation depth (>5 cm). Consequently, the Soil Moisture and Ocean Salinity (SMOS) mission (Kerr et al., 2010) was launched by the European Space Agency in November 2009, as the first-ever satellite dedicated to soil moisture measurement using L-band passive microwave measurements. However, the current spatial resolution remains a significant limitation of the passive microwave approach.

Despite the high sensitivity of the passive microwave radiometer approach to near-surface soil moisture monitoring, it suffers from being relatively low spatial resolution, on the order of 36km, which is a significant limitation for regional applications such as precipitation forecasting and flood prediction, that have a special resolution requirement of better than 10km. This resolution requirement is derived from hydro-meteorological applications such as precipitation forecast systems driven by thermal convection, as well as several applications in hydrologic and atmospheric science, which have distinguishing features or significant physical interactions at this scale (Das et al., 2011). Availability of such soil moisture product is expected to enhance our understanding and forecast capabilities of regional weather systems around the world. Moreover, it is expected to benefit agricultural applications and large watershed or river-basin management activities. While fine-scale soil moisture information can be retrieved by active microwave remote sensing, the observations are less sensitive to changes in soil moisture due to the confounding effects of vegetation conditions and surface roughness, meaning that the retrieved soil moisture estimates usually have a much larger uncertainty.

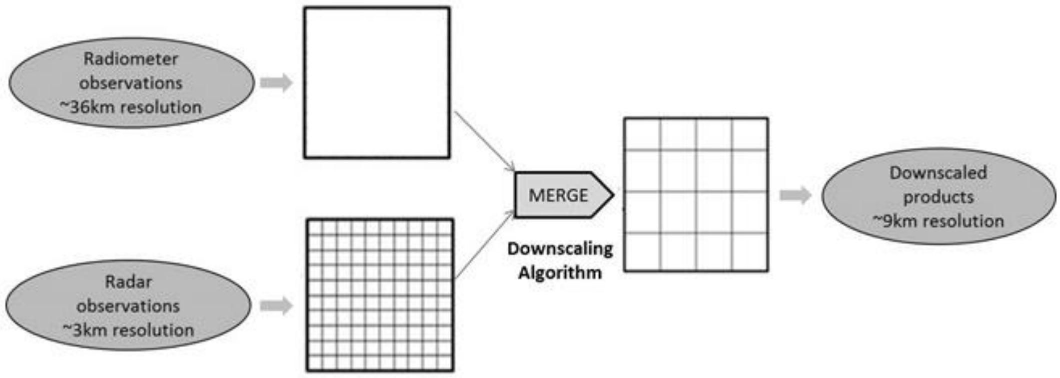

Figure 1-1: Overview of downscaling approach by merging radiometer and radar observation.

NASA's Soil Moisture Active Passive (SMAP) mission (Entekhabi et al. 2010), scheduled to be launched in January 2015 will attempt to overcome this scale issue by using fine scale (3 km) active microwave observations to downscale the coarse scale (36 km) passive microwave observation to medium (9 km) resolution. The rationale behind SMAP is that the synergy between active and passive observations can be used in a downscaling approach to overcome the individual limitations of each observation, ultimately providing soil moisture data at a resolution more suitable for hydro-meteorological applications. Figure 1-1 schematically illustrates the SMAP approach.

In preparation for the SMAP launch, suitable algorithms and techniques need to be developed and validated to ensure that an accurate medium-resolution (~9 km) soil moisture product can be operationally produced from combined SMAP radiometer and radar observations. The currently proposed baseline downscaling method to be applied in the SMAP mission is based on an observed near-linear relationship between radar backscatter (σ) and the brightness temperature (Tb) at the same scale to downscale the brightness temperature to 9 km. The downscaled brightness temperature at 9 km will then be interpreted to soil moisture using the standard passive microwave retrieval model (Das et al., 2014, Entekhabi et al., 2012). An optional method proposed for the SMAP mission would utilize the near-linear relationship between radar backscatter and volumetric soil moisture (rather than brightness temperature) and ultimately retrieve the medium-resolution soil moisture product directly (Das et al., 2011, Entekhabi et al., 2012). An important element of these two methods is that the relationship between the slope parameter and vegetation heterogeneity should be formulated to improve the accuracy of this algorithm. Other downscaling methods, such as the change detection method, which takes advantage of the approximately linear dependence of radar backscatter and brightness temperature change on soil moisture change (Piles et al., 2009, Narayan et al., 2006). A further candidate downscaling approach is based on the Bayesian merging algorithm (Zhan et al., 2006), use a totally different strategy which results in a downscaled soil moisture product directly through the synergy of the active and passive data in a Bayesian framework.

While these methods have been presented elsewhere, they have been mostly tested with synthetic data (e.g. Observation System Simulation Experiment (OSSE) framework), and only very limited experimental data from field campaigns. Such campaigns include the Southern Great Plains experiment in Oklahoma in 1999 (SGP99) (Njoku et al., 2002, Bolten et al., 2003), the Soil Moisture Experiment in Iowa in 2002 (SMEX02) (Narayan et al., 2004, Crosson et al., 2005, Narayan et al., 2006), the Cloud and Land Surface Interaction Campaign in Oklahoma in 2007 (CLASIC) (Bindlish et al., 2009, Yueh et al., 2008), the Canadian Experiment for Soil Moisture 2010 (CanEx-SM10) (Magagi et al., 2013), the Soil Moisture Active Passive Validation Experiment (SMAPVEX2008 and SMAPVEX2012) (Colliander et al., 2012a, Bindlish et al., 2010, Yueh et al., 2009), and the Soil Moisture Active Passive Experiments (SMAPEx) in Australia in 2010 and 2011 (Panciera et al., 2014). Consequently, it is essential that field campaigns with coordinated satellite, airborne and ground-based data collection be undertaken, and algorithms tested giving careful consideration to the data requirements for simulating the SMAP mission and validating the subsequent soil moisture retrievals. Therefore, the algorithm studies in this thesis are based on the SMAPEx field campaign, conducted using active and passive microwave airborne observations to address the scientific requirements pertinent to SMAP.

1.2 Objectives and Scope

Given that current downscaling algorithms are relatively immature and not widely tested using experimental data, the main objective of this thesis is to thoroughly evaluate the performance of proposed downscaling algorithms based on the synergy between active and passive microwave observations. The SMAP requirement is to retrieve near-surface soil moisture at medium-resolution (9 km) with a target accuracy of 0.04 cm^3/cm^3 (in fairly uniform areas with vegetation water content less than 5 kg/m^2).

This research evaluates proposed downscaling approaches using experimental data collected from the SMAPEx field campaigns undertaken in Australia. The SMAPEx field campaigns provide the opportunity to evaluate the SMAP Active-Passive baseline algorithms using data that represents different sets of moisture conditions and land covers. Data were collected from an airborne SMAP simulator consisting of the Polarimetric L-band Multi-beam Radiometer (PLMR) and the Polarimetric L-band Imaging Synthetic aperture radar (PLIS), which provide brightness temperature observations and backscatter observations respectively. These field campaigns are complementary to the other campaigns (as mentioned in Section 1.1) in addressing scientific requirements of the SMAP mission, therefore representing a significant contribution to the limited heritage of airborne experiments mentioned above. Available satellite data, e.g. brightness temperature data from SMOS satellite and backscatter data from ASAR (Advanced Synthetic Aperture Radar onboard ENVISAT satellite) are also assessed. Studies on four soil moisture downscaling methods are presented in this thesis, including the baseline downscaling algorithm and optional downscaling algorithm, change detection method and Bayesian merging method (Das et al., 2014, Das et al., 2011, Piles et al., 2009, Zhan et al., 2006).

1.3 Outline of Approach

The approach of this thesis includes two main parts: i) simulation of SMAP data set from field campaigns and other satellites; and ii) retrieval of medium-resolution (9 km) soil moisture from the active and passive data through different downscaling algorithms. A schematic diagram of the approach can be found in Figure 1-2.

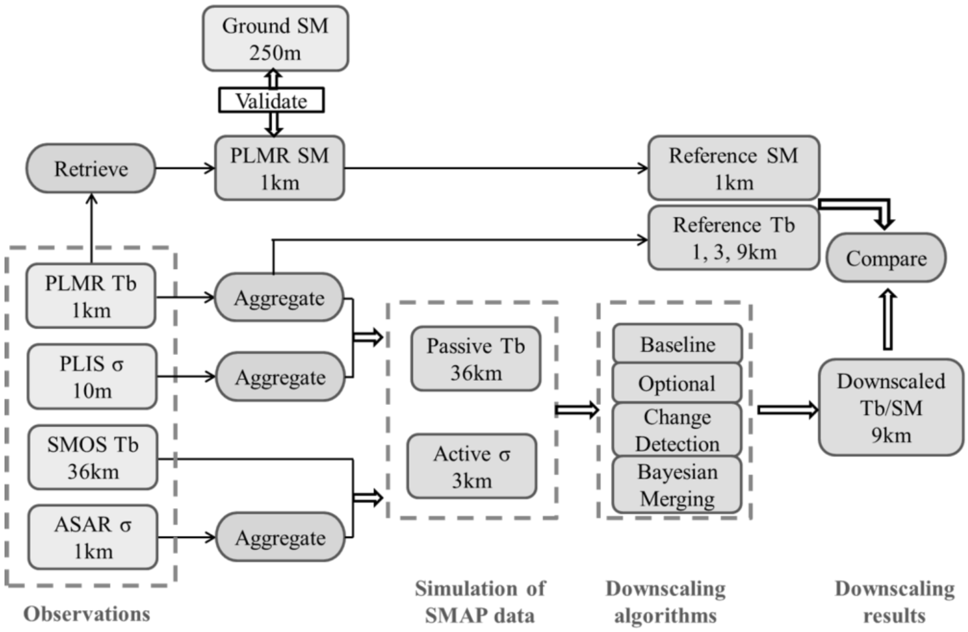

Figure 1-2: Schematic of SMAP data simulation and retrieval of medium resolution soil moisture product. (SM=Soil Moisture; *Tb*=Brightness temperature; *σ*=Backscatter.)

Prior to undertaking the downscaling, data collected from the airborne simulator (PLMR and PLIS) needed particularly to be processed in line with characteristics of the SMAP sensors, in terms of the incidence angle, resolution and azimuth direction of the observations; see details on the characteristics of different sensors in Table 1-1.

Upon preparation of the simulated SMAP data, four downscaling methods are tested in this research: baseline downscaling algorithm (Das et al., 2014), optional downscaling algorithm (Das et al., 2011), change detection method (Piles et al., 2009, Narayan et al., 2006) and Bayesian merging method (Zhan et al., 2006).

The baseline downscaling algorithm is first tested for its ability to downscale brightness temperature from 36 km to 9 km using 3 km backscatter. A more extensive assessment of this baseline algorithm is also conducted in order to test the effect of land covers on the baseline downscaling algorithm at different resolution levels. Consequently, brightness temperature is also downscaled from 9 km to 3 km using 1 km backscatter, and brightness temperature is downscaled from 1 km to 250 m using 100 m backscatter, keeping a similar resolution ratio between radiometer and

Table 1-1: Characteristics of the SMAP, PLMR and PLIS sensors.

Sensor	Frequency	Polarizations	Incidence angle	Spatial resolution of product	Revisit frequency
SMAP radar	1.26 GHz	*hh*, *vv* & *hv*	40˚	3 km	2-3 days
SMAP radiometer	1.4 GHz	*h* & *v*	40˚	36 km	2-3 days
PLIS	1.26 GHz	*hh*, *vv*, *hv* & *vh*	15˚ - 45˚	10 - 30 m*	2-3 days
PLMR	1.4 GHz	*h* & *v*	17˚, 21.5˚ & 38.5˚	1 km*	2-3 days

* when flown at 10,000ft AGL

radar observations and the downscaled product (i.e., approximately 9:1:3) as for SMAP. Using the correlation between brightness temperature and backscatter at coarse scale, the direct output of the baseline downscaling algorithm is the downscaled brightness temperature at medium resolution. According to this approach, it is the downscaled brightness temperature that is inverted to soil moisture, using the standard passive microwave retrieval model (Das et al., 2014, Jackson et al., 1982, Jackson and Schmugge, 1991).

In contrast, the optional downscaling algorithm for SMAP derives the medium-resolution soil moisture product directly from the coarse resolution soil moisture (36 km) and fine resolution backscatter observations (3 km). The change detection method also directly retrieves a medium-resolution soil moisture product. This radar-radiometer change detection algorithm uses the previous radiometer-scale soil moisture retrieval updated with the moisture change evident in the higher resolution radar backscatter change.

The baseline, optional and change detection methods are all defined as linear approaches, based on the assumption of a linear relationship among brightness temperature, backscatter and soil moisture. In contrast, the Bayesian algorithm is a non-linear approach that utilizes the Kalman filter update equations to combine the brightness temperature and backscatter observations (Zhan et al., 2006, Kalman, 1960). This Bayesian method involves three main steps: i) background estimation using the passive microwave retrieval method from coarse resolution brightness temperature; ii) uncertainties of the background states and observations; and iii) observation functions using non-linear microwave emission and backscatter model at the background soil moisture.

Downscaled brightness temperature and soil moisture products obtained from each downscaling algorithm are derived from the simulated SMAP data stream and validated against reference data. In this study, the reference data come from either observed PLMR brightness temperature data or PLMR derived soil moisture.

1.4 Thesis Organization

This thesis is divided into eleven chapters. **Chapter 2** is an extensive review of literature pertaining to the different aspects of the proposed methodology. **Chapter 3** is a description of the key data sets, including the introduction of the study area of this research in the locality of Yanco, in the Murrumbidgee Catchment in Australia, and collection of airborne flights, together with the concurrent ground sampling. **Chapter 4** presents preliminary research on the baseline downscaling algorithm using data from SMOS and ASAR, and points out the need for a more representative simulation of the SMAP data stream. **Chapter 5** develops the process of simulating the SMAP prototype data from airborne sensors data. Based on the simulated SMAP data, the baseline downscaling algorithm for SMAP is tested in **Chapter 6**, and used to downscale the brightness temperature from 36 km resolution to 9 km resolution using backscatter at 3 km resolution. In order to check the effect of land cover on the baseline algorithm, **Chapter 7** presents the application of this baseline algorithm on downscaling brightness temperature from 9 km to 3 km, keeping a similar resolution ratio as in Chapter 6. The baseline downscaling algorithm is further tested in **Chapter 8** for land cover type heterogeneity impacts using 1 km brightness temperature downscaled to 250 m resolution. The baseline algorithm is then contrasted against a range of alternative algorithms after converting the 9 km resolution brightness temperature from Chapter 6 to soil moisture. In **Chapter 9**, the results are compared with two other linear soil moisture downscaling methods, including the optional downscaling method and the change detection method. **Chapter 10** demonstrates an alternative non-linear approach based on Bayesian merging. The conclusions and future work are discussed in **Chapter 11**.

Some sections of this thesis are based on either all or part of the following publications:

- **X. Wu**, J. P. Walker, C. Rüdiger, R. Panciera and D. Gray, "Simulation of the SMAP Data Stream from SMAPEx Field Campaigns in Australia," *IEEE Transactions on Geoscience and Remote Sensing*, vol. 53, no. 4, pp. 1921-1934, 2015.
- **X. Wu**, J. P. Walker, N. N. Das, R. Panciera and C. Rüdiger, "Evaluation of the SMAP Brightness Temperature Downscaling Algorithm using Active-Passive Microwave Observations," *Remote Sensing of Environment*, DOI: 10.1016/j.rse.2014.08.021. In press.
- **X. Wu**, J. P. Walker, C. Rüdiger and R. Panciera. "Effect of Land Cover Type on the SMAP Active-Passive Soil Moisture Downscaling Algorithm Performance," *Geoscience and Remote Sensing Letters*, DOI: 10.1109/LGRS.2014.2364049. In press.
- **X. Wu**, J. P. Walker, C. Rüdiger and R. Panciera. "Comparison of Different Soil Moisture Downscaling Approaches using Active-Passive Microwave Observations," *IEEE Transactions on Geoscience and Remote Sensing*. Under review.
- **X. Wu**, J. P. Walker, C. Rüdiger and R. Panciera. "Evaluation of Bayesian merging method for retrieving medium-resolution soil moisture with SMAPEx data set," *IEEE Transactions on Geoscience and Remote Sensing*. Under review.
- **X. Wu**, J. P. Walker, C. Rüdiger, R. Panciera and N. N. Das, "Downscaling of coarse-resolution radiometer brightness temperature by high-resolution radar backscatter," In Piantadosi, J., Anderssen, R.S. and Boland J. (eds). *20th*

International Congress on Modelling and Simulation (MODSIM2013). Modelling and Simulation Society of Australia and New Zealand, December 2013, pp. 3127-3133. ISBN: 978-0-9872143-3-1.

- **X. Wu**, J. P. Walker, C. Rüdiger, R. Panciera, A. Monerris and N. N. Das, "Towards medium-resolution brightness temperature retrieval from active and passive microwave," In Chan, F., Marinova, D. and Anderssen, R. S. (eds). *The 19th International Congress on Modeling and Simulation (MODSIM2011)*. Modelling and Simulation Society of Australia and New Zealand, 12-16 December 2011, pp. 2023-2029. ISBN: 978-0-9872143-1-7

The following co-authored papers have also contributed to the work of this thesis. My main role was in soil moisture and vegetation samplings during the SMAPEx-3 field campaign, angle normalization of radar observations from PLIS, and in archiving all the SMAPEx data to the web.

- R. Panciera, J. P. Walker, T. J. Jackson, D. Gray, M. A. Tanase, D. Ryu, A. Monerris, H. Yardley, C. Rüdiger, **X. Wu**, Y. Gao and J. Hacker, "The Soil Moisture Active Passive Experiments (SMAPEx): Toward Soil Moisture Retrieval From the SMAP Mission," *IEEE Transactions on Geoscience and Remote Sensing*, vol. 52, no. 1, pp. 490-507, 2014.
- S. Elhassan, **X. Wu**, J. P. Walker, "Standing water detection using radar," In Piantadosi, J., Anderssen, R.S. and Boland J. (eds). *20th International Congress on Modelling and Simulation (MODSIM2013).* Modelling and Simulation Society of Australia and New Zealand, December 2013, pp. 3085-3091. ISBN: 978-0-9872143-3-1

2 Literature Review

This chapter presents the importance of soil moisture estimation and its influence on environmental applications, followed by a review of the theoretical and experimental background to soil moisture measurement using *in-situ* monitoring stations and remote sensing technology, with particular focus on the trade-off between the accuracy and spatial resolution by remote sensing means. Current active and passive microwave downscaling algorithms are then discussed with a focus on NASA's SMAP mission, which is designed to provide a 9 km resolution downscaled soil moisture product by merging active and passive microwave observations. The knowledge gap in existing downscaling algorithms to be addressed by this thesis is then identified. A review of field campaigns for validation of the SMAP downscaling algorithm performance is also provided.

2.1 Importance of Soil Moisture Estimation

The availability of fine scale soil moisture will benefit many applications, including precipitation forecasting, flood prediction, drought monitoring and agriculture-related applications (Entekhabi et al., 1999, Wagner, 2007). Soil moisture is the state variable of the water cycle over land, controlling water fluxes between the atmosphere, land surface and subsurface, through evaporation and plant transpiration (Hong and Kalnay, 2000, Koster et al., 2004, Trenberth, 1998). Because a large amount of heat is exchanged when water changes phase, the water cycle is fundamental to the dynamics of the earth's energy cycle. Since water is the ultimate solvent in the earth system, biogeochemical cycles such as carbon, nitrogen and methane are embedded in the water cycle. Through these dynamics, soil moisture conditions the evolution of weather and climate over continental regions. Therefore, global measurement of soil moisture is crucial to improving our understanding of water cycle processes, ecosystem productivity, and the linkages between the earth's water, energy and carbon cycles. Information on global soil moisture patterns will be transformational for the earth's system science, as it will help characterize the relationship between soil moisture, its freeze/thaw state, and associated environmental constraints to ecosystem processes such as land-atmosphere carbon, water and energy exchange, and vegetation productivity (Leese and Kermond, 2000, Timbal et al., 2001, Seneviratne et al., 2010). For example, numerous studies have shown that the initialization of global weather forecast models with accurate soil moisture information will enhance their prediction skill and extend their forecast lead-times (Shukla and Mintz, 1982, Delworth and Manabe, 1989, Brubaker and Entekhabi, 1996, Pielke, 2001). The quality of weather forecasts is significantly dependent on the availability of accurate initial states for key atmospheric variables, due to the chaotic nature of the atmosphere. While significant effort has been focused on measuring the initial states of temperature, air density, winds, and water vapour to improve weather forecasts, it is now recognized that the next significant advance in the quality of weather forecasts will come from constraining the soil moisture predictions over land.

It has also been shown that soil moisture can be as important as precipitation for the prediction of floods and droughts (Fennessy and Shukla, 1999, Dirmeyer et al., 2000). There is no global *in-situ* or current satellite capability to monitor and map soil moisture with fine resolution and high accuracy, and so estimations are mostly produced from models, with a high degree of uncertainty (Crow et al., 2005). Therefore, the assimilation of accurate soil moisture observations at the scale of severe weather phenomena is expected to improve both drought and flood forecasting, enabling more effective hazard monitoring and mitigation efforts (Douville, 2004).

The use of accurate soil moisture products in agriculture-related applications, such as productivity forecasting, operational crop yield and moisture stress information systems, is also of benefit (Champagne et al., 2012, McGinn and Shepherd, 2003). Soil moisture information, despite the difficulties in quantifying it, is essential for monitoring agricultural landscapes. The impact of moisture stress on crop yield has been examined at various scales and in response to various adaptations and agricultural practices (Campbell et al., 1997, Champolivier and Merrien, 1996, Cutforth et al., 2007, Desjardins and Ouellet, 1980). In general, moisture deficits in the root zone have the greatest impact on agricultural productivity when they occur during reproduction and seed development growth phases (Boken et al., 2005).

Soil moisture information also plays an important role in public health through links to vector borne diseases (Schman, 2005). Moreover, soil moisture information will indirectly benefit human health applications through better weather forecast, leading to an improved prediction of virus spreading rates and heat stress; and floods, leading to an improved disaster preparation and response plan. Techniques for global soil moisture estimation are therefore urgently needed, with the potential to greatly benefit all of society.

2.2 Techniques for Soil Moisture Estimation

Various techniques for estimating soil moisture have been developed and evaluated, including *in-situ* measurements and remote sensing technology.

2.2.1 *In-situ* soil moisture measurement

The soil moisture can be measured *in-situ* either directly or indirectly. The more direct method is the Thermo-gravimetric measurement. According to this approach the amount of water is directly measured based on the weight measurement of a wet sample before and after oven drying at 105 °C for 24 hours (Evett et al., 2008). This thermo-gravimetric measurement is performed for calibration of other indirect soil moisture sensors. However, this direct measurement method is destructive since it requires that the soil sample be removed from the field and analysed in the laboratory. Moreover, it is a time-consuming and impractical way of measuring soil moisture over large areas, and it is not possible to make repetitive observations on the same soil sample or at the same location. Hence, to obtain a time-series of *in-situ* soil moisture at point scale, it is necessary to utilize non-destructive methods. Because of these limitations, a variety of indirect measurements have been developed. The majority of the commercial sensors are based on indirect methods.

Indirect methods measure a proxy variable that is affected by the amount of soil water, and then relates the changes of this variable to the changes in soil moisture through physically based or empirical relationships called calibration curves. For instance, dielectric sensors exploit the changes in soil dielectric properties as a function of soil moisture. These dielectric measurements take advantage of the differences in dielectric permittivity between different soil phases (solid, liquid, and gas). Liquid water has a dielectric permittivity of ~80 (depending on temperature, electrolyte solution, and frequency), air has a dielectric permittivity of ~1, and the solid phase of 4 to 16 (Hallikainen et al., 1985, Wraith and Or, 1999). This contrast makes the dielectric permittivity of soil very sensitive to variation in soil water content (SWC). The measurement of the bulk dielectric permittivity is then used to obtain the volumetric water content through calibration curves. Conversely, time-domain reflectometry (TDR) derives the dielectric permittivity by measuring the travel time of an electromagnetic wave traveling back and forth on the probe, or by measuring the capacitance of the bulk soil (Evett and Parkin, 2005, Gardner et al., 1998, Robinson et al., 1999, Robinson et al., 2003, Walker et al., 2004). Permanent installation of these sensors results in minimum destruction to the soil at the time of insertion. Consequently, the main advantage is that temporal soil moisture content changes can be monitored at the same site.

Another indirect method uses electrical resistivity measurements on the basis that soil resistivity is affected by soil moisture. By this approach, a current is usually transferred into the soil by electrodes, and the value of soil resistivity obtained by measuring the changes in voltage (Walker and Houser, 2002, Samouëlian et al., 2005).

The Neutron scattering method is an alternative indirect way of determining the moisture content of a soil based on the loss of high-energy neutrons as they collide with other atoms, in particular hydrogen contained in the water molecule. In this method, neutrons with high energy are emitted by a radioactive source into the soil and the number of slow neutrons returning to the detector per unit time counted. The soil moisture content is then estimated from a previously determined calibration curve of neutron count versus volumetric moisture content. Conversely, the gamma ray attenuation method, a radiation technique, can be used to determine the soil moisture contained within a 1 to 2 cm soil layer. The changes in wet density are measured and the soil moisture content determined by the density change (Walker et al., 2004, Zegelin, 1996).

Another common indirect method is the measurement of soil thermal properties, exploiting changes in soil thermal properties due to variation of soil moisture. The two main techniques are heat dissipation and heat pulse. The heat dissipation technique uses a heat source (usually a heated needle) and temperature sensors (thermocouples or thermistors), immersed into a porous ceramic that equilibrates with the surrounding soil at a given water content. The needle is heated, and the rate of heat dissipation measured by the temperature sensors. These changes are affected by the thermal conductivity, which depends on the ceramic water content. The thermal conductivity is then obtained through measuring the differential temperature before and after heating (Young et al., 2008). In the heat flux method, the pulse of heat is applied at one location and its arrival at another location determined by measuring the soil temperature at the other location. The time required for the pulse of heat to travel to the second location is a function of soil thermal conductivity, which is related to water content. The heat dissipation sensors are also used to estimate soil water potential, through calibration of the sensors at specific soil water potentials (Reece, 1996).

Although the techniques described here are the most common for measuring *in-situ* soil moisture, other techniques are also being developed, such as acoustic wave methods (Adamo et al., 2004, Blum et al., 2004, Lu, 2007), optical methods (Selker et al., 2006) and gravity measurements (Leiriao et al., 2009).

The major disadvantage of *in-situ* measurements is the relatively small volume of soils affecting the sensor measurement, generally limited to the region immediately adjacent to the probe. Hence, although such sensors can provide detailed and relatively accurate information on the vertical soil moisture profile at a point in space, in order to obtain information of the spatial distribution of soil moisture over large areas a dense network of sensors must be installed. However, these sensors are expensive to install and maintain and consequently soil moisture monitoring over large areas using *in-situ* sensors is neither economically nor logistically practical. Moreover, it should be also noted that *in-situ* sensor generally require soil type-specific calibration to ensure that they are accurately interpreted and represent the volumetric water contents at different field sites (Blonquist Jr. et al., 2005, Kizito et al., 2008, Western and Seyfried, 2005). This is because the calibration equations provided by the manufacturers are limited to a specific soil type under laboratory conditions, and normally cannot be applied to measurements taken in other types of soils (Rüdiger et al., 2010).

2.2.2 Remote sensing of soil moisture

Since accurate monitoring of soil moisture through *in-situ* measurements is complicated by the infeasibility of sustaining a large *in-situ* soil moisture monitoring network globally, and the problem of upscaling from point-scale measurements, extensive research has been conducted toward the retrieval of soil moisture using remote sensing techniques (Hain et al., 2011), particularly from Low-Earth orbit platforms which have the capability of providing the global coverage and frequent revisit time required by hydrological and meteorological applications.

2.2.2.1 Passive microwave techniques

Experimental and theoretical research has shown that passive microwave remote sensing at L-band is the most promising technique for global monitoring of soil moisture, due to its applicability to all-weather conditions, direct and strong relationship of the soil emissivity at microwave wavelengths with soil water content, and the limited impact of vegetation cover and surface roughness on the soil emissivity (Njoku et al., 2002). Passive microwave sensors measure the intensity of microwave emission from the soil, which is related to its moisture content through the large differences in the dielectric constant of dry soil (~3.5) and water (~80) (Schmugge et al., 1974). The microwave emission is thus proportional to the product of the surface temperature and surface emissivity, and commonly referred to as the brightness temperature.

The relationship between soil moisture and brightness temperature varies according to differences in surface roughness, vegetation conditions, and soil texture. In the past decades, methods for retrieving soil moisture from passive observations have been developed and validated with field experiments using ground-based, airborne and satellite instruments (Owe et al., 2001, Njoku et al., 2003, Rüdiger et al., 2009, Panciera et al., 2009). Results from these studies have led to the development of different microwave radiative transfer models that are designed to retrieve soil moisture from passive microwave brightness temperature. For example, global measurements of soil moisture using passive microwave remote sensing are available from the SMOS mission, the Advanced Microwave Scanning Radiometer for EOS (AMSR-E), Special Sensor Microwave Imager (SSM/I) etc. SMOS is dedicated to the monitoring of soil moisture, vegetation biomass, and surface temperature using radiometer measurements at L-band (1.4 GHz) with *h*- and *v*- polarizations ("*h*" represents horizontal while "*v*" is the vertical), and provides a soil moisture product at ~40 km resolution. AMSR-E provides a soil moisture product and associated estimates of vegetation water and surface temperature at C-band and X-band at a spatial resolution of ~56 km. Even higher frequency bands are applied by SSM/I, which measure the brightness temperature at Ka- and Ku band.

The potential for soil moisture retrieval using SSM/I brightness temperature at high-frequency (19.4 GHz) was analysed and assessed using datasets from SMEX02 (Wen et al., 2005). While SSM/I has the ability of providing soil moisture information with a long-term record, the accuracy is limited under high-level vegetation and cloud conditions due to its high frequency. It is therefore not optimal for soil moisture retrieval at higher frequency bands due to stronger vegetation masking and higher impacts by electro-magnetical roughness.

Soil moisture remote sensing studies using passive microwave techniques conducted over several decades have demonstrated the superiority of low-frequency sensors over other remote sensing techniques (Schmugge et al., 1974, Jackson et al., 1993, Paloscia et al., 2001). These studies have also led to the conclusion that emission at 1.4G Hz (L-band) is related to the moisture of a soil layer, the thickness of which depends on the soil characteristics and moisture profile. Although passive microwave sensors at L-band are the most promising for retrieving soil moisture globally, the spatial resolution that can be achieved from passive microwave observations is inherently coarse (currently ~40 km resolution) due to the inverse relationship between wavelength and antenna size and associated technological limitations in deploying large antennas in space. Consequently, soil moisture estimated from the passive microwave remote sensing technique at L-band alone cannot meet the 10 km requirement for hydrological and hydro-meteorological applications.

Products of passive microwave sensing face significant challenges in meeting the medium resolution (~10 km) requirements for hydrometeorology (at regional scale), such as precipitation forecasting and flood and drought predictions. The antenna size of the radiometer is the only factor that we can change to improve resolution. However, increasing the antenna size introduces extremely difficult engineering problems that cannot be solved using conventional technologies. This has been a major reason for looking at innovative approaches which can provide accurate and high resolution observations (Jackson et al., 1999).

Alternatives to passive microwave remote sensing of soil moisture include the use of active (radar) microwave remote sensing (Paloscia et al., 2004, Giacomelli et al., 1995), visible/near-infrared (NIR)/shortwave infrared (SWIR) (Muller and Décamps, 2001) and/or thermal-infrared (TIR) sensing (Anderson et al., 1997, Hain et al., 2009). Nonetheless, these individual approaches have some major drawbacks that hamper their applicability.

2.2.2.2 Active microwave techniques

Since passive microwave remote sensing is limited by its coarse spatial resolution, some other remote sensing techniques have been proposed to provide observations at higher resolution. For instance, active microwave remote sensing techniques can be used to retrieve soil moisture information from 10 m to 3 km resolution. There are primarily two types of radar currently being used for soil moisture retrieval: synthetic aperture radar (SAR) and scatterometers. SAR is coherent radar, where high resolution images are created from the backscatter signals using a synthetic antenna aperture formed by integrating the radar response in the azimuth domain. This allows very high resolution to be achieved, of the order of metres. For example, the European Space Agency (ESA) has used the Earth Remote Sensing (ERS-1 and ERS-2) satellites for soil moisture remote sensing with C-band SAR (Wagner et al., 2003, 2007a). Other SAR observations are available from ENVISAT C-band ASAR (Desnos et al., 2000), C-band RADARSAT-1/2 (Cable et al., 2014, Niang et al., 2012), L-band PALSAR (Carreiras et al., 2012, Shimada et al., 2009), X-band

TerraSAR (Werninghaus, 2004) and X-band COSMO-SkyMed (Covello et al., 2010). The radar sensor onboard SMAP will also use SAR measurements but at L-band and at 3 km resolution (Entekhabi et al., 2010).

Differently than SAR sensors, scatterometers are microwave radar sensors that measure the backscatter of the surface using real aperture (as opposed to synthetic) (Dubois et al., 1995; Schmugge, 1998; Wagner and Scipal, 2000). They were primarily developed for measurement of near surface winds over the ocean, based on the fact that wind determines small scale changes of the sea surface roughness and therefore the backscattering properties. In addition to their original purpose, scatterometers are also used for polar ice studies, vegetation coverage, and SWC measurements. A variety of scatterometers have been launched on board satellites, such as the NASA scatterometer (NSCAT) and the advanced scatterometer (ASCAT) on board of the ESA meteorological operational satellite (MetOp-A) launched in 2006 (Wagner et al., 2003, 2007a). As for active microwave, the magnitude of the signal (backscatter coefficient) is related to soil moisture through the contrast of soil and water dielectric constants. However, in the case of radar the soils signal is more heavily affected by surface roughness and the direct scattering from the vegetation canopy. Therefore, in contrast to the passive microwave remote sensing, the accuracy of active retrieved soil moisture is highly affected by the surface conditions.

2.2.2.3 Optical remote sensing techniques

Apart from the active microwave sensors, optical (visible/NIR/SWIR/TIR) remote sensors can also measure surface reflectance from the sun or surface thermal emission with high spatial resolution. Consequently, bare soil spectral information in visible, near-infrared, and shortwave infrared wavelengths is related to soil moisture as a function of spectral absorption features such as wavelength position, absorption feature depth, width etc. (Pu et al., 2003). However, the optical signal is only from the top millimetres or so of the surface, be it soil or vegetation, making it difficult to interpret. It also has limited ability to penetrate clouds and vegetation canopy, and is highly attenuated by the atmosphere requiring substantial atmospheric correction. In addition, soil reflectance measurements are strongly affected by the soil composition, physical structure and observation conditions, resulting in poor prediction of soil moisture on combined soil type samples (Musick and Pelletier, 1988). Thus soil moisture estimates from visible/infrared sensors usually require surface micro-meteorological and atmospheric information that is not routinely available (Zhang and Wegehenkel, 2006). Due to those constraints, efforts to directly relate reflectance to soil moisture have achieved success only when models have been fit to specific soil types in the absence of vegetation cover (Muller and Décamps, 2001), strongly limiting the applicability of such techniques for global soil moisture retrieval.

Thermal infrared (TIR) remote sensing is based on the fact that soil temperatures are directly influenced by soil moisture with the increase of specific heat and thermal conductivity. The estimation of soil moisture from TIR is primarily related to the use of soil temperature measurements, either singularly or in combination with vegetation indexes. Some studies have indicated that variations in soil temperature are highly correlated with variations in soil moisture (Friedl and Davis, 1994, Chehbouni et al., 2001). Advanced applications of the combination of thermal imagery and spectral vegetation indices employ thermodynamic principles embodied in surface energy balance models to estimate surface evapotranspiration rates, and thus improve soil moisture estimation. Many such approaches based on the consistent negative correlation between soil temperature and vegetation indices such as normalized difference vegetation index (NDVI) have been verified to be powerful in soil moisture estimation (Carlson et al., 1995, Goward et al., 2002). However, like all optical techniques, they also suffer from the limited ability to penetrate clouds and vegetation, being attenuated by the earth's atmosphere, and the strong perturbation by vegetation biomass. Moreover, they are often empirical and thus vary across time and land cover types (Czajkowski et al., 2000).

2.3 Soil Moisture Downscaling

Remote sensing has to confront the challenges of achieving medium resolution (~10 km) combined with sufficient retrieval accuracy to benefit hydrological, meteorological and agricultural applications (0.04 cm^3/cm^3 for uniform areas with vegetation water content less than 5 kg/m^2)(Entekhabi et al., 2012). Moreover, it is evident that fulfilling both such requirements using a single sensor is difficult. Therefore complementary downscaling using a range of observation types has been proposed as an approach to overcome these scale and accuracy issues, by combining the merits from different sensors. Given the limitations of optical techniques with respect to cloud coverage, atmospheric disturbance and vegetation cover, the use of microwave sensors (active and passive) has the best potential to produce reliable global soil moisture products. Consequently, this section introduces the currently available downscaling approaches which have the potential to fulfil the stated requirements on resolution and accuracy.

2.3.1 Approaches

The retrieval accuracy of surface soil moisture is optimal using passive microwave remote sensing but is limited by its coarse resolution. The combination of these radiometric data at coarse spatial resolution with higher resolution data from other sensors offers a potential solution to decompose or disaggregate large pixels into smaller ones. Also, additional information on factors controlling soil moisture variability, such as soil properties, vegetation characteristics, or meteorological observations could be used to disaggregate the observations collected from low resolution passive microwave, given that adequate physical models or empirical relationships apply.

During the past decade, a variety of methods have been proposed to disaggregate the coarse scale passive microwave observations using high resolution observations (Kim and Barros, 2002, Merlin et al., 2006, Merlin et al., 2008a, Panciera et al., 2008, Merlin et al., 2010, Piles et al., 2011, Narayan et al., 2006). The increased effort in this area is a reflection of the fact that L-band passive microwave measurements from space are just beginning to emerge, and high resolution remote sensing data that can be used in downscaling of the coarse resolution data are increasingly available.

2.3.1.1 Optical and passive downscaling approaches

Several downscaling algorithms using optical remote sensing data have been proposed, such as the combination of 1km Advanced Very High Resolution Radiometer (AVHRR) and 25 km Special Sensor Microwave/Image (SSM/I) data (Chauhan, 2003). Another method has used the 1km MODerate resolution Imaging Spectroradiometer (MODIS) data together with soil dependant parameters and wind speed data to downscale ~40 km SMOS retrievals according to a deterministic relationship between near-surface soil moisture and optical-derived soil moisture indices (Merlin et al., 2008a). A physically-based algorithm has also been proposed, incorporating a complex land surface model and high resolution multispectral data and surface variables involved in a land surface atmosphere model (Merlin et al., 2005). This approach combines the ~40 km brightness temperatures with 1 km resolution auxiliary data comprised of visible, near-infrared and thermal infrared remote sensing data, and all the surface variables involved in the modelling of land surface atmosphere interaction available at this scale (soil texture, atmospheric forcing, etc.). The main assumption relies on the relationship between the radiometric soil temperature inverted from the thermal infrared and the microwave soil moisture. An alternate disaggregation approach focuses on the use of topographic and surface properties to reconstruct spatial patterns. For instance, a radiative transfer model is coupled with a hydrological model in order to redistribute the soil water content as a function of topography and soil properties (Pellenq et al., 2003). Similarly, another algorithm downscales coarse resolution soil moisture using empirical relationships between the spatial and temporal variability of soil moisture and patterns of auxiliary data such as topography, soil texture, vegetation water content (VWC), and rainfall (Kim and Barros, 2002).

However, intermediate resolution (~10 km) soil moisture retrievals from the above mentioned downscaling algorithms are limited by the availability of the soil and vegetation properties required as inputs by the methods at global scale and high resolution. In addition, it should be noted that the use of optical data limits the use of these downscaling approaches to clear sky conditions, resulting in the following approaches that can be applied to all weather conditions.

2.3.1.2 Active and passive downscaling approaches

Due to the shortcomings identified with optical methods, downscaling approaches based on the synergy between active (radar) and passive (radiometer) retrievals are being developed, and this technique forms the basis of the forthcoming SMAP mission. Full details on the SMAP mission are discussed in the next section. The main objective of this satellite mission is to provide a downscaled soil moisture product at 9 km spatial resolution, by merging 3 km resolution radar and 36 km resolution radiometer observations from the same platform. The existing algorithms to jointly handle active and passive microwave data at different resolutions include: i) SMAP baseline downscaling algorithm (Das et al., 2014), ii) SMAP optional downscaling algorithm (Das et al., 2011), iii) Bayesian merging method (Zhan et al., 2006) and iv) change detection methods (Narayan et al., 2006, Piles et al., 2009, Njoku et al., 2002).

NASA's SMAP mission is planning to generate what is termed a Level-3 soil moisture data product at ~9 km spatial resolution, by merging the 3 km radar backscatter and 36 km radiometer observations. The baseline downscaling approach adopted by SMAP relies on the assumption of a linear relationship between the radar observations and the brightness temperature at the same resolution, and a vegetation dependent parameter which describes this linear relationship, assumed to be spatially homogeneous across individual SMAP radiometer pixels. Using this approach, the 36 km resolution brightness temperatures are downscaled to 9 km brightness temperatures, after which a 9 km resolution soil moisture product is obtained using a passive microwave radiative transfer retrieval from this brightness temperature. Different to the baseline algorithm, the optional algorithm assumes a linear relationship between soil moisture and radar observations, and directly disaggregates the coarse resolution soil moisture to medium resolution.

Both the baseline and optional algorithms have been tested and evaluated with synthetic OSSE datasets and some experimental data from airborne field campaigns collected by the Passive and Active L-band System (PALS) instrument over various regions of Continental United States (Das et al., 2011, Das et al., 2014, Njoku et al., 2002), resulting in the Root Mean Square Error (RMSE) of downscaled soil moisture retrieval meeting the SMAP target accuracy of 0.04 cm^3/cm^3. However, there are some shortcomings of these two proposed algorithms:

i) the linear relationship between radar backscatter and brightness temperature is influenced by the polarizations available from the radar and radiometer, with the best linear relationship expected to be between radar at *vv*-polarization and radiometer at *v*-polarization (Das et al., 2011) due to the higher degree of correlation observed between them, indicating the effectiveness of this algorithm will be limited by the availability of *vv*-polarization radar data;

ii) the accuracy will be affected by the assumption of homogeneous vegetation characteristics within the radiometer footprint, i.e. reflecting on the assumption of spatially uniform slope of the linear regression between Tb and σ (or between soil moisture and σ for optional algorithm); and

iii) they have not been well tested using experimental data. In particular they have only used the data in some regions of U.S., meaning that various land conditions from around the world have not been tested, potentially impacting the robustness of the linear parameter estimation, and constraining its applicability in forthcoming application in the SMAP mission.

Another downscaling approach is based on the linear relationship between changes in radar backscatter and changes in soil moisture over time. Using PALS data, it was observed that radar and radiometer data show similar sensitivities to soil moisture spatial distributions when observed as temporal changes. The feasibility of using change detection has been demonstrated in many studies such as (Njoku et al., 2002, Narayan et al., 2006). The estimated moderate scale (at 9 km resolution) soil moisture based on this approach had an RMSE of about 0.046 cm^3/cm^3. The theoretical basis and the assumptions behind the change detection algorithm were also used to develop an improved approach (Piles et al., 2009). The rationale behind this approach is that of considering the average surface soil moisture over a sample 9 km region to be composed of weighted averages of the available radar observations within that region and the radiometer retrieval within the radiometer footprint containing the 9 km region. The advantage of this approach is that as more radar retrievals are available within the 9 km region, more spatial structure within a radiometer footprint will become evident, and since the collection of 9 km pixels within the larger scale radiometer footprint are constrained to sum to the value indicated by the radiometer retrieval, the high resolution estimation maintains the overall accuracy of the radiometer retrieval.

The Bayesian merging method, a totally different strategy, is instead based on the use of radiometer brightness temperature, radar backscatter observations and radiative transfer models within a Bayesian probabilistic framework aimed at providing optimal estimates of soil moisture by weighting the various sources of uncertainty associated with the instrument and model (Zhan et al., 2006). This downscaling approach involves three main steps: i) preliminary "background" guess based on a direct inversion of the 36 km radiometer observation (*Tb* at *h*-pol) to soil moisture using passive microwave retrieval method; ii) Calculation of brightness temperature and backscatter estimates at the background soil moisture value using microwave emission and backscatter model; iii) error covariance of the background field and the observations; and iv) medium-resolution soil moisture retrieval by merging the high resolution radar, coarse resolution radiometer, and background state using an implementation of Bayes theorem. This approach was found to significantly reduce the RMSE of medium resolution soil moisture retrievals comparing to direct retrievals from coarse resolution passive microwave observations or from fine resolution active microwave observations, but has only been applied within the context of a synthetic Observing System Simulation Experiment (OSSE).

Other approaches for downscaling passive microwave observations include the temporal interpolation method proposed to couple high and low spatial resolution images of mixed pixels (Cardot et al., 2005), and neural network which was proposed to downscale coarse resolution satellite microwave remote sensing using a coupled hydrologic/radiative transfer model as input for its training (Tsegaye et al., 2003).

Spatial resolution is still a challenge for passive microwave remote sensing of land. Development of downscaling techniques for upcoming microwave remote sensors is of great importance and will considerably increase its range of applications. In particular, the SMAP baseline, optional and other candidate downscaling algorithms have not been widely tested with real data.

2.3.2 SMAP mission

NASA is going to launch the SMAP satellite in January 2015. It is expected that by combining SMAP radar and radiometer data, accurate soil moisture with an intermediate spatial resolution around ~10 km can be obtained. The SMAP mission was recommended by the National Research Council's (NRC) Decadal Survey after a

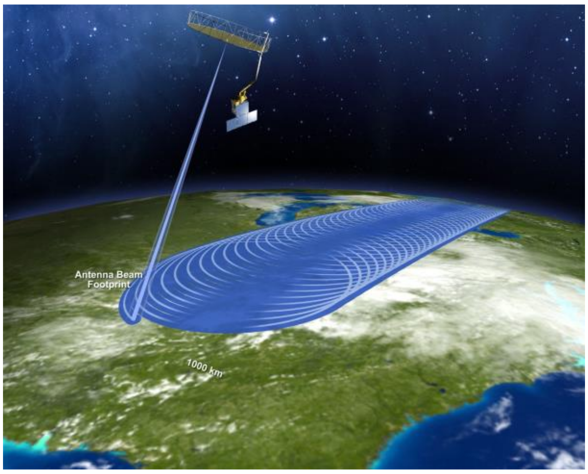

Figure 2-1: Snapshot of SMAP mesh antenna and footprint on Earth (smap.jpl.nasa.gov).

preliminary study commissioned by NASA, the National Oceanic and Atmospheric Administration (NOAA), and the U.S. Geological Survey (USGS), to provide Earth's near surface soil moisture measurements at global scale and to distinguish frozen from thawed land surfaces (National-Research-Council, 2007).

SMAP inherits concept of the NASA Hydros (Hydrosphere State) mission (Entekhabi et al., 2004) that progressed through Phase A development until it was put on hold in 2005 due to NASA budgetary constraints. Due to the expected accuracy, global coverage and spatial resolution, SMAP products are being anticipated across many science and application disciplines including hydrology, climate, carbon cycle, as well as the meteorological, environmental and ecological applications communities.

The payload of SMAP consists of a conically scanning L-band radiometer and radar that share a deployable light-weight mesh antenna with a 6 m diameter so as to solve the size-mass issues of real aperture antennas working at L-band, as seen in Figure 2-1. The first three Stokes parameters and backscatter at *hh*-, *vv*- and *hv*- polarizations will be collected using a radiometer and a radar system, over a footprint of approximately 36 km and 3 km size respectively. The SMAP radar and radiometer share a single feedhorn and parabolic mesh reflector to make coincident measurements of surface backscatter and emission. The reflector rotates about its nadir axis at 14.6 rpm, providing a conically scanning antenna beam with a surface incidence angle of approximately 40°. The selected incidence angle was chosen as the optimal to retrieve soil moisture and vegetation water content simultaneously from the horizontally and vertically polarized brightness temperatures (Entekhabi et al., 2010).

The SMAP radiometer can only provide a resolution on the order of 36 km, which is much larger than the minimum science requirement of 10 km spatial resolution for hydrological modelling. In contrast, the SMAP radar will offer higher resolution observations around 1 km. As the direct soil moisture retrieval from radar observations is a more difficult problem than for microwave radiometer observations, mainly due to the strong impact of surface roughness and vegetation-induced scattering, the objective of SMAP is to utilize the fine resolution yet noisy information provided by the radar to recover the spatial distribution of the soil moisture information provided by the radiometer at coarser resolution.

SMAP aims to provide global soil moisture observations with a 2-3 day revisit time, with its key derived products provided in four levels:

Level 1 products are divided into three categories:

i) Level 1A products are raw data of radar backscatter and radiometer brightness temperature in time order;

ii) Level 1B products are calibrated and geo-located instrument measurements of surface radar backscatter cross section and brightness temperatures derived from antenna temperatures in time order; and

iii) Level 1C products are calibrated and geo-located instrument measurements of surface radar backscatter cross section and brightness temperatures derived from antenna temperatures on swath/Earth grid.

Level 2 products are on half-orbit retrievals of soil moisture derived from radar, radiometer, and the conjunction of radar and radiometer data on a fixed Earth grid with resolutions of 3 km, 36 km, and 9 km respectively.

Level 3 products are daily global composite Level 3 products are daily composites of Level 2 surface soil moisture and freeze/thaw state data.

Level 4 products are model-derived value-added surface and root zone soil moisture data as well as carbon net ecosystem exchange data.

2.3.3 SMAP Calibration/Validation field campaigns

In preparation of the SMAP launch, suitable algorithms and techniques need to be developed and validated to ensure that an accurate medium-resolution soil moisture product can be operationally produced from combined SMAP radiometer and radar observations, and that any remaining issues with the active-only and passive-only retrieval algorithm be addressed. To this end, it has been essential that field campaigns with coordinated satellite, airborne and ground-based data collection be undertaken, giving careful consideration to the diverse data requirements for the range of outstanding scientific questions. Therefore, field campaigns have been conducted using active and passive microwave airborne observations to address the scientific requirements pertinent to SMAP.

These campaigns include the Southern Great Plains experiment in Oklahoma from July 8 to July 21 in 1999 (SGP99) (Njoku et al., 2002, Bolten et al., 2003), which used PALS to study remote sensing of soil moisture in low to moderate vegetated terrain using low-frequency microwave radiometer and radar measurements. Data acquired during SGP99 provided information on the sensitivities of multichannel low-frequency passive and active measurements to soil moisture for vegetation conditions including bare, pasture and crop surface with field-averaged vegetation water contents mainly in the range of 0-2.5 kg/m^2.

The Soil Moisture Experiment 2002 (SMEX02) was conducted from June 25 to July 8 in 2002 in Iowa (Narayan et al., 2004, Crosson et al., 2005, Narayan et al., 2006), with the aim to extend the soil moisture retrieval algorithm using passive and active measurements (from PALS) to areas under moderate to heavy vegetation water content conditions 4-8 kg/m^2. The dominant vegetation types are corn and soybeans.

The Cloud and Land Surface Interaction Campaign (CLASIC) was conducted in 2007 in the Southern Great Plains Oklahoma (Bindlish et al., 2009, Yueh et al., 2008), covering a 3-week period from June 11 to July 6, a time when the Southern Great Plains region was in the process of harvesting the winter wheat and therefore large changes occurred in the surface albedo, latent heat flux and sensible heat flux. The combined passive/active L-band PALS was also mounted to the airborne as part of this campaign, providing the opportunity to collect prototype SMAP data in conjunction with soil moisture measurement and therefore to explore combined algorithm concept for SMAP.

The San Joaquin Valley field campaign (SJV10) was conducted in California USA in summer 2010, as part of an effort to integrate observations of vegetation water content, soil moisture and evapotranspiration into agricultural water management to better understand water balance and fluxes. Primary crop types included pistachios, wheat, cotton and almonds. NASA's Uninhabited Aerial Vehicle Synthetic Aperture Radar (UAVSAR), implemented on the aircraft, provided the measurements required for algorithm development for the SMAP mission.

The Canadian Experiment for Soil Moisture 2010 (CanEx-SM10) was conducted from May 31 to June 17 in 2010, Saskatchewan, Canada (Magagi et al., 2013), with aims to support development and validation of soil moisture algorithms and products from two satellite platforms, the ESA's SMOS mission and NASA's SMAP mission. During this campaign, the airborne measurements were collected from a Canadian L-band radiometer and NASA's L-band UAVSAR radar over an agricultural site and a forested site, so as to enable testing of soil moisture retrieval algorithms over very different soil and vegetation conditions.

The Soil Moisture Active Passive Validation Experiment 2008 (SMAPVEX2008) was conducted from September 29 to October 13 in 2008 in Maryland USA (Colliander et al., 2012a, Bindlish et al., 2010, Yueh et al., 2009), and was designed to investigate the SMAP soil moisture algorithm development. The PALS instrument was flown over agricultural and forested sites on the Eastern Shore in Maryland and Delaware.

The Soil Moisture Active Passive Validation Experiment 2012 (SMAPVEX2012) was conducted from June 6 to July 19 in 2012 in an agricultural region south of Winnipeg Canada (Colliander et al., 2012b), which is one of the primary pre-launch field campaigns for the SMAP mission established to provide data for algorithm evaluation and testing and applications development. The measurements were collected using active and passive instruments including NASA's UAVSAR and the PALS onboard separate aircraft.

Beside the above mentioned field campaigns, all of which were conducted in north America, a series of three field campaigns were undertaken in Australia - the Soil Moisture Active Passive Experiments (SMAPEx) in 2010 and 2011 (Panciera et al., 2014). SMAPEx-1 was conducted from July 5-10, 2010 in the austral winter; SMAPEx-2 was carried out from December 4-8, 2010 in the austral summer; and SMAPEx-3 took place from September 4-23, 2011 in the austral spring, with two more campaigns SMAPEx-4 and SMAPEx-5 scheduled for 2015 after SMAP launch. The study area is a semi-arid agricultural and grazing area located in the Murrumbidgee River catchment. The SMAPEx field campaigns provide the opportunity to evaluate the SMAP Active-Passive baseline algorithms using data that presents with different sets of conditions and land covers. These field campaigns are complementary to the other campaigns in addressing scientific requirements of the SMAP mission, therefore representing a significant contribution to the limited heritage of airborne experiments mentioned above. During the SMAPEx experiments, airborne prototype SMAP data were collected from PLMR and the PLIS, together with ground observations of soil moisture and ancillary data over an area equivalent to a SMAP radiometer footprint (36 km), with the aim to provide SMAP-type data for the development and validation of algorithms and techniques to estimate near-surface soil moisture from the upcoming SMAP mission. More details on the SMAPEx can be found in **Chapter 3**.

2.4 Proposed Methodology

After reviewing the literature and identifying the strengths and weaknesses of currently existing downscaling algorithms, a methodology to retrieve a medium-resolution soil moisture product from active and passive observations is proposed. As the near surface soil moisture retrieval is optimal in the microwave domain, as demonstrated through a number of field experiments using ground-based and aircraft-mounted radiometer and radar sensors, this thesis focuses on maturing the active and passive combination of observations to overcome the individual limitations of each observation type (i.e. the coarse resolution of radiometer and the confounding effect of vegetation and surface roughness on radar retrieval) as will become available from SMAP, with the objective of providing accurate soil moisture information at a resolution more suitable for hydro-meteorological applications.

Due to the limited tests that have been done on the active-passive downscaling algorithms, it is essential to extend the evaluation with more varied data sets collected from field campaigns, exhibiting a variety of land conditions not only found within North-America, but also within other locations, so as to demonstrate the robustness of these downscaling algorithms. Downscaling algorithms tested in this thesis include (i) SMAP baseline downscaling algorithm, (ii) SMAP optional downscaling algorithm, (iii) change detection method and (iv) Bayesian merging method. Data used to evaluate these algorithms were collected from the SMAPEx field campaigns in Australia, due to their different land conditions as compared to other studies. Prior to testing the algorithms, a series of analysis is conducted to address simulation of SMAP-type observation from airborne observations. In particular, differences in terms of incidence and azimuth angle and spatial resolution are carefully addressed. Consequently, the simulation of SMAP data from airborne observations is first studied in this thesis, followed by the demonstration of four different active and passive downscaling algorithms with these simulated data.

2.5 Chapter Summary

This chapter has provided an overview of the importance of soil moisture measurement, a description of the approaches for monitoring soil moisture using *in-situ* and remote sensing technology, and a review of currently available algorithms to obtain soil moisture information from remote sensing at resolutions relevant to hydro-meteorological applications.

Amongst the downscaling algorithms mentioned in this chapter, the one based on the synergy between passive (radiometer) and active (radar) microwave observations is the most promising approach, not only due to its all-weather capabilities, but also because microwave observation is becoming increasingly available from satellites at global scale and has much finer temporal resolution than optical sensors. Moreover, retrievals from radar and radiometer rely less on ancillary information such as meteorological observations and land surface models. However, downscaling algorithms based on this sensor combination are still under development and have thus far received very limited testing using airborne and satellite data although they have been theoretically proven to be effective methods. Consequently, based on this review of available approaches for soil moisture measurement and their limitations, four promising downscaling algorithms using active and passive observations are tested in this PhD research and evaluated using airborne observations collected in semi-arid agricultural area, aggregated to provide SMAP-like data. Such data set represents a valuable test bed across a range of land conditions to demonstrate the relative advantages and limitations of existing downscaling methods for the forthcoming SMAP mission.

3 Data Set

This chapter presents an overview of the Soil Moisture Active Passive Experiment (SMAPEx), including a description of the airborne simulator used to simulate SMAP brightness temperature and backscatter data, ground sampling and monitoring stations. The derived reference soil moisture from Polarimetric L-band Multibeam Radiometer (PLMR) has been previously validated against the ground truth from ground sampling and monitoring stations and so is only briefly referred to here. The observations from the airborne simulator are used to test the feasibility of different soil moisture downscaling algorithms for the forthcoming SMAP mission. In the absence of real SMAP data, SMOS and ASAR provide an alternative source of testing data, and are later used for preliminary research on the performance of the baseline downscaling algorithm.

3.1 Existing Satellite Data

Prior to the test of downscaling algorithm using the simulated SMAP data stream from the airborne simulator, data from other existing satellites such as SMOS and ASAR were also collected in order to provide some preliminary results on the performance of the downscaling algorithms, the baseline algorithm in particular.

The reprocessed L-band Level 1C brightness temperature product of SMOS has an average resolution of ~40 km on a resampled 12.5 km grid spacing with both *h*- and *v*- polarizations and an incidence angle of 40˚, while the C-band backscatter dataset from ASAR in Global Monitoring mode is available at 1 km resolution but only at *hh*-polarization, with the incidence angle ranging from 15° to 45°. The ASAR data are often available for the same day as SMOS overpasses, and can therefore be used as input data to the downscaling procedures as a preliminary study. Details of the application of those satellite data are presented in **Chapter 4**. But since the results of downscaling using those satellite data were not good, presumably due to the inconsistent characteristics of ASAR data compared to SMAP (e.g. polarization and incidence angle), and the high noise contained in the ASAR data, as well as the limited concurrent overpass of SMOS and ASAR over the study area. Therefore, other sources of data were sought as described in the next sections.

3.2 The SMAPEx Campaign

3.2.1 Overview

SMAPEx comprises a series of three campaigns undertaken over an approximately one-year timeframe during 2010 and 2011, specifically designed to encompass the seasonal variation in soil moisture and vegetation: SMAPEx-1 was conducted from 5-10 July 2010 in the austral winter; SMAPEx-2 was carried out from 4-8 December 2010 in the austral summer; and SMAPEx-3 took place from 4-23 September 2011 in the austral spring. The SMAPEx project was specifically designed to contribute to the development of radar and radiometer soil moisture retrieval algorithms for the SMAP mission. The SMAPEx study site is within a semi-arid agricultural and grazing area located in the Murrumbidgee River catchment in south-eastern Australia (-34.67˚N, -35.01˚N, 145.97˚E, 146.36˚E, see Figure 3-1), and forms part of the greater Murray-Darling basin. A general description of the SMAPEx study area and monitoring activities can be found in (Panciera et al., 2014), and full details of three experiments can be found in the Experiment plans on the SMAPEx website (www.smapex.monash.edu.au).

While the 1-week long SMAPEx-1 and -2 campaigns, were focused on providing data for “snapshot” type algorithms, the 3-week long SMAPEx-3 campaign aimed at collecting a longer data record, covering at least part of the growing season, for the development of time-series and change-detection algorithms. SMAPEx-1 was conducted shortly after the sowing of winter crops, with only the emergent plant phase present in the fields under moderately wet soil moisture conditions. SMAPEx-3 captured the intensive growth phase of winter crops in the study area (essentially wheat, barley and canola) under moderately dry conditions, while SMAPEx-2 was characterized by moist conditions and near-peak crop biomass.

The SMAPEx field site was selected due to its relatively flat topography, widely distributed *in-situ* soil moisture monitoring stations, and representation of soil,

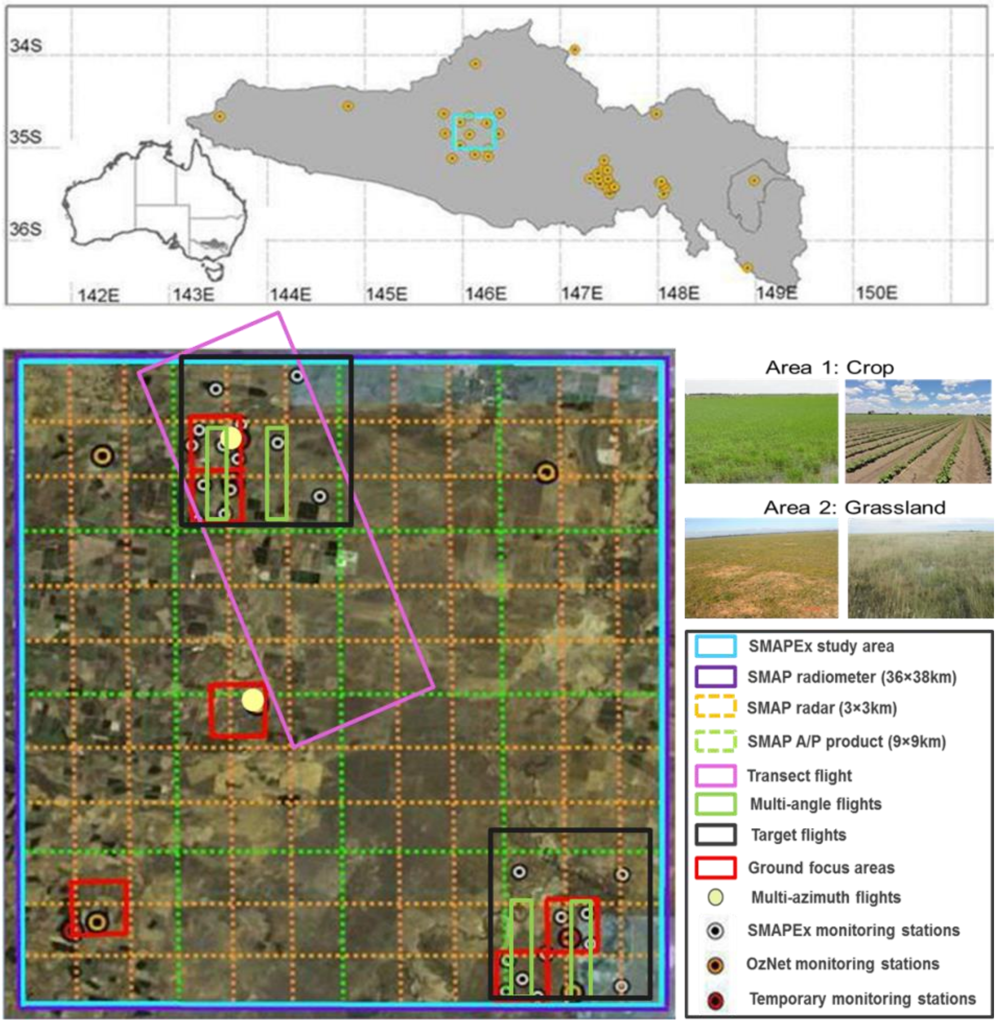

Figure 3-1: Overview of the SMAPEx study area showing the location of the SMAP pixel sized study site in Australia, together with the ground focus areas, monitoring stations and different flights.

vegetation and land use conditions typical of semi-arid environments. The total area covered by the airborne observations corresponds in size to a SMAP-sized radiometer footprint (approximately 36 km × 38 km at such latitudes). More detailed and pertinent descriptions of the data are given in the later chapters as required.

During the course of this PhD study, the author was involved in ground soil moisture sampling and vegetation sampling during the SMAPEx-3 field campaign, and was also responsible for ground sample processing, calibration and normalization of airborne radar observations. The author also archived all the data of

Table 3-1: Summary of SMAPEx flight types

Flight Type	Objectives	Coverage	Ground Resolution	Altitude (AGL)
Regional	Active-Passive retrieval; Downscaling	36 × 38 km	1 km PLMR; 10 m PLIS	10,000 ft
Target	Radar retrieval; Downscaling	9 × 9 km	100 m PLMR; 10 m PLIS	1,000 ft
Multi-angle	Effect of incidence angle	1 × 6 km	1 km PLMR; 10 m PLIS	10,000 ft
Multi-resolution	Effect of resolution	1 × 3.5 km	10 m/50 m/150 m PLIS	5,000 ft
Multi-azimuth	Effect of azimuth	1 × 1 km	10 m PLIS	5,000 ft
Transect	Comparison of PLIS and PALSAR	8 × 22 km	1 km PLMR; 10 m PLIS	10,000 ft

SMAPEx-1, -2 and -3 including the development of a website for data distribution at http://www.smapex.monash.edu.au/.

3.2.2 Airborne simulator

The airborne data were collected using a SMAP airborne simulator allowing the simultaneous acquisition of active and passive microwave remote sensing measurements at the same frequency as the SMAP satellite (L-band), but at a finer resolution and varying incidence angles. The airborne simulator as shown in Figure 3-2 includes the PLMR and the PLIS, which when used together on the same aircraft, provide active and passive microwave observations akin to the expected

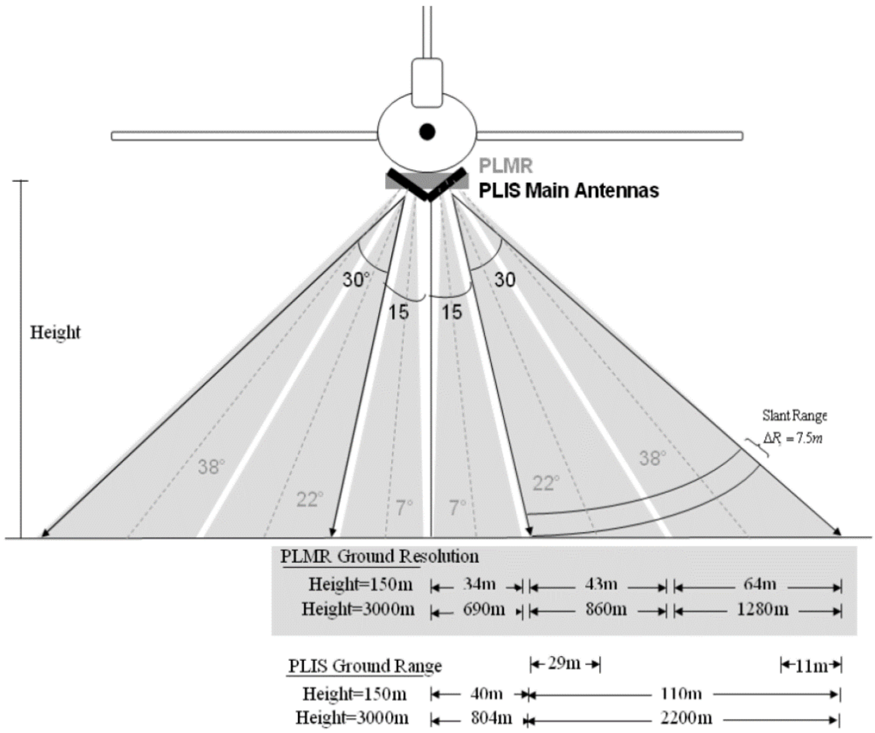

Figure 3-2: PLMR and PLIS viewing configuration on the aircraft.

SMAP data stream. The main characteristics of the SMAP sensors, PLMR, and PLIS, are listed in Table 1-1 (in **Chapter 1**), showing that the airborne sensors from SMAPEx have the same frequency band and the same polarization combinations as SMAP. However, as seen in Figure 3-3, PLIS antennas radiate mainly between 15° - 45° from nadir, providing radar data over a swath of 2.2 km on each side of the aircraft, when operated at 10,000 ft flying height. However, PLMR observes the ground with six across-track beams (±7°, ±21.5° and ±38.5° with 14° across-track beamwidth), providing a full swath coverage of 6 km from 10,000 ft flying height, equivalent to the total PLIS swath when including the nadir gap, but with pixels of approximately 1 km across-track.

In order to closely replicate SMAP data, both the spatial resolution and incidence angle of the airborne observations need to be adapted. Therefore, the 1 km PLMR brightness temperatures and ~10 m PLIS backscatter need to be aggregated to 36 km and 1 km respectively. To achieve this, both PLMR and PLIS observations also need to be normalized to a fixed reference incidence angle (in this case 40°, to resemble the SMAP acquisitions). In addition, since SMAP will make use of a rotating mesh

Figure 3-3: Airborne simulator including Polarimetric L-band Multibeam Radiometer (PLMR); and the Polarimetric L-band Imaging Synthetic aperture radar (PLIS).

antenna to provide observations over the entire swath, both radar and radiometer observations have been collected over a range of azimuthal orientations. Therefore, it will be crucial to understand the potential impact on the observations due to the azimuth viewing angle, and how this changes depending on specific surface conditions (e.g., vegetation type and tillage conditions). Details on the simulation of SMAP data stream are presented in **Chapter 5**.

As shown in Figure 3-1, four main types of flights were conducted during the three SMAPEx field campaigns for the following purposes (details of each flight type can be found in Table 3-1):

1. Regional flights covered the 36 km × 38 km area equivalent to the size of a SMAP pixel in the EASE grid projection at 35° S latitude with a 2-3 days revisit time. The flying altitude was of 10,000 ft AGL, yielding active microwave observations at approximately 10 m spatial resolution and passive microwave, as well as supporting thermal infrared and spectral observations at 1km resolution. Such an altitude was chosen to allow coverage of the entire study area in a timely fashion without compromising the functionality of the airborne instruments and aircraft system, which is a risk at altitudes higher than 10,000 ft AGL. Aggregation of the active and passive microwave data collected during regional flights to the resolution of the SMAP grids provides prototype SMAP radar and radiometer data, for the development of active and passive microwave retrieval algorithms

and techniques to downscale the passive microwave information using the high resolution active microwave data. Application of data from the regional flights is presented in **Chapter 6**, **Chapter 7, Chapter9,** and **Chapter 10**;

2. Target flights covered two 9 km × 9 km sub-areas (Yanco A, "YA" and Yanco B, "YB" areas) at a lower altitude of 1,000ft AGL, collecting active microwave observations at approximately 10 m spatial resolution and passive microwave, supporting thermal infrared and spectral observations at 100 m resolution. The target flights were conducted for the development of radar-only soil moisture retrieval, and investigation on the effect of land covers on the baseline active-passive downscaling algorithm at very high resolution. Application of very high resolution active-passive data from target flights is presented in **Chapter 8**;
3. Special flights (multi-angle/multi-resolution/multi-azimuth flights) provided radar and radiometer data at multiple incidence angles, resolutions and azimuth angles over two focus areas (YA and YB). In order to closely replicate the SMAP data, every portion of the study area should be observed at the same incidence angle, resolution and azimuth viewing angle. However, this could not be achieved with an airborne instrument over an area as large as the SMAPEx study area. Those special flights were therefore designed to provide data for investigating the effect from incidence angle, resolution, and azimuth direction on the observations, and for demonstrating the reliability of the simulation of the SMAP data stream from airborne observations. Application of data from these special flights is presented in **Chapter 5** when developing the simulated SMAP data stream;
4. PALSAR transect flight provided data over a focus transect for cross-comparison of the airborne active microwave data of PLIS with those of the Phased Array L-band Synthetic Aperture Radar (PALSAR) sensor onboard the Advanced Land Observing Satellite (ALOS). This part is out of the scope of this PhD study.

3.2.3 Ground monitoring network

The OzNet hydrological monitoring network (www.oznet.org.au) (Smith et al., 2012) has been operational since 2001 and comprises a total of 62 stations throughout the entire Murrumbidgee River catchment, with 6 in the SMAPEx focus areas. The permanent network provides area-wide surface soil moisture measurements at 0-5 cm using a mix of CS615 water reflectometers and Steven water hydraprobes, with the majority of stations additionally collecting soil moisture profile data across three depths (0-30 cm, 30-60 cm and 60-90 cm). Supplementary parameters including i) rainfall using a tipping bucket rain gauge, ii) soil temperature (2.5 cm and 15 cm) and iii) soil suction are also recorded at many stations.

Of these soil moisture stations, 24 were installed in late 2009 (SMAPEx semi-permanent network) to support the SMAPEx project, continuously monitoring soil moisture at 0-5 cm with a Hydraprobe, and soil temperature at 1 cm, 2.5 cm and 5 cm depths over a variety of land cover conditions. The 24 stations are concentrated on two 9 km × 9 km focus areas within the radiometer pixel (YA and YB), corresponding to two pixels of the SMAP grid at which the active and passive soil moisture product (SMAP L3_SM_A/P product) will be produced. Finally, 10 of the stations within each of areas YA and YB are concentrated on two "sub-areas" of 2.8 km × 3.1 km (at least 4 stations in each sub-area), corresponding to SMAP radar pixels.

The permanent and semi-permanent stations were supplemented by additional 4 identical temporary monitoring stations, one at each of four of the six focus areas. These short-term stations were instrumented with a rain gauge, thermal infrared sensor (Apogee sensors), leaf wetness sensor (MEA LWS v1.1), two soil moisture sensors (Hydraprobes; 0-5 cm and 23-29 cm) and four soil temperature sensors (MEA6507A; 2.5 cm, 5 cm, 15 cm and 40 cm depths) in order to provide time series data during the sampling period.

The distribution of monitoring stations within the SMAPEx study site can be found in Figure 3-1.

3.2.4 Ground sampling

Spatial ground sampling of soil moisture was undertaken concurrently with each flight during each SMAPEx field campaign. During regional flights, sampling was undertaken on a regular grid of 250 m-spaced locations in two 3 km × 3 km focus areas, one of which was characterized by cropping land use and the other by grassland. At each location three surface soil moisture measurements were taken. This allowed the effect of random and experimental errors in local scale soil moisture measurements to be minimized. Soil moisture measurements during SMAPEx were undertaken using the Hydraprobe Data Acquisition System (HDAS). This system allowed navigating to predefined sampling locations and collecting and storing in real-time a variety of spatial data, including the soil moisture, soil temperature and soil salinity provided by the probe as well as a variety of user-prompted observations (land cover type, vegetation canopy height, visual observation of dew presence, visual estimate of surface rock cover fraction, irrigation type).

Vegetation sampling was also undertaken throughout the 3 km × 3 km focus areas. Within each area, the major vegetation types and phenological stages were characterized by making measurements at 5 locations distributed within homogeneous crops/paddocks. At each location, measurements consisted of one destructive sample, 54 LAI and 25 CROPSCAN readings. The LAI and CROPSCAN measurement were then averaged, after quality control, into a single LAI and CROPSCAN reading per location. Additional observations at each location included plant height as well as crop row spacing and direction, and plant spacing in crops.

Intensive vegetation and forest samplings were also conducted during the SMAPEx-3 campaign. The objective of the intensive vegetation sampling within a forested area was to collect detailed plant structural parameters for selected vegetation types (cropping and grassland) and to track the evolution of such parameters across the entire campaign period, for the purpose of radar algorithm development. The intensive forest sampling was conducted to characterize the forest properties such as specie composition, tree height, stem biomass, stem density, basal area etc., for the development of algorithms for high resolution mapping of forest characteristics and soil moisture under forest canopy.

Since the soil surface roughness affects both the radiometric and radar observations, sampling of surface roughness was also performed during SMAPEx-3 at 3 locations within each major land cover type in the 6 focus radar pixel areas and at the 50 sites in the forest sampling area.

In addition to spatial soil moisture and vegetation measurements, other supporting data were also recorded including land cover type, vegetation canopy height, dew presence, gravimetric soil moisture samples, and etc., as the input to soil moisture retrieval algorithms.

3.3 Reference Data

The reference data used to determine the accuracy of each downscaling algorithm were collected from PLMR, including the brightness temperature at 1 km resolution and PLMR retrieved soil moisture at 1 km resolution using passive retrieval method. Retrieval of reference soil moisture at 1 km resolution has been done by Ying Gao (Gao et al., under review).

The reference soil moisture data were inversed from 1 km PLMR brightness temperatures through the *tau-omega* model (Panciera et al., 2009, Merlin et al., 2009), with ancillary parameters on land cover, vegetation water content (VWC), and surface roughness. Due to the relatively short duration of the experiment period surface roughness and vegetation structural parameters were assumed constant through time, while the VWC was varied on a daily basis. Spatial distribution of the static surface roughness parameter h and vegetation parameter b, and an example of VWC on Day 5 are shown in Figure 3-4. According to the work by Gao, the roughness parameter h and vegetation parameter b were calibrated using high resolution brightness temperature data (at ~100 m resolution) and intensive ground SM sampling from SMAPEx campaigns. VWC map was developed from MODIS-derived NDVI together with Landsat-derived land classification map. Other parameters relating to the soil moisture retrieval models are listed in Table 3-2 and Table 3-3, based on the assumption of the same surface conditions across the entire

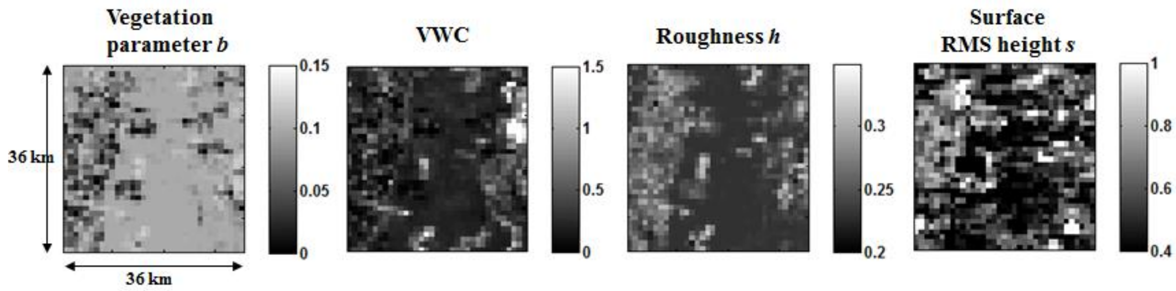

Figure 3-4: Spatial distribution of static surface vegetation parameter *b*, roughness parameter *h* and surface Root-Mean-Square height *s*; also shown is vegetation water content (VWC) map on D5 (15th September, 2011)

Table 3-2: Soil temperature and canopy temperature for soil moisture retrieval.

	D1	D2	D3	D4	D5	D6	D7	D8	D9
Soil temperature T_{surf} (K)	287	284	281	285	285	288	286	285	287
Canopy temperature T_{veg} (K)	300	300	300	300	300	300	300	300	300

site. The soil temperature was averaged up from sampled data and was varied on a daily basis, while the other parameters, i.e. canopy temperature, sand/clay fraction, soil bulk density, and single scattering albedo were obtained from averaging the point sampled data and assumed constant through time. The constant 40° was used for the incidence angle, as the airborne observations have been angle normalized to 40°. Details on the incidence angle normalization can be found in **Chapter 5**. All these parameters have been used for estimating soil moisture at 1 km resolution as the reference by Ying Gao, and they are also used for medium resolution soil moisture retrieval as shown in **Chapter 9** and **Chapter 10**. Also shown in Figure 3-4 is the map of static surface Root-Mean-Square (RMS) height (in cm), obtained from the direct interpolation of sampled RMS according to land cover type, and is used for soil moisture retrieval from radar backscatter as shown in **Chapter 10**.

The derived reference soil moisture map has been validated against ground sampling data and data from permanent monitoring stations under different scales. The accuracy of the reference soil moisture at 1 km resolution was found to be around

Table 3-3: Soil and vegetation parameters across 9 days of SMAPEx-3 field campaign for soil moisture retrieval.

	D1-D9
Sand fraction	0.31
Clay fraction	0.25
Soil bulk density (g/cm^3)	1.3
Single scattering albedo ω	0.1
Incidence angle (˚)	40

0.08 cm^3/cm^3 for cropping area and 0.06 cm^3/cm^3 for grassland area, respectively. The main limitation for retrieving the reference soil moisture map lies in the calibration of ancillary parameters especially the surface roughness parameter and VWC, since only very limited sampled data were available for calibrating the derived parameters across the entire site. These derived soil moisture maps will be used as the basis for validation of active and passive retrieval and downscaling algorithms. Both the brightness temperature reference data and soil moisture reference data at 1 km resolution are further linearly averaged to 3 km and 9 km resolution in order to evaluate downscaling algorithm performance at those resolutions. Those reference maps will be shown in later chapters.

3.4 Chapter Summary

Data for evaluating the downscaling algorithms in this thesis are primarily from the SMAPEx field campaign in Australia and partially from satellites SMOS and ASAR. Three SMAPEx field campaigns were conducted for the purpose of i) providing airborne observations of brightness temperature and backscatter to simulate the prototype SMAP brightness temperature and backscatter data stream; ii) evaluating the accuracy of brightness temperature downscaling algorithms at different resolution levels across a wide range of land cover types and weather conditions; iii) providing the ground truth for validating the expected performance of downscaled soil moisture from the SMAP mission. Due to the very limited experimental data from other campaigns, application of the SMAPEx data set provides an opportunity to study the downscaling algorithm with extensive land conditions that are typical of many landscapes.

4 Preliminary Research

This chapter presents a preliminary evaluation of the baseline downscaling algorithm for the SMAP mission, using the data sets available from existing satellites, i.e. brightness temperature at ~40 km resolution from SMOS and backscatter at 1 km resolution from ASAR. The rationale is to downscale the low resolution (40 km) brightness temperature *Tb* to an intermediate resolution using high resolution (1 km) radar backscatter σ. The downscaled *Tb* are evaluated using airborne *Tb* collected at 1 km resolution within the framework of the SMAPEx project over a ~36 km × 36 km area in south-eastern Australia. The work in this chapter has been published in a peer-reviewed paper at the Modelling and Simulation Conference (Wu et al., 2011).

4.1 Background

Given the importance of soil moisture for hydrological applications, including weather and flood forecasting (Wagner et al., 2003), the SMOS mission was launched by the European Space Agency in 2009 (Kerr et al., 2001). This first-ever dedicated global soil moisture mapping mission has a target accuracy of 0.04 cm^3/cm^3. The passive microwave remote sensing approach has been adopted for this mission due to its high sensitivity to near-surface soil moisture, applicability to all weather conditions, direct correlation with the soil dielectric constant, and reduced effects by vegetation and roughness (Kerr, 2007). However, passive microwave (radiometer) observations suffer from being relatively low spatial resolution, on the order of ~40 km. It is proposed that this scale issue may be overcome by using fine resolution active microwave (radar) observations which is around 1 km resolution, despite being less sensitive to changes in soil moisture due to the confounding effects of vegetation and surface roughness. This is the approach being taken by NASA's SMAP mission, with a scheduled launch in January 2015 (Entekhabi et al. 2010). The rationale behind SMAP is that the synergy between active and passive observations can be used in a downscaling approach to overcome the individual limitations of each observation type, and ultimately provide a soil moisture data set at intermediate resolution (~9 km).

The baseline downscaling algorithm proposed for the SMAP mission is based on an assumed near-linear relationship between radar backscatter and radiometer brightness temperature. Using the airborne PALS instrument and associated data sets collected during the Soil Moisture Experiments (SMEX) 2002, have demonstrated that this is an effective method (Das et al., 2011, Das et al., 2014). But as there has thus far been very limited testing of this algorithm using airborne and/or satellite data beyond the SMEX field campaign, the objective of this chapter is to test the baseline downscaling approach for its viability of application under different conditions.

4.2 Data Set

The SMAPEx (Panciera et al., 2014) field site has been chosen for testing, with airborne brightness temperature data at 1 km resolution as the reference for testing the SMAP baseline downscaling performance. Detailed information on the SMAPEx field campaigns and related data set has been provided in **Chapter 3**, so only pertinent additional information is provided here. The 1 km resolution PLMR observations used in this study were collected from the first campaign SMAPEx-1 (5-10 July in 2010).

The reprocessed L-band Level 1C brightness temperature product of SMOS has an average resolution of 40 km on an approximately 12.5 km hexagonally spaced grid, while the C-band backscatter dataset from ASAR has 1 km resolution. The ASAR data are often available for the same day as SMOS overpasses, and are therefore used as input data for executing the downscaling procedure tested here. Subsequently, the airborne PLMR data from the SMAPEx field campaign are used as the reference *Tb* data at fine spatial resolution (1 km), having an accuracy estimated to be better than 1 K at h-polarization and 2.5 K at v-polarization (Panciera 2009). The PLMR data are therefore used to evaluate the downscaled *Tb* and hence the effectiveness of the downscaling algorithm when using ASAR data together with data from SMOS data at 40° incidence angle, thus testing the viability of this downscaling method in future

Table 4-1: Available coincident overpasses of SMOS and ASAR in 2010; dates in shade are additionally concurrent with PLMR

Season	Month	Dates (in UTC)				
Summer	January	29				
	February	11	14	17		
Winter	July	06	10	23	26	28
	August	05	08	10	13	26
	September	15	20			

applications, both in the context of downscaling SMOS and in preparation for SMAP.

As the radar and radiometer sensors are onboard different satellites, coincident overpasses of the SMAPEx study area for each satellite were first identified. For the purpose of establishing a linear regression between *Tb* and backscatter, all available data were searched for coincident SMOS and ASAR overpasses having full coverage over the SMAPEx study area (regardless of the presence of coincident PLMR validation data). However, for the sake of validating the downscaled *Tb*, only SMOS/ASAR overpasses coincident with PLMR flights could be used.

Concurrent dates for the two satellites are listed in Table 4-1. The 6th July and 10th July are therefore the only dates that could be used to validate the viability of the downscaling algorithm. Any potential limitation due to the available dates will be discussed later. The standard deviation of SMOS observations with their centre point falling within the 40 km SMAPEx area at 40° incidence angle ranged from 1.1 to 6.9 K depending on the date and polarization, while the standard deviation of aggregated ASAR data coincident with the SMOS pixels ranged from 0.07 to 0.27 dB. The mean and standard deviation for SMOS and ASAR data are shown in Figure 4-1. Since the values of PLMR are influenced by physical temperature and incidence angle variations across the flight, the PLMR data have been normalized to a 40° incidence angle and temperature corrected to the effective temperature of 20:30pm (in UTC;

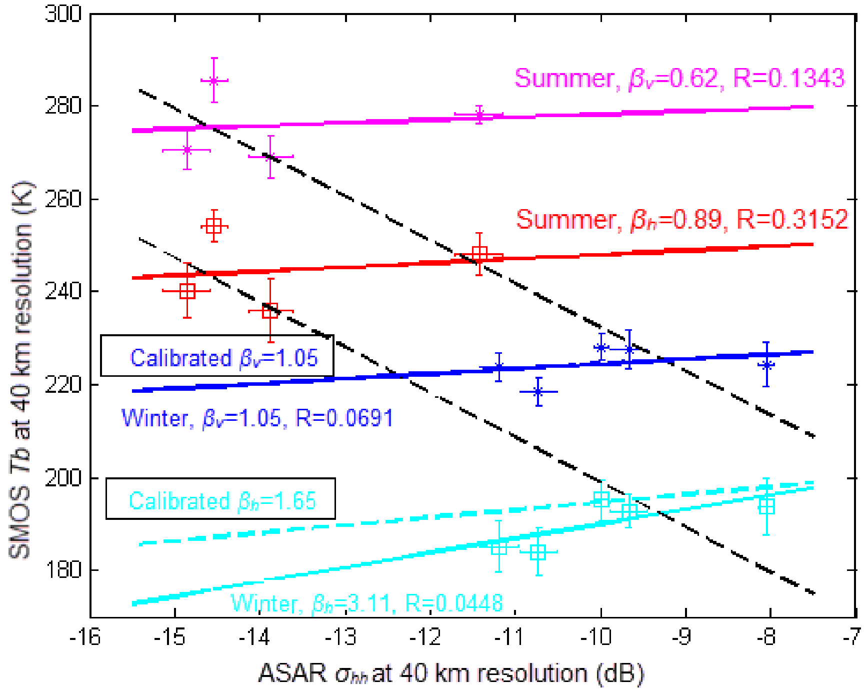

Figure 4-1: Scatter plot between ASAR σ_{hh} and SMOS Tb_h/Tb_v in the SMAPEx area in winter and in summer: four solid coloured lines are the fits in each season at each polarization; two dashed black lines are fits across a year at each polarization; two dashed coloured lines are calibrated fits in winter.

average overpass time of SMOS) following the methodology of Jackson (2001). Moreover, there is a warm bias in SMOS as compared to PLMR data averaged over the same footprint, being approximately 11.5 K at *h*-pol and 8.5 K at *v*-pol when assessed over the Murrumbidgee catchment (Rüdiger et al. 2011). Consequently, SMOS data were de-biased with respect to PLMR data for the purpose of cross-validating the downscaled *Tb*, and hence the de-biased SMOS data are used in this study for downscaling.

4.3 Methodology

The downscaling method used in this study is based on a linear relationship between active and passive observations at the same scale (Das et al. 2011), with a rationale of merging high-accuracy but coarse-resolution passive microwave observations of *Tb* with low accuracy but fine resolution active microwave observations of *σ*, to ultimately obtain the downscaled *Tb* both at *h*-pol and *v*-pol at a medium resolution.

In the following the naming convention of '*C*' (coarse), '*F*' (fine), and '*M*' (medium) is used for the SMOS L1C_*Tb* (40 km), ASAR backscatter σ (1 km), and downscaled *Tb* grid scales (1 to 10 km), respectively. Implementation of this method first requires a linear regression of the available data to derive the coefficients of the relationship

$$Tb_p(C)=A(C)+\beta(C) \times \sigma_{pp}(C), \tag{4-1}$$

where *p* indicates the polarization of *Tb*, including *h*- and *v*-pol; *pp* means co-polarization of radar observations σ, including *hh* or *vv*-pol. Correlations between 4 different combinations of Tb_p and σ_{pp} have been analysed (Das et al., 2011). From that study σ at *vv*-pol is expected to correlate best with *Tb* at both *h* and *v*-pol than σ *hh*-pol. However, ASAR backscatter is only available at *hh*-pol and is thus used to downscale SMOS data in this chapter. In addition, the study of Das et al. (2011) showed that *Tb* at *v*-pol rather than at *h*-pol is expected to have a higher degree of correlation with σ_{hh}. The influence of this polarization limitation from ASAR will be illustrated in the results. The value for $\sigma_{pp}(C)$ is obtained by aggregating 1 km resolution ASAR observations within the coarse footprint *C* (in dB), with $Tb_p(C)$ directly from the SMOS L1C product (in K). At a given scale, parameters $A(C)$ and $\beta(C)$, which in reality depend on vegetation cover and type as well as surface roughness, are assumed time-invariant and homogenous over the entire SMAPEx area in this chapter. Therefore, those two parameters at scale *C* can be estimated by using SMOS L1C_*Tb* and ASAR σ_{hh} data time-series.

In order to downscale to scale *F*, (4-1) can be written as

$$Tb_p(F)=A(F)+\beta(F) \times \sigma_{pp}(F) , \tag{4-2}$$

where $Tb_p(F)$ is the brightness temperature value at a spatial scale of *F* for a particular pixel within *C*, and σ_{pp}, *F* is the corresponding backscatter value from the ASAR. While the default implementation of this algorithm assumes that *A* and β are homogeneous within *C*, in reality it is likely that they vary spatially as a result of different vegetation types and land management practices among others. In this case $A(F)$ and $\beta(F)$ have the same values as $A(C)$ and $\beta(C)$. By averaging both sides of (4-2), one obtains

$$<Tb_p(F)>=<A(F)>+<\beta(F)> \times < \sigma_{pp}(F) > , \tag{4-3}$$

Here < > is used to indicate averaging across C, which yields $<Tb_p(F)>= Tb_p(C)$, as each smaller pixel within C shares the same value of SMOS Tb at that scale. Subtracting Eq. (4-3) from (4-2), and considering A and β are homogeneous and therefore equal at each scale, the downscaled Tb at scale F can be obtained as

$$Tb_p(F)= Tb_p(C) +\beta(C) \times (\sigma_{pp}(F) - \sigma_{pp}(C)) , \tag{4-4}$$

Using (4-4) the downscaled Tb is obtained for each pixel in the SMAPEx area at 1 km, 4 km and 10 km resolution, by averaging the ASAR data at 1 km resolution. Clearly, the downscaled Tb at fine resolution is heavily dependent on the quality of the SMOS Tb, the relative backscatter difference within the coarse grid, and the relationship with Tb as represented by the regression slope that are added to the background value.

The downscaled results at different resolutions are evaluated by comparing them with PLMR Tb data at 1 km, 4 km, and 10 km resolution, respectively, in order to assess the merit of this downscaling method in preparation for SMAP and its potential application to SMOS and ASAR. However, it should be noted that this downscaling algorithm differs from that being developed for SMAP due to limitations in the ASAR data. Specifically, it does not make use of cross-polarized backscatter data that has been shown to account for land management variability (Das et al. 2011).

4.4 Results and Discussion

Given the hypothesis of a time-invariant and homogeneous $\beta(C)$ across the SMAPEx area, the time series of SMOS Tb and ASAR σ were used to estimate $\beta(C)$, using 4 days from summer, together with 12 days from winter (see Table 4-1). The parameter $\beta(C)$ (with the unit of K/dB) was determined to be -9.68 at *h*-pol and -9.43 at *v*-pol (dashed lines in Figure 4-1) and subsequently applied to the proposed downscaling algorithm for the SMOS and ASAR data on 6th and 10th July. When comparing with PLMR Tb, the RMSE of downscaled Tb at 1 km resolution is 22.1 K at *h*-pol, and 19.7 K at *v*-pol on 6th July. Subsequently, $\beta(C)$ was estimated separately for each season, thus reducing the time invariance assumption to a few weeks. In austral

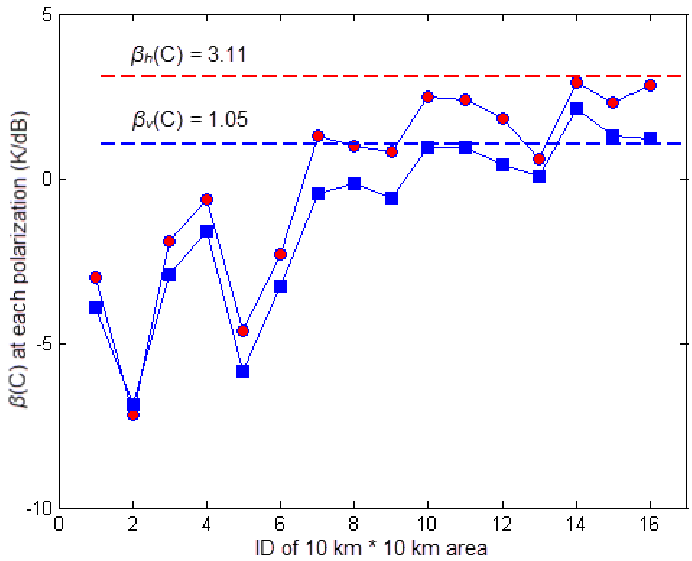

Figure 4-2: Variation of the parameter *β* in 16 sub-areas with a 10 km×10 km size within SMAPEx

summer, a 4-day time series of SMOS and ASAR data (29th Jan., 11th Feb., 14th Feb., 17th Feb.) has been utilized to perform a linear regression, while in winter a 5-day time series (in July) has been used. In this case, *β(C)* was 3.11 at *h*-pol and 1.05 at *v*-pol in winter, and 0.89 at *h*-pol and 0.62 at *v*-pol in summer, being significantly different from the previous estimates of *β(C)* when using data in summer and winter together, see Figure 4-1. Accordingly, applying *β(C)* obtained from the time series in winter to perform downscaling on days 6th and 10th July, resulted in a RMSE of 12.8 K at *h*-pol and 10.5 K at *v*-pol on 6th July, being an improvement of ~10 K over the previous result.

These results suggest that *β(C)* is time-variant with considerable difference according to season, and significant impact on the resultant retrieval of downscaled *Tb*. Further analysis of the parameter *β* is of great importance to control the accuracy of downscaled *Tb*. The variation of *β* in a smaller area than SMAPEx was therefore analysed. This was achieved by dividing the SMAPEx area into sixteen 10 km × 10 km areas and retrieving *β* values from time-series SMOS (10 km) and ASAR (10 km) data over each area. According to the results in Figure 4-2, the ID of each pixel is labelled starting from the top left corner, and moving sequentially across the study

Table 4-2: Difference between de-biased SMOS and aggregated PLMR data, and RMSE of downscaled *Tb*

Date	Polarization	PLMR *Tb* (K)	De-biased SMOS *Tb* (K)	Difference (K)	RMSE of Downscaled *Tb* (K)
July 6th	*h*-pol	196.5	202.0	-5.5	12.8
	v-pol	230.8	233.3	-2.5	10.5
July 10th	*h*-pol	212.7	208.1	4.6	11.2
	v-pol	242.5	240.7	1.8	8.8

area from west to east, followed by north to south. The value of β clearly varies across study site, mainly because the left part of SMAPEx is dominated by cropping area , while the right part is mostly grazing (less irrigation), suggesting that the hypothesis of a constant β (dashed lines in Figure 4-2) over the radiometer pixel may result in poor estimates of downscaled *Tb*. A summary of the RMSE of downscaled *Tb* derived from de-biased SMOS and ASAR data is shown in Table 4-2, together with the comparison between de-biased SMOS *Tb* data and aggregated PLMR data (at 40 km resolution).

In order to eliminate any residual bias or "noise/error" in the SMOS data as compared to PLMR over SMAPEx on the specific downscaling date, estimates of SMOS observations were then obtained from aggregating the 1 km PLMR data directly. However, because only 2 days of coincident PLMR and ASAR data are available, the parameter β estimated previously using time-series de-biased SMOS *Tb* and ASAR σ_{hh} data were used in the analysis that follows. Consequently, the aggregated PLMR *Tb* at 40 km were only used as the value of $Tb_p(C)$ in Eq. (4-4), meaning that the PLMR *Tb* at 1 km resolution collected from 6th and 10th July are first aggregated to 40 km, and then downscaled by 1 km ASAR backscatter σ_{hh} to 1 km, 4 km and 10 km respectively, using the SMOS derived estimates of β (3.11 at *h*-pol and 1.05 at *v*-pol). Example of downscaled *Tb* at *v*-pol on 6th July is shown in Figure 4-3 at different resolutions.

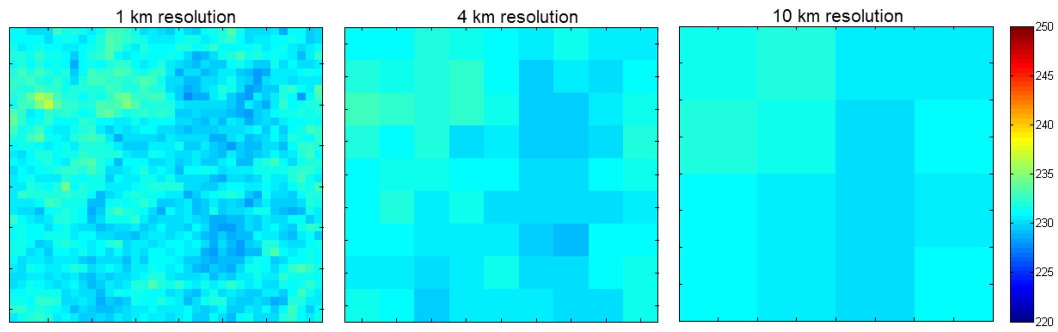

Figure 4-4: Downscaled *Tb* at *v*-pol on 6th July in SMAPEx domain: at 1 km, 4 km and 10 km resolution.

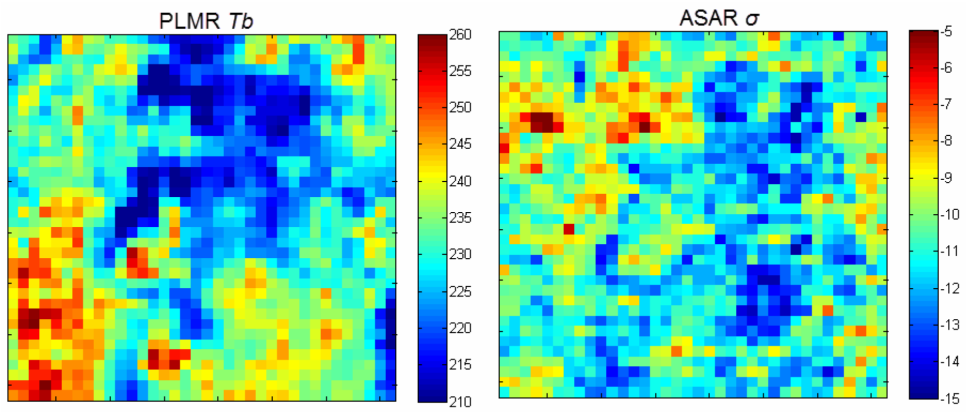

Figure 4-3: PLMR *Tb* at *v*-pol and ASAR data on 6th July in the SMAPEx study area.

As mentioned before, PLMR and ASAR have different characteristics in frequency band, polarization and incidence angle, and their mappings over SMAPEx area on 6th July are shown in Figure 4-4. It can be found that in the up-right quarter of each figure, PLMR and ASAR show similar pattern, while in the remaining area those two patterns turn out to be approximately flipped, indicating the downscaled *Tb* may be poor due to those inconsistent patterns no matter what estimates of β are.

Comparing values of PLMR *Tb* at each polarization between the two days shows a clear increase in brightness temperature on 10th July (illustrated in Table 4-3), which implies a drying of the soil and/or increase in soil temperature. Meanwhile, ASAR data show a decrease in average backscatter on 10th July. With respect to the downscaled *Tb*, a similar drying tendency as PLMR *Tb* turns out from 6th to 10th July.

Table 4-3: RMSE of downscaled *Tb* obtained by merging PLMR and ASAR data on 6th and 10th July

Date	Pol.	Aggregated PLMR (K) at 40 km resolution	Aggregated ASAR (dB) at 40 km resolution	Aggregated Downscaled *Tb* (K) at 40 km resolution	RMSE (K) at 1 km resolution	RMSE (K) at 4 km resolution	RMSE (K) at 10 km resolution
6th July	*h*-pol	196.5	-10.7	196.4	11.7	9.6	7.8
	v-pol	230.8		230.8	10.3	8.5	6.9
10th July	*h*-pol	212.7	-11.2	212.4	10.0	7.6	6.1
	v-pol	242.5		242.4	8.6	6.7	5.2

Values of RMSE given in Table 4-3 show an improvement from 1 km to 10 km resolution for both days. Downscaled *Tb* data at 1-km resolution are the results from implementation of this downscaling method, while downscaled *Tb* data at 4 km and 10 km resolution have used ASAR data averaged to 4 km or 10 km resolution, respectively.

In comparison with the de-biased SMOS results (Table 4-2), the aggregated PLMR data used here have a better performance. For example, comparison of the results for 6th July shows an RMSE improvement of approximately 2 K. Moreover, the downscaled results at *v*-pol are better than *h*-pol. Compared with the correlation of Tb_h and σ_{hh}, Tb_v and σ_{hh} have a better linear relationship, thus indicating it is more suitable for application in this downscaling algorithm. However, the accuracy of downscaled results still suffers from a single polarization of ASAR data, and results are expected to improve for application with *vv*-pol and cross-pol backscatter.

All of the results above have been based on a β value derived from de-biased SMOS and ASAR data, which is 3.11 at *h*-pol and 1.05 at *v*-pol, respectively. In order to test the sensitivity to this parameter, the downscaling method is repeated with a "calibrated" β, obtained by minimising the RMSE between downscaled and observed Tb at 1 km resolution. The calibrated value of β, expected to obtain an optimal downscaled Tb, is estimated as 1.65 at *h*-pol and 1.05 at *v*-pol (dashed coloured lines in Figure 4-1). While the value at *h*-pol is obviously different to that determined earlier in Figure 4-1, the resultant RMSE is not considerably better: at 1 km the RMSE is 11.4 K at h-pol and 10.2 K at *v*-pol on 6th July, and 9.9 K at *h*-pol and 8.6 K at *v*-pol on 10th July.

4.5 Chapter Summary

This chapter presented a test of the feasibility of an existing downscaling approach, using operational SMOS and ASAR datasets. It is shown that the accuracy of the downscaling approach is primarily determined by the pattern agreement of the radar and radiometer observations. Moreover the C-band ASAR σ_{hh} data used in this study indicates little potential for downscaling, confirming earlier results that backscatter at *hh*-pol has poor correlation with Tb (*vv*-pol is expected to yield better results), greatly limiting the effectiveness of this downscaling algorithm.

Consequently, this study demonstrates the requirement for a data set that more closely replicates the characteristics of SMAP in order to test the viability of the SMAP downscaling algorithm. This requires the experimental data to have similar frequencies, resolutions, polarizations and incidence angle to SMAP. For this purpose, simulation of the SMAP data stream from field campaigns is described in next chapter prior to further evaluation of downscaling algorithms.

5 Simulation of the SMAP Data Stream

This chapter develops a simulation of the SMAP data stream using airborne observations from the SMAPEx field campaigns. Based on the findings from **Chapter 4** using currently available satellite data sets, such a data stream is required for evaluation of the available downscaling algorithms for SMAP. In order replicate the characteristics of SMAP data, the airborne observations are processed in terms of spatial aggregation and incidence angle normalization, and assessed for potential azimuth effects. Moreover, the accuracy of these proposed methods for incidence angle normalization and azimuth effect are tested in this study. The work in this chapter has been published (Wu et al., 2015).

5.1 Background

In preparation for the SMAP launch, suitable algorithms and techniques need to be developed and validated to ensure that an accurate intermediate resolution (~10 km) soil moisture product can be operationally produced from combined SMAP radiometer and radar observations. To this end, it is essential that field campaigns with coordinated satellite, airborne and ground-based data collection be undertaken, giving careful consideration to the diverse data requirements for the range of scientific questions to be addressed. Therefore, some field campaigns have been conducted using active and passive microwave airborne observations to address the scientific requirements pertinent to SMAP. Details on such campaigns have been already described in **Chapter 2**, with most of those campaigns conducted in North America. The SMAPEx field campaigns, conducted in Australia in 2010 and 2011, provide an opportunity to rigorously evaluate the SMAP Active-Passive baseline algorithms using data that represents different sets of conditions and land covers. These SMAPEx field campaigns are complementary to other campaigns in addressing the scientific requirements of the SMAP mission, therefore representing a significant contribution to the limited heritage of airborne experiments mentioned previously.

During the SMAPEx campaigns, airborne observations were collected together with ground sampling of soil moisture and ancillary data over an area equivalent to a SMAP radiometer footprint (36 km), with the aim to provide SMAP-type data for the development and validation of algorithms and techniques to estimate near-surface soil moisture from the upcoming SMAP mission. Consequently, the main objective of this chapter is to assess the reliability of simulated SMAP data using aircraft observations from the SMAPEx field campaigns. In particular, this study makes use of flights specifically conducted to assesses the reliability of (i) incidence angle normalization of airborne data to the SMAP reference incidence angle of 40˚; (ii) spatial aggregation of airborne active and passive data to the resolutions of SMAP observations; and (iii) the impact of different azimuthal view angles on the airborne active and passive data.

5.2 Data Set

5.2.1 Experiment overview

Description of the SMAPEx study area and monitoring activities can be found in **Chapter 3**, so only additional pertinent information is provided here. Three types of flights, including the (i) multi-angle flights, (ii) multi-azimuth flights and (iii) multi-resolution flights, were conducted specifically to address the reliability of using SMAPEx airborne data as a proxy of future SMAP space-borne observations, which is the focus of this study. Apart from the airborne observations, spatial ground sampling activities were also conducted in 6 focus areas: YA4, YA7, YB5, YB7, YC and YD ("Y" refers to Yanco; each area has a size of 2.8 km × 3.1 km), which were distributed across the simulated SMAP radiometer pixel. In the following, YA4 and YA7 will be referred to as simply 'YA', YB5 and YB7 as 'YB'. While YA and YD areas were mainly occupied by the irrigated crop, YB and YC were dominated by grass, so as to provide the opportunity to study the impact of azimuth and incidence angle of the specific flights on the resulting observations with respect to different land cover conditions. Data collected from ground sampling are used as the ground truth for algorithm calibration and validation.

The main characteristics of the SMAP sensors, PLMR, and PLIS, have been described in Table 1-1 in **Chapter 1**, from which it is noted that the airborne sensors from SMAPEx have the same frequency band as SMAP, and the same polarization combinations. PLMR has three fixed beams that record at three fixed angles, being 7°, 21.5° and 38.5°, while the PLIS antennas radiate mainly between 15° to 45° continuously, providing data over a large number of incidence angles. In order to closely replicate SMAP data, both the spatial resolution and incidence angle of the airborne observations need to be adapted. Therefore, the 1 km PLMR brightness temperatures and ~10 m PLIS backscatter need to be aggregated to 36 km and 3 km respectively. Moreover, both PLMR and PLIS observations need to be normalized to a constant 40° incidence angle. In addition, since SMAP will make use of a rotating mesh antenna to provide observations over the entire swath, both the radar and radiometer observations will be observed at a range of azimuthal orientations. Therefore, it will be crucial to understand the potential impact on the observations due to the azimuth viewing angle, and how this changes depending on specific surface conditions (e.g., vegetation type and tillage conditions).The accuracy of the PLMR radiometer was assessed against hot (blackbody box) and cold (clear sky) calibration targets before and after each SMAPEx flight, as well with in-flight calibration by low altitude passes of a water body where water temperature and salinity were measured. The radiometer accuracy was estimated to be better than 0.7 K for H-polarization and 2 K for V-polarization including system noise and in flight calibration drift.

Calibration of the PLIS radar was performed using a combination of six trihedral Passive Radar Calibrators (PRC's) deployed across-swath in a homogeneous grassy field, and a distributed forest target. The calibration targets were imaged each day at both the beginning and end of the scientific monitoring flights to check for a potential calibration drift (Panciera et al., 2014).

After radiometric calibration, the difference between observed and theoretical PRC cross section was on average 0.93 dB (absolute radiometric accuracy) with a standard deviation of 0.8 dB relative radiometric accuracy (Panciera et al., 2014). The repeatability of PLIS flights was also calculated, by comparing the start overpass to the end overpass and the resulting Root Mean Square Deviation (RMSD) was approximately 0.9 dB at co-polarization and 1.4 dB at cross-polarization. The possible influence of calibration accuracy during the SMAP data simulation will be described in the following sections. To this end, the accuracy of PLIS observations can meet the radar measurement accuracy requirement of the SMAP, which is around 1.0 dB at co-polarization and 1.5 dB at cross-polarization at 3 km resolution, including the calibration error, contamination terms, and speckle noise.

5.2.2 Flight design

In order to closely replicate SMAP data, every portion of the study area should be observed at the same incidence angle of SMAP (40°). However, this is not easily achieved using a small experimental aircraft with airborne instrumentation over an area as large as the SMAPEx study area within the time constraints of the daily sampling. Therefore, multi-angle flights (see Figure 5-1(a)) were designed to provide data for characterizing the angular variation of brightness temperature and radar backscatter together with reference data observed at 40°±2.5° over portions of the study area. For this testing, data were collected from the SMAPEx-1 and -2 field campaigns. During the SMAPEx-1 field campaign, multi-angle flights were conducted on 3 days: 6th, 8th and 10th of July 2010. During SMAPEx-2, multi-angle flights were performed on 7th December 2010 only, thus allowing evaluation of the normalization skill robustness under the increased biomass conditions of SMAPEx-2 (full-grown crops).

Areas selected as the focus of multi-angle flights were within the two SMAPEx target areas YA and YB (a cropping area and a grassland area, respectively), as shown in Figure 5-1(a). The flying altitude was around 3 km to collect multi-angle active microwave observations at approximately 10 m spatial resolution and passive microwave observations at 1 km resolution. For each flight, two ground strips of radar backscatter were imaged, due to the PLIS configuration, each of approximately 2.2 km in width, together with a radiometer brightness temperature swath of approximately 6 km in width. Eight adjacent parallel flight lines separated by approximately 360 m were conducted in YA and YB, providing radar observations at

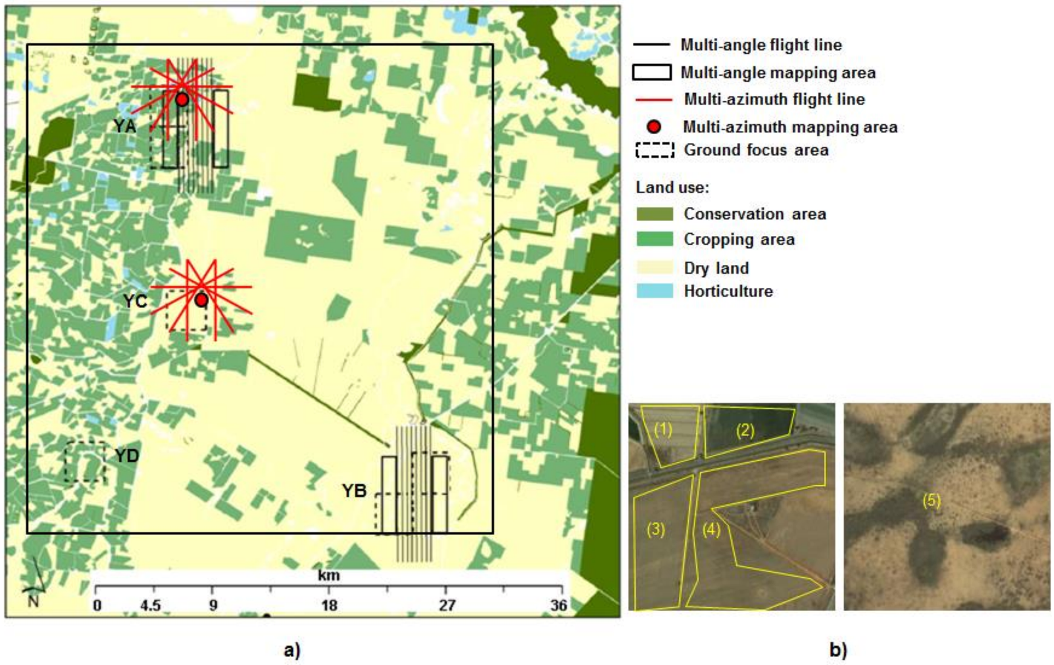

Figure 5-1: (a) Multi-angle flights conducted during SMAPEx-1 and SMAPEx-2 over cropping area YA and grassland YB, at 3,000 m altitude; and multi-azimuth flights conducted on one occasion during SMAPEx-2 over cropping area YA and grassland area YC respectively, at 1,500 m altitude; (b) aerial photos of two multi-azimuth mapping areas (1 km × 1 km) within YA (left) and YC (right) area respectively, and layout of the land cover type within YA (1 - grass, 2 - cotton, 3 - maize and 4 - wheat), and land cover type within YC (5 - uniform grassland).

incidence angles ranging from 15°-45°, and radiometer observations at 7°, 21.5° and 38.5° to the left and right sides of the flight track.

Special multi-resolution PLIS flights were conducted on one occasion during SMAPEx-2 over the YA area in order to understand the accuracy of PLIS spatial aggregation. During those flights, the backscatter from PLIS was observed at 1500 m altitude with 3 different slant-range resolutions (approximately 6 m, 60 m and 180 m respectively), which were then projected on the ground, and in turn resulted in a ground range resolution variable ranging from 4 m – 11 m (at 45°- 15°), 42 m – 115 m, and 127 m – 347 m. The azimuth resolution was unchanged, which is around 1.0 m. After multi-looking and re-sampling in range and azimuth, backscatter with resolutions of 10 m, 50 m and 150 m were eventually obtained.

In order to understand the effect of the azimuth viewing angle on the brightness temperature and backscatter with respect to different land surface features, multi-azimuth flights were taken on one occasion during SMAPEx-2 over two focus areas: a grassland site YC consisted of short (<5 cm) and tall (1-2 m) grasses, and a cropping site YA comprised of a mix of crop (maize, wheat and cotton), grass and bare soil (Figure 5-1). Site YC was selected as a control site, characterized by uniform conditions not expected to result in a detectable azimuthal signature. Conversely, at site YA azimuthal signatures were expected due to the asymmetric characteristics of crop fields (e.g., crop rows etc.). This is discussed in detail in the results section. Flights were performed at an intermediate altitude of 1,500 m in order to maximize the sensitivity of the PLIS radar to changes in backscatter due to the azimuth viewing angle. The ground spatial resolution for the active microwave observations was approximately 10 m, and for passive microwave observations around 500 m. Flights in YA were conducted at 5 different azimuth viewing angles: 30˚, 150˚, 180˚, -90˚, and -30˚; while flights on YC were carried out at 7 different azimuth viewing angles: 30˚, 90˚, 150˚, 180˚, -120˚, -90˚, and -30˚ (the azimuth viewing angle is decided by the angle starting from the north to the looking direction of the flight, ranging from -180˚ to 180˚). Observations were collected at multiple azimuth angles over an overlapping ground area with a size approximating 1 km × 1 km for PLIS, and 3 km × 3 km for PLMR, therefore allowing the investigation of the effect of azimuth viewing angle on a variety of land cover types.

5.3 Methodology

By comparing the characteristics of the SMAP sensors and the airborne sensors in the previous section, three methods are used in this study to produce the prototype SMAP data, including incidence-angle normalization, spatial aggregation and azimuth impact analysis. Details of each method are described in the following sections.

5.3.1 Incidence angle normalization

Due to the large overlap between adjacent swaths from those eight multi-angle flights, radar observations at 40˚±2.5˚ angles were combined from each flight to form two strips, with a size of approximately 2.5 km × 8 km for each. These combined strips were used in this study as the reference to compare with the data normalized to 40°. Similarly, radiometer observations at 38.5° incidence angle from each flight were combined as the reference data, with a total coverage of about 9 km × 10 km, in order to assess the accuracy of normalizing the original data to 40°. Before carrying out the incidence angle normalization, it is necessary to point out that all observations from the aircraft will be angle normalized to 40° to be in accordance with the SMAP viewing angle, however, the reference data used to evaluate the accuracy of normalization were collected at 38.5° for PLMR and at 40°±2.5° for PLIS. Consequently, the difference in PLMR *Tb* between 40° and 38.5° will introduce a component of error to be considered when assessing the results of the normalization method. Analysis of PLMR data by Peischl et al (2012) indicates that the sensitivity of PLMR *Tb* to incidence angle (within the range of 37.5° to 42.5°) is around 0.8 K/degree at *v*-polarization, and -0.6 K/degree at *h*-polarization, resulting in differences in *Tb* between 38.5° and 40° of ~1.2 K and 0.9 K at respectively at *v*- and *h*-pol (Peischl et al., 2012). Although such differences are not entirely negligible, and in the absence of direct PLMR observations at 40°, in this study the PLMR observed *Tb* at 38.5° were taken as a proxy of the 40° reference for the purpose of testing the normalization method. The impact of the *Tb* differences between 40° and 38.5° will be duly considered and discussed in the text when analysing the results of the normalization method. The data from each flight line observed at the original range of incidence angles were then normalized to 40° through a Cumulative Distribution Function (CDF) based method (Ye et al., In Review). The CDF angle-normalization is a nonlinear method based on matching the cumulative frequency distribution of the observations at its original incidence angle to the cumulative frequency of the observations at a reference angle (40° in this case). Based on the assumption of identical heterogeneity under each beam across the entire study area, the value of the observation at a non-reference angle can be adjusted to the one that has the same cumulative frequency when observed at the reference angle. Therefore, observations at a variety of incidence angles can be normalized to the reference angle by searching the values with the same cumulative frequency. Compared to other normalization methods (eg. the Ratio-based method (Jackson, 2001) and the Histogram-based method (Mladenova et al., 2013); both of which are linear methods) this CDF-based method has been shown to produce normalization results comparable to the Histogram-based method, and less noticeable stripe pattern and the higher normalization accuracy compared to the more traditional Ratio-based method. Consequently, this CDF-based method is applied in this study using the data collected from the multi-angle flights, in order to evaluate its performance on different land conditions, polarizations, as well as different resolutions, and in the end to apply to all regional flights from the three SMAPEx campaigns.

5.3.2 Spatial aggregation

The upscaling method utilized in this study is based on linear aggregation. Before aggregating the original 1 km PLMR and 10 m PLIS observations to the SMAP footprint resolutions, it is important to understand the accuracy of the upscaling approach that will be applied to the 38 km × 36 km regional data. Linear aggregation for PLMR has already been verified by (Panciera et al., 2006), showing that the differences in the average brightness temperature were less than 2 K when aggregating from 60 m to 1 km resolution, which is within the instrument error, suggesting that PLMR data from the aircraft could be reliably aggregated to simulate satellite footprint observations.

Prior to the performance evaluation of this linear aggregation for the PLIS radar, the speckle noise of radar data observed at each resolution was analysed. The "observed" 10 m, 50 m and 150 m data were "multi-looked" in range and azimuth direction by averaging all smaller pixels to the larger scales. For instance, the 10 m resolution pixel had 14 looks in azimuth and 2 looks in range, the 50 m resolution had 56 looks in azimuth and 1 look in range, and the 150 m resolution had 140 looks in azimuth and 1 look in range. Since the speckle noise can be determined according to a square root function of the number of looks in both directions (Raney, 1998), the speckle noise for 10 m, 50 m and 150 m was found to be 0.75 dB, 0.55 dB and 0.35 dB, respectively. After linearly aggregating the observed 10 m data to 50 m and 150 m in power units, the speckle noise for the aggregated observations is reduced to 0.16 dB and 0.05 dB, respectively. Therefore, the speckle noise of the "observed" and "aggregated" data at 50 m and 150 m resolution can be expected to have little impact on the assessment of the spatial aggregation method. It should also be noticed that the absolute and relative radar calibration accuracies are the same for the 10 m, 50 m and 150 m data sets. Indeed, the radar calibration performed using the Passive Radar Calibrators (PRC) depends only on the radar frequency and the physical size of the PRC's, both of which are unaffected by the changes in PLIS configuration used to modify the spatial resolution of the radar.

The observed data at 50 m and 150 m resolution were taken as the reference in this study when comparing with the aggregated 50 m and 150 m backscatters from the original 10 m resolution over the same area, thus analysing the reliability of upscaling PLIS to the SMAP footprint through linear aggregation.

5.3.3 Azimuth impact

Changes in radar backscatter and brightness temperature with azimuth angle are theoretically expected due to reflection symmetry of the surface or the Bragg scattering effect, or the combination of these two effects, especially at high spatial resolution. The effects are expected to be cancelled out when applied at coarse resolution such as SMAP resolution level (Yueh et al., 1994a, Yueh et al., 1994b, Schmidl Sobjaerg and Skou, 2003, Colliander et al., 2010). This study will analyse the azimuth effect for high resolution PLIS observations over different crop fields. However, due to the relatively low resolution of PLMR *Tb* (at 500 m), it is difficult to single out a specific row structured crop field with such large size. Instead, the combined fields with various directions of rows are used to analyse the azimuth dependency for PLMR.

The overlapping area of the backscatter images from all azimuth directions was about 1 km × 1 km in size. As displayed in Figure 5-1(b), the overlapping area YA consisted of four individual fields characterized by the following conditions: (1) Grassland field, a fairly uniform and flat field characterized by tall vegetation (160 cm plant height, 1.5 Kg/m^2 water content) and 1 m-high irrigation bays running along the entire field in the east-west direction at intervals of approximately 100 m (remnants of rice fields bays); (2) Cotton field: this was largely bare soils, with sparse plants up to 15 cm in height, characterized by row structure in the north-south direction (approximately 15 cm-deep, 1 m-wide rows); (3) Maize field, characterized by significant above-ground biomass (170 cm plant height, 3.9 Kg/m^2 water content) and row structure in the north-south direction (approximately 20 cm-deep, 1 m-wide rows); and (4) Wheat field, which was fairly flat, with no row structure and senescent short vegetation (80 cm plant height, 0.2 Kg/m^2 water content). Therefore, in YA, the analysis was done in two stages: first, azimuthal effect was analysed for the four individual fields, by calculating radar statistics for each azimuth viewing angle within the individual fields; then, the cumulated azimuthal effect for the four fields was considered. For YC the analysis was done only in the cumulated way since the entire YC area was dominated by the same land cover (i.e., grassland). Therefore, the field with distinct row structure (e.g. grassland, cotton and maize) is expected to have the azimuth signature, while the field without row structure (e.g. wheat field and YC area) is expected to have little variance in backscatter across different azimuth angles.

5.4 Results and Discussion

In this section, the applicability of the incidence angle normalization and linear aggregation methods will be studied, along with the impact of azimuth viewing angle on active and passive microwave observations. Finally, an example simulation of the anticipated SMAP data stream will be presented.

5.4.1 Incidence angle normalization

The CDF-based normalization method was tested with data collected over the focus areas YA and YB from across three days of SMAPEx-1 and one day from SMAPEx-2. As mentioned in the last section, the reference data were obtained by combining all observations at 40°(±2.5°) from PLIS and at 38.5° from PLMR. These reference data were then used to compare with the incidence-angle normalized data of each flight. An example of un-normalized PLIS observations, CDF-normalized data, and the reference map (40°±2.5°) for the same field of view is displayed in Figure 5-2, while an example of PLMR is shown in Figure 5-3.

The statistics of the PLIS normalization are shown in Table 5-1 and Table 5-2. In order to evaluate the effectiveness of the CDF-based normalization method, the RMSD was calculated for both the original observations (incidence angles 15°- 45°)

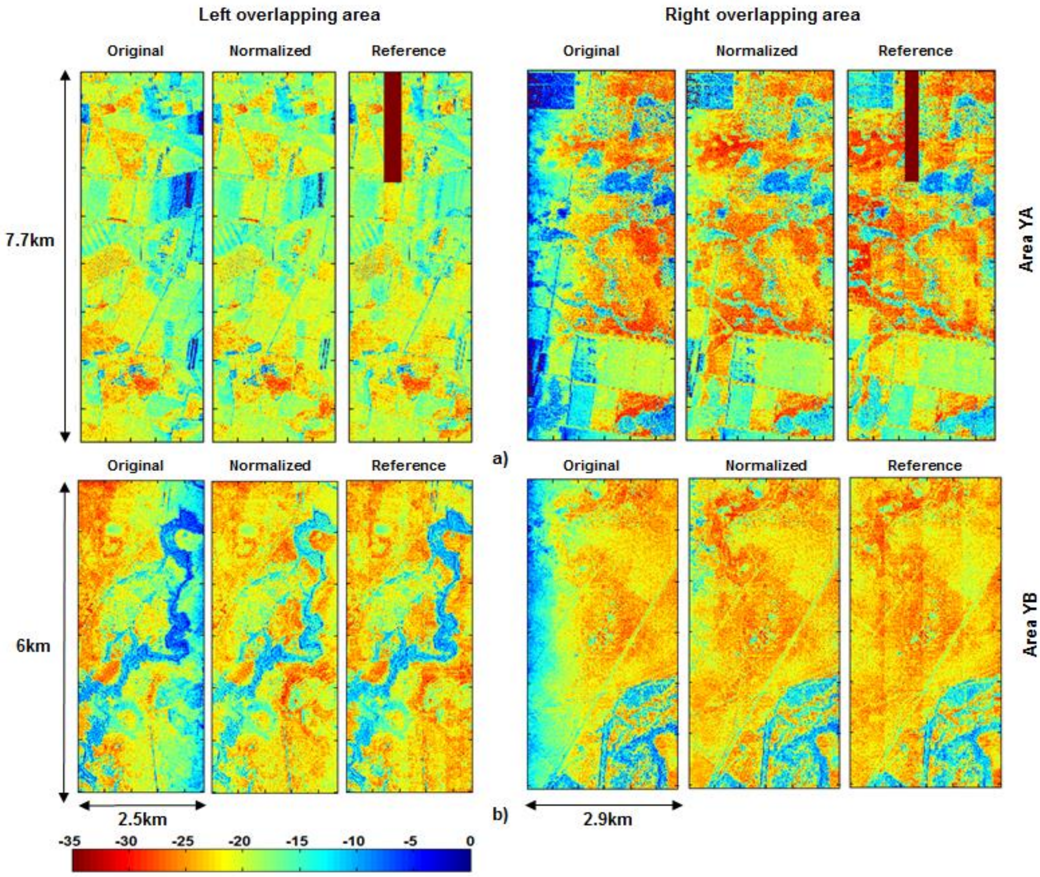

Figure 5-2: Example of incidence angle normalization of PLIS radar data at YA (a) and YB areas (b) at *hh*-polarization on 10th July, 2010, from left (left column) and right (right column) swath coverage. PLIS data are shown as originally observed at incidence angles between 15˚-45˚, normalized to 40˚ using the CFD-based method, and reference observations at 40˚±2.5˚. The gray strip in YA area is some missed data from one of the flights.

and the normalized data, against the reference 40˚ observed data. Results listed in Table 5-1 are the average RMSD of four days from SMAPEx-1 and SMAPEx-2, for YA and YB, respectively, and accordingly the standard deviation of the RMSDs, which in this circumstance can be considered as an index of the stability of this normalization skill across different days or seasons.

As noted from Table 5-1, the normalized data had an improvement of ~2 dB in RMSD over the original data amongst the resolutions from 10 m to 1 km; RMSD in YA reduced from 3.6 dB at 10 m resolution to 0.8 dB at 1 km resolution, mainly because the speckle noise from PLIS was decreased during averaging, as well as the

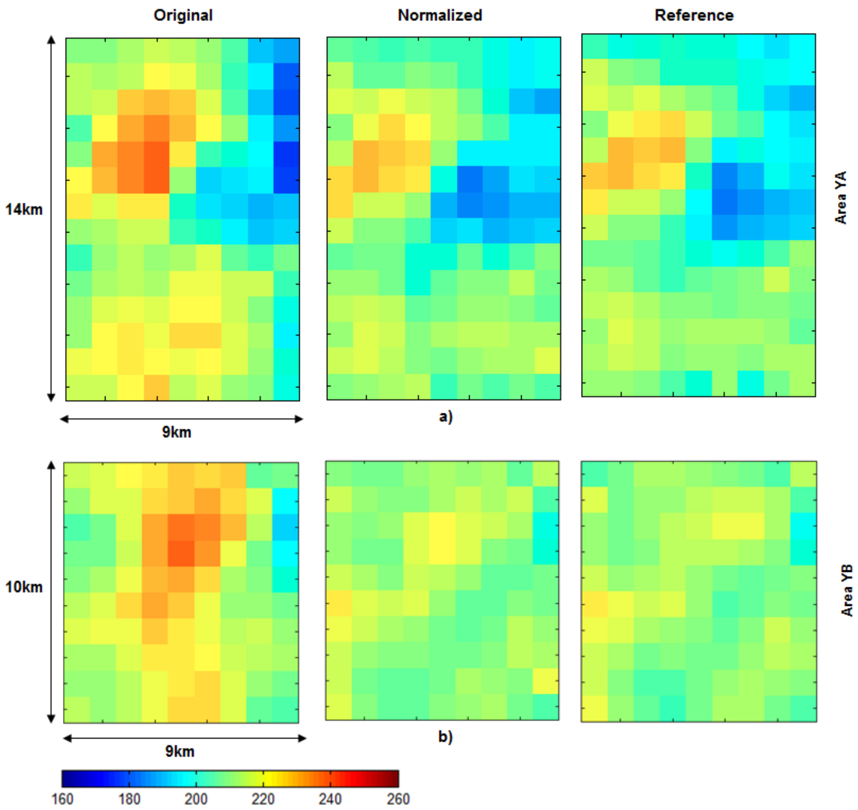

Figure 5-3: Example of incidence-angle normalization of PLMR radiometer brightness temperatures at YA (a) and YB areas (b) at *h*-polarization on 10th July, 2010. PLMR data are shown as originally observed at incidence angles of 7˚, 21.5˚ and 38.5˚ (left), normalized to 40˚ using the CDF-based method (middle), and reference observations at 40˚±2.5˚ (right) .

patchiness in vegetation. In addition, the standard deviation at different resolutions suggested a minor variation of normalization performance on the radar backscatter in response to four different days or two seasons' surface conditions. It is also seen that for the YB area, characterized by grassland, the RMSD was generally slightly lower (~0.3 dB) than for the cropping area YA, indicating that the performance of the CDF normalization method was better on relatively homogeneous areas. Moreover, the RMSD of all three polarizations *hh*, *vv* and *hv* were very similar, with the *hh*-polarization being ~0.2 dB higher than the others, suggesting that the CDF normalization method had fairly consistent performance in terms of polarization.

Table 5-1: Accuracy of the CDF-based incidence angle normalization applied to PLIS radar data. Shown is the Root Mean Square Deviation (RMSD) between radar backscatter originally observed at incidence angles from 15˚ to 45˚ and normalized to 40˚, compared to those observed at 40˚±2.5˚. Each RMSD value shown is the average of the RMSDs calculated for each focus area on 4 occasions, with standard deviation of the RMSDs shown in the bottom row. Errors are presented at various aggregation resolutions (10 m, 100 m, 500 m and 1 km) and different polarizations (*hh*/*vv*/*hv*). All values are in dB.

	YA (cropping area)				YB (grassland area)			
	10 m	100 m	500 m	1 km	10 m	100 m	500 m	1 km
Original (15-45˚)	5.2/4.2 /3.8	4.1/3.2 /2.3	3.3/2.4 /1.7	2.8/1.8 /1.4	5.4/4.2 /3.5	4.6/3.3 /2.1	3.7/2.4 /1.5	3.2/2.0/ 1.2
Normalized (40˚)	3.6/3.2 /3.3	1.9/1.7 /1.5	1.3/1.1 /0.9	0.8/0.7 /0.7	3.3/2.8 /3.1	1.5/1.2 /1.5	1.1/0.8 /1.1	0.9/0.6/ 0.8
Standard deviation of RMSD	0.4/0.2 /0.4	0.2/0.2 /0.2	0.3/0.2 /0.1	0.1/0.2 /0.1	0.2/0.1 /0.1	0.3/0.1 /0.3	0.3/0.2 /0.2	0.3/0.2/ 0.1

The relationship between original incidence angles and RMSD of normalized PLIS data was investigated to understand the normalization performance more thoroughly. The original observations were split into 7 subsets according to their incidence angles, from 15˚ to 45˚, with an increment of 5˚. Data in each subset were normalized to 40˚, and then compared with the data observed at 40˚±2.5˚ at the same locations. Results are shown in Table 5-2. The RMSD of original data with incidence angle of 40˚±2.5˚ was 0 as expected, due to the reference map being the data observed at 40˚±2.5˚. For the remaining data, the errors increased the larger the difference between the reference and original incidence angles became, which was to be expected given the change of the incidence angle. In contrast, the RMSD of normalized data at all incidence angles was similar, showing that the normalization introduces a somewhat constant error. It is noted that the RMSD of the data normalized to 40˚ was not equivalent to 0, but up to 0.4 dB. This negligible change was due to marginal backscatter changes within the 40˚±2.5˚ data taken as the truth

Table 5-2: Accuracy of the CDF-based incidence angle normalization applied to PLIS radar data (10 m resolution) for different incidence angles. Shown is the Root Mean Square Deviation (RMSD) between radar backscatters binned at 5˚ steps and normalized to 40˚ compared to those observed at 40˚±2.5˚. Each RMSD value shown is the average of the RMSDs calculated for each angle bin and focus area on four days, with standard deviation of the RMSDs shown in the bottom row. Errors are presented for different polarizations (*hh*/*vv*/*hv*). All values are in dB.

	YA (cropping area)							YB (grassland area)						
	45˚	40˚	35˚	30˚	25˚	20˚	15˚	45˚	40˚	35˚	30˚	25˚	20˚	15˚
Original	3.6/ 3.3/ 3.7	0/ 0/ 0	4.7/ 4.2/ 3.8	5.4/ 4.2/ 3.7	6.7/ 4.8/ 4.0	10.8/ 8.2/ 4.2	12.8/ 11.2/ 7.8	3.3/ 3.0/ 3.4	0/ 0/ 0	3.8/ 3.1/ 3.3	4.7/ 3.2/ 3.4	7.3/ 4.8/ 3.7	10.4/ 8.2/ 3.6	13.7/ 12.0/ 6.0
Normalized	3.6/ 3.2/ 3.3	0.4/ 0.3/ 0.4	4.2/ 3.9/ 3.6	4.1/ 3.5/ 3.6	4.0/ 3.5/ 3.8	4.3/ 3.8/ 4.0	4.5/ 4.0/ 4.3	3.3/ 2.8/ 3.3	0.4/ 0.3/ 0.6	3.6/ 3.1/ 3.1	3.7/ 3.1/ 3.4	3.7/ 3.2/ 3.5	3.6/ 3.2/ 3.6	4.2/ 3.8/ 4.1
Standard deviation	0.2/ 0.1/ 0.4	0.1/ 0.1/ 0.1	0.5/ 0.4/ 0.5	0.4/ 0.2/ 0.6	0.6/ 0.3/ 0.3	0.5/ 0.3/ 0.5	0.5/ 0.5/ 0.6	0.3/ 0.2/ 0.1	0.0/ 0.1/ 0.1	0.5/ 0.2/ 0.2	0.3/ 0.1/ 0.2	0.3/ 0.2/ 0.3	0.3/ 0.2/ 0.5	0.3/ 0.3/ 0.5

40˚ reference data, caused by fitting the entire data set (including the reference data) to the CDF of the reference data. The 0.4 dB difference could also be due to the fact that the statistical method is known to modulate the output at 40˚.

A similar assessment was made for the normalization of the PLMR observations. Results of applying the CDF-normalization method to the PLMR radiometer observations are shown in Table 5-3. The RMSD between observed and normalized *Tb* (40˚) reduced as the resolution became coarser, i.e. in YA area, from 2.8 K/2.4 K (*h*/*v*) at 1 km to 1.5 K/1.4 K (*h*/*v*) at 3 km resolution. The performance of the CDF normalization method was influenced by different land conditions and performed slightly better in the relatively homogeneous area YB. In YB area, RMSD was 2.1 K/1.8 K (*h*/*v*) at 1 km resolution, and reduced to 1.3 K/1.1 K (*h*/*v*) at 3 km resolution. Similarly to PLIS, the relationship between the normalization performance and the incidence angles of the original data was also assessed. Results

Table 5-3: Accuracy of the CDF-based incidence angle normalization applied to PLMR radiometer data. Shown is the Root Mean Square Deviation (RMSD) between radiometer brightness temperature originally observed at incidence angles 7˚, 21.5˚ and 38.5˚ and normalized to 40˚, compared to those observed at 40˚±2.5˚. Each RMSD value shown is the average of the RMSDs calculated for each focus area on 4 occasions, with standard deviation of the RMSDs shown in the bottom row. Errors are presented at various aggregation resolutions (1 km, 3 km, and 6 km) and different polarizations (*h*/*v*). All values are in K.

	YA (cropping area)			YB (grassland)		
	1 km	3 km	6 km	1 km	3 km	6 km
Original	8.0/7.1	7.0/7.2	6.3/7.8	8.7/7.5	9.2/7.1	7.1/6.2
Normalized	2.8/2.4	1.5/1.4	0.7/1.3	2.1/1.8	1.3/1.1	1.0/0.7
Standard deviation	0.3/0.6	0.1/0.8	0.3/0.9	0.5/0.1	0.4/0.1	0.5/0.3

are presented in Table 5-4. In this case, data were observed at ±7˚, ±21.5˚, and ±38.5˚ from PLMR due to its instrument configuration. Overall, in YA area, the RMSD of data normalized from 7˚ and 21.5˚ were similar, being around ~5.1 K/4.2 K (*h*/*v*) at 1 km resolution and reducing to ~1.8 K/1 K (*h*/*v*) at 6 km. Results for the YB area were again better than YA at 7˚ and 21.5˚, with an improvement about 1.5 K/1.8 K (*h*/*v*) at 1 km resolution. As noted from Table 5-4, results at 38.5˚ were not equivalent to 0, but up to 1.3 K at both polarizations at 1km resolution over the cropping area. This is again mainly due to the difference in *Tb* observed at 38.5˚ but taken as the truth 40˚ reference. Moreover, it should be noted that as the spatial resolution got coarser, the number of pixels available to calculate the RMSD reduced from ~100 at 1 km to only 2 pixels at 6 km, and therefore the results for 6 km resolution were not statistically representative of the performance of the method.

In summary, the RMSD between observed and normalized PLIS data at 40˚ (calculated for each focus area on 4 occasions) was smaller than 3.6 dB (±0.4 dB standard deviation across the 4 dates) in the cropping area and 3.3 dB (±0.2 dB) in grassland at 10m resolution with minimal differences between *hh*, *vv* and *hv* (an overall improvement of ~0.2 dB at *vv*-polarization). For PLMR the RMSD after normalization was found to be around 2.8 K (±0.3 K) in the cropping area and 2.1 K (±0.5 K) in grassland at 1km resolution and at *h*-polarization and an improvement of ~0.4 K at *v*-polarization (as shown in Table 5-3). It should be noted that these values are in the order of the instrument's measurement accuracy. Moreover, the normalization errors consistently decreased when aggregating to coarser spatial resolutions, down to 0.8 dB for PLIS at 1km resolution (see Table 5-1). Therefore, based on these results it is expected that angle-normalization of SMAPEx airborne data will have errors smaller than 0.8 dB when aggregating PLIS data to the SMAP radar resolution (3 km), and less than 1 K when aggregating PLMR data to 36 km resolution, which is within the target accuracy of SMAP. However, to some extent the verification of this normalization was hampered by comparing a limited number of pixels, especially at coarser scale.

5.4.2 Spatial aggregation

Multi-resolution flights were conducted on one occasion during SMAPEx-2 over five smaller focus areas within YA, in order to understand the influence of linear aggregation of PLIS 10 m resolution data to the resolution of the SMAP radar. Data used to verify the upscaling accuracy have been normalized to 40° using the CDF-based method described above. Using the linear aggregation method with backscatter data in power units, the simulated pixels at 50 m and 150 m were produced from the 10 m data as described in the previous section. These were then compared with the reference data observed at 50 m and 150 m resolutions, as shown in Figure 5-4. The reference data were observed directly with PLIS by changing the sensor configuration, which distinguishes this methodology from the previous section and allows estimating the aggregation error by comparing high and low resolution observations directly.

Based on the backscatter observed over those five flight lines, the average RMSD of these areas was found to be ~3.4 dB (with a standard deviation of 0.2 dB) when upscaled to 50 m resolution, and ~2.7 dB (with a standard deviation of 0.3 dB) when upscaled to 150 m resolution, with the error clearly decreasing as the resolution was

Table 5-4: Accuracy of the CDF-based incidence angle normalization applied to PLMR radiometer data (1 km, 3 km and 6 km resolution) for different incidence angle of origin. Shown is the Root Mean Square Deviation (RMSD) between radiometer brightness temperatures at 7˚, 21.5˚ and 38.5˚ and normalized to 40˚ compared to those observed at 40˚. Each RMSD value shown is the average of the RMSDs calculated for each angle bin and focus area on 4 occasions, with standard deviation of the RMSDs shown in the bottom row. Errors are presented for different polarizations (*h*/*v*). All values are in K.

		YA (cropping area)			YB (grassland)		
		7°	21.5°	38.5°	7°	21.5°	38.5°
1 km	Original	16.1/14.2	11.8/9.7	0/0	16.9/14.4	11.0/11.5	0/0
	Normalized	5.1/4.4	4.9/4	1.3/1.3	3.4/2.3	3.7/2.5	0.6/1.6
	Standard deviation	0.8/0.1	1.0/0.4	0.1/0.4	0.4/0.2	0.9/0.2	0.1/0.3
3 km	Original	16.9/14.3	11.5/10.3	0/0	16.3/14.9	10.5/11.5	0/0
	Normalized	5.1/4.2(9)	3.6/2.9(9)	0.8/1.3(9)	2.6/2.6(12)	3.2/1.9(12)	0.5/1.5(12)
	Standard deviation	0.9/1.1	0.8/0.7	0.3/0.3	0.6/0.3	0.8/0.2	0.1/0.2
6 km	Original	11.5/16.3	9.3/10.6	0/0	16.7/13.8	11.5/10.6	0/0
	Normalized	2.6/0.9(1)	1.1/1.1(1)	0.7/1.3(1)	1.2/0.5(2)	1.5/0.8(2)	0.5/1.4(2)
	Standard deviation	0.1/0.1	0.1/1.1	0.2/0.5	1.1/0.6	1.2/1.0	0.1/0.2

reduced. It is important to note that it is difficult to separate the effect from the incidence-angle normalization from the change in scale. However, as the errors are consistent with those from the incidence-angle study, it is assumed that these errors are largely due to the incidence-angle normalization and not the spatial aggregation. Accordingly, no adverse errors are expected when upscaling the high resolution radar data to 3 km (the footprint of SMAP's active sensor). In terms of polarization, similar performances were found at *hh*, *vv* and *hv*-polarization, with minor changes of approximately 0.2 dB.

As mentioned before, the speckle noise for the original 50 m and 150 m and the aggregated 50 m and 150 m data is around 0.55 dB, 0.35 dB, 0.16 dB and 0.05 dB,

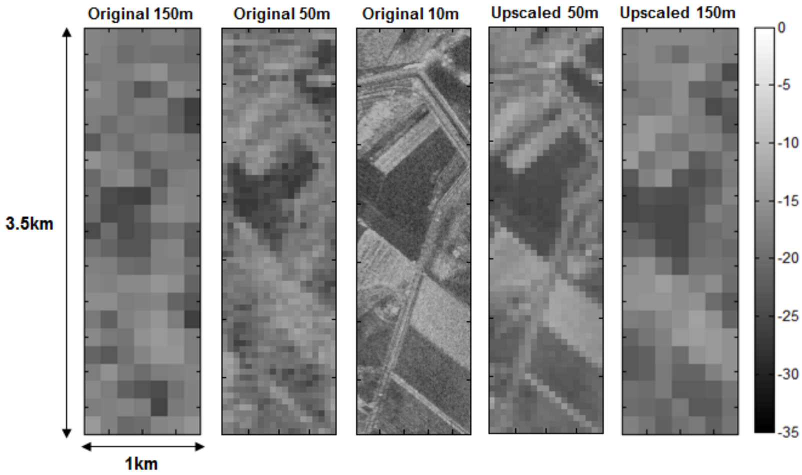

Figure 5-4: Comparison between upscaled and original PLIS data at different resolutions (*hh*-polarization on 7th December, 2010). Data were collected from multi-resolution flights at YA area.

respectively, which may contribute to a portion of the RMSD of 3.4 dB and 2.7 dB at the different resolutions. Consequently, the linear aggregation method is appropriate for producing a simulated 3 km PLIS map in a good agreement with the direct lower resolution measurements. When compared to the expected absolute accuracy of SMAP with ~1.3 K for the radiometer at 36 km resolution, and ~1.0 dB (co-pol) or ~1.5 dB (cross-pol) for the radar at 3 km resolution, it is concluded that data from the aircraft can be reliably averaged up to the satellite footprint resolutions by linear aggregation for the purpose of developing and validating the pre-launch algorithms.

5.4.3 Azimuth impact

Multi-azimuth flights were performed over the cropping area YA and the grassland area YC (see Figure 5-1) in order to investigate the influence of azimuth viewing direction on the radar and radiometer response. PLIS observed images are shown in Figure 5-5(a) at different angles "A" ("A" refers to Azimuth viewing angle).

Data observed at different polarization were used for this azimuth analysis, but only at *hh*-pol for PLIS and *h*-pol for PLMR are shown in Figure 5-5 (can be found in the end of this chapter). Dependence of backscatter (average of each field) on the azimuth direction with respect to different land cover is shown in Figure 5-5(b). Additionally, the standard deviations (SD) of the values across the azimuthal directions were calculated to estimate the total variance of the measurement at each angle. Regarding the azimuthal effect for each field in YA, the strongest backscatters were observed at the azimuthal directions that were perpendicular to the row structure. For example, in the grassland field, the backscatter observed at 180° was the highest among all of the azimuth directions accordingly with the east-west direction of the irrigation bays; in the cotton field, azimuth enhancement was observed at -90° accordingly with the north-south direction of the row structure. These results are consistent with Bragg scattering effect which occurs in perpendicular direction from the row orientation. While in the wheat field, no distinct azimuth enhancement was observed and it had the least standard deviation (SD=1.2 dB) across the azimuth angles when compared to other fields, as it was characterized as a flat field without any row structure. As for the maize field, it did not show the azimuth enhancement at -90° as expected, probably due to the strong attenuation of the surface signal by the significant closed above-ground vegetation. Analysis of the combined fields was also done (SD=1.5 dB) and showed slightly less variance of azimuth effect than the individual grassland field (SD=1.7 dB) or the cotton field (SD=1.9 dB) with clear row structure. This indicates that although azimuthal changes in backscatter can be observed at the level of the individual fields as a consequence of surface asymmetries, when considering the mix of the four fields (as SMAP will do at coarse resolution), the impact of azimuthal differences will tend to smooth each other out. Results for the YC area indicate, as expected, no significant impact of azimuthal differences, with the SD (1.6 dB) of backscatters being smaller than the grassland field or the cotton field analysed in YA and similar to the cumulated backscatter over YA. This is consistent with theoretical consideration given the uniformity of the YA grassland area. Analysis for other polarizations, i.e. *vv* and *hv* were also done for YA and YC, and showed similar conclusion as *hh*-pol.

Dependence of the average brightness temperature from PLMR on the azimuth direction with respect to different land cover is shown in Figure 5-5(c). In this case, azimuth signature was investigated over the combined YA fields or the combined YC fields due to the coarser resolution of PLMR (500 m). As a result, the brightness temperature changes were found across a range of azimuth angles, with the standard deviation around 3.6 K for YC area and 4.0 K for YA area respectively. Again, results at *h*- and *v*-pol show little distinction. As shown in Figure 5-5(c), both YA and YC area had a large difference between the maximum and minimum brightness temperature, around 10 K. This difference was probably due to a water-body was included in the original ellipse footprint of PLMR at one looking direction but was not included at other looking direction, resulting in relatively large difference in brightness temperature.

In summary, azimuthal signature was observed for PLIS and PLMR observations, mainly due to the existence of vegetation row orientations and the asymmetry of surface conditions especially at high spatial resolution, but this signature would be smoothed out at coarse spatial resolution.

5.4.4 Simulated SMAP data stream

Given that the SMAP mission will observe the earth with a constant 40° incidence angle and provide a data set at 3 km for the radar and 36 km resolution for the radiometer, the CDF based normalization approach and linear aggregation methods were applied to the observed PLIS and PLMR data from the regional flights over the entire SMAPEx site. In this way, the SMAP data stream was simulated for a single SMAP pixel for a number of dates, including a 3 week period with observations every 2-3 days. Accordingly, the active microwave observations from PLIS were aggregated from 10 m to 3 km, while the passive microwave observations from PLMR were aggregated from 1 km to 36 km, after being angle-normalized to 40°.

Apart from the 3 km radar and 36 km radiometer data stream simulated for SMAP, 1 km resolution backscatter, and 1 km, 3 km and 9 km resolution brightness temperature data were also produced. This provides the opportunity to evaluate the SMAP soil moisture retrieval algorithms at different spatial resolutions.

An example of the data is shown in Figure 5-6 for one day, in accordance with the configuration of the SMAP satellite. The error of angle normalization was 0.8 dB for backscatter and 2.4 K for brightness temperature observations at 1 km resolution, and this was found to be the largest contributor to the spatial aggregation error.

Given that the errors decreased when aggregated to a larger scale, the accuracy of these data can be considered comparable to the error budget for the SMAP data stream, which is anticipated to be 1.0 dB for backscatter at 3 km resolution and 1.3 K for brightness temperature at 36 km resolution.

5.5 Chapter Summary

Radar and radiometer data collected during the SMAPEx field experiments have been processed to replicate the configuration expected from the SMAP mission, in order to produce a SMAP prototype data set for testing of pre-launch algorithms and techniques. Data from SMAPEx were angle-normalized to 40° and aggregated to the spatial resolutions at which SMAP data will be provided. In this study, the CDF-based normalization method and the linear aggregation approach have been shown to give simulated SMAP data from the airborne SMAP simulator flown during the SMAPEx experiments with an accuracy of approximately 1.0 dB for backscatter at 3 km resolution and 1.3 K for brightness temperature at 36 km resolution. Consequently, the angle-normalization and aggregation techniques analysed in this study have been used to process the radar and radiometer observations collected by the SMAP airborne simulator during the SMAPEx regional flights (covering a 38 km × 36 km area) for the three SMAPEx experiments. These data provide the simulated SMAP data set (available at: www.smapex.monash.edu.au) to be used for pre-launch development of soil moisture retrieval and downscaling algorithms for the SMAP mission in the subsequent chapters.

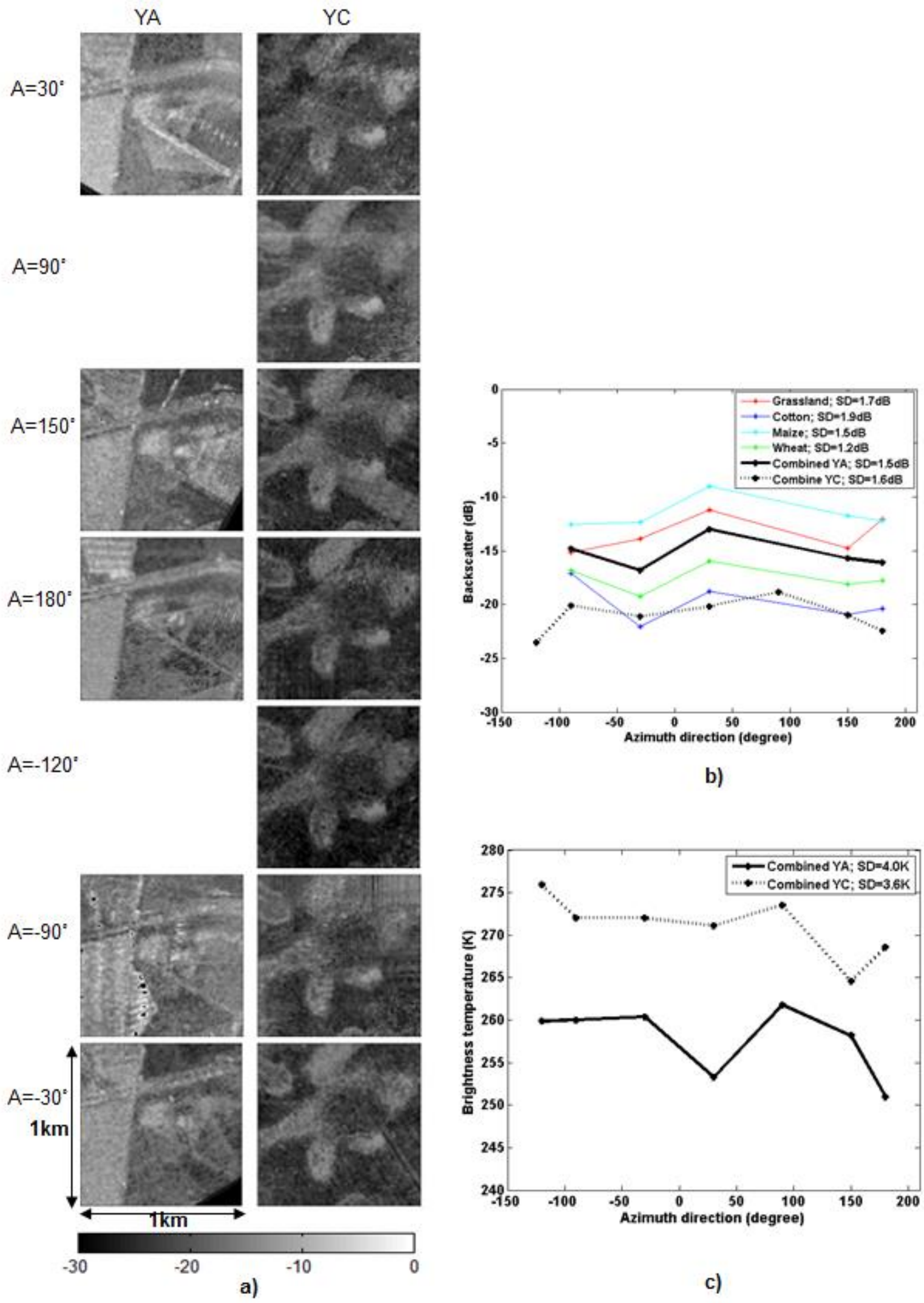

Figure 5-5: (a) Multi-azimuth flights at 10 m resolution over the same field of view within YA and YC areas at a variety of azimuth viewing angles (A), flights at YA area at 90˚ and -120˚ azimuth angles were not conducted during the campaign; (b) dependence of the average backscatter of each field on azimuth direction; (c) dependence of the average brightness temperature on azimuth direction. (Backscatter at *hh*-polarization, brightness temperature at *h*-polarization; data were collected on 7th December, 2010).

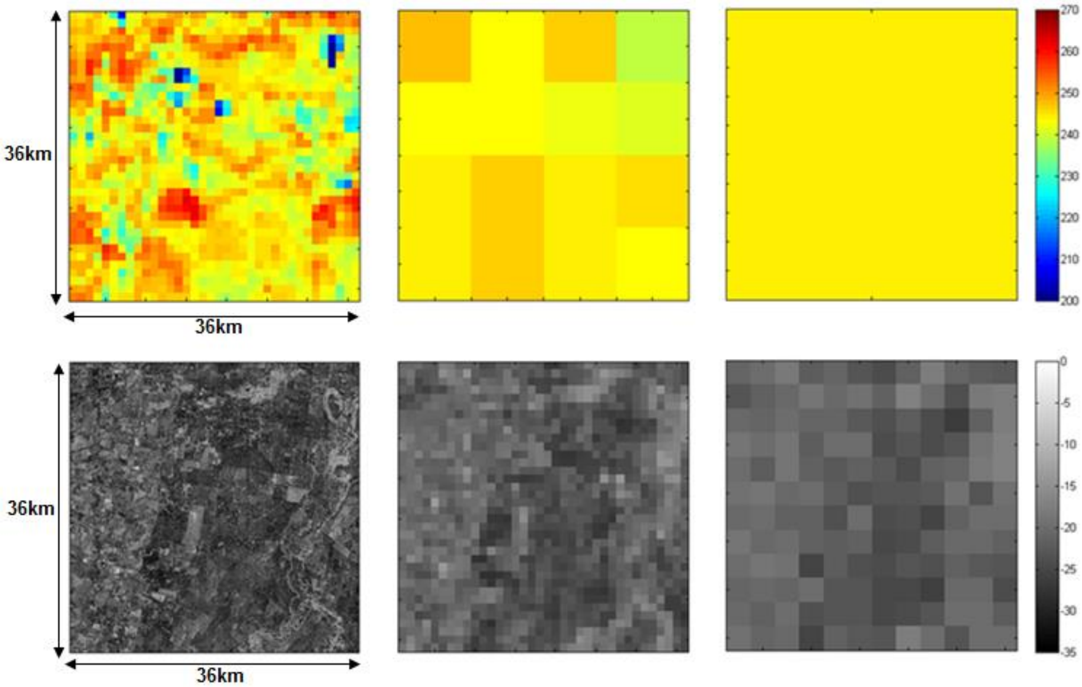

Figure 5-6: An example of simulated SMAP data from SMAPEx-3 on 23rd September, 2011: Brightness temperature (top row) at 1 km resolution (left), aggregated to 9 km resolution (middle), and aggregated to 36 km resolution (right), at *h*-pol; Backscatter (bottom row) at 10 m resolution (left), aggregated to 1 km resolution (middle), and aggregated to 3 km resolution (right), at *hh*-pol.

6 Evaluation of the SMAP Baseline Downscaling Algorithm

This chapter presents an evaluation of the baseline downscaling algorithm proposed for the SMAP mission using the simulated SMAP data set derived in the previous chapter. While this algorithm has already been tested using experimental datasets from field campaigns in the United States., it is imperative that it be tested for a comprehensive range of land surface conditions (i.e. in different hydro-climatic regions) prior to global application. Consequently, this study evaluates the algorithm using data collected from the SMAPEx field campaign in south-eastern Australia, that closely simulate the SMAP data stream for a single SMAP radiometer pixel over a 3-week interval, with repeat coverage every 2-3 days. The work in this chapter has been accepted for publication (Wu et al., In Press-a).

6.1 Background

The baseline brightness temperature downscaling method for the SMAP mission (Das et al., 2014) is based on the assumption of a near-linear relationship between radar backscatter (σ) and radiometer brightness temperature (Tb). This method is tested using airborne passive and active microwave observations collected over a semi-arid landscape during the SMAPEx-3 conducted in Australia in 2011, allowing assessment of the robustness of this baseline downscaling algorithm over different land conditions. According to the approach, the linear regression parameters are estimated using SMAP-type passive and active microwave data at 36 km resolution. These parameters are then applied in the algorithm using aggregated radar data at 3 km to derive downscaled passive microwave observations at 9 km resolution, with the objective to evaluate the accuracy of the brightness temperature downscaling method. Although the ultimate objective of the SMAP mission is to produce a downscaled soil moisture product, this can only be achieved once the assumption that the baseline brightness temperature downscaling procedure is sufficiently accurate. Subsequent to this the standard and well-accepted passive microwave soil moisture retrieval algorithms are applied. Therefore, the purpose of this study is to challenge the baseline brightness temperature downscaling approach as proposed in the SMAP ATBD (Das et al., 2014, Entekhabi et al., 2012) and to test its robustness in terms of the downscaled brightness temperature values, according to the requirements set out in ATBD (Entekhabi et al., 2012). Testing of the final soil moisture retrieval accuracy following the downscaling of the brightness temperature is outside the scope of this chapter, but will be presented later in **Chapter 9**.

6.2 Data Set

Full details on the SMAPEx field campaigns can be found in **Chapter 3**, so only the pertinent details are presented here. As shown in Figure 6-1, the western part of the SMAPEx site is dominated by cropping areas, while the eastern half consists mostly of grassland areas, including a large water body in the north-eastern quarter (approximately 500 m × 5 km in size). Some woodlands along the south-to-north flowing Yanco River, as well as some small forest areas in the far east of the SMAPEx area are also present. This study site represents the heterogeneous land cover conditions that are typical of many landscapes, and thus required to evaluate the robustness of the SMAP active-passive baseline downscaling algorithm performance.

In order to closely replicate the prototype SMAP data stream for development and testing of the downscaling techniques, data collected during the SMAPEx field campaigns have been processed in terms of resolution aggregation (36 km for passive and 3 km for active) and incidence angle normalization (to 40° reference angle), to be in line with the spatial resolutions of SMAP, as shown in the previous chapter. The accuracy of the simulated SMAP data stream used in this study has been determined as comparable to the error budget of the SMAP data stream, which is approximately 1.0 dB for backscatter at 3 km resolution and 1.3 K for brightness temperature at 36 km resolution. The original resolutions of the data sets are 1 km for the PLMR brightness temperatures and 10-30 m for the PLIS backscatter. Since they have been upscaled to 36 km and 3 km respectively for the purpose of application, the PLIS data were also aggregated to 1 km and 9 km to evaluate the performance of the

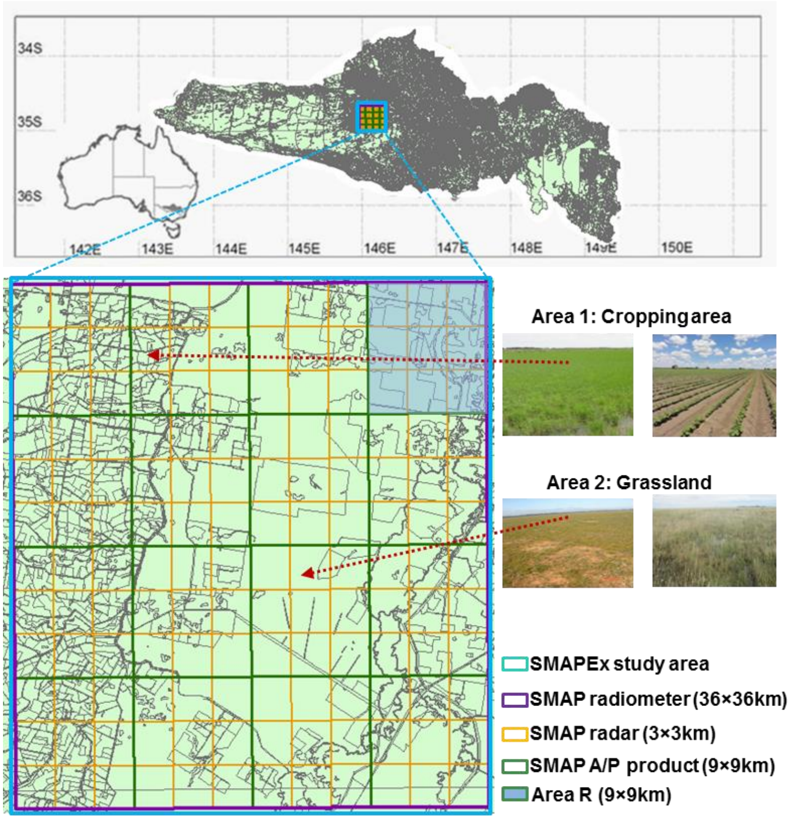

Figure 6-1: Overview of the SMAPEx site showing the SMAP pixel sized study site, and the SMAP grid on which the 36 km resolution radiometer data, 3 km resolution radar data and 9 km resolution active-passive downscaled product will be provided, together with area R in the north-eastern corner where the rainfall events happened during the third SMAPEx field campaign.

SMAP downscaling algorithm at different spatial resolutions (as the native resolution of the SMAP radar is actually 1 km). Moreover, the reference *Tb* data used for evaluation of the downscaling results come from the original 1 km PLMR, and were therefore aggregated to resolutions of 3 km and 9 km for use as reference at a range of scales.

The radiometer and radar data used to test this baseline downscaling algorithm were from the third SMAPEx campaign (September 5-23, 2011), which was conducted during the spring vegetation growing season. This campaign was used since it comprised nine regional flights over a 3-week time period with the 2-3 day revisit time of SMAP. A sample of the simulated SMAP data stream used in this study is shown in Figure 6-2.

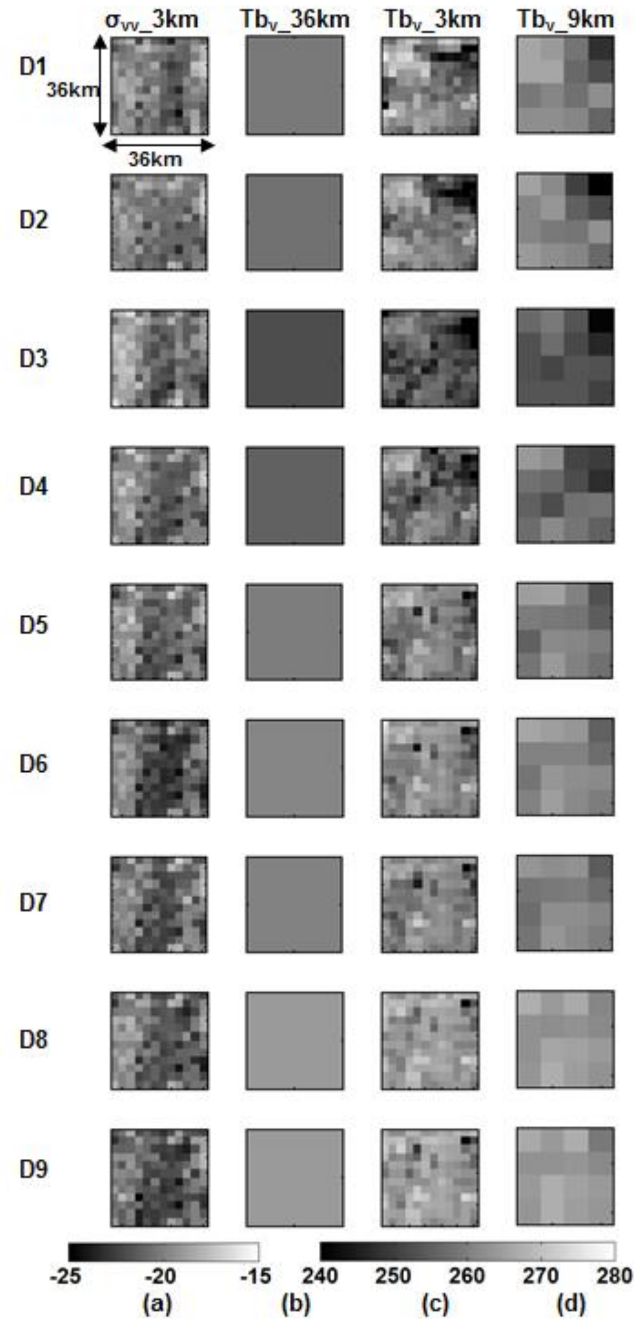

Figure 6-2: Example of the simulated SMAP prototype data from PLMR and PLIS observations across 9 days of SMAPEx-3 experiment (D1 to D9), with incidence angle normalized to 40˚: (a) backscatter (*σ*) at *vv*-polarization and at 3 km resolution aggregated from PLIS; (b) brightness temperature (*Tb*) at *v*-polarization and at 36 km resolution aggregated from PLMR; (c) *Tb* at *v*-polarization and at 3 km resolution aggregated from PLMR; (d) *Tb* at *v*-polarization and at 9 km resolution aggregated from PLMR.

6.3 Methodology

The baseline downscaling algorithm has been tested using satellite data set in **Chapter 4** as a preliminary study. However, due to radar observations were only available at *hh*-polarization from ASAR, this baseline algorithm was tested without taking into account the influence from vegetation conditions (see Eq. (4-4)), as backscatters at *hv*-pol are expected to reflect the vegetation characteristics to some degree according to Das et al (2014). Therefore, this study tests the complete baseline algorithm which includes backscatter at co- and cross-polarization. The algorithm is briefly described in the following paragraphs, while a complete description is available in Das et al. (2014).

In the following the naming convention of '*C*' (coarse), and '*F*' (fine) represents the *Tb* and/or σ at 36 km and 3 km, respectively. Implementation of this method requires a background *Tb* at *C* resolution, with the variation of *Tb* imposed by the distribution of fine scale σ within *C* modulated by $\beta(C)$ using the linear regression between *Tb* and σ at *C* resolution according to:

$$Tb_p(F_j) = Tb_p(C) + \beta(C) \times \{[\sigma_{pp}(F_j) - \sigma_{pp}(C)] + \Gamma \times [\sigma_{pq}(C) - \sigma_{pq}(F_j)]\}\ . \qquad (6\text{-}1)$$

where p indicates the polarization, including *h*- and *v*-pol; and *pp* means co-polarization of radar observations σ, including *hh* or *vv*-pol. Correlations between four different combinations of Tb_p and σ_{pp} have been analysed and will be presented in this chapter. $Tb_p(F_j)$ is the brightness temperature value of a particular pixel "*j*" of resolution *F*, and $\sigma_{pp}(F_j)$ is the corresponding radar backscatter value of pixel "*j*". In this study the value for $\sigma_{pp}(C)$ (in the unit of dB) was obtained by aggregating 10m resolution PLIS data (in power units) within the coarse footprint *C*, with $Tb_p(C)$ aggregated from 1km resolution PLMR observations (in Kelvin). Consequently, $\beta(C)$, which depends on vegetation cover and type as well as surface roughness, is assumed to be time-invariant and homogenous over the entire 36km pixel and that it can be obtained through the time-series of $Tb_p(C)$ and $\sigma_{pp}(C)$. Since the radar also provides fine resolution cross-polarization (*hv*-pol) backscatter measurements at resolution *F*, which is mainly sensitive to vegetation and surface roughness, the sub-grid heterogeneity of vegetation/surface characteristics within resolution *C* can be captured as $[\sigma_{pq}(C) - \sigma_{pq}(F_j)]$ by the radar, where *pq* represents *hv*-pol. This heterogeneity indicator is then converted to variations in co-polarization *pp* backscatter by multiplying a sensitivity parameter Γ for each particular grid cell *C* and season defined as $\Gamma = [\delta\sigma_{pp}(F_j) / \delta\sigma_{pq}(F_j)]_C$. In other words, the term $\Gamma \times [\sigma_{pq}(C) - \sigma_{pq}(F_j)]$ can be described as the projection of the cross-polarization sub-grid heterogeneity onto the co-polarization space, thus converting the information of vegetation and surface characteristics to the variation of co-polarization backscatter. This term is converted to brightness temperature through multiplication by $\beta(C)$ in Eq. (6-1).

Using Eq. (6-1) in this study, the 36 km resolution *Tb* are downscaled to 3 km resolution. The *Tb* at the intermediate resolution, i.e. 9 km, can be obtained by two methods: i) directly upscaling the 3 km downscaled *Tb* to 9 km through linear aggregation; or ii) first averaging the backscatter data (in power unit) from 3 km to 9 km, and subsequently use it in place of the fine resolution backscatter data in Eq. (6-1). Both methods are assessed in this study. Moreover, due to the high resolution backscatter provided by the SMAPEx airborne instruments, the 36 km resolution *Tb* can be downscaled to 1 km resolution using 1 km resolution σ, thus assessing the skill of this downscaling algorithm at three different scales: 1 km, 3 km and 9 km.

The downscaled *Tb* at fine resolution is heavily dependent on the quality of the overall radiometer data at coarse scale, the relative backscatter difference within the coarse grid, and the relationship with *Tb* as represented by the regression slope that is added to the background value. The performance of the downscaling algorithm at different resolutions is evaluated by comparing the downscaled *Tb* with the PLMR *Tb* data at 1 km, 3 km and 9 km resolution (aggregated from its original 1 km resolution), respectively, in order to assess the merit of this downscaling method in preparation for SMAP.

6.4 Results and Discussion

6.4.1 Robustness of the linear active-passive relationship

The robustness of the linear relationship between *Tb* and σ is tested in this section for the six possible polarization combinations (i.e. Tb_h and σ_{hh}, Tb_v and σ_{hh}, Tb_h and σ_{vv}, Tb_v and σ_{vv}, Tb_h and σ_{hv}, Tb_v and σ_{hv}), aiming to determine the best combination for estimating the parameter β. Consequently, the brightness temperature and backscatter observations from PLMR and PLIS were spatially aggregated to 3 km resolution, resulting in a total of 144 pixels within the study area, presenting different levels of vegetation heterogeneity. Examples of those data are shown in Figure 6-2(a) and (c).

The correlation coefficient R^2, used to quantify the correlation between Tb and σ for each 3 km pixel, was calculated using the entire time series of Tb and σ of each individual pixel. Results for the different polarization combinations are shown in Figure 6-3. Out of those, σ at *vv*-polarization showed the best correlation with Tb at both *h*- and *v*-polarization; these results are in good agreement with those presented in Das et al. (2011). Therefore, the relationships of σ_{vv} and Tb_v were used to estimate β at *v*-pol, while σ_{vv} and Tb_h were used to estimate β at *h*-pol, thus retrieving the downscaled Tb at *h*- and *v*-pol, respectively.

The influence of vegetation conditions on the correlation between Tb and σ was also investigated. The Radar Vegetation Index (RVI) was introduced as an indicator of the compound vegetation conditions (including vegetation water content, vegetation biomass etc.), which can be obtained directly from the radar observations using the different polarizations by

$$\mathrm{RVI} = 8 \times \sigma_{hv}/(\sigma_{vv} + \sigma_{hh} + 2 \times \sigma_{hv}), \tag{6-2}$$

where the radar backscatter values are in units of power (Kim and van Zyl, 2009). Figure 6-3 shows the average RVI values in each 3 km pixel calculated from the 9 days of radar observations aggregated to 3 km, in order to characterize the vegetation conditions. This was done assuming that vegetation conditions (and thus their associated RVI values) did not change significantly across the 3-week period. For this experiment, the standard deviation (in time) of the RVI was found to be less than 0.1 across the entire study area.

While the R^2 between Tb and σ was generally larger in the western two thirds than in the east of the SMAPEx area, the values of RVI were smaller in the west than in the east. Although it was expected that the highest correlation would be for low vegetation areas, the reason for the higher RVI in the east is due to some small forests in the area and trees along the Yanco River (see Figure 6-3). This indicates

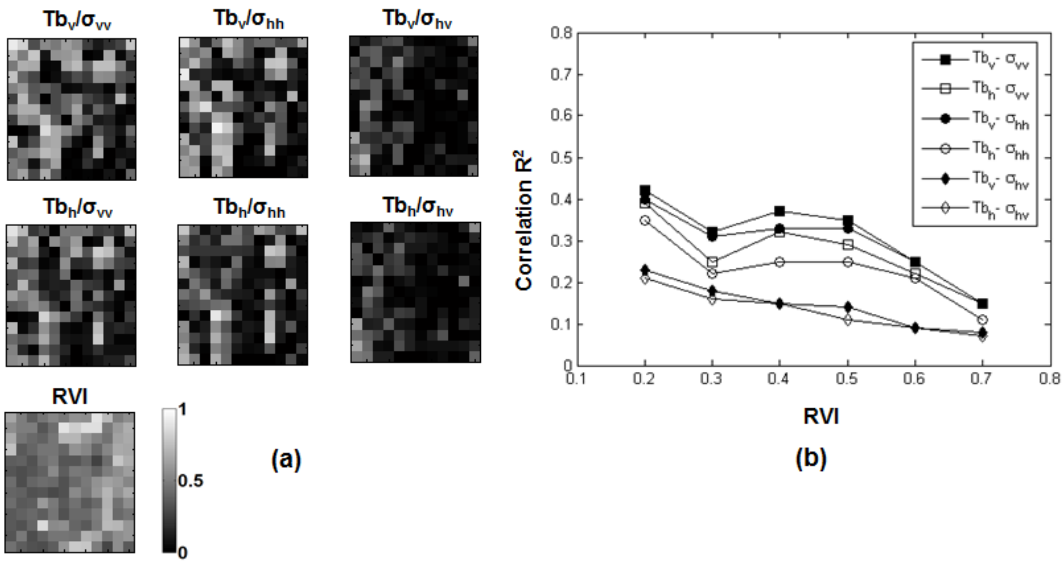

Figure 6-3: (a) Correlation between brightness temperature (*Tb*) and backscatter (*σ*) at different polarizations as shown, and spatial distribution of average Radar Vegetation Index (RVI) across the 9 days (both correlation coefficient and RVI are displayed on a scale from 0-1) at 3 km spatial resolution; (b) plot of these correlation coefficient between *Tb* and *σ* at different polarizations according to RVI.

that the downscaling algorithm performance will be poorer in areas with denser vegetation.

The sensitivity of *Tb* to changes in *σ* was analysed using the slope of the linear regression (parameter *β*) as a measure of quality. The relationship between *β* and RVI is displayed in Figure 6-4 and Figure 6-5, with Figure 6-4 showing the relationship between Tb_v and σ_{vv} anomalies under different vegetation conditions (i.e. different RVI), and the sensitivity parameter *β* estimated from observations of Tb_v and σ_{vv} within the entire study area. Both RVI and *β* were aggregated to 3 km resolution. These scatter plots show that: 1) Tb_v and σ_{vv} has a near-linear relationship; 2) the magnitude of *β* reduces as vegetation density increases, indicating that the sensitivity of brightness temperature to backscatter decreases, thus showing the dependence of sensitivity on the vegetation density. Figure 6-5 shows the parameter *β* and its associated Standard Deviation plotted as a function of the RVI. The Standard Deviation of *β* estimation is higher at the RVI extremes, mainly due to the limited counts of *Tb* and *σ* pairs for those values. According to the numbers of points in each plot, most of the points are within the range of RVI from 0.3 to 0.6, indicating

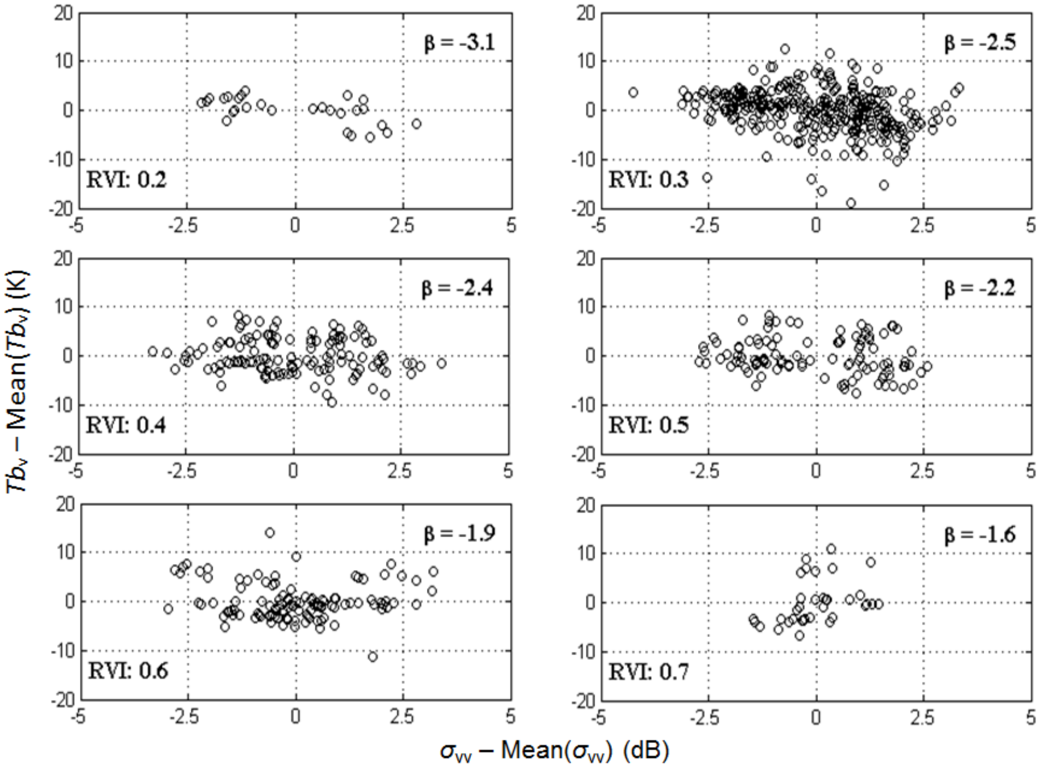

Figure 6-4: Relationship between brightness temperature at *v*-polarization (Tb_v) and backscatter anomalies at *vv*-polarization (σ_{vv}) at 3 km resolution, for different vegetation characteristics according to the Radar Vegetation Index (RVI) calculated from 3 km radar observations.

that vegetation with RVI 0.3-0.6 dominates this study area. Investigation of the relationship between RVI and the accuracy of the downscaling algorithm for a specific area is out of the scope of this study, but will possibly provide a direct method of estimating the downscaling performance globally from SMAP radar observations.

Given that σ_{vv} showed the best correlation with Tb_v, the sensitivity parameter β for performing the downscaling in this study has been estimated based on the combination of Tb_v and σ_{vv}. In this particular downscaling algorithm, β was estimated from Tb and σ data both aggregated to 36 km resolution, in order to align with the resolutions of SMAP. As a result, using the 9-days' time series of aggregated Tb_v and σ_{vv}, β over the entire area has been estimated as approximately -2.2 K/dB, with the average RVI across the whole area being around 0.5, aligning with the correlation between β and RVI as shown in Figure 6-4 and Figure 6-5. The same approach was

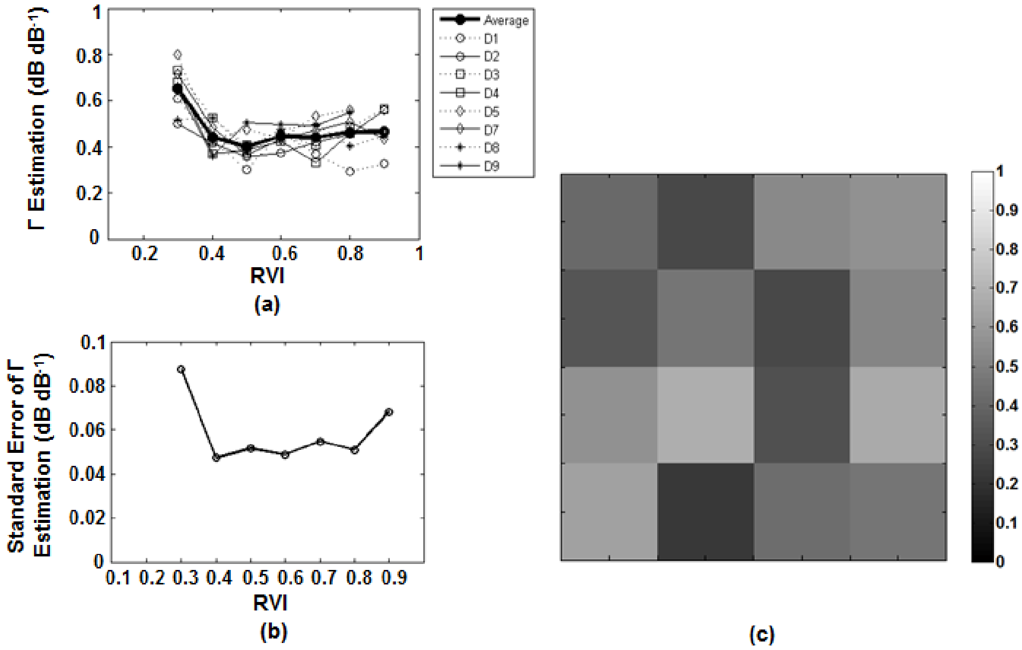

Figure 6-5: Estimation of parameter *Γ*: (a) *Γ* plotted as a function of the Radar Vegetation Index (RVI) on different days; (b) standard deviation of *Γ* estimation; and (c) example of *Γ* distribution over the entire study area on Day 9; each pixel has a size of 9 km × 9 km. (low: 0.3; high: 0.6)

applied to estimate β using Tb_h and σ_{vv}, for the downscaling of Tb at *h*-pol. In this case, similar trends for β estimation and its standard error were found with respect to RVI, as shown in Figure 6-5. However, the magnitude of β at different RVI is on average 1.2 K/dB higher than that estimated from Tb_v and σ_{vv}, implying that the sensitivity of Tb_h to σ_{vv} is higher than the sensitivity of Tb_v to σ_{vv}. Regardless of the actual variation of vegetation within the entire area, β was estimated as a single value across the 36 km area as outlined in the SMAP baseline active-passive algorithm. Based on this preliminary analysis of the relationship between RVI and β, it is suggested that a more detailed investigation of the spatial distribution of β within the 36 km area should be undertaken, including an investigation of a potential spatially varying β implementation in the SMAP baseline algorithm.

6.4.2 Estimation of *Γ*

The parameter Γ, i.e. the sensitivity of σ_{vv} to σ_{hv}, can be estimated using snapshots of σ_{vv} and σ_{hv} values at each pixel within a certain area. Since radar backscatter σ at *hv*-pol

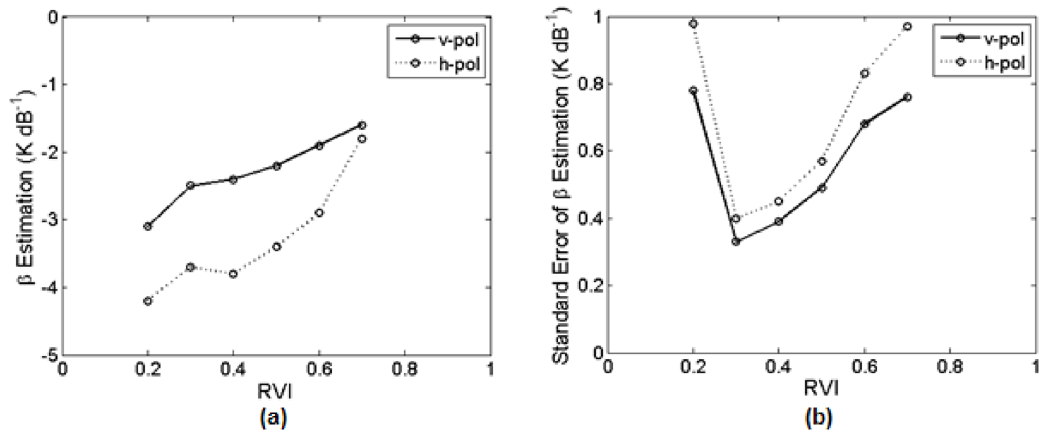

Figure 6-6: Dependency of regression parameter *β* (a) and associated Standard Deviation (b) of estimation from Radar Vegetation Index (RVI) at 3 km resolution. The *β* at *h*- and *v*-polarization was estimated using backscatter (*σ*) at *vv*-polarization for brightness temperature (*Tb*) at *h*- and *v*-polarization.

is more related to the vegetation canopy than to the soil, the distribution of σ_{hv} across the entire area can be used to characterize the heterogeneity of vegetation conditions in that area. Therefore, downscaling results can be improved by including the influence of vegetation on the backscatter observation, by converting the σ_{hv} variation within the entire area to σ_{vv} variation, by multiplying with the sensitivity Γ.

In order to obtain an estimate for the parameter Γ, the study area was divided into 16 sub-areas of 9 km by 9 km in size, and the value of Γ calculated using the snapshots of all σ_{vv}-σ_{hv} pairs at 1 km resolution contained within each of those sub-areas, allowing an analysis of the relationship between estimation of Γ and RVI. Accordingly, the day-to-day variation and average of Γ with respect to RVI is shown in Figure 6-6, together with an example of the distribution of Γ at each 9 km sub-area across the entire study area on Day 9 (23rd September, 2011). It is shown that for RVI values ranging from 0.4 to 0.9 the estimation of Γ is similar, on the order of 0.45, while for RVI values less than 0.4, Γ is much higher, indicating that the sensitivity of σ_{vv} to σ_{hv} increases when the vegetation cover reduces. Again, larger standard deviations were found for both extremes due to low counts of pixels.

6.4.3 Accuracy of downscaling

According to the baseline approach the downscaled brightness temperature at fine resolution are a function of the background *Tb* value plus a variation of *Tb* within the entire area derived from the variation of the backscatter from the mean. In this study, the background *Tb* is taken as the aggregated 36 km *Tb* from PLMR, and the variation of *Tb* at higher resolution is characterized by the variation of σ_{vv} from PLIS observations, aggregated to the downscaling resolution. The influence of vegetation is then deduced using σ_{hv}, due to its strong correlation with vegetation conditions. Consequently, the downscaled *Tb* results were retrieved at resolutions of 1km, 3 km and 9 km, either from aggregating the 1 km resolution downscaled *Tb* to 3 km and 9 km resolution respectively, or from first aggregating the 1 km resolution radar observations to 3 km and 9 km before using them to disaggregate the 36 km *Tb*. Both methods were applied and showed similar results; results shown in this chapter are based on the former method. Prior to applying the downscaling algorithm, the main water body in the far north-eastern section of the area, and some irrigated cropping areas within the western part of the regional area, were removed (these areas collectively represented approximately 1% of the entire study region) to reduce the influence of surface water on the resulting downscaling accuracy.

Based on the estimation of β at *h*- and *v*-polarization and the day to day matrix of Γ estimates derived in the previous sections, the baseline downscaling algorithm performance was evaluated for each of the nine days of SMAPEx airborne acquisitions. In order to analyse the influence of vegetation characteristics on the resulting downscaled *Tb*, the downscaling algorithm was applied in two scenarios: in scenario "A1", the vegetation heterogeneity across the study area was ignored; in scenario "A2", the vegetation heterogeneity across the study area was taken into account. In other words, A1 was characterized by setting Γ=0, while A2 used $\Gamma \neq 0$ in Eq. (6-1). In the following the results of the downscaling is compared amongst the two scenarios.

Downscaling results on each day of SMAPEx-3 are shown in Table 6-1 for different resolutions and polarizations. It is noted from Table 6-1 that the downscaled results at *v*-polarization had relatively lower RMSE than those at *h*-polarization, likely due to

Table 6-2: Accuracy of the SMAP baseline downscaling algorithm. Root Mean Square Error (RMSE) between downscaled brightness temperature (*Tb*) and reference *Tb* is shown for the entire study area across the 9-days (D1 to D9) with respect to polarization and resolution of the final downscaled product; results based on scenario A1 (Γ=0) and scenario A2 ($\Gamma \neq 0$) are shown.

Downscaling resolution (km)		D1		D2		D3		D4		D5		D6		D7		D8		D9		Average	
		h	*v*	*h*	*v*	*h*	*v*	*h*	*v*	*h*	*v*	*h*	*v*	*h*	*v*	*h*	*v*	*h*	*v*	*h*	*v*
1	A1	11.7	9.1	10.4	8.2	10.5	7.9	10.6	8.3	9.1	6.8	9.0	6.7	8.1	6.0	8.4	6.2	8.2	5.8	9.5	7.2
	A2	10.5	8.4	9.5	8.0	9.0	7.1	9.2	8.0	8.1	6.2	8.1	6.1	6.3	5.2	7.0	5.6	6.6	5.1	8.2	6.6
3	A1	9.1	7.0	7.7	6.1	7.6	5.6	7.6	5.9	5.8	4.4	6.2	4.3	5.1	3.6	5.4	3.8	5.2	3.6	6.6	4.9
	A2	8.6	6.7	7.3	6.0	5.6	4.6	6.8	5.5	4.9	4.2	5.2	4.1	4.2	3.3	4.2	3.3	3.3	3.2	5.5	4.5
9	A1	6.0	4.7	4.7	3.9	4.9	3.5	4.9	3.8	3.2	2.5	3.3	2.4	2.5	1.8	3.2	2.2	2.9	1.8	3.9	2.9
	A2	5.8	4.5	4.6	3.7	3.9	3.1	4.0	3.5	2.5	2.4	2.4	2.1	1.5	1.5	2.0	1.7	1.9	1.5	3.1	2.6

Table 6-1: Downscaling algorithm performance in terms of Root Mean Square Error (RMSE) when using backscatter at *hh*- and *vv*-polarizations, together with the RMSE difference between these two polarizations.

Downscaling resolution (km)	σ_{vv}		σ_{hh}		Difference	
	h	*v*	*h*	*v*	*h*	*v*
1	8.2	6.6	9.1	7.2	-0.9	-0.6
3	5.5	4.5	6.2	5.0	-0.7	-0.5
9	3.1	2.6	3.3	3.3	-0.2	-0.2

the better correlation between σ_{vv} and Tb_v than between σ_{vv} and Tb_h. Moreover, there is an obvious reduction of RMSE at both polarizations when applied to a larger scale, e.g. from 1 km to 3 km and 9 km respectively, which can be attributed to the reduction of random (white) noise following the aggregation of the backscatter data.

Apart from resolution and polarization, the RMSE was further reduced when taking into account the variation of vegetation across the entire area, confirming that the Γ term in Eq. (6-1) can be used to compensate the influence of vegetation conditions to some degree, thus yielding a more accurate finer resolution brightness temperature product. Quantitative results are provided in Table 6-1, showing that the average RMSE of the 9 days at *v*-polarization was lower by 1-2 K than at *h*-polarization, and decreased by approximately 5 K when aggregating from 1 km to 9 km. As before, after considering the influence of vegetation heterogeneity (scenario A2 with $\Gamma \neq 0$), the RMSE of downscaled *Tb* had an improvement of 1.2 K at *h*-polarization and 0.5 K at *v*-polarization over the results based on the assumption of a homogeneous vegetation (scenario A1, Γ=0). Moreover, during 5 out of 9 days the RMSE was found to be around 2.4 K at 9 km resolution, which is within the target error of the SMAP mission (2.4 K when the vegetation water content is less than 5 kg/m^2), confirming that the baseline downscaling algorithm has the potential to retrieve medium-resolution brightness temperature with an error of around 2.4 K over heterogeneous areas.

In order to confirm that the use of σ_{vv} is more efficient than σ_{hh}, as suggested from the correlation analysis between *Tb* and σ, an additional test was performed using coarse resolution *Tb* and fine resolution σ_{hh} to retrieve *Tb* at scales of 1 km, 3 km and 9 km. The performance levels of the algorithm using σ_{vv} and σ_{hh} are presented in Table 6-2, showing that the RMSE based on σ_{vv} is around 0.2 to 0.9 K lower than that based on σ_{hh}, confirming the results from Figure 6-3 where there was a stronger correlation of σ_{vv} to *Tb* than σ_{hh}.

Examples of downscaled *Tb* maps are shown in Figure 6-7 for Day 9 at 1 km, 3 km and 9 km resolution, alongside the reference data from PLMR, and the pixel-by-pixel *Tb* difference between downscaled and reference values. It is noted that the downscaling errors are generally larger in the western part of the study area than the central section, which is mainly due to the western part being dominated by irrigated and dry-land cropping areas, while the central area is largely covered by grassland. A consequence of the large heterogeneity of the cropping areas was a relatively large RMSE in those areas, as highlighted by the RMSE behaviour from west to east of the entire region in Figure 6-8. Dependence of RMSE for the 36 strips (each with 1 km width when progressing from west to east and having 36 km length in the north-south direction) covering the SMAPEx study area is displayed in Figure 6-8. Overall, the RMSE of the central area, the dominantly grassland area between distance 18 km to 28 km, is around 2 K lower than elsewhere.

As shown in Figure 6-3 to 6-5, β estimation should be lower than -3 K/dB (at *v*-pol) and -4 K/dB (at *h*-pol) in the western area and should be higher than -2 K/dB (at *h*- & *v*-pol) in the eastern area due to the variation in RVI across the entire region. However, since the constant value of β from 36km *Tb* and σ is used in this study, which is -2.2 K/dB (at *v*-pol) and -3.4 K/dB (at *h*-pol), there is an under-estimation

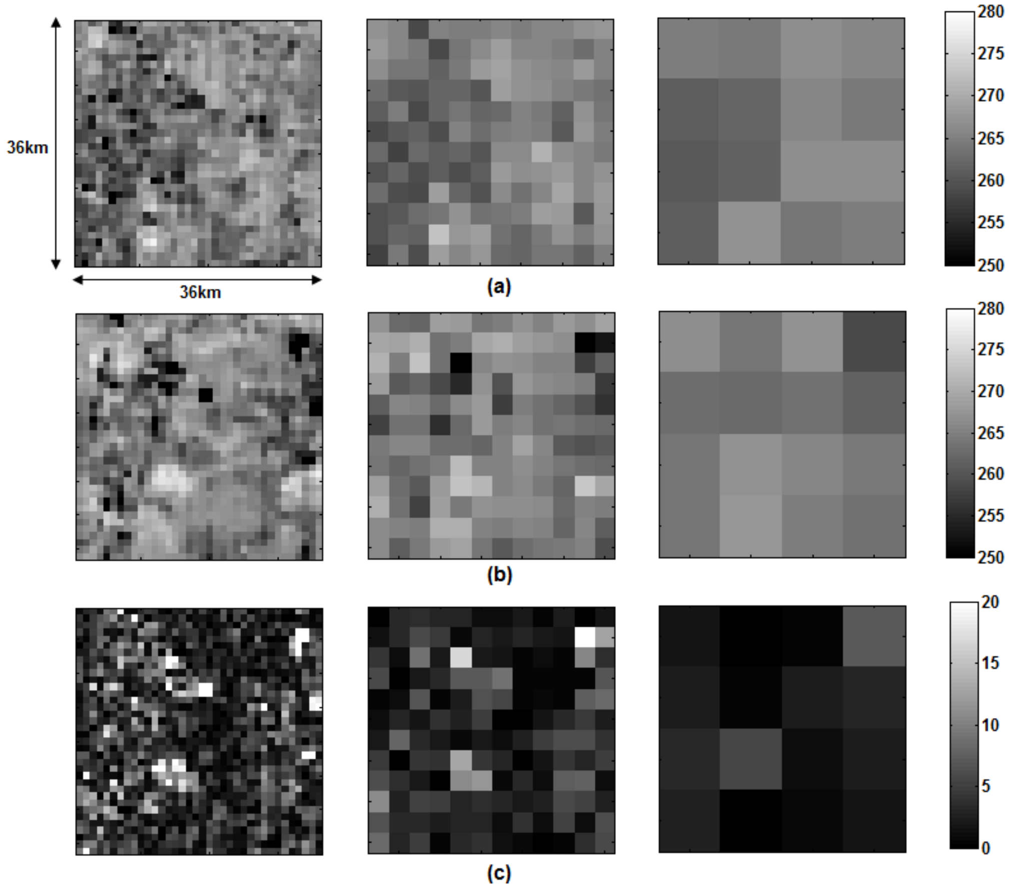

Figure 6-7: An example of downscaling results on SMAPEx-3 Day 9 (23rd Sept., 2011): (a) Downscaled brightness temperature (*Tb*) at *v*-polarization for 1 km, 3 km & 9 km resolution; (b) Reference *Tb* at *v*-polarization for 1 km, 3 km & 9 km resolution; and (c) Absolute difference between downscaled *Tb* and reference *Tb* of each 1 km, 3 km & 9 km resolution pixel.

in the west and over-estimation in the east, which is directly related to the magnitude of β variation from the nominal value used and therefore further influencing the accuracy of this downscaling algorithm. Moreover, the RMSE in the east is relatively high, due to the influence from the large areas of woodland along the river which runs approximately south to north in that part, and some other areas of dense forest.

A further evaluation of the skill of this particular downscaling algorithm was through the correlation between downscaled and reference *Tb* at 9 km resolution (Figure 6-9 and Figure 6-10). While these two black dashed lines represents RMSE less than 2.4 K (the SMAP target), the outer two black solid lines represent RMSE less than 4 K (the SMOS target). It is noted from Figure 6-9 and 10 that more than 93% of the

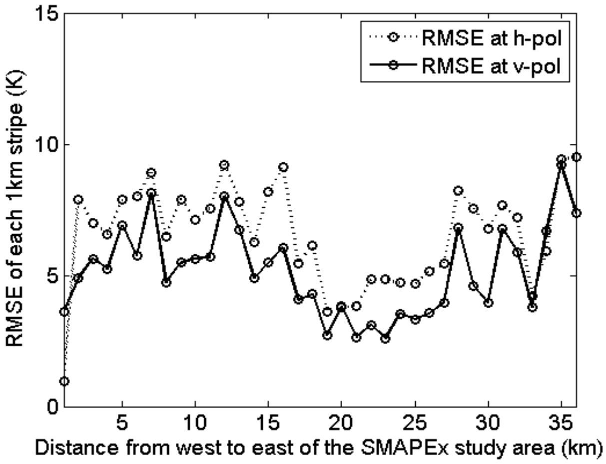

Figure 6-8: Downscaling Root Mean Square Error (RMSE) at 1 km resolution for each strip, having 36 km length in north-south direction and 1 km width in west-east direction, starting from the west of the SMAPEx study area and progressing to the east, on Day 9 (23rd September, 2011); cropping area in the west, relatively homogeneous grassland area in the middle, and woodland along the river and some forest in the east.

points from D3 ("D" represents "Day") to D9 are within the SMOS target range, and five of them (from D5 to D9) have more than 90% of points within the SMAP target range, showing that the baseline downscaling algorithm can provide accurate *Tb* at 9 km.

Nonetheless, the results of the first days i.e. D1 to D4 displayed relatively poor performance when compared to the later days. In particular, D1 and D2 contain significant noise levels. One possible reason is attributed to increased heterogeneity in near surface soil moisture due to the heavy rainfall events in the north-eastern part of the study area at the beginning of SMAPEx-3 as shown in Figure 6-1 and Figure 6-2(c), subsequently resulting in more heterogeneous radiometer and radar observations. It is shown in Figure 6-9 and Figure 6-10 that D1 to D4 had a higher standard deviation of *Tb* (reference *Tb*) when compared to the other days. Since *Tb* is more sensitive to the immediate soil moisture changes due to the rain in this region, the value of *Tb* drop according to soil moisture increase is more significant than the radar backscatter changes, as the latter is more influenced by the vegetation cover and consequently less sensitive to the soil moisture changes. Consequently, the sensitivity of backscatter to *Tb* change decreases, resulting in an obvious difference in

β for the area subjected to rainfall when compared with the other drier areas, which would have dominated the derivation of the β value used. This is underlined by the RMSE in the north-eastern part (area R) of the study area being around 3 K higher than throughout the remaining area (at 3 km resolution), impacting the overall large RMSE for that day, as shown in Figure 6-11. In addition, the average RVI of area R is ~0.56, which is approximately 0.15 higher than the average RVI of the entire area, further affecting the correlation between *Tb* and σ in this particular area. The reason is that higher RVI is a consequence of denser vegetation and therefore more influence of the vegetation on the radar observations, and accordingly a higher error when downscaling due to the lower correlation between *Tb* and σ at higher RVI values (see Figure 6-3). Therefore, both denser vegetation and more heterogeneous wetness conditions associated to rainfall events have worked together to result in the higher errors on D1 to D4. The influence from the rain event reduced during the dry-down, especially after D4, as shown through the decrease in RMSE from D5 onwards.

A comparison between this downscaling algorithm and the minimum performance was also conducted. The minimum performance was defined as a uniform *Tb* according to the value of *Tb* at 36 km resolution. In this case, the average RMSE across all 9 days was around 4.8 K at *h*-pol and 4.2 K at *v*-pol at 9 km resolution, being approximately 1.6 K higher than for the baseline downscaling algorithm.

The above analysis on the accuracy of the downscaling algorithm was done after removing the water-bodies and irrigated fields, which collectively represented approximately 1% of the entire SMAPEx study area. The downscaling performance was also evaluated when including the water bodies that had previously been masked out in the aggregation procedure, in order to simulate more realistic SMAP data (as many water bodies will not be reliably identified for masking). Consequently, this allowed the effect of relatively small water bodies on the accuracy of the downscaling approach to be quantified. Without removing the water-bodies, the average RMSE of all nine days at 9 km resolution increased to 3.6 K and 3.4 K at *h*- and *v*-polarization, respectively, which is approximately 0.7 K higher than results with the water-bodies accurately removed. Therefore, when applying the baseline downscaling algorithm to

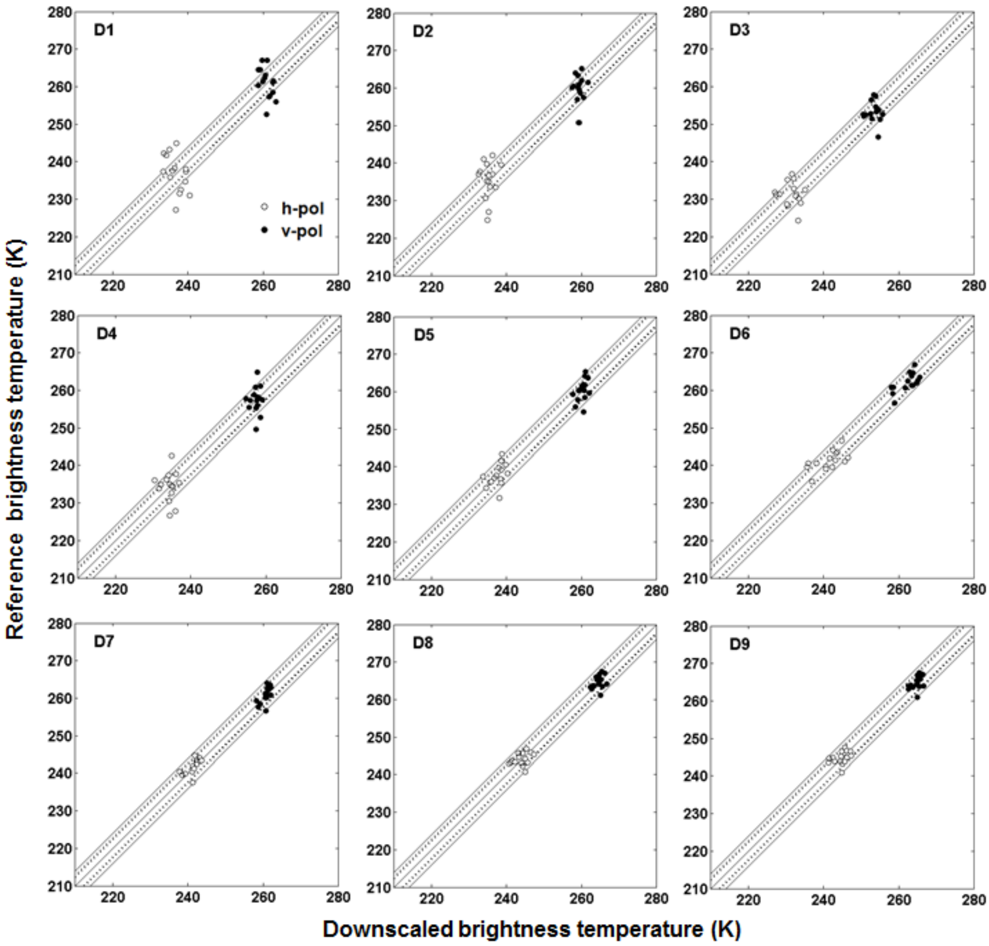

Figure 6-9: Scatter plots of downscaled and reference brightness temperature (*Tb*) at 9 km resolution on each of SMAPEx-3 Day 1 to Day 9, at *h*-pol (open circles) and *v*-pol (solid circles); inner black solid line: RMSE is 0 K; two black dashed lines: RMSE=2.4 K (SMAP *Tb* target accuracy); outer two black solid lines: RMSE=4 K (SMOS *Tb* target accuracy).

an area that includes more than 1% of water-bodies the downscaling error would be even larger.

To account for any day-to-day soil temperature variation, β was also estimated using the emissivity and σ, with emissivity calculated as *Tb* divided by soil temperature on that day. The new estimate of β was then multiplied by the soil temperature, before substituting for the previous value of β based on *Tb* and σ. However, the average RMSE of downscaling *Tb* based on this new estimation of β was 3.4 K at *h*-pol and 2.7 K at *v*-pol at 9 km resolution, being only slightly different to previous results.

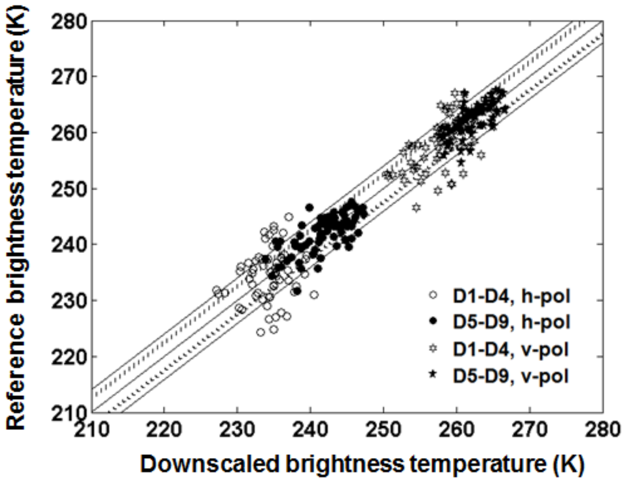

Figure 6-11: Scatter plots of downscaled and reference brightness temperature (*Tb*) at 9 km resolution for all SMAPEx-3 acquisitions (Day 1 to Day 9), at *h*-pol and *v*-pol. Solid circles and stars represent data from SMAPEx-3 Day 5 to Day 9, while the open circles and stars represent data from SMAPEx-3 Day 1 to Day 4. Inner black solid line: RMSE is 0 K; two black dashed lines: RMSE=2.4 K (SMAP *Tb* target accuracy); outer black solid lines: RMSE=4 K (SMOS *Tb* target accuracy).

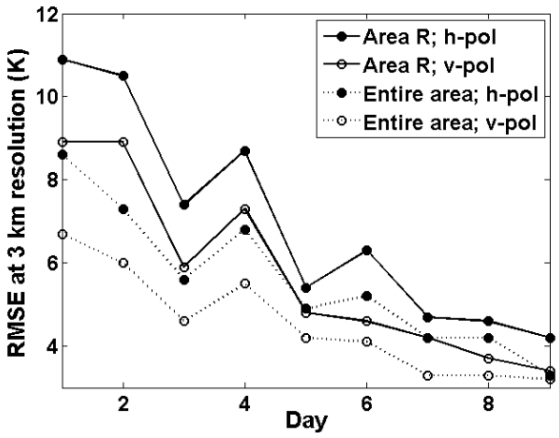

Figure 6-10: Comparison between the Root Mean Square Error (RMSE) of the north-eastern (area "R") of the SMAPEx study area, and RMSE of the entire study area. Calculations are for 3 km resolution at both polarizations across 9 days.

6.4.4 Reliability of baseline downscaling algorithm

In this study, the accuracy of downscaling results was primarily determined by the parameter β as shown in Eq. (6-1). The main limitation of the downscaling method introduced in Das et al, 2014 is the assumption of a constant β across the entire study area. The parameter β, used to denote the sensitivity of Tb to σ, in reality varies with respect to the land surface conditions, as shown in Figure 6-4 and Figure 6-5. Therefore, the assumption of a constant value of β could not represent the real distribution of β due to the heterogeneity of the study area. For example, if the study area was entirely covered by homogenous grassland, then the use of a single β would be more appropriate for use in downscaling. However, as shown in the above results, the variation on land cover types across the entire site, or soil moisture heterogeneity due to raining events in some particular areas, or some water-bodies, or surface roughness, or vegetation evolution due to different seasons would result in different value of β across the site.

As β was estimated from time-series of Tb and σ at 36 km, more accurate regression could be obtained from a longer time period so as to make it statistically significant. However, the vegetation and roughness conditions are changing as time goes on, which will result in different β estimates through time. Therefore, a moving window of β estimation should be adopted when applying the downscaling algorithm to a long time period. This is not done in this study but should be acknowledged for future application.

6.5 Chapter Summary

The objective of this study was to test the robustness of the baseline downscaling approach proposed for the SMAP mission, using a simulated SMAP data stream from the SMAPEx field campaign in Australia. The errors associated with the downscaling algorithm were assessed for several resolutions of the final downscaled product and at both *h*- and *v*- polarizations. While it was shown that the baseline downscaling algorithm has the potential to fulfil the accuracy requirements of SMAP, it was also shown that the accuracy of the downscaling approach was primarily determined by the correlation between Tb and σ, which seemed to differ according to vegetation characteristics across the SMAP sized pixel. Moreover, it was found that an improvement in the parameterization of β and Γ may be obtained through use of the RVI. Consequently, the next two chapters undertake a more detailed exploration of the impact that homogeneity in land surface characteristics may have on the applicability of the baseline downscaling algorithm of SMAP.

7 Effect of Land Cover Type

This chapter assesses the impact of land cover type on the baseline downscaling algorithm performance. The previous chapter found that downscaling error from the baseline algorithm was higher in the cropping areas than for the grassland areas. It was therefore hypothesised that this is due to both the more heterogeneous conditions in the cropping areas and a different physical relationship between radar backscatter and radiometer brightness temperature under these conditions. Consequently, this chapter breaks the single 36 × 36 km SMAPEx area into sixteen 9 km × 9 km sub-areas and classifies them according to their dominant land cover type. The different relationships and baseline downscaling algorithm behaviour is then assessed according to the respective land cover type. The work in this chapter has been accepted for publication (Wu et al., In Press-b).

7.1 Background

The baseline downscaling algorithm for SMAP was studied in **Chapter 6** using airborne observations from the SMAPEx-3 field campaign. This was by necessity applied to a single SMAP radiometer-sized site without differentiating the land cover types across the entire site. That study was found to yield mediocre results, believed to be due to the diversity in land cover. Thus a more extensive assessment of this baseline algorithm over a variety of land cover types was proposed in order to investigate the influence of different land cover on the resulting downscaling performance, and the possible downscaling algorithm improvement if a spatially variable β were to be implemented.

The SMAPEx study area is composed of land covers including irrigated and non-irrigated cropping fields, grasslands, small forests, riverside trees and some water bodies. Rather than applying the downscaling algorithm to the entire area as a single SMAP pixel, as done in (Wu et al., In Press-a), the objectives of this study are to: i) evaluate the accuracy of the SMAP baseline downscaling algorithm with respect to different land cover types by dividing the entire SMAPEx site into distinct 9 km sub-regions according to the dominant land cover; and ii) assess the assumed linear relationship between brightness temperature (*Tb*) and backscatter (σ) and how β varies with land cover type. Understanding the influence of surface heterogeneity on the resulting downscaling performance is important for its application to the forthcoming SMAP mission at global scale.

7.2 Data Set

Data used in this study were collected from the third field campaign (SMAPEx-3) which was conducted during 5-23rd September 2011. The regional flights provided a 9-day time series of SMAP-like observations with a 2-3 days revisit time over a 36 km × 38 km area, equivalent to one pixel of the SMAP EASE grid at 35° S latitude; for application in this study data were processed to 1 km, 3 km and 9 km spatial resolution for *Tb* and 1km spatial resolution for σ. Full details of SMAPEx field campaign has been described in **Chapter 3**, and the airborne data processing to match SMAP observations are given in **Chapter 5**, so only the details pertinent to this study are reported here.

Whereas in the case of SMAP the 36 km resolution *Tb* will be downscaled to 9 km resolution using 3 km resolution σ, in this study 9 km resolution *Tb* pixels aggregated from the original 1 km resolution PLMR data are downscaled to 3 km resolution using 1 km resolution σ. The reason for choosing 9 km focus areas with 9 km *Tb* and 1 km σ was to test the downscaling algorithm over a larger variety of land cover than that possible when considering the whole SMAPEx site as a single SMAP pixel, as done in previous chapter. Moreover, the choice of 3 km as the final downscaling resolution was to maintain a similar resolution ratio between radiometer and radar observations and the downscaled product, i.e. approximately 9:1:3, as for SMAP. By distinguishing the land cover type of each 9 km × 9 km pixel, this study provides a more in-depth testing of the baseline downscaling algorithm, while also providing performance statistics of the baseline downscaling algorithm with respect to the different land covers of each 9 km pixel.

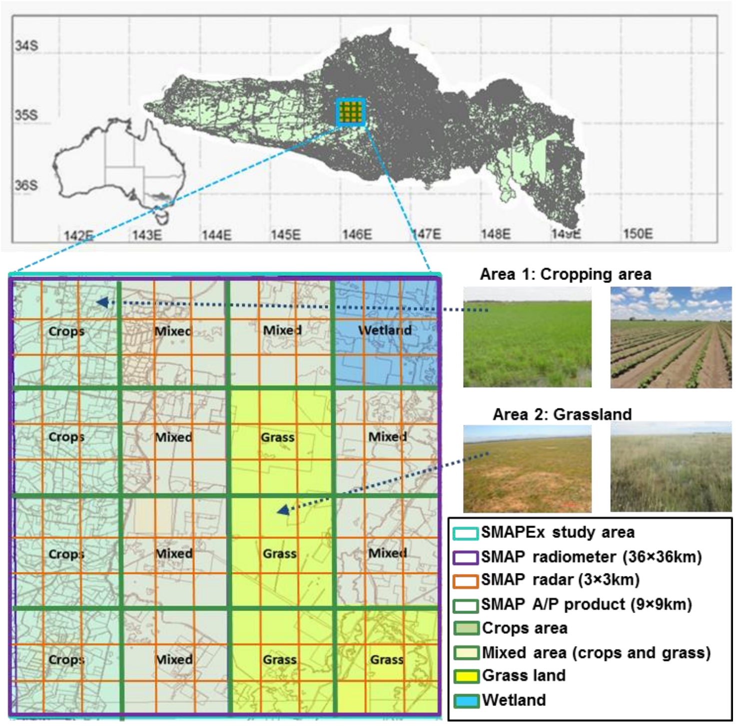

Figure 7-1: Overview of the SMAPEx site showing the SMAP radiometer-pixel sized study area (approximately 36 km × 36 km), and the sixteen 9 km × 9 km areas used in this study, classified according to four dominant land cover types (crop, grassland, mixed crop/grassland, and wetland).

The various 9 km × 9 km areas and their dominant land cover type are shown in Figure 7-1 whereby: i) four pixels are mostly occupied by crops (a mix of bare soil, barley and wheat at intermediate growth stage and mature canola fields); ii) four pixels with grasslands; iii) seven pixels with mixed land cover types, approximately 50% crop and 50% grassland; and iv) one pixel with a 5 km^2-sized water-body, termed here as "wetland". Before implementation of this algorithm, water-bodies were removed in all pixels except the wetland pixel, so as to analyse the downscaling performance according to different land cover types but without the influence from water-bodies. Additionally, inclusion of the wetland allows the water-body impact on the downscaling accuracy to be investigated.

7.3 Methodology

The baseline downscaling algorithm has been already described in Chapter 6, as shown in Eq. (6-1). The only difference is in this study '*C*' and '*F*' represents the

PLMR Tb (9 km) and PLIS σ (1 km) respectively. Consequently, β(C), which depends on vegetation cover and type as well as surface roughness, is assumed to be time-invariant and homogenous over the each 9 km pixel and that it can be obtained through the time-series of Tb and σ at 9 km resolution. Using Eq. (6-1), downscaled Tb at 3 km resolution in this study can be obtained in two ways: (i) by aggregating Tb downscaled to 1 km to 3 km resolution, or (ii) by directly downscaling to 3 km resolution. Having been studied in (Wu et al., In Press-a), the two methods provide very similar results and also showed that σ at *vv*-pol has a better correlation with Tb than σ at *hh*-pol, and therefore σ at *vv*-pol was used in this study to estimate β and applied to Eq. (6-1).

7.4 Results and Discussion

7.4.1 Estimation of β and Γ

The robustness of the linearity assumption between Tb and σ is tested in this section, as well as the spatial variation of the slope parameter β according to land cover type. It is assumed in the SMAP mission that the parameter β relating Tb and σ is constant across each 36 km pixel, while in this study the sensitivity parameter β is assumed constant across each 9 km pixel and estimated using the 9 day time series of Tb and σ at 9 km resolution. In terms of linearity between Tb and σ for different polarizations, it has been previously found that σ at *vv*-pol had the best correlation with Tb at *h*- and *v*-pol at 36km resolution (Wu et al., In Press-a). This was confirmed in this study by using Tb and σ at 9 km resolution, with respectively σ at *hh*-pol having a 0.1 lower correlation coefficient (R) and σ at *hv*-pol having a 0.25 lower R, than σ at *vv*-pol. Therefore, in accordance with the SMAP ATBD (Entekhabi et al., 2012)) and Das et al (Das et al., 2014) the σ at *vv*-pol was chosen to downscale Tb in this study.

The parameter β and associated correlation coefficients between Tb and σ for the different land cover types are presented in Figure 7-2. The β (unit K/dB) for each land cover type was calculated by merging all sub-areas with the same land cover. The β_h was estimated from Tb_h and σ_{vv} while β_v was estimated from Tb_v and σ_{vv}. It is noted from Figure 7-2 that the sensitivity of Tb to σ was higher in the wetland (blue dots) than other land cover type, likely due to the higher scattering properties of the

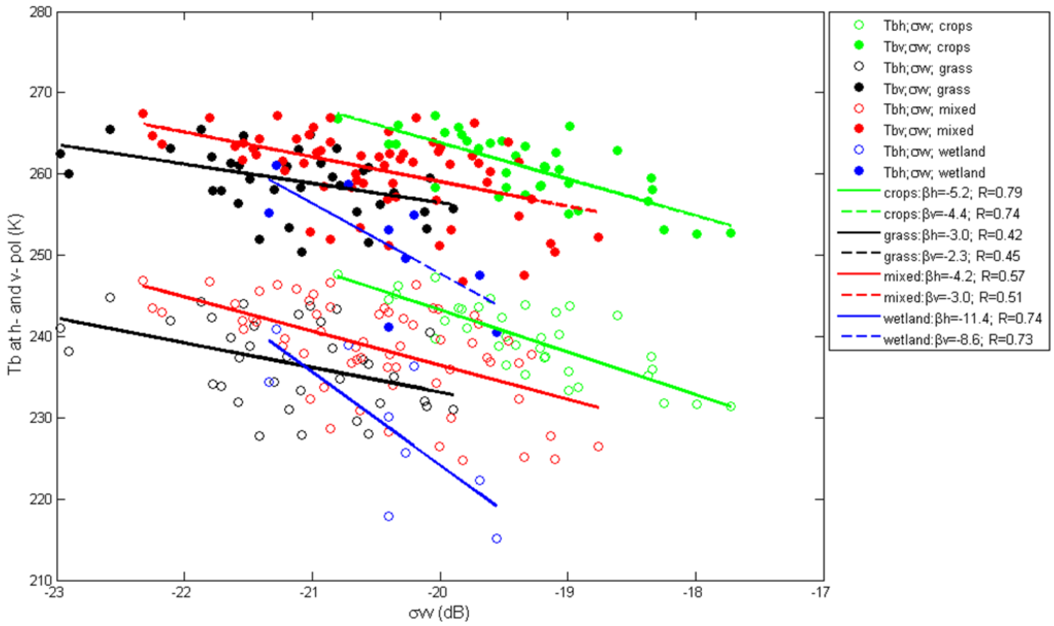

Figure 7-2: Plot of *β* estimation using a 9 day time-series of *Tb* at *h*- and *v*-pol and σ_{vv} for the four different land covers. Also shown is the correlation coefficient (*R*). The *β* for each land cover was calculated by merging all the sub-areas with the same land cover type.

water-body contained in the wetland. These *β* values, ranging from -8.6 to -2.3 at *v*-pol and -11.4 to -3.0 at *h*-pol according to land cover type can be compared to the *β* value at 36km resolution that was estimated around -2.2 at *v*-pol and -3.4 at *h*-pol from (Wu et al., In Press-a). According to these results, the assumption of a constant *β* within an entire SMAP 36 km pixel may be a limitation when applying the downscaling algorithm to SMAP data because of the heterogeneity across SMAP sized pixels. For example, the different vegetation types, vegetation water content, and surface roughness etc., which impose a different sensitivity of *Tb* to *σ*, are all considered to have the same sensitivity (*β*) across each coarse resolution pixel.

An important consideration in estimating *β* is the trade-off between robustness of the regression due to the number of data points used in the estimation, and the impact of seasonality due to the length of the data window that is used. It is expected that using more data would attribute to a more accurate linear regression, but the 2-3 day repeat would result in a longer window that could also introduce error due to the change of land cover condition. The value of *β* varies according to different seasons (Wu et al., 2011). Consequently, a temporal moving-window period was adopted over which vegetation phenology and surface characteristics can be considered constant (Das et al., 2014). In this study, data over a 3 week period were used for deriving a relatively high fidelity algorithm parameter. While the possibility of a temporal change in β due to changes of land cover conditions is acknowledged, this length was found to give the best results and is consistent with that used in other studies.

The parameter Γ used to denote the sensitivity of σ_{vv} to σ_{hv} was estimated from snapshots of σ_{vv} and σ_{hv} values at each 3 km pixel within the entire 9 km coarse scale pixel. In this study, 9 pairs of σ_{vv} and σ_{hv} in each 9 km area were used to calculate Γ for each 9 km area within the SMAPEx site, and for each day of data. The range of Γ due to heterogeneity in vegetation was from 0.2 to 0.6. The average values of Γ were 0.34(±0.06 standard deviation) for grassland, 0.43(±0.14) for the mixed area, 0.46(±0.26) for wetland and 0.52(±0.13) for the cropping area. Since radar backscatter σ_{hv} is more related to vegetation conditions than to soil moisture, the variation of σ_{hv} across the whole area can therefore reflect the heterogeneity of vegetation conditions to some extent, which can be further converted to σ_{vv} through the sensitivity Γ and thus reduce the influence of vegetation on the PLIS observations.

7.4.2 Downscaling results

Downscaling results at fine resolution ("*F*" in Eq. (6-1)) are based on the background *Tb* plus the variation of *Tb* within the entire area. The background *Tb* used here came from the aggregated 9 km *Tb* from PLMR, and the variation of *Tb* from 1km radar observations at *vv*- and *hv*-pol, together with the sensitivity parameter β and parameter Γ as estimated above. The 9 km *Tb* were downscaled to 1 km and 3 km resolutions in order to evaluate the performance of this downscaling algorithm at different resolution levels. Consequently, the baseline downscaling algorithm was applied to the 9 day data set, and the resulting downscaled *Tb* at both 1 km and 3 km resolution across the 9 days compared with the reference *Tb* from PLMR at the same resolutions.

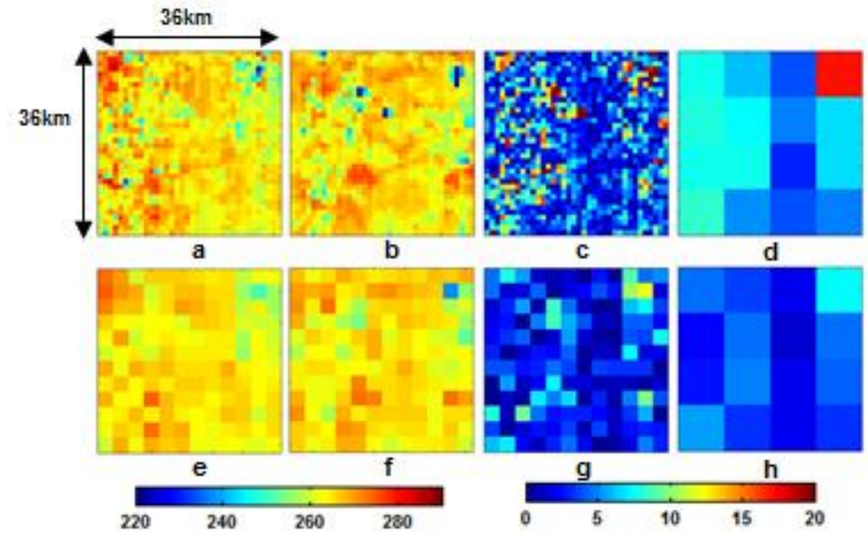

Figure 7-3: An example of downscaling results on Day9 (23rd September 2011): a. Downscaled *Tb* at *v*-pol, 1 km resolution; b. PLMR observed *Tb* at *v*-pol, 1 km resolution; c. Absolute difference between a and b; d. RMSE of 1 km resolution data in each 9 km pixel; e to h. as for above but at 3 km resolution.

Figure 7-3 shows an example of downscaling for *v*-pol at different resolutions on Day 9 (23rd September, 2011), including the downscaled *Tb*, reference *Tb*, and their absolute difference, as well as the RMSE for each 9km pixel. More statistics across the 9 days are provided in Table 7-1 with respect to different land covers, different resolutions and different polarizations. By combining the land classification from Figure 7-1 with the RMSE at 1 km and 3 km resolution from Table 7-1, it was found that the grassland area had the best downscaling performance due to its relative homogeneity, while the wetland area had the largest error. However, this poor result for wetland is due to the fact that the water-body has a considerable impact on the relationship between *Tb* and σ when not removed prior to downscaling, resulting in a poor estimation in the *Tb* variation across this particular 9 km pixel.

In terms of downscaling resolution, the RMSE is reduced when going from 1 km to 3 km, and it can therefore reasonably be expected to continue decreasing when upscaling to SMAP resolution. This is due in part to the reduced heterogeneity captured from observations at coarser spatial scale. Moreover, it is noted from Table 7-1 that downscaled results at *v*-polarization have relatively lower RMSE than those at *h*-polarization, mainly due to the better linearity between σ_{vv} and Tb_v than that

Table 7-1: RMSE (K) of downscaled *Tb* with respect to different land covers (C=crops; G=grassland; M=mixed area; W=wetland), at different polarizations (*h*- or *v*-) and resolutions (1 km and 3 km) across 9-days (D1 to D9 of SMAPEx-3).

	D1		D2		D3		D4		D5		D6		D7		D8		D9		Ave.	
	h	*v*	*h*	*v*	*h*	*v*	*h*	*v*	*h*	*v*	*h*	*v*	*h*	*v*	*h*	*v*	*h*	*v*	*h*	*v*
C_1km	8.2	7.6	8.3	7.3	8.5	7.8	9.2	7.9	8.1	7.1	8.2	7.0	7.5	6.1	8.3	6.1	8.0	5.7	8.2	6.9
G_1km	5.6	5.2	4.8	4	5.6	4.7	5.3	4.7	4.6	3.9	4.6	4.0	4.2	3.6	4.2	3.6	4.5	3.9	4.8	4.1
M_1km	9.7	7.4	9.1	7.0	8.7	7.8	9.3	8.3	8.9	6.9	7.6	6.6	8.5	6.7	7.9	6.1	7.9	6.0	8.6	6.9
W_1km	16.7	15.7	16.0	15.2	15.2	14.1	15.1	14.7	16.0	15.3	16.2	14	16.2	14.6	15.6	15.1	16	14.7	15.8	14.8
C_3km	5.7	4.5	4.6	3.6	5.8	4.8	4.8	3.7	4.4	3.7	3.1	2.3	3.3	2.8	3.5	3.0	3.7	3.0	4.3	3.4
G_3km	3.6	3.0	2.8	2.2	3.3	2.5	2.9	2.7	2.5	2.3	2.6	2.3	2.4	2.0	2.1	1.9	2.3	2.0	2.7	2.3
M_3km	6.8	5.4	6.7	5.4	5.1	4.0	6.9	5.5	5.6	4.4	5.4	4.1	5.2	4.1	4.6	3.5	4.7	3.6	5.6	4.4
W_3km	10.6	9.9	9.6	9.1	9.5	8.7	8.8	8.7	8.8	8.9	10.1	8.1	9.3	8.8	9.5	9	5.6	5.1	9	8.5

between σ_{vv} and Tb_h. However, there is an obvious reduction of RMSE at both polarizations when aggregating to larger scale, e.g. a reduction of 4 K for cropping area, 2 K for grassland, 3 K for mixed area and 6 K for the wetland when aggregating from 1 km to 3 km resolution.

Regarding the downscaling algorithm performance for different land covers, it is shown in Table 7-1 that the average RMSE at 3 km resolution is around 2.7 K and 2.3 K at *h*- and *v*-pol respectively for the grassland, 4.3 K and 3.4 K for the cropping area, 5.6 K and 4.4 K for the mixed area, and 9 K and 8.5 K for the wetland. Since the grassland is relatively homogeneous in terms of surface and vegetation conditions, while the cropping and mixed area have much greater variation in vegetation characteristics and surface roughness, the heterogeneity in conditions for the cropping and mixed areas has resulted in a poorer estimation of β compared to the grassland, and thus influenced the downscaling accuracy. Moreover, as indicated from the wetland results, the water-body that covered approximately 10% of the coarse area pixel that contained it had a great influence on downscaling accuracy, due to the large difference in *Tb* between the water-body and the surrounding area, highlighting the need to clean the *Tb* data for water bodies prior to downscaling.

The downscaled *Tb* target error is around 2.4 K for SMAP (Entekhabi et al., 2012) and 4 K for SMOS (Kerr et al., 2010). While the results in Table 7-1 and Figure 7-4 show that the downscaling performance over the grassland area has fulfilled the SMAP target, results in the cropping area and mixed area are around 2 K higher than the SMAP target. This implies that while the SMAP baseline downscaling approach should perform adequately within relatively homogeneous environments, it is unlikely to meet the target accuracy in areas with varied land surface conditions. In order to assess the effect of irrigated fields within the cropping areas, irrigated farms were additionally removed prior to aggregation and downscaling, with an improvement in RMSE of approximately 1.2 K at 1 km resolution and 0.4 K at 3 km resolution over the previous results. By combining different land cover types, downscaled *Tb* across the entire 36 km × 36 km area had an overall RMSE around 7.2 K at *h*-pol and 6.1 K at *v*-pol at 1km resolution, and 3.8 K at *h*-pol and 3.1 K at *v*-pol at 3 km resolution. In comparison with the results at the same resolution levels from (Wu et al., In Press-a), the results here showed an improvement of around 0.8 K at 1 km and 1.5 K at 3 km resolution respectively, indicating that a spatially variable β across SMAP pixels may have the potential to retrieve more accurate downscaling results than using a single value of β across the entire area.

7.5 Chapter Summary

The objective of this study was to test the proposed baseline downscaling approach for the SMAP mission under a range of land surface conditions, using airborne active and passive data collected during the SMAPEx-3 field campaign in Australia. Results indicated that application of the downscaling algorithm to grassland areas was able to meet the target error for SMAP downscaled *Tb*. However, other land cover types such as crops and mixed land use (e.g. crops and grassland) had an error of 2 K higher than the target, likely due to the more complicated surface conditions. Moreover, comparing these results with from **Chapter 6** suggests that a spatially distributed β may result in a better downscaling accuracy than using the assumption of single value of β across entire SMAP pixels.

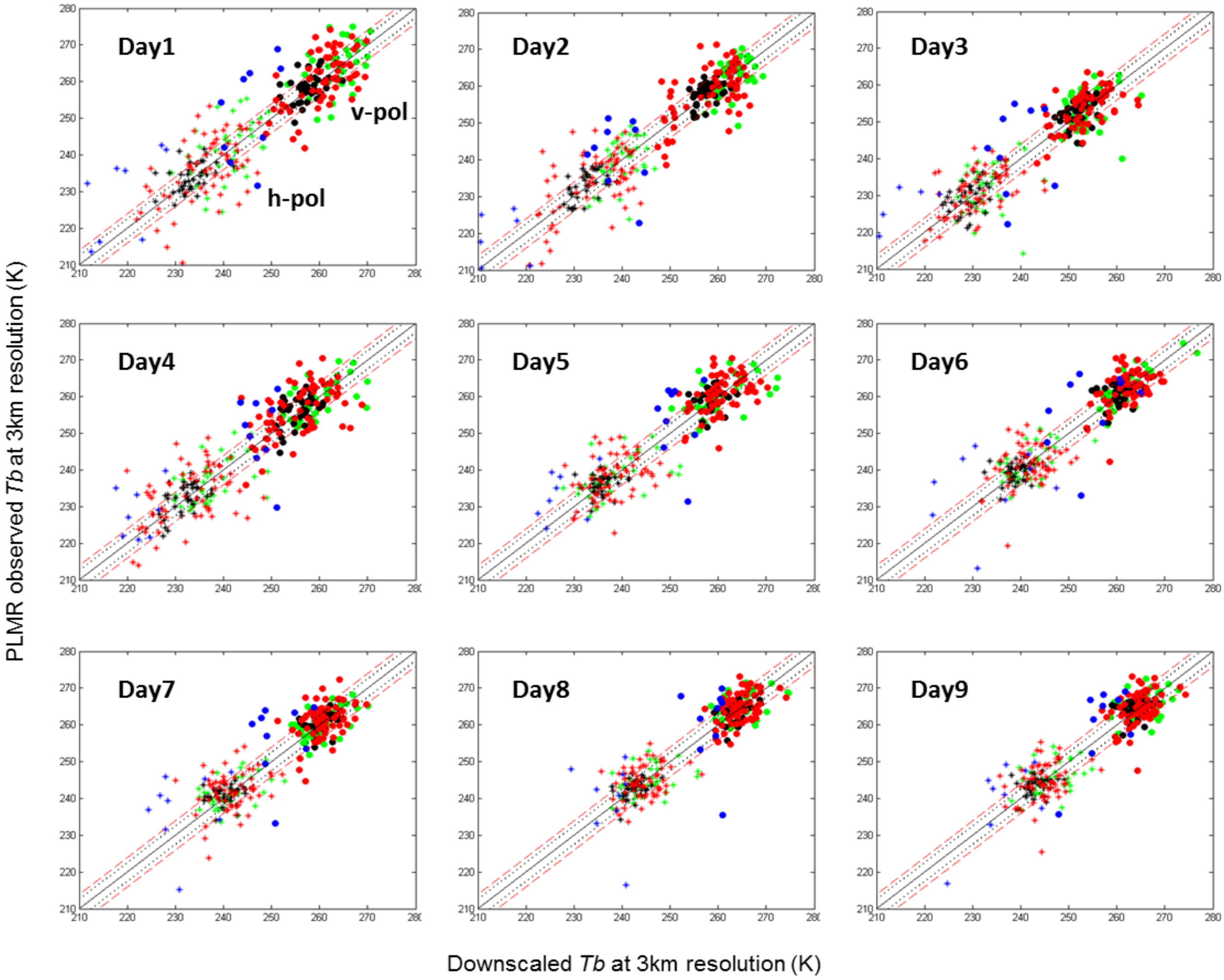

Figure 7-4: Relationship between downscaled and PLMR observed *Tb* at 3 km resolution for *h*- (cross) and *v*-pol (circle) across 9 days. Colour for each land cover type: green=crop, black=grassland, red=mixed crop/grassland, and blue=wetland. Black dotted lines represent the 2.4 K target error for SMAP, while the red dash lines are the 4 K target error for SMOS.

8 Effect of Land Surface Heterogeneity

For completeness of testing heterogeneity impacts on the baseline downscaling algorithm, this chapter presents a study using very high resolution radar backscatter (~ 100 m) to downscale "high" resolution brightness temperature from 1 km to 250 m resolution. These scales were chosen to provide a similar resolution ratio to that of SMAP. Use of such high resolution data allows application at the paddock scale, thus allowing land cover impacts to be more thoroughly assessed. However, there is a trade-off to be considered, that soil moisture is more highly variable at small scale, and that the radar and radiometer data will be less accurate at finer resolution due to residual errors in incidence angle correction and azimuth effect that are smoothed when averaging to coarser resolutions. The work in this chapter has been published in a peer-reviewed paper at the Modelling and Simulation Conference (Wu et al., 2013).

8.1 Background

As described in **Chapter 6** and **Chapter 7**, the baseline downscaling algorithm proposed for SMAP has been studied at two resolution levels. **Chapter 6** presented the downscaling of 36 km brightness temperature to 9 km resolution by using 3 km resolution radar backscatter, while **Chapter 7** illustrated the potential increase in skill for pixels with a consistent land cover type by applying the same downscaling approach at 9 km resolution brightness temperature. These studies demonstrated that downscaling accuracy was affected by the land cover type of the pixel itself and the heterogeneity of land cover conditions across the pixel. To further assess the impact of land cover, this chapter presents an investigation on baseline algorithm performance using very high resolution observations. In this study, 1 km resolution radiometer data are disaggregated to 250 m resolution using 100 m resolution radar observations, keeping the same ratio of the SMAP mission (from 36 km to 9 km) but at scales which are comparable with the size of agricultural fields, including crop and grassland focus areas.

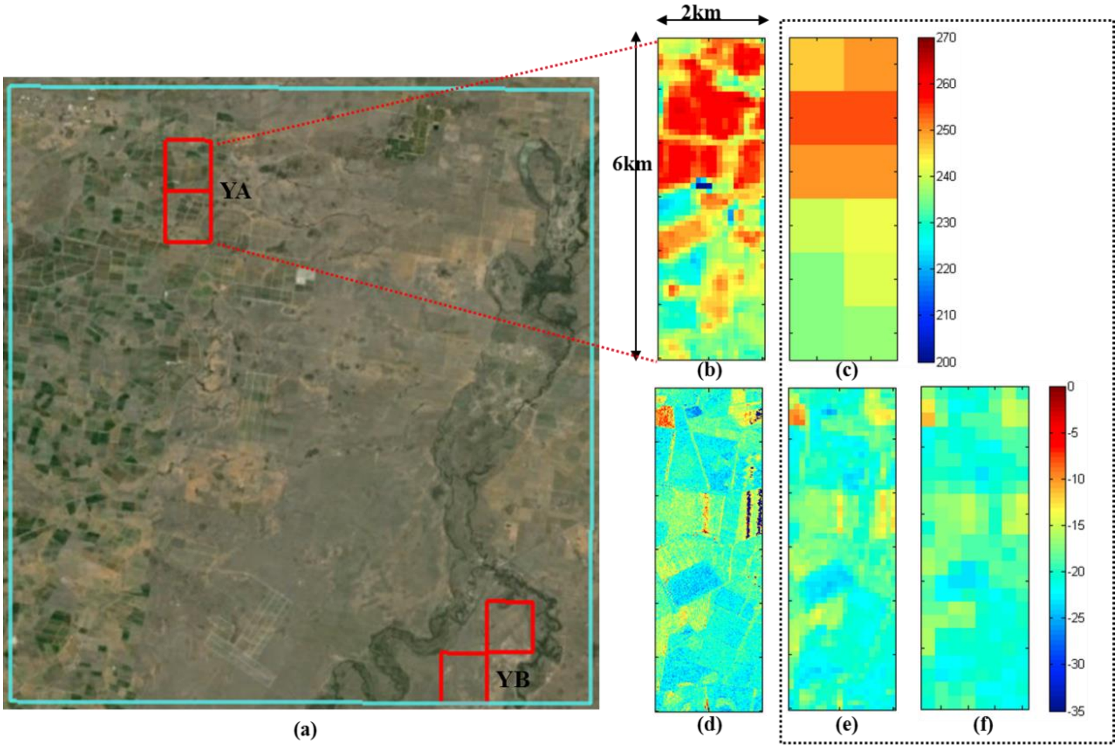

Figure 8-1: (a) Overview of SMAPEx study site (38 km×36 km size) and target areas YA and YB which are used to test the downscaling algorithm; (b) PLMR radiometer brightness temperatures (*Tb*) over the YA target area at *v*-polarization and 100 m resolution , and (c) aggregated to 1 km resolution; (d) observed 10 m resolution PLIS radar backscatters (*σ*) over the YA area at *vv*-polarization, aggregated to (e) 100 m resolution and (f) 250 m resolution, respectively.

8.2 Study Site

Data used in this study were collected from the second field campaign SMAPEx-2 from 6^{th} to 10^{th} July 2010, which included 3 days of Regional flights over the entire SMAPEx area and 2 days of Target flights, each conducted over a focus area ("YA" and "YB", see Figure 8-1a). Full details of SMAPEx field campaign has been described in **Chapter 3**, and the airborne data processing to match SMAP observations are given in **Chapter 5**, so only the details pertinent to this study are reported here.

While the YA area is dominated by crops with variations in vegetation characteristics and land conditions, the YB area is a grassland site with relatively homogenous conditions. Data collected from Regional flights included 1 km resolution PLMR *Tb* and 10 m resolution PLIS *σ*, which in this study were used to analyse the relationship between *Tb* and *σ*; data obtained from the Target flights included 100 m resolution PLMR *Tb* and 10 m resolution PLIS *σ* which were used to perform the *Tb* downscaling from 1 km to 250 m resolution.

In order to closely replicate the viewing configuration of SMAP, both the PLMR and PLIS data were normalized for incidence angle variation to the constant 40° angle of SMAP, using a CDF based method (Ye et al., In Review). The error of this normalization method for PLMR is 2.4 K at 1 km resolution; for PLIS it is 3.3 dB at 10 m resolution and 1.7 dB when aggregated to 100 m resolution.

The observed 100 m resolution PLMR data from Target flights were linearly aggregated to 1 km resolution, and the observed 10 m resolution PLIS data aggregated to 100 m and 250 m in order to evaluate the downscaling algorithm at different resolutions. An example of the aggregated data over YA area is shown in Figure 8-1.

8.3 Methodology

Similar to previous chapters, this chapter also tests the baseline downscaling algorithm proposed for SMAP, with full equation shown in Eq. (6-1) of **Chapter 6**. But in this study, 'C' (coarse), and 'F' (fine) in Eq. (6-1) represents the brightness temperature *Tb* at 1 km resolution and backscatter *σ* at 250 m resolution, respectively. Consequently, *β* is obtained through *Tb* at 1 km and *σ* at 1 km resolution. Using Eq. (6-1) the downscaled *Tb* is obtained for each pixel in the YA or YB area at 250 m resolution; other scale resolutions such as 100 m can be obtained by using 100 m resolution PLIS data, instead of 250 m resolution, as the input of the fine resolution PLIS data in Eq. (6-1). This study downscales the 1 km resolution *Tb* to 250 m resolution, to test the ability of this baseline downscaling algorithm at the same resolution ratio as SMAP, which aims to downscale 36 km resolution *Tb* observations to 9 km. Furthermore, the downscaling algorithm is applied with a 100 m target downscaled resolution to evaluate the performance of the downscaling approach at different scales. The downscaled *Tb* at fine resolution (including 100 m and 250 m) is heavily dependent on the quality of the overall PLMR *Tb* at each 1 km by 1 km pixel, the relative backscatter difference within the coarse grid (1 km), and the relationship with *Tb* as represented by the regression slope that adds to the background value *Tb*. The downscaled results at different resolutions are evaluated by comparing with PLMR *Tb* data at the original resolution of 100 m and 250 m respectively.

8.4 Results and Discussion

8.4.1 Estimation of β and Γ

Prior to carrying out the downscaling algorithm, the relationship between *Tb* at both polarizations (*h* and *v*) and σ at two polarizations (*hh* and *vv*) was determined to verify the linear relationship assumption which is the foundation of the approach, and to estimate parameter β to be used in Eq. (6-1). The parameter Γ also has to be estimated to represent the sensitivity of σ_{vv} to σ_{hv}.

As described, this baseline downscaling algorithm is based on the assumption that brightness temperature Tb_p is linearly related to the backscatter σ_{pp} at the same scale. Therefore, the robustness of this linear relationship is tested in this section using the four different combinations of Tb_p and σ_{pp}. The aim is to determine the best combination of radiometer and radar channels for estimating parameter β. In this case, data from the three Regional flights were used. Parameter β was calculated using the regression between the PLMR *Tb* (observed at 1 km) and the PLIS σ (aggregated to 1 km) collected over each 1 km pixel in YA or YB area. Two different values of parameter β were estimated: one value for the YA area (characterizing the sensitivity of Tb_p to σ_{pp} over crops), and a second value for the YB area (characterizing the sensitivity over grassland). The average β across each area, obtained from 3 days' time-series over 12 pixels within this area, together with its standard error (around 1.0 K/dB for different polarization), are listed in Table 8-1. The σ at *vv*-polarization had the best correlation to *Tb*, with correlation coefficient R = 0.65 and 0.81 for crops and grassland respectively. Conversely, σ at *hh*-polarization was less correlated to *Tb*, and showed little correlation at *hv*-polarization (R = 0.28 and 0.37). Therefore, σ at *vv*-polarization and at hh-polarization will be used to downscale PLMR *Tb* to

Table 8-2: Relationship between *Tb* (K) and *σ* (dB) at different polarizations over the YA and YB areas, *β* is the regression slope of *Tb* and *σ*, while *R* is the correlation coefficient between *Tb* and *σ*. A total of 36 pairs *Tb* and *σ* were used to estimate *β*, with standard error (in bracket) across each area.

	YA (crops)		YB (grassland)	
	Tb_h	Tb_v	Tb_h	Tb_v
σ_{vv}	β : -4.3(1.2)	β : -3.2(1.0)	β : -3.0(1.0)	β : -2.3(0.8)
	R : 0.62	R : 0.65	R : 0.72	R : 0.80
σ_{hh}	β : -5.2(1.3)	β : -3.8(0.9)	β : -4.5(0.9)	β : -3.3(0.7)
	R : 0.59	R : 0.61	R : 0.65	R: 0.71
σ_{hv}	β : -5.1(1.2)	β : -4.1(1.2)	β : -4.7(1.0)	β :-3.0(0.9)
	R: 0.21	R: 0.28	R : 0.34	R : 0.37

Table 8-1: RMSE (K) of downscaling algorithm using σ_{vv} and σ_{hh} (in bracket) at different polarizations and at different resolutions (100 m and 250 m) over YA and YB areas.

	YA (crops)		YB (grassland)	
	h-pol	*v*-pol	*h*-pol	*v*-pol
100 m	10.2(12.7)	8.6(10.1)	7.5(8.3)	5.7(6.6)
250 m	9.0(11.1)	7.1(8.8)	5.8(6.9)	4.6(5.5)

further confirm the influence of the correlation between *Tb* and *σ* at different polarization on the performance of the downscaling algorithm. Moreover, the magnitudes of *β* values over the YA area are larger than those over the YB area, indicating that the sensitivity of *Tb* to *σ* is stronger over crops than over grassland. Or in other words, the sensitivity of *σ* to *Tb* is stronger for grassland. This is mainly because radar backscatter is more sensitive to vegetation conditions than the *Tb*, which results in poorer correlation between *σ* and *Tb* in the YA area than in YB area.

The availability of only 3 days' time-series will influence the robustness of β estimation and further influence the accuracy of downscaling.

The parameter Γ was estimated using the pairs of σ_{vv} and σ_{hv} within each 1 km pixel, so as to obtain the regression slope Γ at each 1 km pixel. Consequently, Γ varies across the entire YA or YB area, with a range from 0.1 to 0.5 for both areas.

8.4.2 Downscaling results

Based on the respective value of β and Γ matrix over YA and YB, the 1 km *Tb* aggregated from Target flights were downscaled to 100 m and 250 m resolution, by using PLIS σ at 100 m and 250 m resolution (aggregated from 10 m resolution) respectively. The downscaled *Tb* was then compared with the reference *Tb* directly measured from PLMR at 100 m and 250 m resolution in order to evaluate the accuracy of the downscaling algorithm. Figure 8-2 and Figure 8-3 show the downscaled *v*-polarized *Tb* and the difference between downscaled and reference *Tb* at different resolutions over YA and YB area respectively. By comparing the differences over YA and YB, it is noted that results over the YB area show an overall smaller error than over YA, which could be attributed to the influence of heterogeneous vegetation in the YA area on the accuracy of the downscaling algorithm. Quantitative details are displayed in Table 8-2, from which it can be seen that the RMSE of YB has an improvement of approximately 3 K at *h*-polarization and 2.5 K at *v*-polarization over YA, confirming the results from Figure 8-2 and Figure 8-3. In addition, results at *v*-polarization are better than those at *h*-polarization for both the YA and YB area, with an improvement of around 2 K. This is due to σ_{vv} being more strongly related to *Tb* at *v*-polarization than *Tb* at *h*-polarization during the estimation of β. Moreover, the results at 250 m resolution were more accurate than those at 100 m, on the order of 1 K improvement in terms of RMSE. This is possibly because the speckle noise of radar backscatter is reduced when upscaling from 100 m to 250 m resolution, and the error of incidence angle normalization is reduced from 100 m to 250 m resolution. Additionally, the estimation of β at 1 km resolution is closer to β at 250 m than at 100 m resolution. It is noted that downscaled results based on σ_{hh} resulted in an RMSE on the order of ~1.8 K greater than when using σ_{vv}, confirming the conclusion from Table 8-1 that σ_{vv} is better

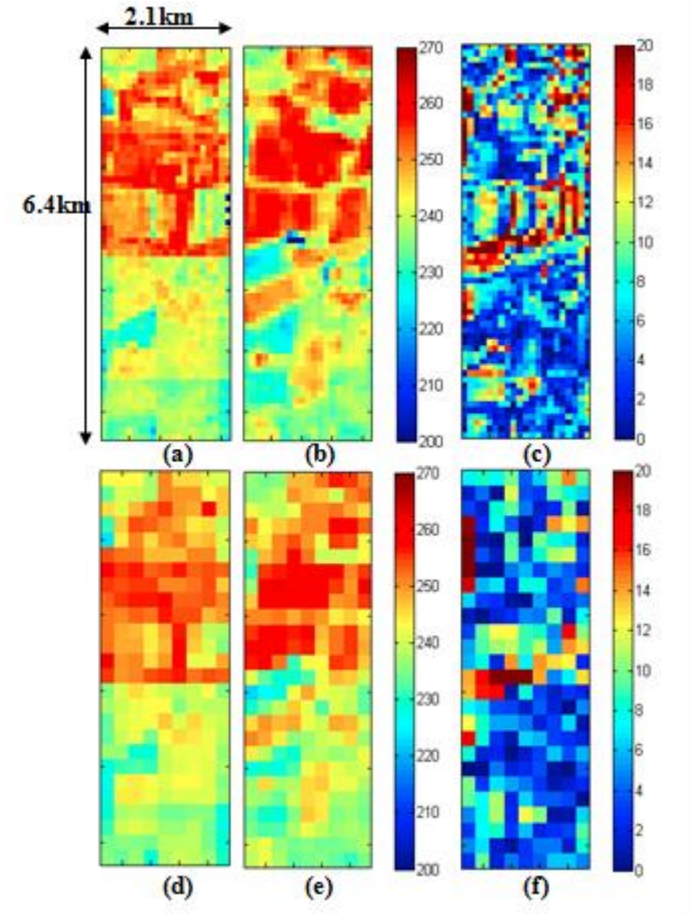

Figure 8-2: Evaluation of the downscaling algorithm at *v*-polarization over the YA area: (a) Downscaled *Tb* at 100 m resolution; (b) Reference *Tb* at 100 m resolution and (c) the difference; (d) Downscaled *Tb* at 250 m resolution; (e) Reference *Tb* at 250 m resolution; and (c) the difference.

correlated with *Tb*. The influence from the variation in β (as indicated by the standard error in Table 8-1) was also analysed which was found to result in approximately 2 K error in the downscaled *Tb* at 100 m resolution. Therefore, a better estimation of β can be expected from longer time-series observations over each 1km pixel, thus improving the downscaling performance.

To further evaluate the skill of the downscaling algorithm, the correlation between downscaled *Tb* and the reference *Tb* was studied with respect to different land cover at 100 m and 250 m resolution, with results displayed in Figure 8-4. While the black line represents a RMSE between downscaled and reference *Tb* of 0 K, the dashed line represents RMSE of ±4 K. It is noted from Figure 8-4 that the variation of *Tb*

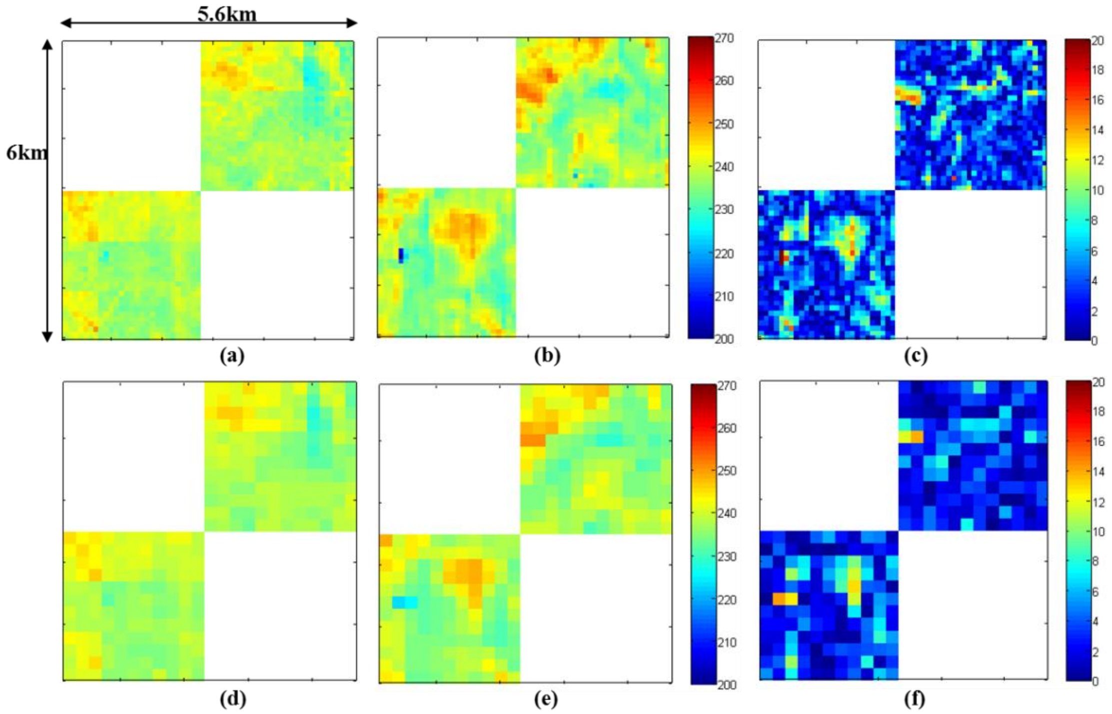

Figure 8-3: Evaluation of the downscaling algorithm at *v*-polarization over the YB area: (a) Downscaled *Tb* at 100 m resolution; (b) Reference *Tb* at 100 m resolution and (c) the difference; (d) Downscaled *Tb* at 250 m resolution; (e) Reference *Tb* at 250 m resolution; and (f) the difference.

over the YA area is much larger than the YB area, in response to the wider range of vegetation and land cover across the cropping area YA than the relatively homogenous area YB. In addition, a greater fraction of the data at 100 m resolution is outside the 4 K error range than at 250 m resolution, due to the reasons stated above. It is also noted that a greater fraction of the data fell within the 4 K range over the YB area than for the YA area. Thus, it can be noted that the downscaling algorithm has an overall better performance over grassland than the cropping area.

The target error of downscaled *Tb* at 9 km resolution of the SMAP mission is around 2.4 K for vegetation water content less than 5 kg/m^2, which is much lower than that achieved here. The reasons for larger errors when using the downscaling algorithm in this study may include: i) the availability of only 3 days of Regional flights for estimating parameter β, as the accuracy of β estimation influences the resulting accuracy of downscaling, which is expected to be improved when using a longer time series of data; ii) the incidence angle normalization prior to the downscaling

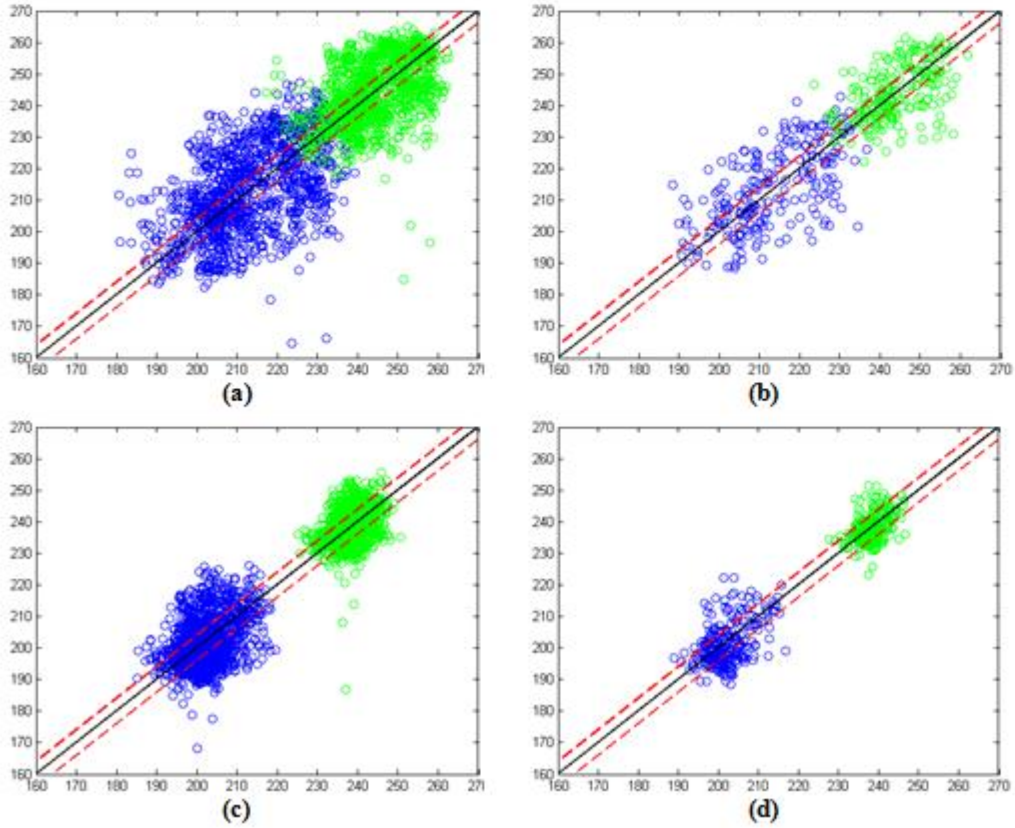

Figure 8-4: Agreement between downscaled *Tb* (horizontal) and reference *Tb* (vertical) at *v*-polarization: (a) at 100 m resolution over YA area; (b) at 250 m resolution over YA area; (c) at 100 m resolution over YB area; and (d) at 250 m resolution over YB area.

algorithm induced an error around 1.5 dB for PLIS at 250 m resolution and around 2.4 K for PLMR at 1 km resolution.

8.5 Chapter Summary

The objective of this study was to test the effects of land cover heterogeneity on the baseline downscaling approach for the SMAP mission over homogeneous fields, using very high resolution data from the SMAPEx campaigns in Australia. In this study, radar backscatter aggregated to 100 m and 250 m resolution were used to downscale radiometer brightness temperature at 1 km resolution to 100 m and 250 m resolution respectively. The results showed that the method still worked best with the downscaling result over relatively homogenous grassland having 3 K improvement when compared to heterogeneous cropping areas. It is thus shown that the accuracy of the downscaling approach is primarily determined by the heterogeneity of vegetation characteristics across the study area, as well as variations in the sensitivity of brightness temperature to radar backscatter, as reflected in the parameter β.

9 Comparison with Alternate Linear Methods

The previous chapters have focussed on evaluating the brightness temperature downscaling algorithm. Consequently, this chapter coverts the downscaled brightness temperature to soil moisture and compares the results with two different soil moisture downscaling algorithms, which are also based on active and passive measurements from the SMAPEx-3 field campaigns. The three algorithms include: i) baseline soil moisture downscaling algorithm proposed for SMAP; ii) optional downscaling algorithm for SMAP; and iii) an alternate method – change detection method. Paper of this work is currently under review.

9.1 Background

In preparation of the SMAP launch, suitable algorithms and techniques need to be developed and validated to ensure that an accurate intermediate resolution soil moisture product can be operationally produced from combined SMAP radiometer and radar observations. The proposed baseline downscaling method for the SMAP mission is based on an observed near-linear relationship between radar backscatter and the brightness temperature at the same scale, with the downscaled brightness temperature at ~9 km then interpreted to soil moisture using the passive microwave retrieval model (Das et al., 2014, Entekhabi et al., 2012). An optional method proposed for the SMAP mission utilizes the near-linear relationship between radar backscatter and volumetric soil moisture (rather than brightness temperature) and ultimately retrieves the medium-resolution soil moisture product directly (Das et al., 2011, Entekhabi et al., 2012). An important element of these two methods is that the relationship between the slope parameter and vegetation heterogeneity should be formulated to improve the accuracy of this algorithm. A further candidate downscaling approach is based on the change detection method, which takes advantage of the approximately linear dependence of radar backscatter and brightness temperature change on soil moisture change (Piles et al., 2009, Narayan et al., 2006). Each of these three method are referred to as linear methods; other non-linear downscaling methods, such as the Bayesian merging algorithm (Zhan et al., 2006), use a totally different strategy which results in a downscaled soil moisture product directly through the synergy of the active and passive data in a Bayesian framework.

Given that current downscaling algorithms are relatively immature and not widely tested using experimental data, the main objective of this study is to evaluate the performance of these three linear downscaling algorithms using active and passive microwave observations from the SMAPEx-3 field campaign undertaken in Australia (Panciera et al., 2014). Evaluation of the non-linear Bayesian merging method is provided in the next chapter. The SMAPEx field campaigns provide the opportunity to evaluate the SMAP Active-Passive baseline algorithms using data that presents a range of conditions and land covers. Data were collected from the airborne simulator mounted with PLMR and PLIS, which can provide the brightness temperature observations and backscatter observations respectively.

9.2 Data Set

A full description of the SMAPEx field campaign and data set can be found in **Chapter 3**, so only the pertinent details are provided here. The radiometer and radar data used in this study were collected from the third SMAPEx field campaign (September 5-23 2011), which was conducted during the spring vegetation growing season. This campaign was used since it comprised nine regional flights over a 3-week time period with the 2-3 day revisit time of SMAP. Those 1 km resolution brightness temperatures from PLMR and 1 km resolution backscatters from PLIS airborne observations have been spatially aggregated to 36 km and 3 km respectively, so as to simulate the SMAP data stream. Examples of the simulated SMAP data used in this study are shown in Figure 5-6 and Figure 6-2. Apart from the airborne observations, ancillary data such as surface roughness, VWC and etc. are also used in this study for retrieving soil moisture from brightness temperature.

9.3 Methodology

9.3.1 Baseline downscaling algorithm

The baseline downscaling algorithm to be implemented by SMAP is based on the assumption of a near-linear relationship between Tb and σ. Details on this method have been stated in **Chapter 6**. The output of this baseline downscaling algorithm in **Chapter 6** was downscaled brightness temperature at medium resolution. Therefore, the main work concerning this downscaling algorithm in this study is to interpret the obtained downscaled Tb to downscaled soil moisture product, using the tau-omega (τ-ω) passive microwave retrieval algorithm with soil and vegetation parameters (Panciera et al., 2009). In order to differentiate the parameter β for each algorithm, the one used in baseline algorithm is denoted by β_1 in this study.

9.3.2 Optional downscaling algorithm

The optional downscaling algorithm for SMAP (Das et al., 2011) is similar to the baseline but use the soil moisture instead of brightness temperature in Eq. (6-1). Implementation of this method requires a background soil moisture θ at C resolution, with the variation of θ imposed by the distribution of fine scale σ within C modulated by $\beta_2(C)$ of the linear regression between θ and σ at C resolution according to:

$$\theta(F_j) = \theta(C) + \beta_2(C) \times \{[\sigma_{pp}(F_j) - \sigma_{pp}(C)] - \Gamma \times [\sigma_{pq}(C) - \sigma_{pq}(F_j)]\}, \quad (9\text{-}1)$$

where $\theta(F_j)$ is the soil moisture of a particular pixel "j" of resolution F, $\theta(C)$ aggregated from 1 km resolution PLMR retrieved soil moisture product (through the passive microwave retrieval algorithm). $\beta_2(C)$, in the unit of cm^3/cm^3/dB, which is also assumed to be time-invariant and homogenous over the entire 9 km pixel and can be obtained through the time-series of $\theta(C)$ and $\sigma_{pp}(C)$. Other terms in Eq. (9-1) are all the same as Eq. (6-1), with variation of soil moisture within C denoted by σ and Γ , and then converted to soil moisture at fine scale through multiplication by $\beta_2(C)$. The main differences between optional and downscaling algorithms are: i) estimation of the sensitivity parameter β from θ and σ, or from Tb and σ; and ii) soil moisture retrieved in direct or in-direct way, the latter needs to go into the (τ-ω) retrieval model.

9.3.3 Change detection method

This change detection method uses the linear relationship between temporal change of radar backscatter and temporal change of soil moisture at the same scale (Piles et al., 2009). It has the same assumption as the optional downscaling algorithm, but is different in retrieving medium-resolution soil moisture:

$$\theta\,(F_j,t) = \theta\,(C, t\text{-}t_R) + \beta_3(C) \times \{\sigma_{pp}(F_j,t) - \sigma_{pp}(F_j,t\text{-}t_R)\}, \tag{9-2}$$

where $\theta\,(F_j,t)$ is the soil moisture of a particular pixel "j" of resolution F and at time t, $\theta\,(C, t\text{-}t_R)$ is aggregated from 1 km resolution PLMR retrieved soil moisture product (through the passive microwave retrieval algorithm) at time $t\text{-}t_R$. t_R is the revisit time of the observations, 2-3 days for the SMAP case. $\theta\,(C, t\text{-}t_R)$ is then updated with soil moisture change evident in the fine resolution radar backscatter σ at different time. $\beta_3(C)$, which is also assumed to be time-invariant and homogenous over the entire site, can be obtained through the time-series of $\theta(C)$ and $\sigma_{pp}(C)$.

While the optional algorithm is based on a background soil moisture value and the variation across the entire area characterized by radar observations, this change detection method indicates that a soil moisture estimates at a given time can be obtained as the previous soil moisture estimate plus a change in soil moisture, which is given by the actual radar estimates and the value of regression slope β_3. The first estimates are likely to be noisy due to the high uncertainty on the first calculated slopes. However, when a reasonable number of estimates are available, the uncertainty on calculating the slope becomes much lower, leading to robust soil moisture estimations.

9.4 Results and Discussion

9.4.1 Estimation of β and Γ

For each method mentioned above, the estimation of the sensitivity parameter β is different. Results for β estimation can be found in Table 9-1. For the baseline downscaling algorithm, β was estimated from Tb and σ at 36 km resolution. As stated

Table 9-1: Estimation of *β* and Γ for each downscaling algorithm. β_1 is estimated from brightness temperature *Tb* and backscatter σ_{vv} at 36 km resolution; β_2 is estimated from soil moisture *θ* and σ_{vv} at 36 km resolution; β_3 is estimated from *θ* and σ_{vv} at 36 km resolution; *Γ* is estimated from snapshots of σ_{vv} and σ_{hv} at 1 km resolution in each 9 km by 9 km pixel.

	β	Γ
Baseline	β_1 *h*-pol: -3.4 (K/dB) β_1 *v*-pol: -2.2 (K/dB)	0.2-0.45
Optional	β_2: 0.018 (cm^3/cm^3/dB)	0.2-0.45
Change detection	β_3: 0.018 (cm^3/cm^3/dB)	-

in **Chapter 6**, *σ* at *vv*-pol showed the best correlation with *Tb* and therefore was used for estimating β_1. Therefore, β_1 was calculated at *h*- and *v*-pol, being -3.4 K/dB and -2.2 K/dB respectively, since *Tb* was observed at two polarizations *h*- and *v*-pol. Different to the baseline algorithm, the sensitivity of soil moisture *θ* to backscatter *σ* in the optional algorithm was analysed using the slope of the linear regression as a measure of quality and therefore the parameter β_2 was obtained, being 0.018 cm^3/cm^3/dB. Since β_3 of the change detection method also indicate the sensitivity of soil moisture to backscatter, it was therefore obtained as the same value as β_2.

Regardless of the actual variation of vegetation within the entire area, the sensitivity parameter *β* was estimated as a single value across the 36 km area as outlined in the SMAP baseline active-passive algorithm. According to previous work done in **Chapter 6** to **Chapter 8**, the magnitude of *β* was actually affected by the land cover types, vegetation biomass and the existence of water bodies. For instance, the magnitude of *β* is relative large in the flooding or irrigated area, and decreases in the vegetated area, and in grassland *β* is the smallest. Therefore, the assumption of a constant *β* in this study may influence the resulting accuracy of downscaled product when compare with the reference. It is suggested that a more detailed investigation of the spatial distribution of *β* within the 36 km area should be undertaken, including an investigation of a potential implementation in the SMAP baseline algorithm. But this is out of the scope of this study.

Since the observed σ from radar is not only related to the soil moisture, but also to the vegetation conditions, use of Γ in baseline and optional downscaling algorithm aims to remove/reduce the influence from vegetation on σ and to make it more strongly correlated to the soil moisture. For these two methods, parameter Γ, the sensitivity of σ_{vv} to σ_{hv}, was estimated using the same method from the snapshots of σ_{vv} to σ_{hv} values at each 9 km × 9 km pixels within the entire SMAPEx study area. In order to obtain an estimate for the parameter Γ, the study area was divided into 16 sub-areas of 9 km by 9 km in size, and the value of Γ calculated using the snapshots of all σ_{vv}-σ_{hv} pairs at 1 km resolution contained within each of those sub-areas, allowing an analysis of the relationship between estimation of Γ and vegetation conditions. Results are displayed in Table 9-1, with Γ ranging from 0.2-0.45 according to vegetation conditions at different locations.

9.4.2 Downscaling results

As discussed above, downscaled soil moisture product was obtained through three linear downscaling algorithms: i) baseline algorithm: the downscaling results at fine resolution are a function of the background Tb value plus a variation of Tb within the entire area derived from the variation of the backscatter from the mean. For this algorithm, the background Tb is the aggregated 36 km Tb from PLMR, and the variation of Tb at higher resolution is characterized by the variation of σ_{vv} from PLIS observations, together with the β_1 from the sensitivity of Tb to σ; ii) optional algorithm: the downscaling results at fine resolution are a function of the background θ value plus a variation of θ within the entire area derived from the variation of the backscatter. The background θ is aggregated from 1 km PLMR retrieved soil moisture to 36 km, and the variation of θ at higher resolution is also characterized by the variation of σ_{vv} from PLIS and the sensitivity parameter β_2 of θ to σ_{vv}. The influence of vegetation is then deduced for both baseline and optional algorithm using σ_{hv}, due to its strong correlation with vegetation conditions; and iii) change detection: the downscaling results at fine resolution are a function of the previous background θ updated by the changes of σ_{vv}.

Table 9-2: Root Mean Square Error (RMSE, cm^3/cm^3) of downscaled soil moisture from the different downscaling algorithm across the 9 days (D1 to D9) of SMAPEx-3 at 1 km, 3 km and 9 km resolution.

Algorithm	Resolution	D1	D2	D3	D4	D5	D6	D7	D8	D9	average
Baseline	**RMSE_1km**	0.045	0.051	0.039	0.039	0.033	0.038	0.038	0.029	0.031	0.038
	RMSE_3 km	0.037	0.044	0.030	0.028	0.022	0.026	0.028	0.018	0.020	0.028
	RMSE_9 km	0.027	0.032	0.021	0.020	0.013	0.020	0.013	0.010	0.012	0.019
Optional	**RMSE_1 km**	0.048	0.053	0.047	0.040	0.037	0.040	0.041	0.038	0.032	0.042
	RMSE_3 km	0.037	0.042	0.035	0.030	0.028	0.025	0.025	0.028	0.022	0.030
	RMSE_9 km	0.025	0.029	0.025	0.021	0.018	0.020	0.015	0.019	0.015	0.021
Change detection	**RMSE_1 km**	N/A	0.061	0.054	0.041	0.040	0.043	0.041	0.039	0.035	0.044
	RMSE_3 km	N/A	0.056	0.046	0.031	0.027	0.026	0.028	0.028	0.024	0.033
	RMSE_9 km	N/A	0.046	0.039	0.027	0.020	0.025	0.019	0.019	0.012	0.026

Consequently, the downscaled θ results from three algorithms were retrieved at resolutions of 1 km, 3 km and 9 km, from linearly aggregating the 1 km resolution downscaled θ to 3 km and 9 km resolution respectively. Data used to test these algorithms were collected on 9 days of SMAPEx-3 field campaign. Prior to applying the downscaling algorithms, the main water body in the far north-eastern section of the area, and some irrigated cropping areas within the western part of the regional area, were removed (these areas collectively represent approximately 1% of the entire study region) to reduce the influence of surface water on the resulting downscaling accuracy. The accuracy of three downscaling algorithms at different spatial resolutions was evaluated against the reference soil moisture θ which was previously introduced in **Chapter 3**.

Downscaling results on each day of SMAPEx-3 are shown in Table 9-2 for each downscaling algorithm at different resolutions. It is noted from Table 9-2 that the downscaled results of baseline and optional algorithms are similar in terms of the RMSE. For baseline algorithm, the average RMSE across 9 days was 0.038 cm^3/cm^3, 0.028 cm^3/cm^3 and 0.019 cm^3/cm^3 at 1 km, 3 km and 9 km resolution, respectively. While the average RMSE for optional algorithm showed the similar results with minor increment of approximately 0.002-0.003 cm^3/cm^3 depending on the resolution. In comparison, change detection method had a largest RMSE among these three algorithms, being 0.006 cm^3/cm^3 larger than the baseline algorithm. One possible reason, contributing this relatively poor performance of change detection method, is the influence from vegetation that has not been taken into account.

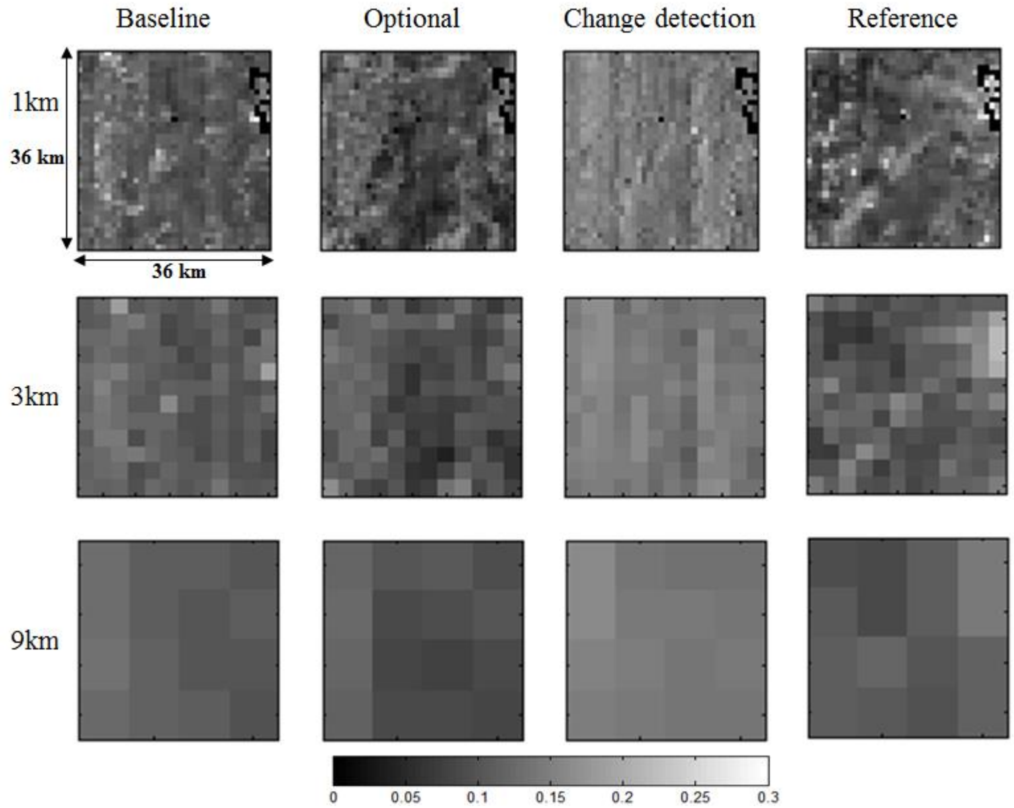

Figure 9-1: Comparison of downscaled soil moisture maps (cm^3/cm^3) from each downscaling algorithm (baseline, optional and change detection) and the reference at different resolutions (1 km, 3 km, and 9 km). Data were collected on D3 (10th September 2011) of SMAPEx-3. Pixels at 1 km resolution in the northeast of the study area are the water-bodies which have been removed prior to conducting the downscaling algorithm.

Unlike baseline or the optional method, the change detection method did not use σ_{hv} and the parameter Γ to compensate the influence of vegetation on the soil moisture retrieval.

It is noted from Table 9-2 that RMSE of each algorithm generally decreased from the beginning to the end of 9 days. Results of the first days i.e. D1 to D3 displayed relatively poor performance when compared to the later days. In particular, D1 and D2 contain significant noise levels. One possible reason is attributed to the heavy rainfall events that led to wet soil and vegetation conditions in the north-eastern part of the study area at the beginning of SMAPEx-3, subsequently affecting the radiometer and radar observations. D1 to D3 had a higher variation of *Tb* or θ (reference) when compared to the other days. Since *Tb* is more sensitive to the

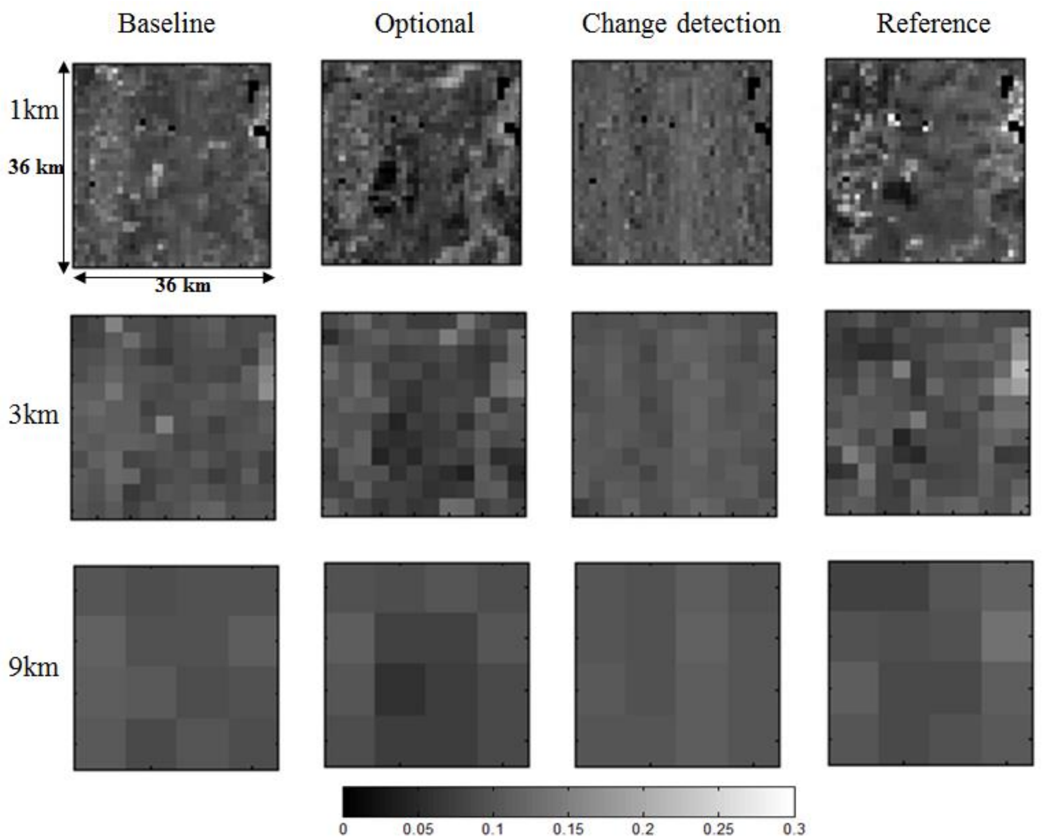

Figure 9-2: As for Figure 9-3 but on D5 (15th September 2011) of SMAPEx-3.

immediate soil moisture changes due to the rain in this region, the value of *Tb* drop according to soil moisture increase is more significant than the radar backscatter changes, as the latter are more influenced by the vegetation cover and consequently less sensitive to the soil moisture changes. Consequently, the sensitivity of backscatter to Tb/θ decreases, resulting in an obvious difference in the sensitivity parameter β for the area subjected to rainfall when compared with the other drier areas, which would have dominated the derivation of β itself. The influence from surface heterogeneity due to the rain event reduced during the dry-down period, especially after D3, as shown through the decrease in RMSE from D3 onwards.

In terms of resolution, there is an obvious reduction of RMSE when applied to a larger scale, e.g. from 1 km to 3 km and 9 km respectively, which can be attributed to the reduction of random (white) noise following the aggregation of the backscatter data.

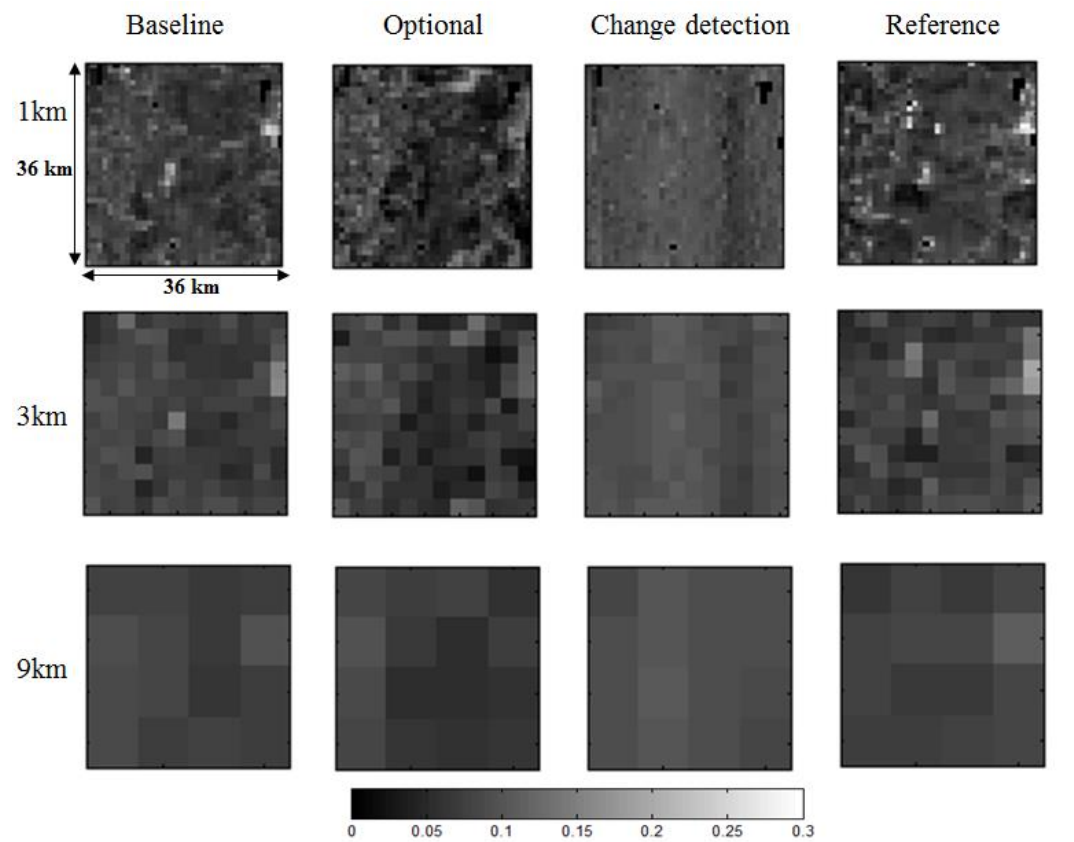

Figure 9-3: As for Figure 9-3 but on D8 (21st September 2011) of SMAPEx-3.

Performance on three days (D3, D5 and D8) have been picked up to represent the weather conditions from wet, medium and dry, as shown in Figure 9-1 to Figure 9-3. The water-bodies have been removed as shown in the 1 km resolution maps in Figure 9-1, Figure 9-2 and Figure 9-3. Comparison between downscaled soil moisture product from different downscaling algorithm and the reference soil moisture with respect to different resolution are shown in these figures. According to the patterns shown in the reference, areas in the right end and in the left end were dominated by the cropping, while areas in the middle were mainly occupied by grassland. Therefore in terms of soil moisture, grassland was drier than the cropping site as shown in those figures. The pattern of optional algorithm largely matched that of the reference, especially on D8; while the pattern of change detection method could hardly represent the actual pattern; the baseline algorithm could show similar pattern as the reference but with poorer performance than optional one. Both of baseline and optional algorithm showed an improvement on the pattern match from D3 to D8, while the performance of change detection did not improve the detection of

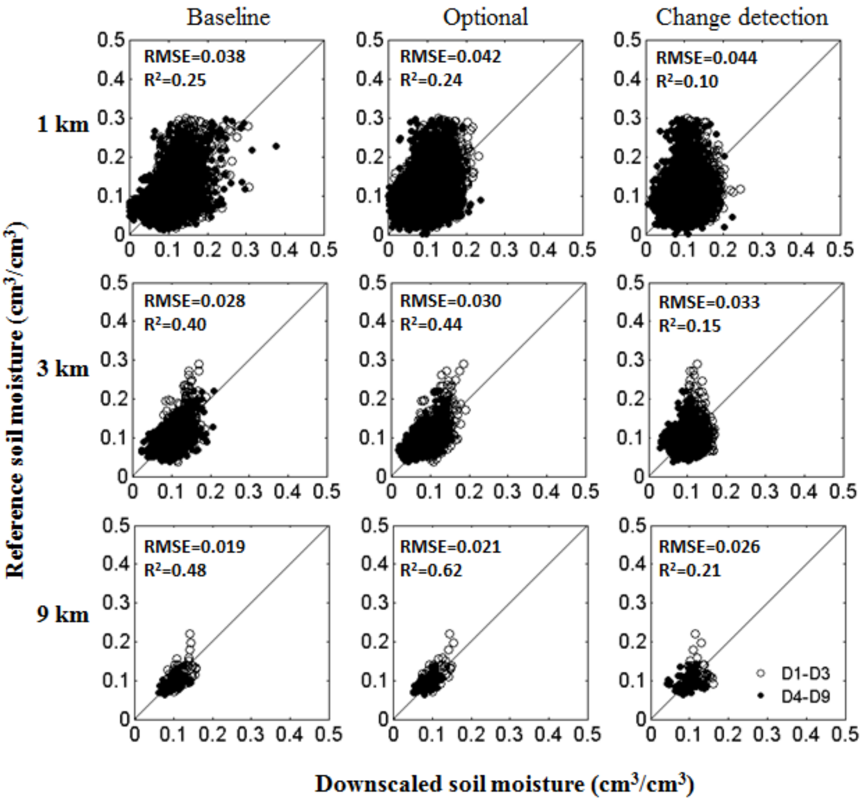

Figure 9-4: Comparison between reference and downscaled soil moisture maps from the baseline, optional and change detection methods at 1 km, 3 km, and 9 km resolution. Performance of each method was evaluated in terms of Root-Mean-Square-Error (RMSE, in unit of cm^3/cm^3) and correlation (R^2) between downscaled and reference soil moisture. Data are from all 9 days of SMAPEx-3, with data from Day 1 to Day 3 denoted by open circles, while data from Day 4 to Day 9 denoted by solid circles.

pattern from the beginning to the end. To this end, although all of these three downscaling algorithm had similar RMSE when compared to the reference, the ability to correctly detect the pattern as shown in the reference map is another key factor to examine the performance of downscaling algorithm.

In order to quantify the degree of pattern match, a further evaluation of the skill of each particular downscaling algorithm was through the correlation (R^2) between downscaled and reference θ at 1 km, 3 km and 9 km resolution (See Figure 9-4) by combining 9 days' data. It is noted that the correlation at 1 km was quite poor, primarily due to the high noise level of the observations at 1 km resolution; the

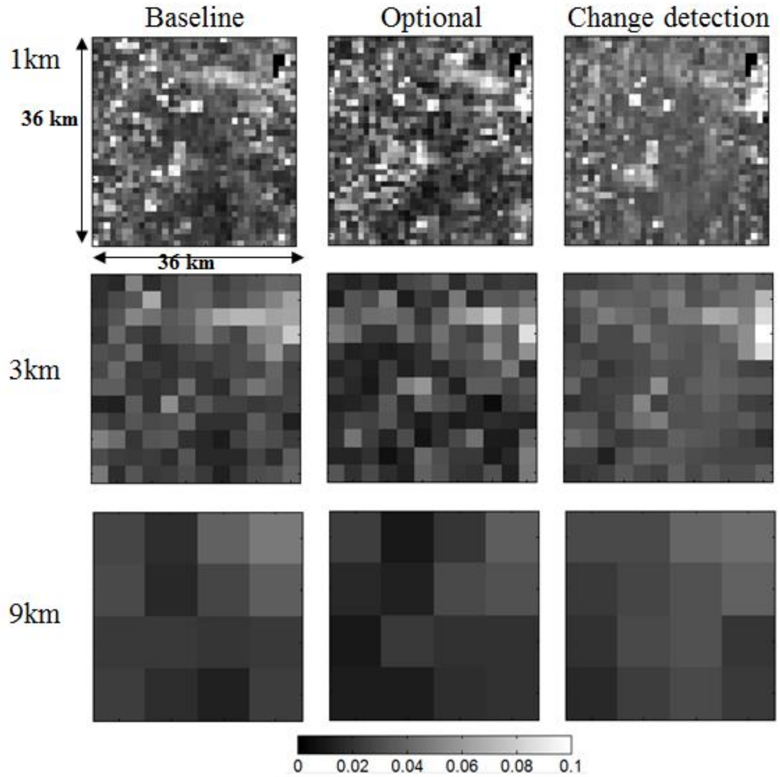

Figure 9-5: Spatial distribution of Root-Mean-Square-Error (RMSE, in unit of cm^3/cm^3) for baseline downscaling algorithm, optional downscaling algorithm and change detection method across the entire SMAPEx site at 1 km, 3 km and 9 km resolution, respectively. RMSE for each pixel was calculated from the downscaled soil moisture and the reference soil moisture at this pixel across 9 days of SMAPEx-3.

correlation was improved by approximately 0.23, 0.48 and 0.11 respectively for baseline, optional and change detection method when observations were averaged to larger scale from 1 km to 9 km. By comparing the behaviour of each algorithm at 9 km resolution, the optional algorithm showed the best correlation with reference soil moisture around 0.62, being approximately 0.14 higher than the baseline; change detection was observed to have poorest correlation between its retrieved soil moisture and the reference, around 0.21, when compared to other algorithm. To this end, by assessing RMSE and the correlation between downscaled soil moisture and reference, the optional downscaling algorithm had the best performance and would be recommended for use in SMAP.

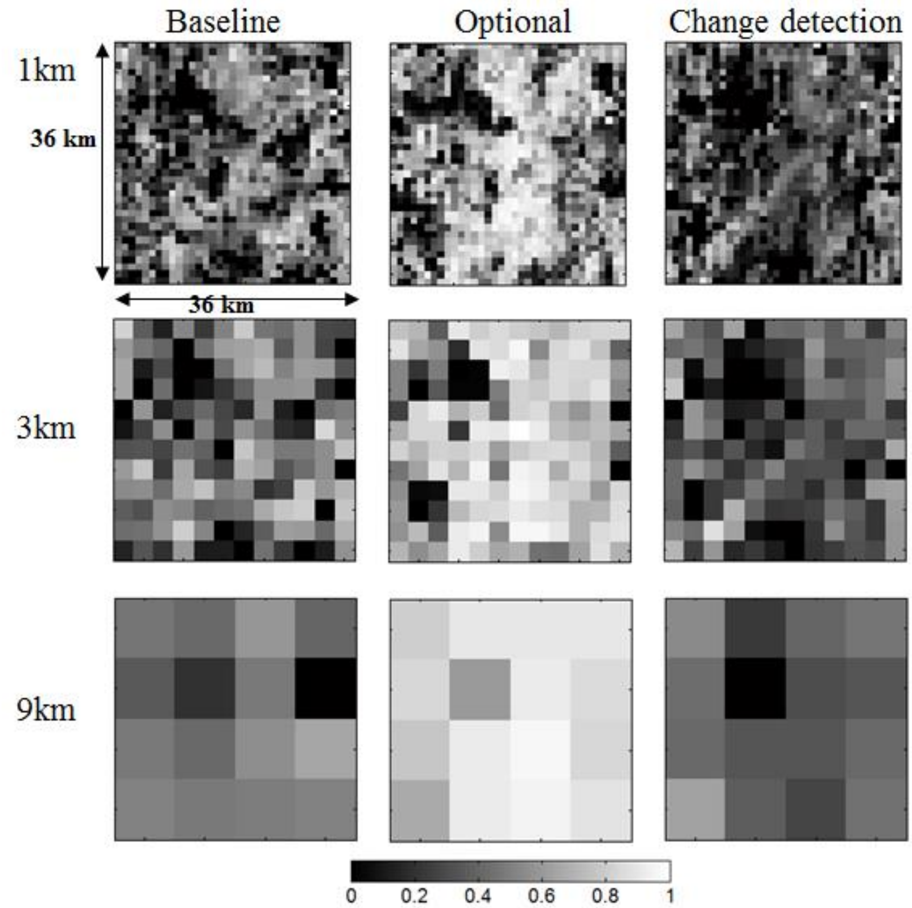

Figure 9-6: Spatial distribution of correlation coefficient (R^2) for baseline downscaling algorithm, optional downscaling algorithm and change detection method across the entire SMAPEx site at 1 km, 3 km and 9 km resolution, respectively. R^2 for each pixel was calculated from the downscaled soil moisture and the reference soil moisture at this pixel across 9 days of SMAPEx-3.

The above analysis was also undertaken when including the water bodies that had previously been masked out in the aggregation procedure, in order to simulate more realistic SMAP data (as many water bodies will not be reliably identified for masking). Consequently, this was done to quantify the effect of relatively small water bodies on the accuracy of the downscaling approach. Without removing the water-bodies, the average RMSE of all nine days at 9 km resolution increased by approximately 0.01 cm^3/cm^3, for each type of downscaling algorithm.

In order to differentiate the impact from land cover types on the downscaling performance, the spatial distribution of RMSE and the correlation coefficient R^2 was also obtained at different resolution levels across the entire study area, as shown in Figure 9-5 and Figure 9-6. Both RMSE and R^2 were calculated from the series of downscaled soil moisture and the reference soil moisture at each pixel across 9 days, and at three resolution levels: 1 km, 3 km and 9 km. As shown in Figure 9-5, the optional and the baseline downscaling algorithm showed minor difference in terms of the spatial plot of RMSE, but overall these two were better than the change detection method. With respect to the land cover types, it could be observed from Figure 9-5 that the left side of the study area dominated by crops had greater error than the middle part that was occupied by grasslands, indicating the higher heterogeneity in the croplands attributed to a worse performance of downscaling. Moreover, the northeast area also had poor performance probably due to the increased surface heterogeneity as a consequence of raining events during the first couple days.

In terms of the correlation between downscaled soil moisture and reference, the optional downscaling algorithm showed the best performance as shown in Figure 9-6, in line with the results in Figure 9-4. Again, the downscaled results in the grasslands were more correlated to the reference than in the croplands, which was probably due to the influence from the crops on the radar observations. The croplands, which had more variations in the vegetation conditions, surface roughness, row structure etc., had introduced more noise to the radar observations and therefore hampered the accuracy of downscaling using those radar observations. To this end, the relatively homogenous grasslands had overall better performance in downscaling with lower RMSE and higher correlation to the soil moisture truth than the complicated croplands.

9.5 Chapter Summary

The objective of this study was to test the robustness of three downscaling algorithms using active and passive observations from SMAPEx field campaign in Australia. These three algorithms included: the baseline algorithm and optional algorithm proposed for the SMAP mission, and a change detection method. The errors associated with each downscaling algorithm were assessed for different spatial resolution levels. All three algorithms were found to perform poorly in the early days of the experiment due to a rainfall event in the study area that created a large spatial heterogeneity in terms of soil moisture content. While all three methods met the RMSE requirement at 9 km resolution during the last 2 weeks of the experiment, which were characterized by a drying down period, the ability to detect the spatial pattern varied considerably. The change detection method had the poorest spatial correlation while the optional algorithm showed best spatial correlation. Due to the mixed results obtained for these three methods at the SMAPEx study site, it is important to test if non-linear methods are able to achieve a better result.

10 Comparison with Bayesian Merging Method

This chapter investigates the Bayesian merging method using the same experimental data set as **Chapter 9**, being from the SMAPEx-3 field campaign. This method differs from the three linear downscaling algorithms evaluated in the last chapter, in that the method studied here is a non-linear downscaling algorithm based on the Bayes Theorem. The medium-resolution soil moisture product is obtained using a background soil moisture estimate that is updated according to the difference between observed and predicted brightness temperatures and backscatter coefficient at multiple polarizations. Results are assessed against a validated reference soil moisture map derived from airborne radiometer observations at 1 km resolution.

10.1 Background

The baseline and optional downscaling algorithm proposed for SMAP, together with another candidate downscaling algorithm called the change detection method (Piles et al., 2009), have been evaluated in **Chapter 9**, with results showing that the optional downscaling algorithm provided the overall best medium-resolution soil moisture results amongst those linear downscaling algorithms. However, as the three downscaling algorithms presented in earlier chapter are all based on an assumed linear relationship between radar and radiometer observations, it is considered valuable to test an alternative method for SMAP. For instance, the Bayesian merging method, which retrieves medium-resolution soil moisture in a totally different way (Zhan et al., 2006). The Bayesian method showed promising results in retrieving a soil moisture product at medium resolution, with a RMSE of 0.027 cm^3/cm^3 using low noise radar data and 0.044 cm^3/cm^3 using high noise radar data (Zhan et al., 2006). However, this Bayesian method has only been tested using synthetic data. Therefore, the objective of this chapter is to test the Bayesian method using the same experimental data set as for the three linear methods compared in **Chapter 9**, and to

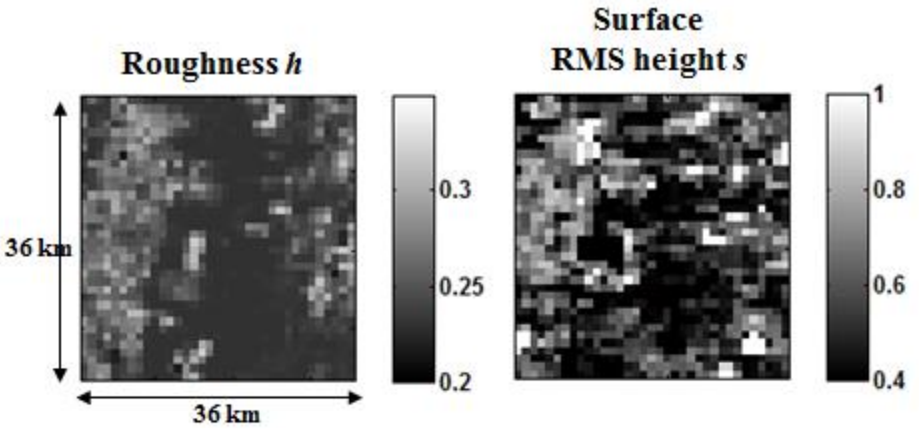

Figure 10-1: Spatial distribution of static surface roughness parameter *h* (cm) and surface Root-Mean-Square height *s* (cm).

thus recommend an optimal downscaling algorithm for the forthcoming SMAP mission.

10.2 Data Set

Data from the SMAPEx-3 field campaign were used in this study. Details on the SMAPEx study area, surface conditions, airborne instrument and acquisition etc. can be found in **Chapter 3**. Apart from the observations from aircraft (i.e. *Tb* at 36 km at *h*- and *v*-pol from PLMR, and σ at 1 km at *hh*-, *vv*- and *hv*-pol from PLIS), vegetation and surface condition data were also needed. These data were used for background soil moisture retrieval from radar and radiometer observations alone, and for forward modelling of predicted backscatter and brightness temperature from given soil moisture values. Information on the ancillary data, including the surface roughness parameter *h*, surface Root-Mean-Square height *s*, VWC, vegetation parameter *b* which depends on vegetation type, surface temperature T_{surf}, canopy temperature T_{veg}, sand/clay fraction, soil bulk density, incidence angle and single scattering albedo ω, can be found in **Chapter 3**.

Importantly, radiometer retrieval and radar retrieval use different roughness parameters, being surface roughness *h* and RMS height *s* respectively, as shown in Figure 10-1. The roughness parameter required for the radar retrieval model can be obtained either from i) the RMS height map as shown in Figure 10-1, derived from interpolation of point sampled RMS height for each 1 km pixel according to field measurements and a land use map; or from ii) the relationship with the surface roughness parameter *h* used in the passive retrieval, being approximately 2.6 times *h* (Wigneron et al., 2011). Both options have been tested, with the former showing poorer results in terms of the accuracy of radar retrieval, probably due to the uncertainties involved in the estimation of 1 km resolution RMS height from the limited point sampled data. Therefore, *s* was estimate as 2.6 times *h* in this study, for the purpose of radar retrieval and backscatter prediction.

10.3 Methodology

The Bayesian merging method used in this study is based on Bayes Theorem. It is simply stated in this chapter with full details available in (Zhan et al., 2006). The optimal estimates of soil moisture $\theta(F)$ at fine resolution "F" (1 km, 3 km or 9 km resolution in this study) can be derived from an initial estimate of the background soil moisture θ_b, updated according to the difference between the observations Z and predicted observation $h([\theta_b])$ through the Kalman filter state update equation (Kalman, 1960)

$$[\theta(F)] = [\theta_b] + [K]\times\{[Z] - h([\theta_b])\}, \qquad (10\text{-}1)$$

which is effectively an implementation of Bayes Theorem. When applied to the SMAPEx area, $[\theta(F)]$ is the vector of final retrieved soil moisture at each 1 km pixel across the entire 36 km area, and $[\theta_b]$ is the vector of background soil moisture also on each 1 km pixel across the entire SMAP footprint. In this application the background is taken as the soil moisture retrieved from either Tb_h at 36 km resolution using the single channel passive microwave retrieval method (Panciera et al., 2009) as a spatially uniform field, or from the 1 km resolution PLIS backscatter using the single channel active microwave retrieval method, based on a combination of three active retrieval models (Dubois et al., 1995, Oh et al., 1992, Wang and Schmugge, 1980). Details on the active models can be found in (Zhan et al., 2006). Both alternative background soil moisture sources are tested. The vector $[Z]$ is the observations of Tb_h and Tb_v at 36 km resolution, and σ_{hh}, σ_{vv}, and σ_{hv} at 1 km resolution. The observation function $h([\theta_b])$ provides the predictions of brightness temperature and backscatter from the radiometer and radar forward models for a vegetation-covered soil using the background soil moisture θ_b on the 1km resolution grid. Details on these models can be found in (Zhan et al., 2006). The matrix [*K*] is the Kalman gain based on the uncertainties of the background states and observations through

$$[K] = [P][H^T] \,/\, ([H][P][H^T] + [R]), \tag{10-2}$$

where [*P*] represents the error covariance matrix of the background soil moisture field. In this study it is estimated by comparing the reference soil moisture taken from the work of Gao et al. (under review) to the background soil moisture [θ_b], or as the difference between the two alternative background fields, being from radar and from radiometer. The results from both approaches are compared, with the purpose to identify a practical way of estimating [*P*] operationally. Matrix [*R*] is the observation error covariance matrix based on the instrument characteristics and data processing accuracy, especially the accuracy of calibration and incidence angle normalization, as seen in **Chapter 5**. Matrix [*H*] is the linearized observation operator, which is the first derivative (Jacobian) of $h([\theta_b])$ obtained from

$$[H] = \delta h([\theta_b]) \,/\, \delta[\theta]. \tag{10-3}$$

The observation vector [*Z*] contains two 36 km brightness temperatures (at *h*- and *v*-pol) and three backscatter observations (at *hh*-, *vv*- and *hv*-pol) for each 1 km × 1 km pixels; totally 3890 observations across the entire area. Each vector/matrix can be written as

$$[Z] = [Tb_h\ Tb_v\ \ \sigma_{hh,1}\ \sigma_{vv,1}\ \sigma_{hv,1} \cdots \sigma_{hh,1296}\ \sigma_{vv,1296}\ \sigma_{hv,1296}]^T_{3890\times 1} \tag{10-4}$$

$$h([\theta]) = [Tb_h(\theta_b)\ \ Tb_v(\theta_b)\ \ \sigma_{hh,1}(\theta_b)\ \sigma_{vv,1}(\theta_b)\ \sigma_{hv,1}(\theta_b) \ldots\ \sigma_{hh,1296}(\theta_b)\ \sigma_{vv,1296}(\theta_b)\ \sigma_{hv,1296}(\theta_b)]^T_{3890\times 1} \tag{10-5}$$

$$[H] = \begin{bmatrix} \delta Tb_h/\delta\theta_{f,1} & \cdots & \delta Tb_h/\delta\theta_{f,1296} \\ \vdots & \ddots & \vdots \\ \delta\sigma_{hv,1296}/\delta\theta_{f,1} & \cdots & \delta\sigma_{hv,1296}/\delta\theta_{f,1296} \end{bmatrix}^T_{3890\times 1296.} \tag{10-6}$$

In Eq. (10-4)-(10-6), 1296 is the number of 1 km × 1 km pixels across the site and 3890 is the total number of observations: one brightness temperature observation at each of *h* and *v* polarizations and 1296 backscatter observations at each of *hh*, *vv* and *hv* polarization. The 1296 diagonal elements of matrix [*P*] are assigned the error covariance of the background soil moisture with the off diagonal elements set to be zero, assuming that each 1 km pixel has uncorrelated soil moisture error. The 3890 diagonal elements of matrix [*R*] are assigned based on the accuracy of the radiometer and radar observations with the off diagonal elements again set to be zero, assuming that observation errors are uncorrelated both spatially and between correlations.

The final downscaled soil moisture field [$\theta(F)$] is validated against the 1 km soil moisture reference map derived from the 1 km PLMR (Gao et al., under review). Results of the Bayesian algorithm are also compared to the "best" linear algorithm in **Chapter 9**, and with the soil moisture inversions from 36 km brightness temperature at *h*-pol and 1 km resolution backscatter at *hh*-pol. Downscaled soil moisture products are also evaluated at 3 km and 9 km resolution. Results on these resolutions can be obtained using two methods: i) by linearly aggregating the downscaled 1 km soil moisture to 3 km and 9 km respectively; or ii) by directly using the 3 km or 9 km resolution radar observations rather than the 1 km resolution radar observation as the input of [*Z*]. Both methods will be evaluated.

10.4 Results and Discussion

10.4.1 Passive-only and active-only soil moisture retrievals

The background soil moisture field can be estimated from direct inversion of either the 36 km radiometer brightness temperature or from the 1 km radar backscatter. Based on the observations and available ancillary parameters as stated in Section 10.2, the 36 km resolution soil moisture was obtained from the 36 km radiometer brightness temperature at *h*-pol using the single channel τ-ω model (Panciera et al., 2009). The time series of radiometer observations and retrieved soil moisture across the 9 days of SMAPEx-3 are in Table 10-1. Similarly, the background soil moisture field was obtained from the 1 km resolution radar backscatter at *hh*-pol through the active soil moisture retrieval model as shown in (Zhan et al., 2006).

Table 10-1: Time series of observed brightness temperature (*Tb*, in K) at *h*-pol and *v*-pol at 36 km resolution across the 9 days of SMAPEx-3, and the soil moisture (cm^3/cm^3) estimated from the Tb_h values using the single channel passive microwave retrieval method. Also shown are forward model estimated brightness temperatures at 36 km resolution (from radiometer inversed background soil moisture) and their first derivatives (Jacobian), at *h*-pol and *v*-pol at 36 km resolution across 9 days of SMAPEx-3.

	D1	D2	D3	D4	D5	D6	D7	D8	D9
Observed Tb_h (K)	235	234	230	232	237	240	241	244	244
Observed Tb_v (K)	259	258	252	256	260	261	260	264	264
Estimated Tb_h (K)	230	218	229	231	235	237	238	242	242
Estimated Tb_v (K)	265	256	262	264	267	269	269	272	272
Jacobian of Tb_h ($K/(cm^3/cm^3)$)	-305	-269	-290	-286	-298	-295	-305	-316	-313
Jacobian of Tb_v ($K/(cm^3/cm^3)$)	-188	-190	-188	-181	-181	-177	-181	-180	-178
Background soil moisture (cm^3/cm^3)	0.099	0.094	0.120	0.122	0.095	0.095	0.088	0.074	0.078

An example of radar retrieved soil moisture at 1 km resolution on days D3, D5 and D8 is shown in Figure 10-2, where a contrast in soil moisture values can be seen between the grassland in the middle area and the cropping land on west and east sides. It should be noted that the accuracy of soil moisture retrieval from radar is highly affected by the surface roughness and vegetation structural parameters. However, default parameters relating vegetation and roughness were used during soil moisture retrieval and forward modelling, which may influence the accuracy of retrieval from radar and so also affect the accuracy of the downscaled soil moisture. Apart from being taken as the background soil moisture field, these radar and

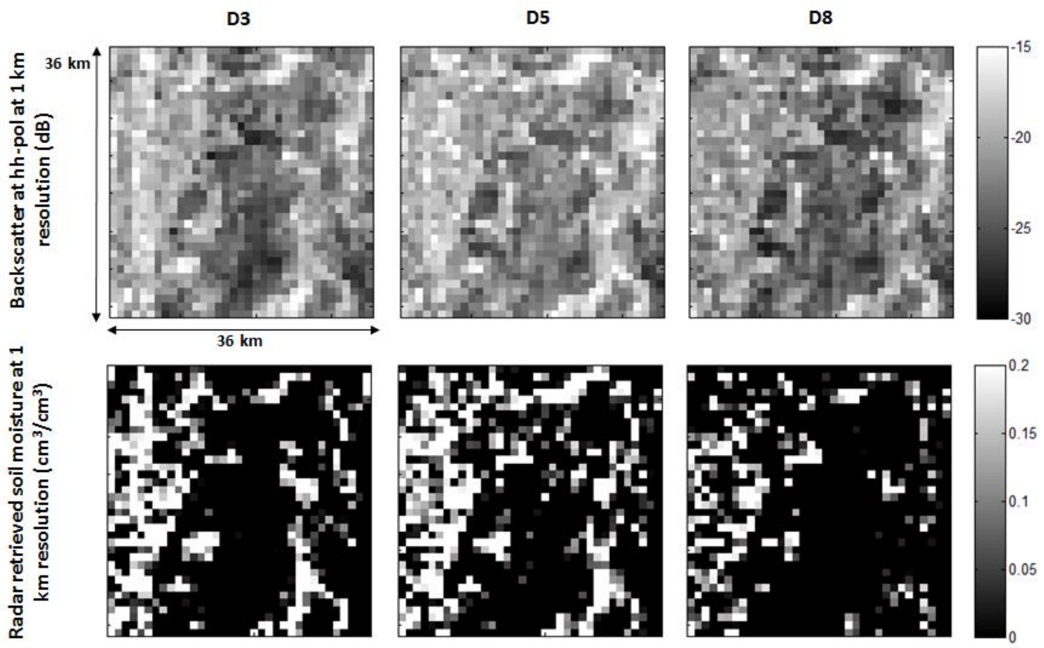

Figure 10-2: Radar observations at *hh*-pol at 1 km resolution on D3, D5 and D8 of SMAPEx-3, together with the soil moisture (cm^3/cm^3) maps retrieved from those radar observations.

radiometer inversed soil moistures will also be compared with the downscaled soil moisture product obtained from the Bayesian merging algorithm in the end.

10.4.2 Selection of the background soil moisture

In order to decide whether the radar retrieved soil moisture or the radiometer retrieved soil moisture is more suitable as the background soil moisture, a preliminary selection was conducted. During this selection, the radiometer inversed soil moisture and the radar inversed soil moisture was chosen as the background soil moisture individually, and the error covariance [*P*] of the background soil moisture obtained from comparison between the background soil moisture and the reference soil moisture, as discussed in the previous section.

The forward model estimate of *Tb* and σ and their first derivatives (Jacobian) were obtained using the background soil moisture from the radiometer or radar inversion accordingly. When using the radiometer inversed 36 km soil moisture as the background, the time series of the estimated *Tb* and its Jacobian are shown in Table 10-1 across the 9 days, with an example of estimated σ and the Jacobian on D5

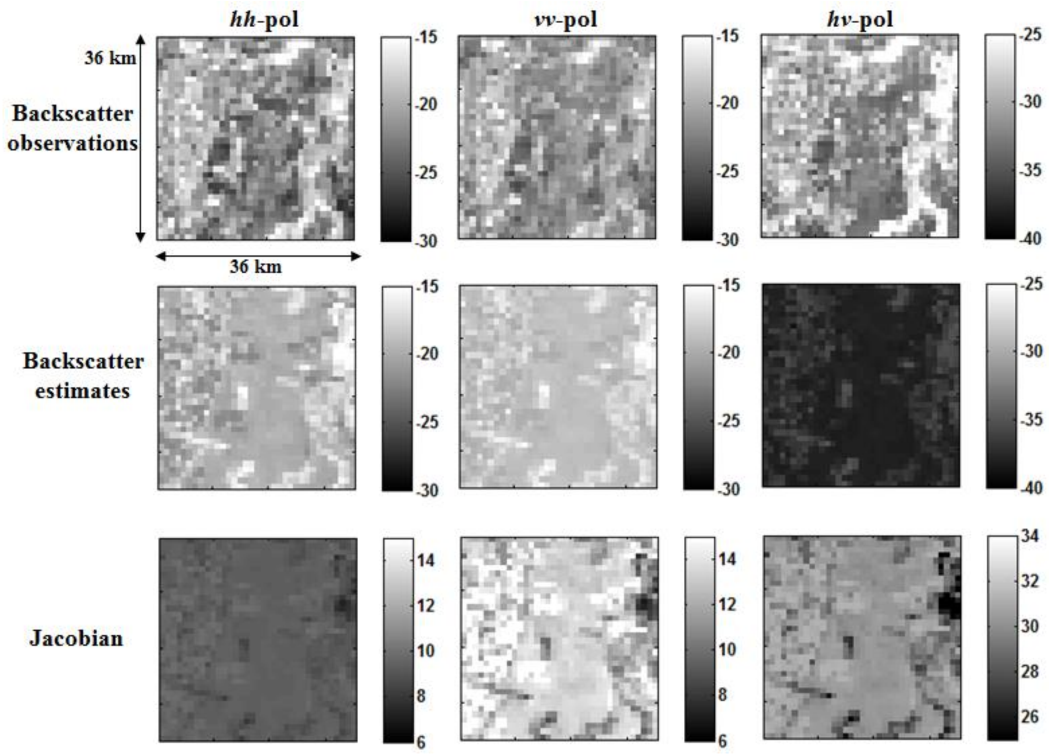

Figure 10-3: Example of radar backscatter observations, estimates and first derivatives (Jacobian) at *hh*-pol, *vv*-pol and *hv*-pol on D5 (15th September, 2011), using the 36 km resolution background soil moisture derived from the radiometer on D5. Different colour-bar scales are used for *hh*-pol, *vv*-pol and *hv*-pol.

shown in Figure 10-3. In this case, the RMSE of the estimated and observed brightness temperature across 9 days was around to be 6 K at *h*-pol and 7 K at *v*-pol, while the RMSE of the estimated and observed backscatter was around 2.1 dB at *hh*-pol, 1.6 dB at *vv*-pol and 10.1 dB at *hv*-pol. When using the radar inversed 1 km soil moisture as the background, the time series of estimated *Tb* and its Jacobian are shown in Table 10-2 across the 9 days, with an example of estimated σ and the Jacobian on D5 shown in Figure 10-4. Consequently, the RMSE of the estimated and observed brightness temperature across the 9 days was around 11 K at *h*-pol and 13 K at *v*-pol, being much higher than when using the radiometer retrieved soil moisture as the background. The RMSE of the estimated and observed backscatter was around 3.1 dB at *hh*-pol, 2.4 dB at *vv*-pol and 11.3 dB at *hv*-pol.

Table 10-2: Time series of observed brightness temperature (*Tb*, in K) at *h*-pol and *v*-pol at 36 km resolution across 9 days of SMAPEx-3, and average soil moisture (cm³/cm³) estimated from radar backscatter (σ_{hh}) using the active microwave retrieval method. Also shown are forward model estimated brightness temperatures (using spatially aggregated 1 km resolution radar inversed background soil moisture) and their first derivatives (Jacobian), at *h*-pol and *v*-pol at 36 km resolution across 9 days of SMAPEx-3.

	D1	D2	D3	D4	D5	D6	D7	D8	D9
Observed Tb_h (K)	235	234	230	232	237	240	241	244	244
Observed Tb_v (K)	259	258	252	256	260	261	260	264	264
Estimated Tb_h (K)	224	225	241	243	240	253	253	257	256
Estimated Tb_v (K)	262	261	269	272	270	278	278	279	279
Jacobian of Tb_h (K/(cm³/cm³))	-287	-292	-329	-325	-313	-339	-348	-356	-349
Jacobian of Tb_v (K/(cm³/cm³))	-189	-192	-182	-173	-178	-158	-167	-162	-159
Background soil moisture (cm³/cm³)	0.124	0.119	0.070	0.068	0.081	0.047	0.046	0.035	0.04

This evaluation was performed on each of the 9 flight days of SMAPEx-3, with similar results obtained for each day; day D5 is taken as an example here and shown in Figure 10-5. Using the radiometer inversed soil moisture as the background, the RMSE against the reference was 0.025 cm³/cm³ at 1 km resolution. In terms of the correlation between downscaled and reference soil moisture, the R^2 approximated to 0.85. In contrast, when using radar inversed soil moisture as the background, the resulting RMSE against the reference was 0.145 cm³/cm³ and the R^2 in this case was around 0.06. Results on other days were similar to those on D5, indicating that use of radiometer inversed soil moisture as the background had much better results on the accuracy of downscaled soil moisture than use of radar inversed soil moisture as the

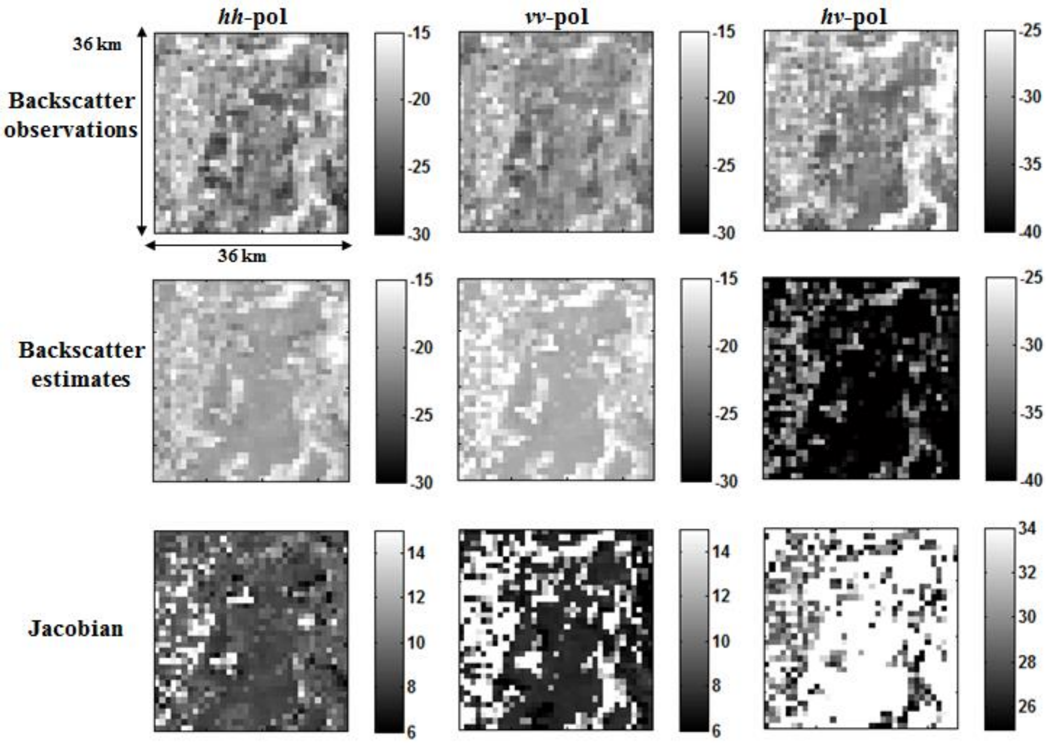

Figure 10-4: Example of radar observations, backscatter estimates and the first derivatives (Jacobian) at *hh*-pol, *vv*-pol and *hv*-pol on day D5 (15th September, 2011), using 1 km resolution background soil moisture from radar on D5. Different colour-bar scales are used for *hh*-pol, *vv*-pol and *hv*-pol.

background. The main reason for the poor results using radar inversed soil moisture as the background could be attributed to the poor background soil moisture field from use of default ancillary parameters during retrieval and forward estimation. Therefore, based on this comparison of using radar and radiometer inversed soil moisture individually as the background, the use of radiometer inversion was selected for further evaluation of the Bayesian method.

10.4.3 Downscaled results of the Bayesian merging algorithm

The radiometer retrieved soil moisture was selected as the background soil moisture field, upon which the predictions of the brightness temperature and backscatter values were obtained, as listed in Table 10-1 and Figure 10-3. As for the error covariance [*P*] of the background soil moisture, it was obtained from comparing the background soil moisture to the radar retrieved soil moisture in this case, as the true soil moisture map at fine resolution is not available for SMAP. The [*P*] estimated

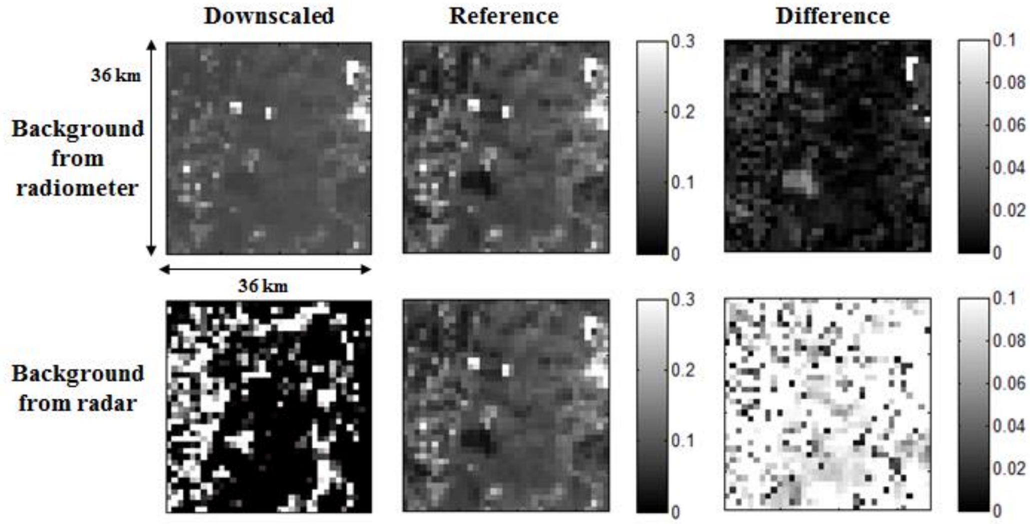

Figure 10-5: Comparison of downscaled soil moisture products on D5 (15th September, 2011) from different backgrounds, i.e. either the 36 km resolution soil moisture inversed from PLMR brightness temperature (*Tb*), or 1 km resolution soil moisture inversed from PLIS backscatter. Downscaled results are evaluated against the reference soil moisture retrieved from 1 km resolution PLMR Tb single channel retrieval.

from background and radar retrieved soil moisture was compared to the "true" [*P*], which was estimated from the background and reference soil moisture maps. Across 9 days of SMAPEx-3, the average RMSE of the estimated and "true" diagonal elements of [*P*] were compared, being around 0.04 $(cm^3/cm^3)^2$. Therefore, even without considering the correlation approximation, it is expected that the diagonal [*P*] values approximated from two alternative background fields will influence the accuracy of the soil moisture downscaling. However, the following downscaling results are based on the estimated [*P*] as the true soil moisture map at fine resolution will not be available for actual SMAP application, but are compared with those based on the "true" diagonal elements of [*P*] so as to evaluate the impact on the downscaling accuracy.

The downscaled soil moisture at 1 km resolution was obtained for each of 9 days through the Bayesian merging method. Results at other resolutions (i.e. 3 km and 9 km) were also obtained using the two methods describe previously: i) by linearly aggregating the downscaled 1 km soil moisture to 3 km and 9 km respectively; or ii)

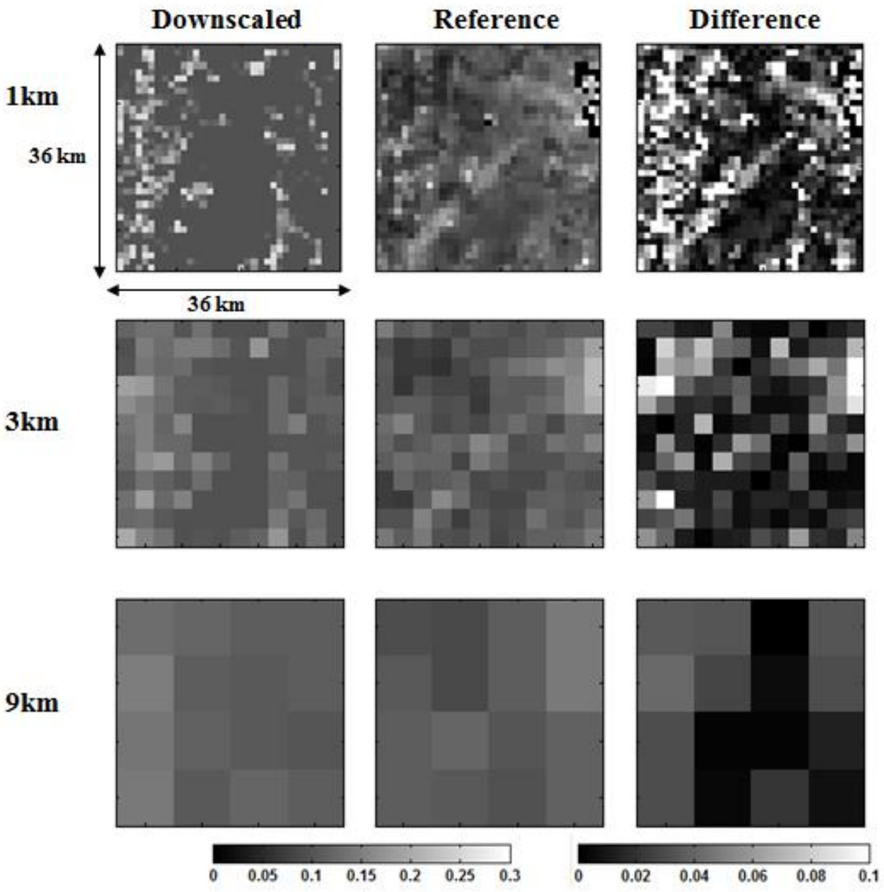

Figure 10-6: Comparison of downscaled soil moisture maps (cm³/cm³) from Bayesian merging algorithm and the reference at different resolutions (1 km, 3 km, and 9 km). Data were collected on D3 (10th September 2011) of SMAPEx-3. Pixels in black at 1 km resolution in the northeast of the reference map are the water-bodies which have been removed prior to conducting the downscaling algorithm. Also shown is the absolute difference for each pixel by comparing the downscaled soil moisture and the reference soil moisture.

by directly using the 3 km or 9 km resolution radar observations rather than the 1 km resolution radar observation as the input. Both methods have been conducted with a minor difference in the accuracy of downscaled soil moisture, being less than 0.002 cm^3/cm^3 at 9 km resolution. Consequently, all of the figures and statistics showed here are from the first method.

Three days, including D3, D5 and D8, have been chosen from the full 9 days experiment period as an example of the downscaling results. Day D3 represented the "wet" condition as a raining event happened during the first couple of days, D8

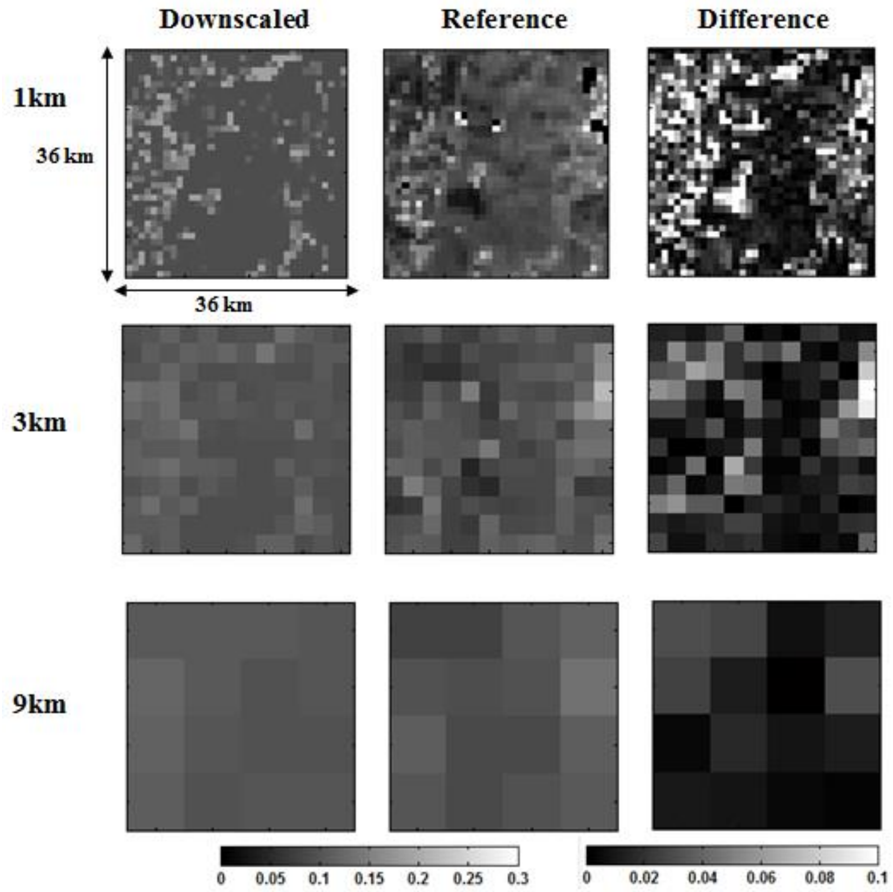

Figure 10-7: As for Figure 10-6 but on D5 (15th September 2011) of SMAPEx-3.

represented the “dry” condition after a drying-down period, and D5 was selected to represent the status in between. Results on those three days are shown in Figure 10-6, Figure 10-7 and Figure 10-8, with the water-bodies removed prior to conducting the downscaling procedure.

By comparing the downscaled soil moisture to the reference soil moisture map, it is noted from Figure 10-6, 10-7 and 10-8 that the error of downscaling was greater in the eastern and western area than in the middle area of the SMAPEx site, probably due to the effect from different land cover types. The eastern and western areas were dominated by cropping sites which had various conditions in terms of vegetation types, heights, VWC, biomass and roughness etc., while the middle area was mainly occupied by relatively homogeneous grassland with more uniform surface conditions. As radar observations were more affected by the vegetated area than the grassland area, the accuracy of radar observations to reflect the actual distribution of soil

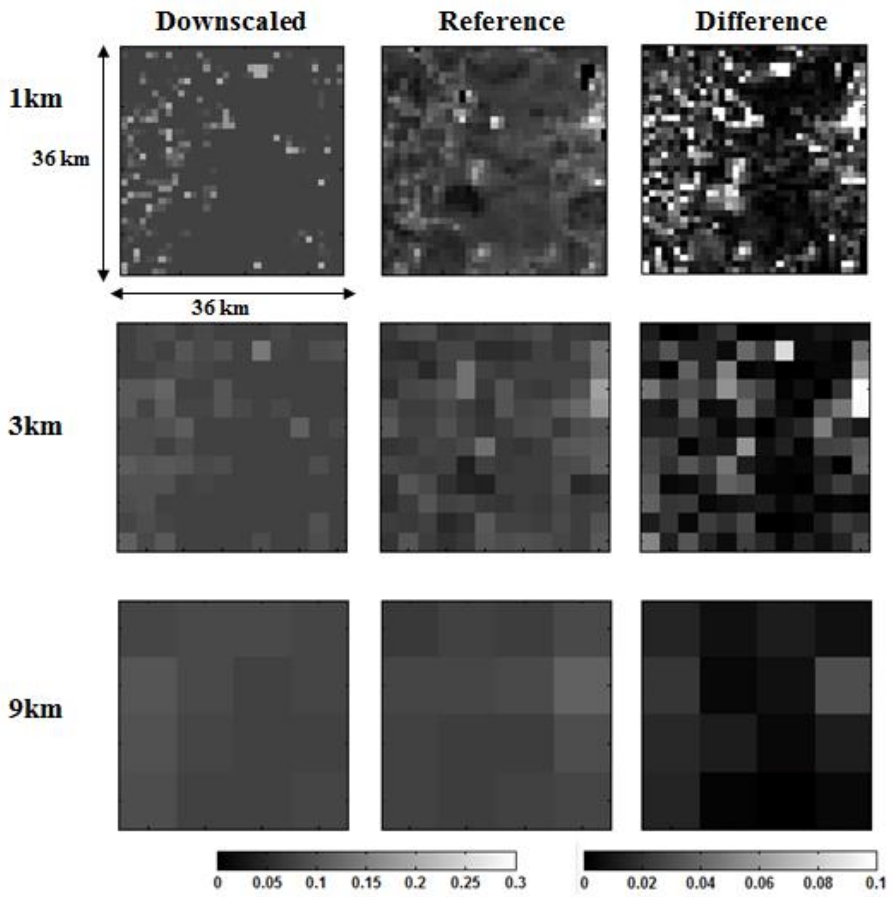

Figure 10-8: As for Figure 10-6 but on D8 (21st September 2011) of SMAPEx-3.

moisture across the entire site was hampered by the heterogeneity in vegetation. However, the influence from the surface conditions was lowered when aggregated to larger scale, as the variations in the vegetation and surface roughness etc. were smoothed out by averaging the pixels at 1 km to 3 km and to 9 km resolution. Consequently, the error of downscaling reduced from 1 km to 9 km, as expected. By comparing the pattern in the downscaled soil moisture map to the pattern in the reference map it was found that results on D3 was poorest in terms of pattern match among those three days. The reference map at 1 km resolution in Figure 10-6 had higher soil moisture content, not only in the cropping areas but also shown in a strip spreading from the left-bottom corner to the centre of the SMAPEx site, because of rain in that area. However, the downscaled result in Figure 10-6 could not capture this soil moisture pattern. In contrast, results on D5 and D8 showed better pattern match than D3, mainly because the heterogeneity across the entire site reduced.

By comparing the results for D5 as shown in Figure 10-5 and Figure 10-7 based on different [*P*], the RMSE of downscaled soil moisture at 1 km resolution was around 0.020 cm^3/cm^3 in Figure 10-5 when using the "true" [*P*] and 0.043 cm^3/cm^3 in Figure 10-7 when using the approximate [*P*]. The latter had a higher error due to the poorer estimation of [*P*]. Consequently, it is expected that more accurate estimation of [*P*], including correct consideration of the correlations would contribute to better downscaled results. Results on other days can be found in Table 10-3, from which it is noted that the RMSEs based on the "true" [*P*] are generally lower than those based on the [*P*] approximated from radiometer and radar retrieved soil moisture, across all 9 days. The average RMSE using the "true" [*P*] was around 0.019 cm^3/cm^3 at 1 km, 0.017 cm^3/cm^3 at 3 km and 0.013 cm^3/cm^3 at 9 km respectively, which would be the "best" performance of the Bayesian merging method given that the estimation [*P*] is improved to be very close to the "true" [*P*].

According to Table 10-3, the error of downscaling reduced when aggregating from 1 km to 9 km, with an improvement in accuracy of around 0.030 cm^3/cm^3. It is also noticed that the error of downscaling reduced following the drying down from D1 to D9 due to the corresponding decreased heterogeneity of the surface conditions. This is consistent with results found from the other methods, as also shown in Table 10-3. The poorest results were found from the radar-only retrieval method, probably due to the strong influence from vegetation and surface roughness conditions and the poor predictive skill of this model using default parameters. This was followed by the radiometer-only retrieval, which used a uniform soil moisture value across the entire site. Clearly the best downscaling results were found from the more sophisticated downscaling methods that rely upon merging data from the active and passive approaches, with an improvement of approximately 0.01 cm^3/cm^3 over the radiometer-only method and 0.04 cm^3/cm^3 over the radar-only method at 9 km resolution. The optional method and the Bayesian method (when using the approximate [*P*]) showed minor difference in terms of RMSE, with both being around 0.02 cm^3/cm^3 at 9 km resolution.

Table 10-3: Root Mean Square Error (RMSE, in the unit of cm^3/cm^3) of downscaled soil moisture from the different downscaling methods across the 9 days (D1 to D9) of SMAPEx-3 at 1 km, 3 km and 9 km resolution. * Bayesian downscaling results based on the "True" error covariance [*P*].

Algorithm	Resolution	D1	D2	D3	D4	D5	D6	D7	D8	D9	Average
Bayesian	**1km**	0.048	0.059	0.059	0.062	0.043	0.045	0.046	0.048	0.041	0.050
	3 km	0.038	0.046	0.039	0.039	0.029	0.031	0.026	0.029	0.026	0.034
	9 km	0.026	0.030	0.024	0.027	0.017	0.020	0.009	0.017	0.013	0.020
Bayesian*	**1km**	0.018	0.022	0.022	0.022	0.020	0.016	0.015	0.018	0.018	0.019
	3 km	0.016	0.021	0.017	0.016	0.017	0.015	0.015	0.016	0.016	0.017
	9 km	0.013	0.020	0.011	0.012	0.012	0.013	0.012	0.012	0.012	0.013
Optional	**1km**	0.048	0.053	0.047	0.040	0.037	0.040	0.041	0.038	0.032	0.042
	3 km	0.037	0.042	0.035	0.030	0.028	0.025	0.025	0.028	0.022	0.030
	9 km	0.025	0.029	0.025	0.021	0.018	0.020	0.015	0.019	0.015	0.021
Radiometer retrieval	**1km**	0.064	0.095	0.059	0.056	0.061	0.056	0.051	0.050	0.052	0.061
	3 km	0.044	0.068	0.04	0.038	0.042	0.037	0.029	0.032	0.033	0.040
	9 km	0.032	0.059	0.025	0.025	0.024	0.022	0.017	0.019	0.020	0.027
Radar retrieval	**1km**	0.154	0.161	0.146	0.143	0.144	0.129	0.121	0.113	0.115	0.136
	3 km	0.099	0.096	0.091	0.092	0.084	0.083	0.070	0.071	0.069	0.084
	9 km	0.070	0.057	0.064	0.071	0.052	0.065	0.050	0.056	0.053	0.060

Apart from the evaluation on individual days, comparison of these four methods was also conducted by combining all 9 days of results, as shown in the scatterplots in Figure 10-9. The RMSE indicated in Figure 10-9 was calculated by comparing all 9 days' time series of downscaled soil moisture with time series of reference soil moisture. The correlation between downscaled soil moisture and reference across 9 days, denoted by correlation coefficient R^2, was also studied. Again, the radar-only retrieval method showed the poorest correlation between downscaled and reference soil moisture, confirming that radar alone has little potential to provide a medium resolution soil moisture product with high accuracy without first making significant improvements to the algorithm and/or its parameterisation. Although the radiometer-only retrieval method had a RMSE close to that of the optional and Bayesian methods, it showed very poor spatial correlation between the downscaled and reference soil moisture, attributed to the fact that the same soil moisture was used at each 1 km × 1 km pixel. Therefore variation of soil moisture across the entire site was not well captured by the radiometer-only method, with the more sophisticated methods adding considerable spatial skill. In term of the Bayesian merging method, its downscaled soil moisture at 1 km resolution was found to be poorly related to the reference soil moisture, with this situation improving considerably at 9 km resolution, which was similar to the scenario for the optional method. Consequently, the optional and Bayesian merging methods were found to have similar correlation between downscaled and reference soil moisture at 9 km resolution, but the optional method showed a superiority in downscaling soil moisture when applied at higher resolutions. Results from the 9 days were divided into two groups (i.e. D1-D3 and D4-D9) in order to differentiate the behaviour of downscaling algorithm with and without influence from the rain period. As shown in Figure 10-9, downscaled soil moisture on D1-D3 were less correlated to the reference than those on D4-D9, due to the more heterogeneous surface conditions on the first couple of days following the rain event.

The RMSE and R^2 for each pixel have also been calculated by using the time series of downscaled soil moisture value and reference soil moisture across the 9 days at that pixel. The spatial distribution of RMSE and R^2 for the different methods can be found in Figure 10-10 and Figure 10-11. In comparison to the other methods, the radar-only retrieval method showed the greatest error and poorest correlation in retrieving medium resolution soil moisture. The large errors for the radar-only retrieval were expected due to the difficulty associated with the radar inversion modelling.

In terms of the impact from land cover type, the cropping areas had higher RMSE and lower R^2 when compared to the grassland areas, as shown in the downscaled

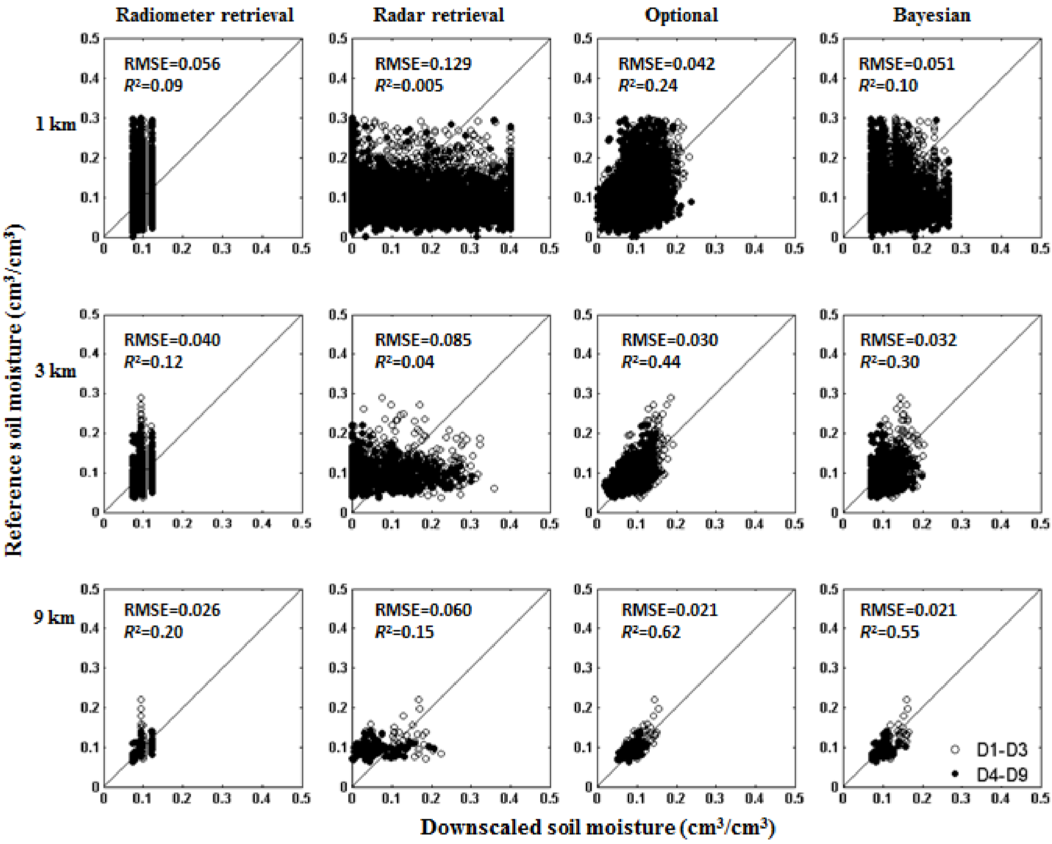

Figure 10-9: Scatterplot of the reference and downscaled soil moisture from the radiometer-only retrieval method, radar-only retrieval method, the optional downscaling algorithm for SMAP and the Bayesian merging method, at 1 km, 3 km, and 9 km resolution. Performance of each method was evaluated in terms of Root-Mean-Square-Error (RMSE, in unit of cm^3/cm^3) and correlation (R^2) between downscaled and reference soil moisture. Data are from all 9 days of SMAPEx-3, with data from Day 1 to Day 3 denoted by open circles, while data from Day 4 to Day 9 denoted by solid circles.

map from the optional method and Bayesian method, due to the strong influence from vegetation and surface roughness on radar observations. But when averaging to larger scale, the difference in RMSE and R^2 across the entire site decreases. Especially at 9 km, the Bayesian downscaling algorithm showed very promising results in terms of RMSE and R^2.

The above analysis was done by removing the water-bodies which constituted approximately 1% of the study area. A study on the influence from water-bodies was also carried out in order to simulate more realistic SMAP data. In this case, a higher

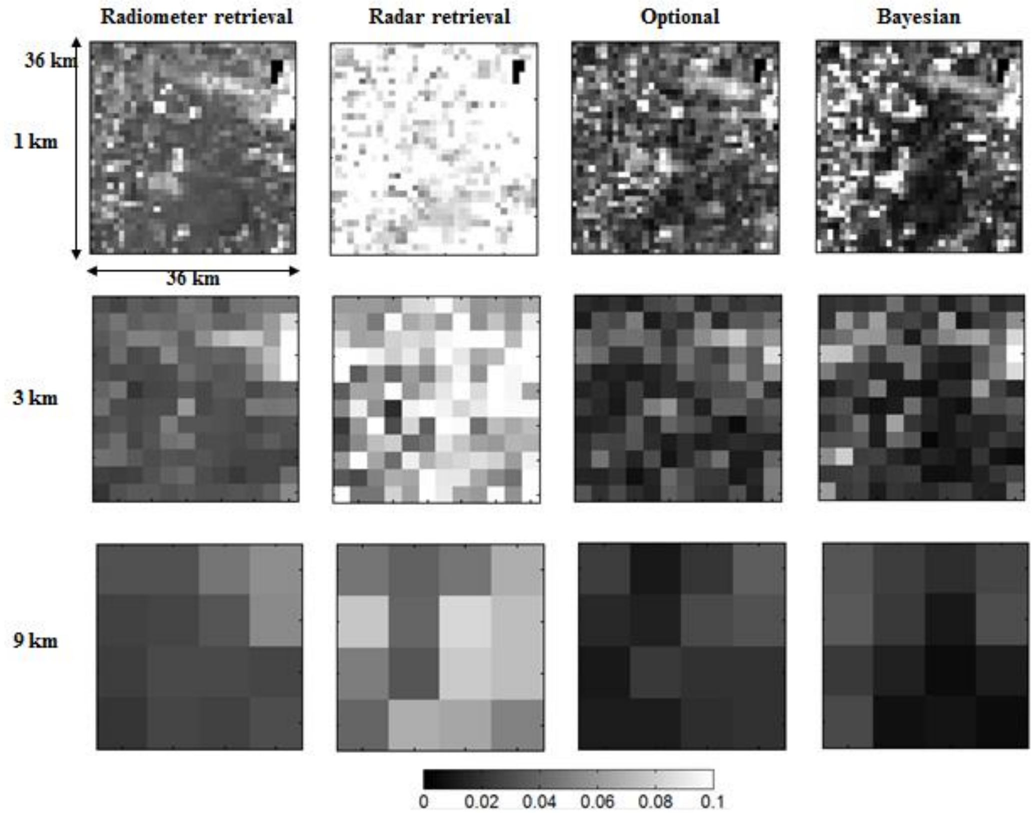

Figure 10-10: Spatial distribution of Root-Mean-Square-Error (RMSE, in unit of cm^3/cm^3) for radiometer-only retrieval method, radar-only retrieval method, the optional downscaling algorithm for SMAP and the Bayesian merging method across the entire SMAPEx site at 1 km, 3 km and 9 km resolution, respectively. RMSE for each pixel was calculated from the downscaled soil moisture and the reference soil moisture at this pixel across 9 days of SMAPEx-3.

average RMSE (across the 9 days) was obtained, being 0.056 cm^3/cm^3 at 1 km, 0.038 cm^3/cm^3 at 3 km and 0.023 cm^3/cm^3 at 9 km resolution for the Bayesian merging method when including the existence of water-bodies.

10.5 Chapter Summary

The Bayesian merging method was tested for its ability to provide a medium resolution soil moisture map by using coarse resolution radiometer observations and fine resolution radar observations. The main objective of this study was to assess the feasibility of this downscaling approach for its application in the SMAP mission, by using experimental data rather than the synthetic data used in its development. The data set used here was from the SMAPEx-3 field campaign in Australia; the same as for the three linear downscaling algorithms tested in **Chapter 9**. A finding from this study was that the accuracy of the Bayesian merging method was affected by the accuracy of soil moisture retrieval from fine resolution radar observations; it is expected that a better radar retrieval algorithm would likely improve the Bayesian method performance. Moreover, the downscaling performance was better in the homogenous grassland areas than the cropping areas which contained more heterogeneous surface conditions. In comparison to other medium resolution soil moisture retrieval methods, this non-linear Bayesian merging method had similar results in terms of RMSE and correlation R^2 at 9 km resolution as the best linear downscaling algorithms tested in an earlier chapter, and had much better results than radar-only or radiometer-only retrieval methods. The main limitation of the Bayesian method was the use of default parameters involved in the radar retrieval model. Accordingly, it is expected that by using an improved radar model the Bayesian merging method will have great potential to retrieve a more accurate soil moisture product at medium resolution then the alternative methods.

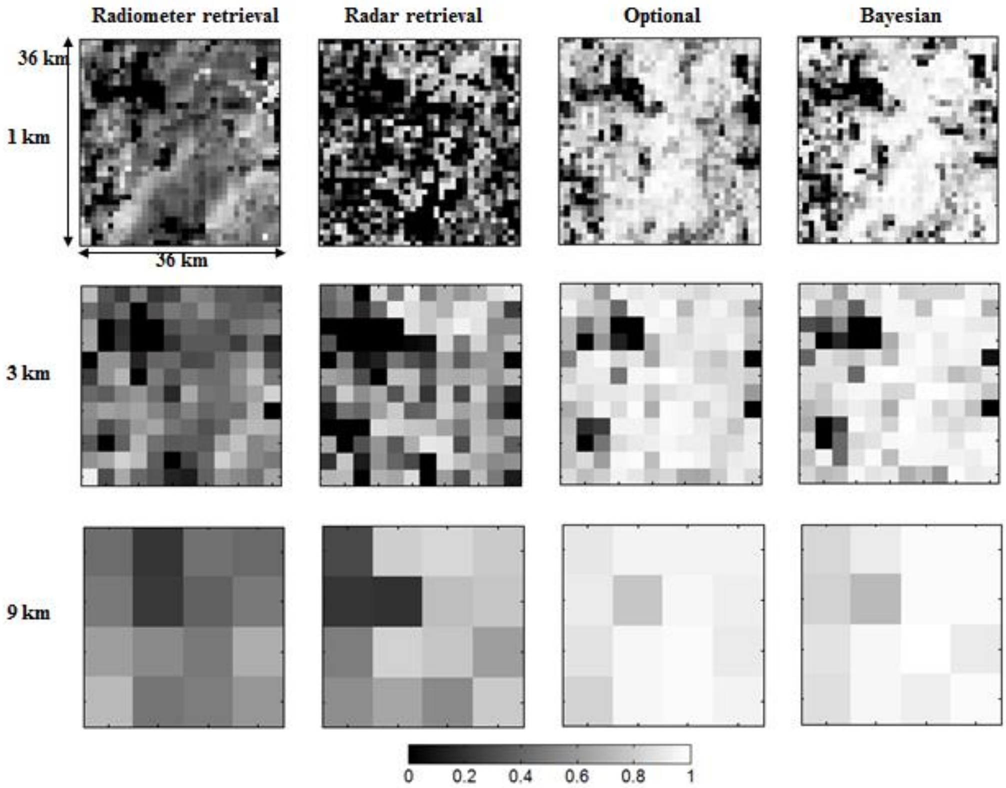

Figure 10-11: Spatial distribution of correlation coefficient (R^2) for radiometer-only retrieval method, radar-only retrieval method, the optional downscaling algorithm for SMAP and the Bayesian merging method across the entire SMAPEx site at 1 km, 3 km and 9 km resolution, respectively. R^2 for each pixel was calculated from the downscaled soil moisture and the reference soil moisture at this pixel across 9 days of SMAPEx-3.

11 Conclusions and Future Work

11.1 Conclusions

The objective of this research was to test candidate active-passive soil moisture downscaling algorithms with a comprehensive experimental data set, for development of pre-launch algorithms of the SMAP mission. Existing active-passive downscaling algorithms including the baseline and optional downscaling algorithms for SMAP, a change detection method, and the Bayesian merging method have been selected. Previously these had been mostly studied with synthetic data. Therefore, the main contribution of this research was to provide an extensive study on alternate soil moisture downscaling algorithms using a consistent and comprehensive data set from field campaigns conducted in Australia, thus providing a solid recommendation on the preferred method when applied to the real world.

11.1.1 Preliminary research

Given the importance of applying the downscaling algorithm to experimental data, the first step of this research was to test the baseline downscaling algorithm with existing satellite data, as described in **Chapter 4**. Radiometer observations from the SMOS satellite and radar observations from ASAR (onboard ENVISAT) were used for this purpose, as they were the best options for closely simulating the data from SMAP. In this study the value of β was estimated using regression on pairs of SMOS Tb and ASAR σ data at the same resolutions within the SMAPEx area. The robustness of β was subjected to the number of available Tb and σ data pairs. The variation of β with seasons was illustrated, showing that β must be applied based on the specific land surface conditions, in order to ensure the accuracy of downscaled results. Another issue pertaining to β was the size of study area. Since β is related to vegetation type, surface roughness, land management and other factors, the robustness of its value is affected by the heterogeneity of the study area. At the beginning of this study, β was assumed to be time-invariant and homogenous in the entire area, which increased the errors obtained with the downscaling algorithm.

Results from this study indicated downscaling results using the baseline algorithm with SMOS *Tb* and ASAR σ_{hh} data generally did not meet the accuracy requirement, having a downscaled RMSE of not better than 5 K at 10 km resolution. While a better downscaling performance would be expected using an improved parameterization of β based on more pairs of radar and radiometer data for linear regression, and/or accommodating spatial variation, the main limitation from this particular study was felt to be from the characteristics of the available radar data. Limitations from frequency band, available polarization, limited concurrent overpass and high noise level have likely resulted in the failure to meet the performance requirement of the SMAP baseline downscaling algorithm using data from these two satellites. Consequently, it was concluded from this study that an experimental data set with identical characteristics to SMAP should be utilized in order to test the downscaling algorithm performance.

11.1.2 Simulation of the SMAP data stream

The SMAPEx field campaigns, conducted in Australia, provide the opportunity to simulate SMAP observations from an airborne simulator with radar and radiometer mounted together. Apart from the airborne observations, ground sampling was conducted concurrently with the aim to provide a reference brightness temperature and soil moisture data set for evaluating the downscaling algorithm performance. However, in order to simulate the prototype SMAP data stream, data collected from the aircraft simulator had to be processed in terms of spatial aggregation and incidence angle normalization so as to closely replicate features of the SMAP data.

Results suggest that the RMSD of the normalization method would be less than 0.8 dB for radar data from PLIS when aggregating the pixels to larger than 1 km; the RMSD would be less than 1 K for radiometer data from PLMR when upscaling to a resolution coarser than 6 km. In terms of upscaling, the error of linear aggregation for PLIS in power units is expected to be less than 2.7 dB when upscaling to larger than 150 m resolution, with the majority of this error being due to incidence-angle normalization, while for PLMR the upscaling error is around 2 K. Multi-azimuth observations from PLIS and PLMR were analysed for several fields, suggesting that fields with distinct row structure would induce obvious azimuthal signature at high spatial resolution. However, such signatures tended to cancel each other out at coarse resolution, as the surface characteristics became more heterogeneous. Thus, the potential impact of the SMAP rotating antenna and the subsequent azimuthal impacts on the radar and radiometer data is expected to be minimal at the resolutions of SMAP. Moreover, it was concluded that the CDF-normalization method may be used together with linear aggregation to simulate the SMAP data stream from the SMAPEx dataset. After evaluating the accuracy of each method in **Chapter 5**, results indicated that airborne observations from the SMAPEx field campaigns can be reliably used to simulate the SMAP data stream for subsequent use in active-passive soil moisture algorithm development.

11.1.3 Evaluation of the SMAP baseline downscaling algorithm

Using the simulated SMAP data, the baseline downscaling algorithm proposed for the SMAP mission was tested in **Chapter 6**. The rationale behind this algorithm is an assumption of linearity between brightness temperature and backscatter. The product of this step is a downscaled brightness temperature at 9 km resolution. The average RMSE of downscaled *Tb* across 9 days at 9 km resolution was 3.1 K and 2.6 K at *h*- and *v*-polarization respectively, which increased to 5.5 K and 4.5 K at 3 km resolution, and 8.2 K and 6.6 K at 1 km resolution. The algorithm was found to perform poorly in the early days of the experiment due to spatial heterogeneity caused by a large rainfall event in the study area. In contrast, the last 5 days of the experiment, characterized by a drying down period and no rainfall, showed an increase in the algorithm performance, with an RMSE consistently better than 2.4 K at 9 km resolution, indicating that the baseline downscaling algorithm has the potential to fulfil the requirements of SMAP.

It was also shown that the accuracy of the downscaling approach was primarily determined by the correlation between *Tb* and σ, which was in fact affected by the vegetation characteristics across the entire study area and the sensitivity of brightness temperature relative to radar backscatter, as quantified by the slope β of the linear regression. Moreover, it was found that σ at *vv*-polarization was best correlated to *Tb* at both polarizations, therefore being more suitable for use in the downscaling algorithm than σ at *hh*- and *hv*-polarization. While a better estimation of β at 36 km scale may be expected from SMAP than that achieved here, due to the relatively short nature of this experiment, the impact from spatial variability is expected to be of greater consideration. Henceforth, it is indicated from this study that the baseline downscaling algorithm could perform well over the relatively homogenous grassland, but that performance is poorer than the SMAP error budget in the cropping area due to the influence from greater heterogeneity. Consequently, a single value of β (the sensitivity of Tb to σ) across the entire SMAPEx site was not adequate for correctly representing the sensitivity between Tb to σ when applied to a heterogeneous area. It is suggested that improved spatially distributed estimation of β should be undertaken in order to improve the downscaling, such as through the correlation between β and RVI from fine resolution radar observations.

11.1.4 Effect of land cover type and land surface heterogeneity

Based on the finding of **Chapter 6**, use of a spatially varied parameter β according to land cover type was studied in **Chapter 7**. The main findings from this study included: i) the sensitivity of Tb to σ varied significantly with respect to land cover types, with the highest value found in wetland areas (with water body included) and the lowest value in grassland area; ii) the accuracy of the downscaling algorithm in grassland areas could meet the accuracy requirements of SMAP while in cropland areas it could not due to the higher complexity of land surface conditions; and iii) the influence from as little as 6% coverage by water-bodies was confirmed to have a significant impact on the downscaling performance and should therefore be removed prior to downscaling. Further to this study, the baseline downscaling algorithm was tested in **Chapter 8** using very high resolution (i.e. 1 km Tb was disaggregated to 250 m using 100 m resolution σ), in order to test the robustness of the baseline algorithm at different resolutions and to further assess the impact of land surface heterogeneity under more homogeneous pixel footprints. The main conclusion from this study was that the accuracy of the downscaling approach was primarily determined by the land cover/use type, due to the strong impact on the parameter β. The baseline downscaling algorithm of SMAP as tested in **Chapter 6-8** maintained the same downscaling ratio as will be applied in SMAP, i.e. 36:9:3.

11.1.5 Comparison with alternate linear methods

The output from the baseline downscaling algorithm of SMAP was a downscaled *Tb*, which then had to be converted to downscaled soil moisture. Consequently, the main objective of **Chapter 9** was to evaluate the derived soil moisture from the baseline algorithm and to compare the results across three alternative soil moisture downscaling algorithms: i) the baseline soil moisture downscaling algorithm for SMAP, which is based on a downscaled brightness temperature; ii) the optional soil moisture downscaling algorithm for SMAP, which uses the fine resolution radar observations to downscale the coarse resolution soil moisture to medium-resolution soil moisture directly; and iii) a change detection method, which is based on the assumption of a linear relationship between *Tb* and σ, but using the concept of temporal changes in fine resolution radar observations to update the soil moisture spatial distribution at the previous time.

The average RMSE of downscaled soil moisture across the 9 days at 9 km resolution was 0.019 cm^3/cm^3, 0.021 cm^3/cm^3 and 0.026 cm^3/cm^3 for baseline, optional, and change detection methods, respectively. While all three methods met the RMSE requirement at 9 km resolution, the ability to detect the spatial pattern varied considerably. The change detection method had the poorest spatial correlation. Consequently the optional algorithm produced the best overall downscaling results, with comparable RMSE to the baseline method, but with much higher correlation between downscaled product and reference soil moisture.

The assumption of a constant β across entire SMAPEx may influence the resulting accuracy of each downscaling algorithm. While a better estimation of the distribution of β across the entire site may be obtained through its correlation with land cover, vegetation water content, surface roughness etc. in future study, providing the opportunity to retrieve medium resolution soil moisture product more accurately.

11.1.6 Comparison with Bayesian merging method

In contrast to the linear downscaling algorithms, a non-linear downscaling algorithm – the Bayesian merging method – was also assessed. This non-linear algorithm uses the concept of Bayes theorem to update initial background soil moisture with both fine resolution radar observations and coarse resolution radiometer observations simultaneously. Previously, this method had only been tested using synthetic data, meaning that this was the first study to test it with realistic experimental data. The RMSE of downscaled soil moisture at 9 km resolution from the Bayesian merging method was around 0.02 cm^3/cm^3, being similar to the "best" linear algorithm – the optional downscaling algorithm tested in **Chapter 9**. However, the non-linear Bayesian merging method had slightly poorer results in terms of the spatial correlation when compared to the optional algorithm. The main limitation of this Bayesian method was the accuracy of the radar model. It is expected that by using a more accurate radar parameterisation that the Bayesian merging method will surpass the retrieval accuracy of the optional model.

To fully test the added skill of these downscaling methods, the optional and Bayesian merging method results were also compared to traditional inversions of the radar at the downscaled resolution directly, and from the radiometer observations when assuming a uniform spatial field. The poorest results were from the radar-only retrieval method, probably due to the strong influence from vegetation and surface roughness conditions and the use of default parameters. This was followed by the radiometer-only retrieval, due to the uniform soil moisture distribution assumption across the entire site. Based on this analysis the optional algorithm is recommended as the currently preferred approach due to its simplicity of application and slightly better results when compared to the Bayesian algorithm. However, both methods have the potential to provide better retrievals of soil moisture, through a better estimation of β in the optional algorithm and a better radar algorithm in the Bayesian algorithm.

11.2 Future work

Improvement and future work mainly include:

1. A better estimation for β may obtained from its correlation with vegetation characteristics, e.g. land cover type and RVI etc., with the aim to obtaining a distribution map of β across the entire study area. Therefore, study on the parameterization of β from vegetation characteristics will be conducted in the

future work, thus having the ability to retrieving better results for baseline and optional downscaling algorithms for SMAP. This future work mainly includes the collection of time series of radiometer and radar observations from aircraft in order to obtain the value of β through regression. RVI can be simply obtained from the fine resolution radar observations at different polarizations, and therefore will be able to be studied on its correlation with β.

2. Performance of the Bayesian merging method may get improved by using dynamic maps of ancillary parameters involved in the soil moisture retrievals. More accurate parameters including the surface roughness, VWC, land cover classification, other vegetation parameters etc., will be obtained through investigations on the retrieval of those parameters; moreover, different radar retrieval models will be evaluated in order to decide the "best" for application in Bayesian method.
3. The effect from seasonality/time on the downscaling algorithms will be conducted, with data collected from different seasons, e.g. from SMAPEx-1, -2 and -3 field campaigns.
4. Future work will also include the studies on retrieving temporal changes of soil moisture at medium resolution (~9 km). Again, those four downscaling methods, baseline, optional, change detection and Bayesian merging method, will be investigated on their ability to retrieve medium-resolution soil moisture changes.
5. Alternative downscaling approaches will be investigated in future, which may use the land surface model output or/and the high resolution *Tb* data from shorter wavelengths to downscale the coarse resolution soil moisture.

References

ADAMO, F., ANDRIA, G., ATTIVISSIMO, F. & GIAQUINTO, N. 2004. An acoustic method for soil moisture measurement. *Instrumentation and Measurement, IEEE Transactions on,* 53**,** 891-898.

ANDERSON, M. C., NORMAN, J. M., DIAK, G. R., KUSTAS, W. P. & MECIKALSKI, J. R. 1997. A two-source time-integrated model for estimating surface fluxes using thermal infrared remote sensing. *Remote sensing of environment,* 60**,** 195-216.

BINDLISH, R., JACKSON, T., COSH, M., YUEH, S. & DINARDO, S. 2010. Combined passive and active microwave observation of soil moisture during SMAPVEX08. *Proc. IEEE International Geoscience and Remote Sensing Symposium 2010.* Honolulu, USA.

BINDLISH, R., JACKSON, T., RUIJING, S., COSH, M., YUEH, S. & DINARDO, S. 2009. Combined Passive and Active Microwave Observations of Soil Moisture During CLASIC. *Geoscience and Remote Sensing Letters, IEEE,* 6**,** 644-648.

BLONQUIST JR., J. M., JONES, S. B. & ROBINSON, D. A. 2005. Standardizing Characterization of Electromagnetic Water Content Sensors: Part 2. Evaluation of Seven Sensing Systems. *Vadose Zone Journal,* 4**,** 1059-1069.

BLUM, A., FLAMMER, I., FRIEDLI, T. & GERMANN, P. 2004. Acoustic Tomography Applied to Water Flow in Unsaturated Soils. *Vadose Zone J.,* 3**,** 288-299.

BOKEN, V. K., CRACKNELL, A. P. & HEATHCOTE, R. L. 2005. Monitoring and Predicting Agricultural Drought - A Global Study. Oxford University Press.

BOLTEN, J. D., LAKSHMI, V. & NJOKU, E. G. 2003. Soil moisture retrieval using the passive/active L- and S-band radar/radiometer. *Geoscience and Remote Sensing, IEEE Transactions on,* 41**,** 2792-2801.

BRUBAKER, K. L. & ENTEKHABI, D. 1996. Analysis of Feedback Mechanisms in Land-Atmosphere Interaction. *Water Resour. Res.,* 32**,** 1343-1357.

CABLE, J. W., KOVACS, J. M., SHANG, J. & JIAO, X. 2014. Multi-Temporal Polarimetric RADARSAT-2 for Land Cover Monitoring in Northeastern Ontario, Canad. *Remote Sensing,* 6**,** 2372-2392.

CAMPBELL, C. A., SELLES, F., ZENTNER, R. P., MCCONKEY, B. G., BRANDT, S. A. & MCKENZIE, R. C. 1997. Regression model for predicting yield of hard red spring wheat grown on stubble in the semiarid prairie. *Modele de prediction par regression du rendement du ble de printemps roux vitreux cultive en continu dans la zone semi-aride des Prairies,* 77**,** 43-52.

CARDOT, H., MAISONGRANDE, P. & FAIVRE, R. 2005. Varying-Time Random Effects Models for Longitudinal Data: Spatial Disaggregation and Temporal Interpolation of Remote Sensing Data. *Journal of Applied Statistics,* 30**,** 1185-1999.

CARLSON, T. N., GILLIES, R. R. & SCHMUGGE, T. J. 1995. An interpretation of methodologies for indirect measurement of soil water content *Agricultural and Forest Meteorology,* 77**,** 191-205.

CARREIRAS, J. M. B., VASCONCELOS, M. J. & LUCAS, R. M. 2012. Understanding the relationship between aboveground biomass and ALOS PALSAR data in the forests of Guinea-Bissau (West Africa). *Remote Sensing of Environment,* 121**,** 426-442.

CHAMPAGNE, C., BERG, A. A., MCNAIRN, H., DREWITT, G. & HUFFMAN, T. 2012. Evaluation of soil moisture extremes for agricultural productivity in the Canadian prairies. *Agricultural and Forest Meteorology,* 165**,** 1-11.

CHAMPOLIVIER, L. & MERRIEN, A. 1996. Effects of water stress applied at different growth stages to Brassica napus L. var. oleifera on yield, yield components and seed quality. *European Journal of Agronomy,* 5**,** 153-160.

CHAUHAN, N., MILLER, S., & ARDANUY, P. 2003. Spaceborne soil moisture estimation at high resolution: a microwave-optical/IR synergistic approach. *International Journal of Remote Sensing,* 22**,** 4599-4622.

CHEHBOUNI, A., NOUVELLON, Y., KERR, Y. H., MORAN, M. S., WATTS, C., PREVOT, L., GOODRICH, D. C. & RAMBAL, S. 2001. Directional effect on radiative surface temperature measurements over a semiarid grassland site. *Remote Sensing of Environment,* 76**,** 360-372.

COLLIANDER, A., CHAN, S., KIM, S.-B., DAS, N., YUEH, S., COSH, M., BINDLISH, R., JACKSON, T. & NJOKU, E. 2012a. Long term analysis of PALS soil moisture campaign measurements for global soil moisture algorithm development. *Remote Sensing of Environment,* 121**,** 309-322.

COLLIANDER, A., KIM, S., YUEH, S., COSH, M., JACKSON, T. & NJOKU, E. 2010. Azimuthal Signature of Coincidental Brightness Temperature and Normalized Radar Cross-section Obtained Using Airborne PALS Instrument. *Progress in Electromagnetics Research symposium, 2010. PIERS 2010.*

COLLIANDER, A., YUEH, S., CHAZANOFF, S., DINARDO, S., O'DWYER, I., JACKSON, T., MCNAIRN, H., BULLOCK, P., WISEMAN, G., BERG, A., MAGAGI, R. & NJOKU, E. Airborne active and passive L-band measurements using PALS instrument in SMAPVEX12 soil moisture field campaign. 2012b. 85240G-85240G-6.

COVELLO, F., BATTAZZA, F., COLETTA, A., LOPINTO, E., FIORENTINO, C., PIETRANERA, L., VALENTINI, G. & ZOFFOLI, S. 2010. COSMO-SkyMed an existing opportunity for observing the Earth. *Journal of Geodynamics,* 49**,** 171-180.

CROSSON, W. L., LIMAYE, A. S. & LAYMON, C. A. 2005. Parameter sensitivity of soil moisture retrievals from airborne L-band radiometer measurements in SMEX02. *Geoscience and Remote Sensing, IEEE Transactions on,* 43**,** 1517-1528.

CROW, W. T., BINDLISH, R. & JACKSON, T. J. 2005. The added value of spaceborne passive microwave soil moisture retrievals for forecasting rainfall - runoff partitioning. *Geophysical Research Letters,* 32.

CUTFORTH, H. W., MCGINN, S. M., MCPHEE, K. E. & MILLER, P. R. 2007. Adaptation of pulse crops to the changing climate of the northern Great Plains. *Agronomy Journal,* 99**,** 1684-1699.

CZAJKOWSKI, K. P., GOWARD, S. N., STADLER, S. J. & WALZ, A. 2000. Thermal Remote Sensing of Near Surface Environmental Variables: Application Over the Oklahoma Mesonet. *The Professional Geographer,* 52**,** 345-357.

DAS, N. N., ENTEKHABI, D. & NJOKU, E. G. 2011. An Algorithm for Merging SMAP Radiometer and Radar Data for High-Resolution Soil-Moisture Retrieval. *IEEE Transactions on Geoscience and Remote Sensing,* 49**,** 1504-1512.

DAS, N. N., ENTEKHABI, D., NJOKU, E. G., SHI, J. J. C., JOHNSON, J. T. & COLLIANDER, A. 2014. Tests of the SMAP Combined Radar and Radiometer Algorithm Using Airborne Field Campaign Observations and Simulated Data. *IEEE Transactions on Geoscience and Remote Sensing,* 52**,** 2018-2028.

DELWORTH, T. & MANABE, S. 1989. The Influence of Soil Wetness on Near-Surface Atmospheric Variability. *J. Climate,* 2**,** 1447-1462.

DESJARDINS, R. L. & OUELLET, C. E. 1980. Determination of importance of various phases of wheat growth on final yields. *Agric. Meteorol.,* 22**,** 129-136.

DESNOS, Y. L., BUCK, C., GUIJARRO, J., SUCHAIL, J. L., TORRES, R. & ATTEMA, E. 2000. ASAR-Envisat's Advanced Synthetic Aperture Radar: Building on ERS Achievements towards Future Earth Watch Missions. *ESA Bulletin,* 102.

DIRMEYER, P. A., ZENG, F. J., DUCHARNE, A., MORRILL, J. C. & KOSTER, R. D. 2000. The Sensitivity of Surface Fluxes to Soil Water Content in Three Land Surface Schemes. *Journal of Hydrometeorology,* 1**,** 121-134.

DOUVILLE, H., & CHAUVIN, F. 2004. Relevance of soil moisture for seasonal climate predictions: a preliminary study. *Climate Dynamics,* 16**,** 719-736.

DUBOIS, P. C., VAN ZYL, J. & ENGMAN, T. 1995. Measuring soil moisture with imaging radars. *Geoscience and Remote Sensing, IEEE Transactions on,* 33**,** 915-926.

ENTEKHABI, D., ASRAR, G. R., BETTS, A. K., BEVEN, K. J., BRAS, R. L., DUFFY, C. J., DUNNE, T., KOSTER, R. D., LETTENMAIER, D. P., MCLAUGHLIN, D. B., SHUTTLEWORTH, W. J., VAN GENUCHTEN, M. T., WEI, M.-Y. & WOOD, E. F. 1999. An Agenda for Land Surface Hydrology Research and a Call for the Second International Hydrological Decade. *Bulletin of the American Meteorological Society,* 80**,** 2043-2058.

ENTEKHABI, D., DAS, N. N., NJOKU, E. G., JOHNSON, J. & SHI, J. C. 2012. Algorithm Theoretical Basis Document: L2 & L3 Radar/Radiometer Soil Moisture (Active/Passive) Data Products, Initial Release, v. 1.

ENTEKHABI, D., NJOKU, E. G., HOUSER, P., SPENCER, M., DOIRON, T., YUNJIN, K., SMITH, J., GIRARD, R., BELAIR, S., CROW, W., JACKSON, T. J., KERR, Y. H., KIMBALL, J. S., KOSTER, R., MCDONALD, K. C., O'NEILL, P. E., PULTZ, T., RUNNING, S. W., JIANCHENG, S., WOOD, E. & VAN ZYL, J. 2004. The hydrosphere State (hydros) Satellite mission: an Earth system pathfinder for global mapping of soil moisture and land freeze/thaw. *Geoscience and Remote Sensing, IEEE Transactions on,* 42**,** 2184-2195.

ENTEKHABI, D., NJOKU, E. G., O'NEILL, P. E., KELLOGG, K. H., CROW, W. T., EDELSTEIN, W. N., ENTIN, J. K., GOODMAN, S. D., JACKSON, T. J., JOHNSON, J., KIMBALL, J., PIEPMEIER, J. R., KOSTER, R. D., MARTIN, N., MCDONALD, K. C., MOGHADDAM, M., MORAN, S., REICHLE, R., SHI, J. C., SPENCER, M. W., THURMAN, S. W., LEUNG, T. & VAN ZYL, J. 2010. The Soil Moisture Active Passive (SMAP) Mission. *Proceedings of the IEEE,* 98**,** 704-716.

EVETT, S. R., HENG, L. K., MOUTONNET, P. & NGUYEN, M. L. 2008. *Field estimation of soil water content: A practical guide to methods, instrumentation, and sensor technology,* Vinne, Austria, Intl. Atomic Energy Agency.

EVETT, S. R. & PARKIN, G. W. 2005. The continuing maturation of technology and theory. *Vadose Zone Journal,* 4, 986-991.

FENNESSY, M. J. & SHUKLA, J. 1999. Impact of Initial Soil Wetness on Seasonal Atmospheric Prediction. *Journal of Climate,* 12, 3167-3180.

FRIEDL, M. A. & DAVIS, F. W. 1994. Sources of variation in radiometric surface temperature over a tallgrass prairie. *Remote Sensing of Environment,* 48, 1-17.

GAO, Y., WALKER, J. P., YE, N., MONERRIS, A., PANCIERA, R., RYU, D. & RUDIGER, C. under review. Calibration and Validation of the Tau-Omega model with SMAPEx Data Sets for Passive Microwave Soil Moisture Retrieval. *IEEE Transactions on Geoscience and Remote Sensing.*

GARDNER, C. M. K., DEAN, T. J. & COOPER, J. D. 1998. Soil Water Content Measurement with a High-Frequency Capacitance Sensor. *Journal of Agricultural Engineering Research,* 71, 395-403.

GIACOMELLI, A., BACCHIEGA, U., TROCH, P. A. & MANCINI, M. 1995. Evaluation of surface soil moisture distribution by means of SAR remote sensing techniques and conceptual hydrological modelling. *Journal of Hydrology,* 166, 445-459.

GOWARD, S. N., XUE, Y. & CZAJKOWSKI, K. P. 2002. Evaluating land surface moisture conditions from the remotely sensed temperature/vegetation index measurements - An exploration with the simplified simple biosphere model. *Remote Sensing of Environment,* 79, 225-242.

HAIN, C. R., CROW, W. T., MECIKALSKI, J. R., ANDERSON, M. C. & HOLMES, T. 2011. An intercomparison of available soil moisture estimates from thermal infrared and passive microwave remote sensing and land surface modeling. *J. Geophys. Res.,* 116, D15107.

HAIN, C. R., MECIKALSKI, J. R. & ANDERSON, M. C. 2009. Retrieval of an Available Water-Based Soil Moisture Proxy from Thermal Infrared Remote Sensing. Part I: Methodology and Validation. *Journal of Hydrometeorology,* 10, 665-683.

HALLIKAINEN, M. T., ULABY, F. T., DOBSON, M. C., EL-RAYES, M. A. & LIL-KUN, W. 1985. Microwave Dielectric Behavior of Wet Soil-Part 1: Empirical Models and Experimental Observations. *Geoscience and Remote Sensing, IEEE Transactions on,* GE-23**,** 25-34.

HONG, S. Y. & KALNAY, E. 2000. Role of sea surface temperature and soil-moisture feedback in the 1998 Oklahoma-Texas drought. *Nature,* 408**,** 842-844.

JACKSON, T. J. 2001. Multiple resolution analysis of L-band brightness temperature for soil moisture. *Geoscience and Remote Sensing, IEEE Transactions on,* 39**,** 151-164.

JACKSON, T. J., HSU, A. Y. & O'NEILL, P. E. 2002. Surface Soil Moisture Retrieval and Mapping Using High-Frequency Microwave Satellite Observations in the Southern Great Plains. *Journal of Hydrometeorology,* 3**,** 688-699.

JACKSON, T. J., LE VINE, D. M., HSU, A. Y., OLDAK, A., STARKS, P. J., SWIFT, C. T., ISHAM, J. D. & HAKEN, M. 1999. Soil moisture mapping at regional scales using microwave radiometry: the Southern Great Plains Hydrology Experiment. *Geoscience and Remote Sensing, IEEE Transactions on,* 37**,** 2136-2151.

JACKSON, T. J., LE VINE, D. M., SCHIEBE, F. R. & SCHMUGGE, T. J. Large area mapping of soil moisture using passive microwave radiometry in the Washita'92 experiment. Geoscience and Remote Sensing Symposium, 1993. IGARSS '93. Better Understanding of Earth Environment., International, 18-21 Aug 1993 1993. 1009-1012 vol.3.

JACKSON, T. J. & SCHMUGGE, T. J. 1991. Vegetation effects on the microwave emission of soils. *Remote Sensing of Environment,* 36**,** 203-212.

JACKSON, T. J., SCHMUGGE, T. J. & WANG, J. R. 1982. Passive microwave sensing of soil moisture under vegetation canopies. *Water Resources Research,* 18**,** 1137-1142.

KALMAN, R. E. 1960. A New Approach to Linear Filtering and Prediction Problems. *Transactions of the ASME – Journal of Basic Engineering*, 35-45.

KERR, Y. 2007. Soil moisture from space: Where are we? *Hydrogeology Journal,* 15, 117-120.

KERR, Y. H., WALDTEUFEL, P., WIGNERON, J. P., DELWART, S., CABOT, F., BOUTIN, J., ESCORIHUELA, M. J., FONT, J., REUL, N., GRUHIER, C., JUGLEA, S. E., DRINKWATER, M. R., HAHNE, A., MARTI, X, N-NEIRA, M. & MECKLENBURG, S. 2010. The SMOS Mission: New Tool for Monitoring Key Elements ofthe Global Water Cycle. *Proceedings of the IEEE,* 98, 666-687.

KERR, Y. H., WALDTEUFEL, P., WIGNERON, J. P., MARTINUZZI, J., FONT, J. & BERGER, M. 2001. Soil moisture retrieval from space: the Soil Moisture and Ocean Salinity (SMOS) mission. *IEEE Transactions on Geoscience and Remote Sensing,* 39, 1729-1735.

KIM, G. & BARROS, A. P. 2002. Downscaling of remotely sensed soil moisture with a modified fractal interpolation method using contraction mapping and ancillary data. *Remote Sensing of Environment,* 83, 400-413.

KIM, Y. & VAN ZYL, J. J. 2009. A Time-Series Approach to Estimate Soil Moisture Using Polarimetric Radar Data. *Geoscience and Remote Sensing, IEEE Transactions on,* 47, 2519-2527.

KIZITO, F., CAMPBELL, C. S., CAMPBELL, G. S., COBOS, D. R., TEARE, B. L., CARTER, B. & HOPMANS, J. W. 2008. Frequency, electrical conductivity and temperature analysis of a low-cost capacitance soil moisture sensor. *Journal of Hydrology,* 352, 367-378.

KOSTER, R. D., DIRMEYER, P. A., GUO, Z., BONAN, G., CHAN, E., COX, P., GORDON, C. T., KANAE, S., KOWALCZYK, E., LAWRENCE, D., LIU, P., LU, C.-H., MALYSHEV, S., MCAVANEY, B., MITCHELL, K., MOCKO, D., OKI, T., OLESON, K., PITMAN, A., SUD, Y. C., TAYLOR, C. M., VERSEGHY, D., VASIC, R., XUE, Y. & YAMADA, T. 2004.

Regions of Strong Coupling Between Soil Moisture and Precipitation. *Science,* 305**,** 1138-1140.

LEESE, J. & KERMOND, J. 2000. Importance of Soil Moisture in Weather and Climate Prediction. *NOAA Research Spotlight Feature Article*.

LEIRIAO, S., HE, X., CHRISTIANSEN, L., ANDERSEN, O. B. & BAUER-GOTTWEIN, P. 2009. Calculation of the temporal gravity variation from spatially variable water storage change in soils and aquifers. *Journal of Hydrology,* 365**,** 302-309.

LU, Z. 2007. The Phase Shift Method for Studying Nonlinear Acoustics in a Soil. *Acta Acustica united with Acustica,* 93**,** 542-554.

MAGAGI, R., BERG, A. A., GOITA, K., BELAIR, S., JACKSON, T. J., TOTH, B., WALKER, A., MCNAIRN, H., O'NEILL, P. E., MOGHADDAM, M., GHERBOUDJ, I., COLLIANDER, A., COSH, M. H., BURGIN, M., FISHER, J. B., SEUNG-BUM, K., MLADENOVA, I., DJAMAI, N., ROUSSEAU, L. P. B., BELANGER, J., JIALI, S. & MERZOUKI, A. 2013. Canadian Experiment for Soil Moisture in 2010 (CanEx-SM10): Overview and Preliminary Results. *Geoscience and Remote Sensing, IEEE Transactions on,* 51**,** 347-363.

MCGINN, S. M. & SHEPHERD, A. 2003. Impact of climate change scenarios on the agroclimate of the Canadian prairies. *Canadian Journal of Soil Science,* 83**,** 623-630.

MERLIN, O., AL BITAR, A., WALKER, J. P. & KERR, Y. 2010. An improved algorithm for disaggregating microwave-derived soil moisture based on red, near-infrared and thermal-infrared data. *Remote Sensing of Environment,* 114**,** 2305-2316.

MERLIN, O., CHEHBOUNI, A., KERR, Y. H. & GOODRICH, D. C. 2006. A downscaling method for distributing surface soil moisture within a microwave pixel: Application to the Monsoon '90 data. *Remote Sensing of Environment,* 101**,** 379-389.

MERLIN, O., CHEHBOUNI, A. G., KERR, Y. H., NJOKU, E. G. & ENTEKHABI, D. 2005. A combined modeling and multispectral/multiresolution remote sensing approach for disaggregation of surface soil moisture: application to SMOS configuration. *Geoscience and Remote Sensing, IEEE Transactions on,* 43**,** 2036-2050.

MERLIN, O., WALKER, J. P., CHEHBOUNI, A. & KERR, Y. 2008a. Towards deterministic downscaling of SMOS soil moisture using MODIS derived soil evaporative efficiency. *Remote Sensing of Environment,* 112**,** 3935-3946.

MERLIN, O., WALKER, J. P., PANCIERA, R., ESCORIHUELA, M. J. & JACKSON, T. J. 2009. Assessing the SMOS Soil Moisture Retrieval Parameters With High-Resolution NAFE'06 Data. *Geoscience and Remote Sensing Letters, IEEE,* 6**,** 635-639.

MLADENOVA, I. E., JACKSON, T. J., BINDLISH, R. & HENSLEY, S. 2013. Incidence Angle Normalization of Radar Backscatter Data. *Geoscience and Remote Sensing, IEEE Transactions on,* 51**,** 1791-1804.

MULLER, E. & DÉCAMPS, H. 2001. Modeling soil moisture–reflectance. *Remote Sensing of Environment,* 76**,** 173-180.

MUSICK, H. B. & PELLETIER, R. E. 1988. Response to soil moisture of spectral indexes derived from bidirectional reflectance in thematic mapper wavebands. *Remote Sensing of Environment,* 25**,** 167-184.

NARAYAN, U., LAKSHMI, V. & JACKSON, T. J. 2006. High-resolution change estimation of soil moisture using L-band radiometer and Radar observations made during the SMEX02 experiments. *IEEE Transactions on Geoscience and Remote Sensing,* 44**,** 1545-1554.

NARAYAN, U., LAKSHMI, V. & NJOKU, E. G. 2004. Retrieval of soil moisture from passive and active L/S band sensor (PALS) observations during the Soil Moisture Experiment in 2002 (SMEX02). *Remote Sensing of Environment,* 92**,** 483-496.

NATIONAL-RESEARCH-COUNCIL 2007. Earth science and applications from space: national imperatives for the next decade and beyond. *National Academies Press*.

NIANG, M. A., NOLIN, M., BERNIER, M. & PERRON, I. 2012. Digital Mapping of Soil Drainage Classes Using Multitemporal RADARSAT-1 and ASTER Images and Soil Survey Data. *Applied and Environmental Soil Science,* 2012**,** 17.

NJOKU, E. G., JACKSON, T. J., LAKSHMI, V., CHAN, T. K. & NGHIEM, S. V. 2003. Soil moisture retrieval from AMSR-E. *Geoscience and Remote Sensing, IEEE Transactions on,* 41**,** 215-229.

NJOKU, E. G., WILSON, W. J., YUEH, S. H., DINARDO, S. J., LI, F. K., JACKSON, T. J., LAKSHMI, V. & BOLTEN, J. 2002. Observations of soil moisture using a passive and active low-frequency microwave airborne sensor during SGP99. *Geoscience and Remote Sensing, IEEE Transactions on,* 40**,** 2659-2673.

OH, Y., SARABANDI, K. & ULABY, F. T. 1992. An empirical model and an inversion technique for radar scattering from bare soil surfaces. *Geoscience and Remote Sensing, IEEE Transactions on,* 30**,** 370-381.

OWE, M., DE JEU, R. & WALKER, J. 2001. A methodology for surface soil moisture and vegetation optical depth retrieval using the microwave polarization difference index. *Geoscience and Remote Sensing, IEEE Transactions on,* 39**,** 1643-1654.

PALOSCIA, S., MACELLONI, G., SANTI, E. & KOIKE, T. 2001. A multifrequency algorithm for the retrieval of soil moisture on a large scale using microwave data from SMMR and SSM/I satellites. *Geoscience and Remote Sensing, IEEE Transactions on,* 39**,** 1655-1661.

PALOSCIA, S., SANTI, E., PETTINATO, S. & ANGIULLI, M. Soil properties estimates from SAR data by using a bayesian approach combined with IEM. Geoscience and Remote Sensing Symposium, 2004. IGARSS '04. Proceedings. 2004 IEEE International, 20-24 Sept. 2004 2004. 819-822.

PANCIERA, R., WALKER, J. P., JACKSON, T. J., GRAY, D. A., TANASE, M. A., DONGRYEOL, R., MONERRIS, A., YARDLEY, H., RUDIGER, C., XIAOLING, W., YING, G. & HACKER, J. M. 2014. The Soil Moisture Active Passive Experiments (SMAPEx): Toward Soil Moisture Retrieval From the SMAP Mission. *IEEE Transactions on Geoscience and Remote Sensing,* 52**,** 490-507.

PANCIERA, R., WALKER, J. P., KALMA, J. D., KIM, E. J., HACKER, J. M., MERLIN, O., BERGER, M. & SKOU, N. 2008. The NAFE'05/CoSMOS Data Set: Toward SMOS Soil Moisture Retrieval, Downscaling, and Assimilation. *Geoscience and Remote Sensing, IEEE Transactions on,* 46**,** 736-745.

PANCIERA, R., WALKER, J. P., KALMA, J. D., KIM, E. J., SALEH, K. & WIGNERON, J.-P. 2009. Evaluation of the SMOS L-MEB passive microwave soil moisture retrieval algorithm. *Remote Sensing of Environment,* 113**,** 435-444.

PANCIERA, R., WALKER, J. P., MERLIN, O., KALMA, J. D. & KIM, E. J. 2006. Scaling properties of L-band passive microwave soil moisture: From SMOS to paddock scale. *Proc. 30th Hydrol. Water Resour. Symp***,** 4-8.

PEISCHL, S., WALKER, J. P., RYU, D., KERR, Y. H., PANCIERA, R. & RUDIGER, C. 2012. Wheat Canopy Structure and Surface Roughness Effects on Multiangle Observations at L-Band. *Geoscience and Remote Sensing, IEEE Transactions on,* 50**,** 1498-1506.

PELLENQ, J., KERR, Y. & BOULET, G. Scaling and assimilation of SMOS data for hydrology. Geoscience and Remote Sensing Symposium, 2003. IGARSS '03. Proceedings. 2003 IEEE International, 2003 2003. 3064-3066 vol.5.

PIELKE, R. A., SR. 2001. Influence of the spatial distribution of vegetation and soils on the prediction of cumulus Convective rainfall. *Rev. Geophys.,* 39**,** 151-177.

PILES, M., CAMPS, A., VALL-LLOSSERA, M., CORBELLA, I., PANCIERA, R., X000FC, DIGER, C., KERR, Y. H. & WALKER, J. 2011. Downscaling SMOS-Derived Soil Moisture Using MODIS Visible/Infrared Data. *Geoscience and Remote Sensing, IEEE Transactions on,* PP**,** 1-11.

PILES, M., ENTEKHABI, D. & CAMPS, A. 2009. A Change Detection Algorithm for Retrieving High-Resolution Soil Moisture From SMAP Radar and Radiometer Observations. *IEEE Transactions on Geoscience and Remote Sensing,* 47**,** 4125-4131.

PU, R., GE, S., KELLY, N. M. & GONG, P. 2003. Spectral absorption features as indicators of water status in coast live oak (Quercus agrifolia) leaves. *International Journal of Remote Sensing,* 24**,** 1799-1810.

RANEY, R. K. 1998. Radar Fundamentals: Technical Perspective. *Chapter 2 in Principles and Applications of Imaging Radar, Manual of Remote Sensing, Third Edition, ,* Volume 2, ASPRS, John Wiley and Sons Inc., Toronto. .

REECE, C. F. 1996. Evaluation of a Line Heat Dissipation Sensor for Measuring Soil Matric Potential. *Soil Sci. Soc. Am. J.,* 60**,** 1022-1028.

ROBINSON, D. A., GARDNER, C. M. K. & COOPER, J. D. 1999. Measurement of relative permittivity in sandy soils using TDR, capacitance and theta probes: comparison, including the effects of bulk soil electrical conductivity. *Journal of Hydrology,* 223**,** 198-211.

ROBINSON, D. A., JONES, S. B., WRAITH, J. M., OR, D. & FRIEDMAN, S. P. 2003. A Review of Advances in Dielectric and Electrical Conductivity Measurement in Soils Using Time Domain Reflectometry. *Vadose Zone J.,* 2**,** 444-475.

RÜDIGER, C., CALVET, J.-C., GRUHIER, C., HOLMES, T. R. H., DE JEU, R. A. M. & WAGNER, W. 2009. An Intercomparison of ERS-Scat and AMSR-E Soil Moisture Observations with Model Simulations over France. *Journal of Hydrometeorology,* 10**,** 431-447.

RÜDIGER, C., WESTERN, A. W., WALKER, J. P., SMITH, A. B., KALMA, J. D. & WILLGOOSE, G. R. 2010. Towards a general equation for frequency domain reflectometers. *Journal of Hydrology,* 383**,** 319-329.

SAMOUËLIAN, A., COUSIN, I., TABBAGH, A., BRUAND, A. & RICHARD, G. 2005. Electrical resistivity survey in soil science: a review. *Soil and Tillage Research,* 83**,** 173-193.

SCHMAN, J., & DAY, J. 2005. Achieving operational hydrologic monitoring of mosquitoborne disease. *Emerging Infectious Diseases,* 11**,** 1343-1350.

SCHMIDL SOBJAERG, S. & SKOU, N. 2003. Polarimetric signatures from a crop covered land surface measured by an L-band polarimetric radiometer. *IEEE International Geoscience and Remote Sensing Symposium, 2003. IGARSS '03. Proceedings.*

SCHMUGGE, T., GLOERSEN, P., WILHEIT, T. & GEIGER, F. 1974. Remote sensing of soil moisture with microwave radiometers. *Journal of Geophysical Research,* 79**,** 317-323.

SELKER, J., VAN DE GIESEN, N., WESTHOFF, M., LUXEMBURG, W. & PARLANGE, M. B. 2006. Fiber optics opens window on stream dynamics. *Geophysical Research Letters,* 33**,** L24401.

SENEVIRATNE, S. I., CORTI, T., DAVIN, E. L., HIRSCHI, M., JAEGER, E. B., LEHNER, I., ORLOWSKY, B. & TEULING, A. J. 2010. Investigating soil moisture–climate interactions in a changing climate: A review. *Earth-Science Reviews,* 99**,** 125-161.

SHI, X. K., WEN, J., WANG, L., ZHANG, T. T., TIAN, H., WANG, X., LIU, R. & ZHANG, J. H. 2009. Application of satellite microwave remote sensed brightness temperature in the regional soil moisture simulation. *Hydrol. Earth Syst. Sci. Discuss.,* 6**,** 1233-1260.

SHIMADA, M., ISOGUCHI, O., TADONO, T. & ISONO, K. 2009. PALSAR Radiometric and Geometric Calibration. *Geoscience and Remote Sensing, IEEE Transactions on,* 47**,** 3915-3932.

SHUKLA, J. & MINTZ, Y. 1982. Influence of Land-Surface Evapotranspiration on the Earth's Climate. *Science,* 215**,** 1498-1501.

SMITH, A. B., WALKER, J. P., WESTERN, A. W., YOUNG, R. I., ELLETT, K. M., PIPUNIC, R. C., GRAYSON, R. B., SIRIWARDENA, L., CHIEW, F. H. S. & RICHTER, H. 2012. The Murrumbidgee soil moisture monitoring network data set. *Water Resources Research,* 48**,** W07701.

TIMBAL, B., POWER, S., COLMAN, R., VIVIAND, J. & LIROLA, S. 2001. Does Soil Moisture Influence Climate Variability and Predictability over Australia? *Journal of Climate,* 15**,** 1230-1238.

TRENBERTH, K. 1998. Atmospheric moisture residence times and cycling: Implications for rainfall rates and climate change. *Climate Change,* 39**,** 667-694.

TSEGAYE, T. D., CROSSON, W. L., LAYMON, C. A., SCHAMSCHULA, M. & JOHNSON, A. 2003. Scaling Methods in Soil Physics. CRC Press.

WAGNER, W., BLSCH, G., PAMPALONI, P., VALVET, J., BIZARRI, B., WIGNERON, J. AND KERR, Y. 2007. Operational readiness of microwave remote sensing of soil moisture for hydrologic applications. *Nordic Hydrology,* 38**,** 1-20.

WAGNER, W., SCIPAL, K., PATHE, C., GERTEN, D., LUCHT, W. & RUDOLF, B. 2003. Evaluation of the agreement between the first global remotely sensed soil moisture data with model and precipitation data. *Journal of Geophysical Research: Atmospheres,* 108**,** 4611.

WALKER, J. P. & HOUSER, P. R. 2002. Evaluation of the OhmMapper Instrument for Soil Moisture Measurement. *Soil Sci. Soc. Am. J.,* 66**,** 728-734.

WALKER, J. P., WILLGOOSE, G. R. & KALMA, J. D. 2004. In situ measurement of soil moisture: a comparison of techniques. *Journal of Hydrology,* 293**,** 85-99.

WANG, J. R. & SCHMUGGE, T. J. 1980. An Empirical Model for the Complex Dielectric Permittivity of Soils as a Function of Water Content. *Geoscience and Remote Sensing, IEEE Transactions on,* GE-18**,** 288-295.

WEN, J., JACKSON, T. J., BINDLISH, R., HSU, A. Y. & SU, Z. B. 2005. Retrieval of Soil Moisture and Vegetation Water Content Using SSM/I Data over a Corn and Soybean Region. *Journal of Hydrometeorology,* 6**,** 854-863.

WERNINGHAUS, R. 2004. TerraSAR-X mission. *Proc. SPIE 5236, SAR Image Analysis, Modeling, and Techniques VI,* 5236**,** 9-16.

WESTERN, A. W. & SEYFRIED, M. S. 2005. A calibration and temperature correction procedure for the water-content reflectometer. *Hydrological Processes,* 19**,** 3785-3793.

WIGNERON, J., CHANZY, A., KERR, Y. H., LAWRENCE, H., JIANCHENG, S., ESCORIHUELA, M. J., MIRONOV, V., MIALON, A., DEMONTOUX, F., DE ROSNAY, P. & SALEH-CONTELL, K. 2011. Evaluating an Improved Parameterization of the Soil Emission in L-MEB. *Geoscience and Remote Sensing, IEEE Transactions on,* 49**,** 1177-1189.

WRAITH, J. M. & OR, D. 1999. Temperature effects on soil bulk dielectric permittivity measured by time domain reflectometry: Experimental evidence and hypothesis development. *Water Resources Research,* 35**,** 361-369.

WU, X., WALKER, J. P., DAS, N. N., PANCIERA, R. & RÜDIGER, C. In Press-a. Evaluation of the SMAP Brightness Temperature Downscaling Algorithm using Active-Passive Microwave Observations. *Remote Sensing of Environment*.

WU, X., WALKER, J. P., PANCIERA, R., RUDIGER, C. & DAS, N. N. Downscaling of coarse-resolution radiometer brightness temperature by high-resolution radar backscatter. *In:* PIANTADOSI, J., ANDERSSEN, R. S. & J., B., eds. The 20th International Congress on Modeling and Simulation (MODSIM2013), 2013 Adelaide, Australia. Modelling and Simulation Society of Australia and New Zealand, 3127-3133.

WU, X., WALKER, J. P., RÜDIGER, C. & PANCIERA, R. In Press-b. Effect of land cover type on the SMAP active/passive soil moisture downscaling algorithm performance. *Geoscience and Remote Sensing Letters, IEEE*.

WU, X., WALKER, J. P., RÜDIGER, C., PANCIERA, R. & GRAY, D. 2015. Simulation of the SMAP Data Stream from SMAPEx Field Campaigns in Australia. *IEEE Transactions on Geoscience and Remote Sensing,* 53**,** 1921-1934.

WU, X., WALKER, J. P., RUDIGER, C., PANCIERA, R., MONERRIS, A. & DAS, N. N. Towards medium-resolution brightness temperature retrieval from active and passive microwave. *In:* CHAN, F., MARINOVA, D. & ANDERSSEN, R. S., eds. The 19th International Congress on Modeling and Simulation (MODSIM2011), 2011 Perth, Australia. Modelling and Simulation Society of Australia and New Zealand, 2023-2029.

YE, N., WALKER, J. P. & RÜDIGER, C. In Review. A cumulative distribution function method for normalising multi-angle microwave observations. *Geoscience and Remote Sensing, IEEE Transactions on*.

YOUNG, M. H., CAMPBELL, G. S. & YIN, J. 2008. Correcting Dual-Probe Heat-Pulse Readings for Changes in Ambient Temperature All rights reserved. No part of this periodical may be reproduced or transmitted in any form or by any means, electronic or mechanical, including photocopying, recording, or any information storage and retrieval system, without permission in writing from the publisher. *Vadose Zone J.,* 7**,** 22-30.

YUEH, S., DINARDO, S., CHAN, S., NJOKU, E., JACKSON, T. & BINDLISH, R. 2008. Passive and Active L-Band System and Observations during the 2007 CLASIC Campaign. *Geoscience and Remote Sensing Symposium, 2008. IGARSS 2008. IEEE International. Proceedings.*

YUEH, S., DINARDO, S., CHAN, S., NJOKU, E., JACKSON, T. & BINDLISH, R. 2009. PALS-ADD and airborne campaigns to support soil moisture and sea surface salinity missions. *Proc. IEEE International Geoscience and Remote Sensing Symposium 2009.* Cape Town, South-Africa.

YUEH, S. H., KWOK, R. & NGHIEM, S. V. 1994a. Polarimetric scattering and emission properties of targets with reflection symmetry. *Radio Science,* 29**,** 1409-1420.

YUEH, S. H., WILSON, W. J., NGHIEM, S. V., FUK, K. L. & RICKETTS, W. B. 1994b. Polarimetric passive remote sensing of ocean wind vectors. *Geoscience and Remote Sensing Symposium, 1994. IGARSS'94. IEEE International. Proceedings.*

ZEGELIN, S. 1996. Soil Moisture Measurement. In: *Field Measurement Techniques in Hydrology - Workshop Notes. In:* COOPERATIVE RESEARCH CENTRE FOR CATCHMENT HYDROLOGY, C. C. (ed.). Clayton.

ZHAN, X., HOUSER, P. R., WALKER, J. P. & CROW, W. T. 2006. A method for retrieving high-resolution surface soil moisture from hydros L-band radiometer and radar observation. *IEEE Transactions on Geoscience and Remote Sensing,* 44**,** 1534-1544.

ZHANG, Y. & WEGEHENKEL, M. 2006. Integration of MODIS data into a simple model for the spatial distributed simulation of soil water content and evapotranspiration. *Remote Sensing of Environment,* 104**,** 393-408.